# Mechanistic and inhibition studies on Isocitrate Dehydrogenase 1

A thesis submitted to the Board of the Faculty of the Mathematical, Physical and Life Sciences Division for the degree of

**Doctor of Philosophy** in **Chemical Biology**

**Shuang LIU**




Pembroke College | Department of Chemistry | University of Oxford
Michaelmas Term 2019

# DECLARATION

I declare that the work described and the figures presented in this thesis are entirely my own, except where I have acknowledged help and/or data from a named person, or given reference to a published source.

Shuang Liu

Pembroke College, University of Oxford, Michaelmas Term 2019

# ACKNOWLEDGEMENTS

I would like to thank all the people who have contributed in various ways to my DPhil life at Oxford.

My deepest thanks go to my supervisor, Professor Chris Schofield, for his unfailing trust, support, optimism, and encouragement to explore new ideas throughout my DPhil. He has made me strive to be a better academic researcher. He has also made it possible for me to carry out part of my work at Evotec (Abingdon, UK), which has been an extremely valuable industry experience, especially with the help from Mark Whittaker, John Scott, Stephanie Duclos and Sandrine Thieffine.

I am extremely grateful for the generous funding received from A*STAR (Singapore) that supported my studies from my undergraduate degree to my DPhil (and now to my Postdoc).

Special thanks to Martine Abboud for patiently guiding me especially when I first started my project on IDH, and for providing me with all the IDH1 proteins necessary for my research; to Victor Mikhailov for spending almost a year with me optimising and performing non-denaturing MS experiments; to Mohammadali Foroozandeh who is extremely knowledgeable in NMR and has made all the DOSY work possible to solve my longstanding puzzle; to Lennart Brewitz for being a warm-hearted gentleman and skilled chemist and for providing me with all the synthetic 2OG analogues; to Yu Nakashima who has impressively collected X-ray data on more than 50 crystals (including salt) and solved their structures; to Xiao Liu who has been a close friend and student who helped me complete parallel studies on IDH2 very meticulously.

I must acknowledge Choon Boon Cheong for sacrificing a significant amount of his time proofreading my entire thesis, literally sentence by sentence. I would also like to thank Chris, Martine and Lennart for their very detailed editings, as well as Ali, Tom, James, Jacqueline and Erica for their constructive feedback on the individual chapters.

The greatest appreciation goes to my parents for their unconditional love and support in pursuing my career, despite me not being able to accompany them since I was abroad at a young age. Lastly, a special thank you to Xiyu Jiao for lighting up my life- I feel really fortunate to have met him.

# TABLE OF CONTENTS

**Abstract** ..... 1

**List of Abbreviations** ..... 2

**Chapter 1. Introduction** ..... 4

1.1 IDH mutations in cancer ..... 4

1.2 Cellular impacts of IDH mutations ..... 8

1.2.1 Elevated levels of 2HG ..... 9

1.2.2 Depletion of NADPH and oxidative damage ..... 12

1.2.3 2OG availability and regulation of HIF ..... 13

1.2.4 Other downstream alterations ..... 15

1.3 Controversies and complexities ..... 16

1.3.1 Variable clinical outcomes in gliomas and AML ..... 16

1.3.2 Causation or correlation? ..... 17

1.3.3 Improved survival in glioma with IDH1 mutations ..... 17

1.3.4 Beyond targeting inhibition of IDH mutants ..... 18

1.4 Therapeutic advances with mutant IDH1/2 inhibitors ..... 23

1.5 Overview of the thesis ..... 27

**Chapter 2. Basic Characterisation of wt IDH1 and R132H IDH1** ..... 29

2.1 Kinetic comparison of wt IDH1 and R132H IDH1 ..... 29

2.2 Structural comparison of wt and R132H IDH1 ..... 33

2.3 Binding studies of (co)substrates to IDH1 ..... 37

2.3.1 Role of $Mg^{2+}$ ions in IDH1 catalysis- an unexpected observation ..... 39

2.4 (Co)substrates requirement of IDH1 ..... 40

2.4.1 D-isocitrate is the substrate for wt IDH1 ..... 40

2.4.2 Phosphate group in NADP(H) is key in cofactors binding to IDH1 ..... 41

2.4.3 $Mg^{2+}$ and $Mn^{2+}$ are active metal ions for IDH1 ..... 44

2.5 Effect of pH on IDH1 activity ..... 45

2.6 Preliminary inhibitor screening against IDH1 ..... 48

2.7 Summary ..... 54

2.8 Supplementary Figures ..... 55

**Chapter 3. Metal ions play a key role in the allosteric inhibition of R132H IDH1** ..... 57
3.1 Metal ions in biology ..... 57
3.2 Biochemical studies of metal ions for IDH1 ..... 58
3.3 Effect of metal ions on substrate binding to IDH1 ..... 61
3.3.1 Binding of isocitrate to wt IDH1 ..... 62
3.3.2 Binding of weakly bound ligands to IDH1 ..... 66
3.4 Competition studies of IDH1 substrates and inhibitors ..... 70
3.4.1 Binding of isocitrate and inhibitors to wt IDH1 is mutually exclusive ..... 70
3.4.2 Metal ions help isocitrate but not 2OG to stay bound to IDH1 ..... 72
3.4.3 Inhibitors displace metal ions from R132H IDH1 ..... 75
3.4.4 Metal ions affect efficacy of R132H IDH1 inhibitors ..... 78
3.5 Mode of inhibition of R132H IDH1 inhibitors ..... 79
3.6 Summary ..... 82
3.7 Supplementary Figures ..... 83
**Chapter 4. Studies on metabolite-metal ion complexes using DOSY** ..... 87
4.1 A more 'symmetrical' isocitrate ..... 87
4.2 DOSY ..... 93
4.3 Isocitrate with different metal ions ..... 97
4.4 Other metabolites and metal ions ..... 102
4.5 Variable temperature studies on the isocitrate-$Mg^{2+}$ complex ..... 111
4.6 Summary ..... 113
**Chapter 5. Inhibitor Profiling of IDH1** ..... 114
5.1 Biochemical characterisation of inhibitors of IDH variants ..... 114
5.1.1 Absorbance-based assays ..... 116
5.1.2 NMR reaction monitoring ..... 119
5.2 Biophysical characterisation of inhibitors of IDH variants ..... 120
5.2.1 DSF analyses on IDH inhibition ..... 120
5.2.2 ITC analyses on IDH inhibition ..... 122
5.2.3 Non-denaturing MS analyses on IDH inhibition ..... 123
5.2.4 NMR Spectroscopy analyses on IDH inhibition ..... 128
5.2.5 CD analyses on IDH inhibition ..... 130
5.3 PROTAC ..... 131

5.4 Summary ..... 136
5.5 Supplementary Figures ..... 137
**Chapter 6. Covalent inhibitors of R132H IDH1** ..... 139
6.1 Time-dependent inhibition studies ..... 141
6.2 Covalent modifications as measured by denaturing LC-MS ..... 144
6.3 Binding studies ..... 151
6.3.1 Non-denaturing MS ..... 151
6.3.2 DSF ..... 155
6.3 Summary ..... 156
6.4 Supplementary Figures ..... 157
**Chapter 7. Two-way functional 2OG analogues** ..... 160
7.1 TCA cycle intermediates and their analogues ..... 160
7.2 Synthetic 2OG analogues ..... 165
7.2.1 Biochemical studies on synthetic 2OG analogues ..... 165
7.2.2 Product identification by Anion Exchange Chromatography-MS ..... 170
7.2.3 Mechanistic studies by NMR spectroscopy ..... 172
7.3 Summary ..... 175
7.4 Supplementary Figures ..... 176
**Chapter 8. Conclusions** ..... 177
**Appendix Novel approaches for antibody-based targeted drug delivery** ..... 180
A.1 Introduction ..... 180
A.2 The model system and the strategies employed ..... 181
A.3 Results ..... 184
A.4 Conclusion ..... 186
**Experimental methods** ..... 187
**References** ..... 203

# Mechanistic and inhibition studies on Isocitrate Dehydrogenase 1

A thesis submitted for the degree of Doctor of Philosophy in Chemical Biology
Shuang Liu
Pembroke College, Michaelmas Term 2019

## ABSTRACT

Genes encoding for IDH1 and IDH2 are frequently mutated in multiple cancer types including gliomas and AML. IDH variants, notably R132H IDH1, result in a gain-of-function leading to substantially enhanced production of the 'oncometabolite', 2-hydroxyglutarate. Drug development by pharmaceutical companies has yielded potent R132H IDH1 inhibitors, unusually nearly all of which work by an allosteric mechanism, implying undetermined processes during substrate and inhibitor binding to IDH1. Mechanistic studies revealed the fundamental role of metal ions in facilitating substrate binding to wt IDH1 and R132H IDH1. DOSY NMR experiments revealed structures of such metabolite-metal ion complexes in solution that are distinct from the published X-ray crystal structures. The studies also suggested that R132H IDH1 selective inhibitors likely work by displacing the protein-bound metal ion, providing the mechanistic basis for mutant IDH inhibition and the opportunities for improved therapies through metal ion interference. Comparative studies on clinically relevant mIDH inhibitors showed that the mIDH1 inhibitors bind to wt IDH1 and R132H IDH1 with similar binding affinities despite their inhibitory selectivity for the variant. In light of the recently emerged resistance to IDH targeting drugs, several novel therapeutic strategies for treating IDH malignancies were then investigated, including the targeted degradation of R132H IDH1, covalent inhibition of R132H IDH1 through selective cysteine-reacting inhibitors, as well as exploiting substrate analogues as active site binding inhibitors. It is hoped that both the mechanistic and inhibition studies described in this work will help enable the development of improved therapies targeting IDH.

# LIST OF ABBREVIATIONS

| | |
|---|---|
| **2HG** | 2-Hydroxyglutarate |
| **2OG** | 2-Oxoglutarate |
| **2TY** | 2× Tryptone yeast extract |
| **ADC** | Antibody-drug conjugates |
| **AEC-MS** | Anion exchange chromatography mass spectrometry |
| **AKT** | Protein kinase B |
| **ALKBH** | 2OG-dependent AlkB homolog |
| **AML** | Acute myeloid leukemia |
| **AMP** | Antigen-mimicking peptide |
| **APS** | Ammonium persulfate |
| **ATRX** | Alpha-thalassemia mental retardation syndrome X-linked gene |
| **BLI** | Biolayer interferometry |
| **CD** | Circular Dichroism |
| **CDKN2A** | Cyclin dependent kinase inhibitor 2A |
| **CoA** | Coenzyme A |
| **CPMG** | Carr–Purcel–Meiboom–Gill |
| **Cryo-EM** | Cryogenic electron microscopy |
| **DIPEA** | *N*,*N*-Diisopropylethylamine |
| **DMF** | Dimethylformamide |
| **DNMT1** | DNA methyltransferase 1 |
| **DOSY** | Diffusion-ordered spectroscopy |
| **DSF** | Differential scanning fluorimetry |
| ***E. coli*** | *Escherichia coli*, a gram-negative bacterium |
| **EDTA** | Ethylenediaminetetraacetic acid |
| **Fab** | Fragment antigen-binding |
| **FTO** | Fat mass and obesity-associated protein |
| **GBM** | Glioblastoma multiforme |
| **gnomAD** | Genome aggregation database |
| **GSH** | Reduced glutathione |
| **HATU** | Hexafluorophosphate azabenzotriazole tetramethyl uronium |
| **HEPES** | 4-(2-hydroxyethyl)-1-piperazineethanesulfonic acid |
| **HER2** | Human epidermal growth factor receptor 2 |
| **HGMD** | Human gene mutation database |
| **HIF** | Hypoxia-inducible factor |
| **ICP-MS** | Inductively coupled plasma mass spectrometry |
| **IDH** | Isocitrate dehydrogenase |
| **IPTG** | Isopropyl β-D-1-thiogalactopyranoside |
| **ITC** | Isothermal titration calorimetry |
| $k_{cat}$ | Turnover rate of an enzyme converting substrate to product |
| $K_D$ | Dissociation constant, the ligand concentration at which half of the protein molecules have ligand bound |
| $K_M$ | Michaelis constant, the substrate concentration at which the reaction reaches half of $V_{max}$ |

| | |
|---|---|
| **KDM** | Histone lysine demethylase |
| **KRAS** | Ki-ras2 Kirsten rat sarcoma viral oncogene homolog |
| **LC-MS** | Liquid chromatography mass spectrometry |
| **LC-MS/MS** | Liquid chromatography tandem mass spectrometry |
| **m/z** | Mass over charge |
| **MAb** | Monoclonal antibody |
| **MET** | Mesenchymal epithelial transition |
| **mIDH** | Mutant forms of isocitrate dehydrogenase |
| **MS** | Mass spectrometry |
| **NA** | Not applicable |
| **$NADP^+$** | Nicotinamide adenine dinucleotide phosphate |
| **NADPH** | Reduced nicotinamide adenine dinucleotide phosphate |
| **ND** | Not determined |
| **NMR** | Nuclear magnetic resonance |
| **NOESY** | Nuclear overhauser effect spectroscopy |
| **NOG** | *N*-Oxalylglycine |
| **PBS** | Phosphate-buffered saline |
| **PDB** | Protein data bank |
| **PDGFRA** | Platelet-derived growth factor receptor alpha |
| **PEG** | Polyethylene glycol |
| **PFG** | Pulsed field gradient |
| **PHD** | Prolyl hydroxylase domain |
| **PI3K** | Phosphoinositide 3-kinase |
| **PIK3CA** | Phosphatidylinositol-4,5-bisphosphate 3-kinase catalytic subunit alpha |
| **PROTAC** | Proteolysis targeting chimera |
| **PTEN** | Phosphatase and tensin homolog |
| **r.t.** | Room temperature, typically 298K |
| **Ref** | Reference |
| **RTK** | Receptor tyrosine kinases |
| **SD** | Standard deviation |
| **SDS** | Sodium dodecyl sulfate |
| **SDS-PAGE** | Sodium dodecyl suphate-polyacrylamide gel electrophoresis |
| **SEM** | Standard error of the mean |
| **$T_m$** | Melting temperature |
| **TBST** | Tris-buffered saline with 0.1% (v/v) Tween 20 |
| **TBTA** | Tris[(1-benzyl-1H-1,2,3-triazol-4-yl)methyl]amine |
| **TCA** | Tricarboxylic (cycle), also known as the citric acid cycle or the Krebs cycle |
| **TCEP** | Tris(2-carboxyethyl)phosphine |
| **TEMED** | *N*,*N*,*N*',*N*'-Tetramethylethylenediamine |
| **TET** | Ten-eleven translocation |
| **TFA** | Trifluoroacetic acid |
| **TP53** | Tumour suppressor protein 53 |
| **Tris** | Tris(hydroxymethyl)aminomethane |
| **$V_{max}$** | Maximum velocity |
| **VHL** | Von Hippel–Lindau |
| **wt** | Wildtype |

# CHAPTER 1. INTRODUCTION

## 1.1 IDH mutations in cancer

Metabolic reprogramming is a hallmark of cancer and correlates with mutations in genes encoding for enzymes involved in metabolism[1]. The tricarboxylic (TCA) cycle, normally consisting of eight enzymes catalysed reactions and their corresponding metabolic intermediates (**Figure 1.1**), represents a central metabolic pathway for processing glucose, amino acids and fatty acids in aerobic organisms. Among the TCA cycle enzymes, succinate dehydrogenase (SDH), fumarate hydratase (FH) and malate dehydrogenase (MDH) can undergo germline loss-of-function mutations associated with conditions such as paraganglioma, Reed syndrome and hereditary leiomyomatosis and renal cell cancer (HLRCC)[2–4]. By contrast, mutations in isocitrate dehydrogenase (IDH) 1 and 2 genes are somatic and found in >80% of gliomas[5,6] and 20–30% of acute myeloid leukaemia (AML)[7–9]. The gene encoding for IDH1 is by far the most frequently mutated metabolic gene found in cancer[10]. IDH1 and its variants are the main subjects of investigation of the work described in this thesis. Variants of IDH1 and IDH2 acquire a gain-of-function ability to convert 2-oxoglutarate (2OG) to 2-hydroxyglutarate (2HG), resulting in substantially elevated 2HG levels in tumours bearing IDH mutations[11].

There are three human IDH isoforms *i.e.* IDH1, IDH2 and IDH3. IDH1 localises to the cytoplasm whilst IDH2 and IDH3 localise to mitochondria. IDH1 and IDH2 are both homodimeric and have ~70% sequence identity and ~80% sequence similarity[12]; IDH3 is heterotetrameric and has a sequence distinct from the much more closely related sequences of IDH1/2. The *IDH1* and *IDH2* genes can undergo mutations which are linked to cancer[13]; by contrast, no tumour-associated mutations have been reported in the *IDH3* gene.

IDH3 catalyses the $NAD^+$-dependent oxidative decarboxylation of D-isocitrate to 2OG in the TCA cycle. The IDH3 reaction is reported to be irreversible[14]. IDH1 and IDH2 catalyse the $NADP^+$-dependent oxidative decarboxylation of D-isocitrate to 2OG, in a reversible manner[15]. The reverse reaction of IDH1/2 enables the control of relative cellular abundance of isocitrate and 2OG[16]. 2OG can be converted back to isocitrate by

IDH1/2, and ultimately to acetyl-CoA to support fatty acid biosynthesis[17]. Cancer associated substitutions in IDH1 and IDH2 impair the wildtype activity, and also introduce a neomorphic ability for the enzyme to convert 2OG to D-2-hydroxyglutarate (D-2HG), using NADPH as the cofactor[11] (**Scheme 1.1**).

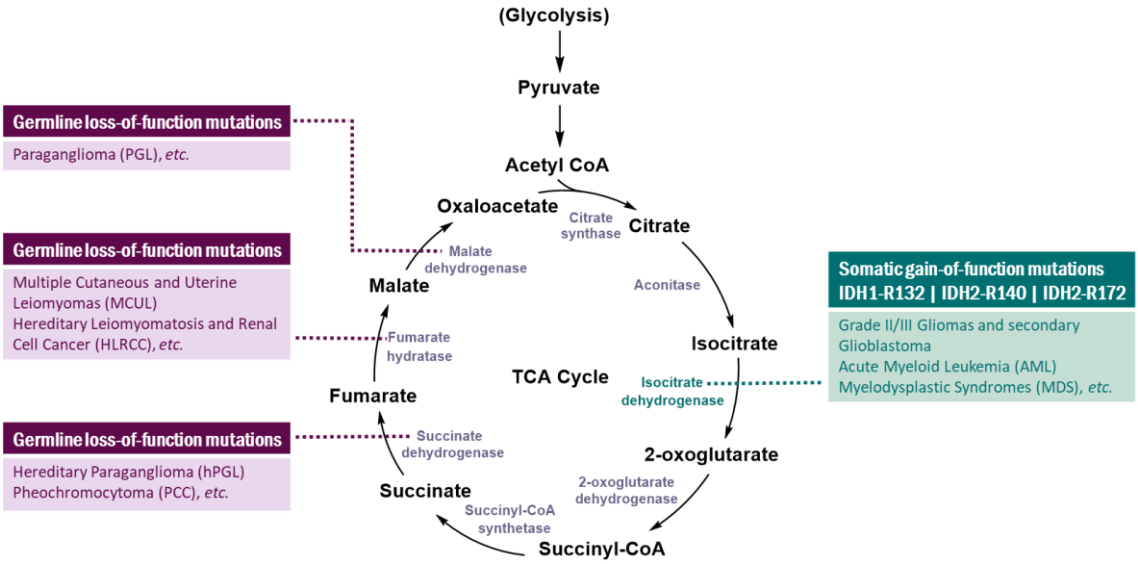
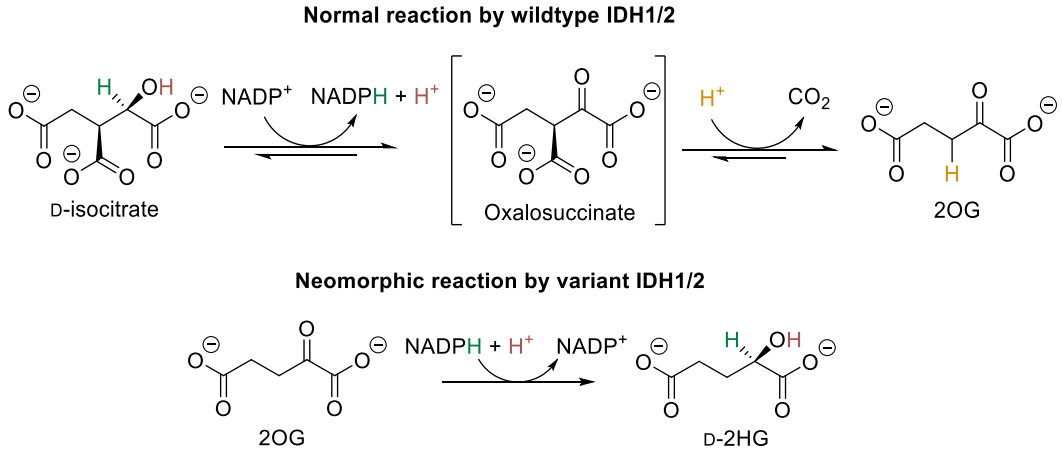



**Figure 1.1**. Mutations of tricarboxylic acid cycle enzymes involved in cancer. Malate dehydrogenase, fumarate hydratase and succinate dehydrogenase undergo germline loss-of-function mutations associated with conditions such as paraganglioma[2–4]. Isocitrate dehydrogenases undergo somatic gain-of-function mutations as exemplified by IDH1 R132, IDH2 R140 and IDH2 R172 variants, some of which are drug targets for treatment of gliomas, glioblastoma and acute myeloid leukemia[18].




**Scheme 1.1**. Oxidative and reductive reactions catalysed by wildtype (wt) and variant IDH1/2 respectively. The reversible conversion of isocitrate to 2OG and $CO_2$ by wt IDH1/2 is proposed to proceed by (1) oxidation of isocitrate to the unstable intermediate oxalosuccinate with $NADP^+$ as the hydride acceptor[9,19], followed by (2) spontaneous decarboxylation of oxalosuccinate to give 2OG[20]. Variant IDH1/2 catalyses the irreversible reduction of 2OG to 2HG using NADPH as the hydride donor.

The two most common cancer types associated with IDH1/2 variants are gliomas and AML, discussed in detail below. In this context, gliomas refer to grade II/III gliomas as well as secondary glioblastoma multiforme (GBM) which is grade IV and is derived from grade II/III gliomas[21]. IDH1/2 variants have also been reported in other rare cancers including cholangiocarcinomas, chondrosarcomas and angioimmunoblastic T-cell lymphoma (AITL)[9].

Treatment of gliomas relies mainly on surgery and chemotherapy. Surgical resection is rarely curative for higher grade gliomas and GBMs due to their infiltrative characteristics[6]. Traditional chemotherapeutic agents such as Temozolomide, are not only cytotoxic to normal cells due to their DNA-damaging mechanisms (strategies for targeted delivery of cytotoxic anticancer agents are discussed in **Appendix**), but are also associated with recurrence of tumours[22]. Consequently, the 5-year survival rates for GBM patients have remained low at <5% with no improvement over three decades[23].

The first correlation between *IDH* gene mutations and human cancer was established in a genome sequencing analysis of GBM in 2008, where heterozygous point mutations in the IDH1 encoding gene occurred nearly exclusively in secondary GBM[24]. In 2009, both *IDH1* and *IDH2* gene mutations were identified in grade II/III gliomas[25]. Overall, *IDH1/2* gene mutations are present in >80% of grade II/III gliomas especially oligodendroglioma, and secondary GBM[5,6]. Only 6% of patients with primary GBM have *IDH1/2* gene mutations, suggesting a distinct mechanism of tumorigenesis for different subtypes of gliomas[24,26]. Notably, the IDH1 R132H variant, in which an arginine is replaced by a histidine, represents 80% of all IDH mutations in gliomas[18,27–29]. IDH1 R132H is therefore used as a model enzyme in this thesis to study IDH variants.

Soon after the identification of recurring *IDH1/2* gene mutations in gliomas, IDH1[30] and IDH2[31] gene mutations in AML were reported in 2009 and 2010 respectively. On average, the prevalence of *IDH1/2* gene mutations in AML patients is 20%[7–9].

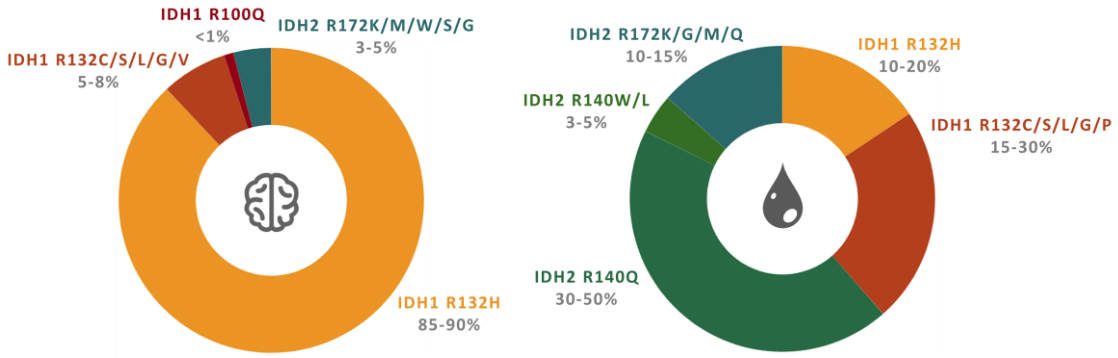



**Figure 1.2**. Pie chart representation of distribution of IDH1 and IDH2 variants found in grade II/III gliomas and secondary glioblastomas (left) and AML (right), based on data summarised in a review by Losman and Kaelin[9].

**Figure 1.2** illustrates the distribution of *IDH1* and *IDH2* gene mutations in gliomas and AML. In gliomas, the majority (>90%) of *IDH* gene mutations are in IDH1, and are dominated by the R132H IDH1 variant. More rarely, substitutions are also found at R172 of IDH2[25,29]; R172 is structurally analogous to R132 of IDH1. This is in contrast to AML where *IDH2* gene mutations occur at similar or higher frequencies compared to *IDH1* gene mutations[9]. The most common substitution in AML is IDH2 R140Q which is exclusive to AML. The analogous IDH1 R100Q is rare and only found in grade II/III gliomas[32,33]. All the arginine residues substituted (IDH1 R132/R100 and IDH2 R172/R140) are mainly involved in binding the substrate isocitrate at the IDH1/2 active sites[12]. Interestingly, *IDH1* and *IDH2* gene mutations are mutually exclusive, *i.e.* no patients harbouring both *IDH1* and *IDH2* gene mutations have yet been identified[9,34].

## 1.2 Cellular impacts of IDH mutations

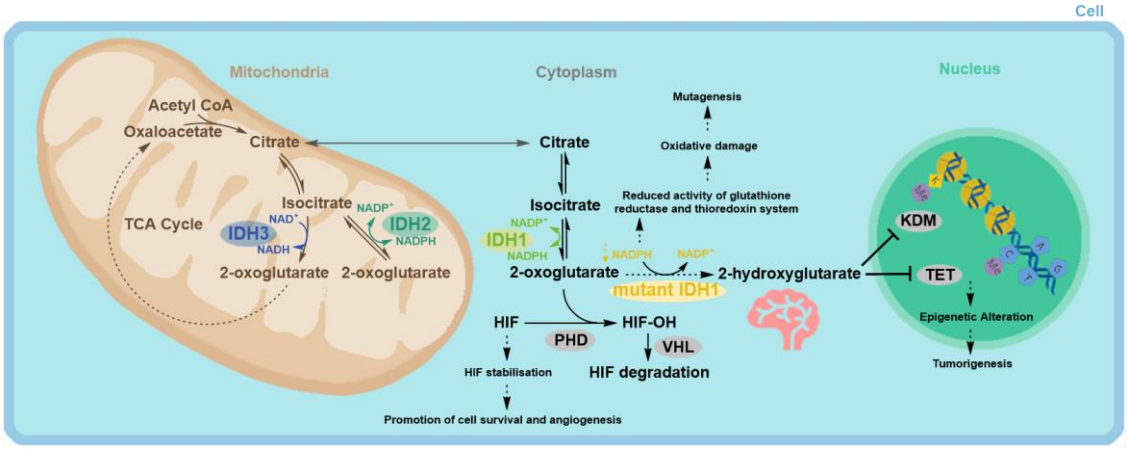



**Figure 1.3**. Schematic representation of the roles of wt IDH1/2/3, and the multiple effects of mutant IDH1 in cells. Different subcellular localisation (IDH1: cytoplasm; IDH2/3: mitochondria) and cofactor usage (IDH1/2: $NADP^+$; IDH3: $NAD^+$) distinguish the three human IDH isoforms. Cellular effects of mutant IDH1 stem from the accumulation of 2HG, the depletion of NADPH and the reduced availability of 2OG.

As shown in **Figure 1.3**, the potential cellular impacts of NADPH-dependent conversion of 2OG to D-2HG catalysed by mutant IDH1 can be analysed from three perspectives: increased levels of the product D-2HG, depletion of the cofactor NADPH, and changes in levels of 2OG that is a cosubstrate for the 2OG-dependent dioxygenases.

The vast majority of studied 2OG-dependent dioxygenases catalyse the oxidation of substrates using $O_2$ and $Fe^{2+}$, with concurrent conversion of 2OG to succinate and $CO_2$. There are around 70 human 2OG-dependent dioxygenases[9] that have a diverse range of biological roles including hypoxic sensing, nucleic acid repair and modification, collagen biosynthesis and fatty acid metabolism. Several 2OG-dependent dioxygenases are therapeutic targets for diseases such as anaemia[35,36].

With respect to IDH malignancies, the following discussion focuses on the Jumonji C domain-containing histone lysine demethylases (JmjC KDMs) and the ten-eleven translocation (TET) enzymes (**Section 1.2.1**), as well as the hypoxia inducible factor (HIF) prolyl hydroxylases (PHDs) (**Section 1.2.3**). It is, however, recognised that the cellular impacts of IDH mutations may extend to other 2OG-dependent dioxygenases, such as those involved in nucleic acid modifications (*e.g.* the AlkB homologues and fat mass and

obesity-associated protein (FTO)), collagen biosynthesis, ribosomal modification, and lipid metabolism (**Table 1.1**).

### 1.2.1 Elevated levels of 2HG

The IDH1/2 variants produce the D- isomer of 2HG ((*R*)-2HG) due to asymmetric enzyme catalysis[11]. D-2HG can accumulate in millimolar concentrations and >100-fold excess in glioma and AML patients harbouring *IDH* gene mutations[11,37,38]. Consequently, 2HG serves as a biomarker for *IDH1/2* gene mutations in gliomas[39,40]. Low levels of D-2HG can normally be cleared by conversion to 2OG by a D-2HG dehydrogenase (D2HGDH), but the clearance rate is likely insufficient to suppress the high levels of 2HG produced by IDH variants[11,41]. D2HGDH is a mitochondrially localised enzyme, a property which contributes to its ineffectiveness in clearing cytosolic 2HG produced by IDH1 variants. One study showed that D2HGDH, as a 2OG contributor, influences IDH activity in the mitochondria, but not in the cytosol[42]. Interestingly, mutations of the genes encoding for D2HGDH and L-2HG dehydrogenase (L2HGDH) are associated with rare diseases[43,44].

Due to the structural similarity between 2HG and 2OG, it has been proposed that elevated levels of 2HG competitively inhibit 2OG-dependent epigenetic regulators, including the JmjC KDM[45–49] and the TET enzymes, both of which are involved in chromatin modifications[46,50]. Both KDM and TET control gene expression by mediating histone demethylation and oxidation of *N*-methylcytosine on DNA, respectively.

Histone methylation and demethylation patterns are controlled by balanced activities of histone methylases and demethylases. Histones play a key role in the chromatin structures and hence their (de)methylation regulates gene expression. The JmjC KDMs demethylate *N*-methylated lysine and, possibly, *N*-methylated arginine[51] residues of histones. Disruption of histone lysine methylation as a result of impaired KDM activity has been linked to multiple cancer types including prostate and lung cancers[52]. D-2HG has been reported to inhibit the JmjC enzymes KDM2A, KDM4A, KDM4C and KDM7A *in vitro*[45–47]. Xu *et al.* showed an increase in histone methylation on H3K4, H3K9, H3K27, and H3K79 following ectopic expression of R132H IDH1 in glioma cells[46]. By contrast, in IDH1 mutant oligodendroglioma samples, Lu *et al.* reported an increase in H3K9

trimethylation that is associated with repressive transcription but no significant change in H3K4 trimethylation that is associated with active transcription, suggesting that *IDH* gene mutations may regulate repressive histone methylation *in vivo*[47] (**Figure 1.4**).

The TET enzymes catalyse the oxidation of C-5 methylated cytosines in DNA by hydroxylating 5-methylcytosine (5mC) to 5-hydroxymethycytosine (5hmC), which can then undergo further oxidation to 5-formylcytosine (5fC) and 5-carboxylcytosine (5caC)[53]. TET catalysed oxidation of 5-methylcytosine has been proposed to enable direct demethylation as well as demethylation via base excision repair[54]. Unmethylated cytosines result in an open chromatin structure, enabling active gene transcription. D-2HG has been reported to inhibit 33% of TET2 activity at 10 mM in enzymatic assays[46].

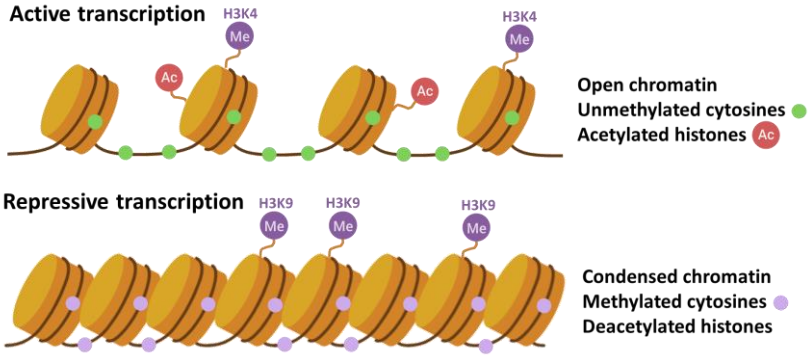



**Figure 1.4**. Graphical representation of regulation of gene transcription, adapted from Moore *et al.*[55] Chromatin comprises of histones (orange cylinder) wrapped by DNA (brown line). Active transcription in the form of open chromatin is associated with unmethylated cytosines by TET, acetylated histone, and histone tail trimethylation at H3K4. Repressive transcription in the form of closed chromatin is associated with methylated cytosines, deacetylated histones and histone tail trimethylation at H3K9.

Competitive inhibition of the jmjC KDMs and the TETs by D-2HG could contribute to the histone and DNA hypermethylation displayed in IDH mutant gliomas and AML[45–50,56]. These epigenetic alterations block differentiation of cancer cells, allowing cancer cells to grow and proliferate continuously, thereby promoting tumorigenesis[57]. **Table 1.1** shows the diverse cellular consequences that may result from elevated levels of D-2HG. The combined studies indicate that the effects of 2HG on chromatin may be complex. It should also be noted that 2HG is not a potent inhibitor of any 2OG-dependent dioxygenases, though its high concentrations in tumour cells may compensate for its

weak inhibition. The reduction in 2HG levels in cells bearing IDH mutations may also rescue 2OG oxygenase activity.

Also presented in **Table 1.1** are the proposed cellular impacts from the abnormal accumulation of succinate[58] and fumarate[59], as a result of mutated SDH and FH, respectively. Given their structural similarity to 2OG, fumarate, succinate and 2HG may share a common pathway by competitively inhibiting 2OG-dependent dioxygenases, including the PHDs, the JmjC KDMs and the TETs. Together, these provide mechanistic insights to how mutations in metabolic enzymes may contribute to tumorigenesis[10,13].

| Metabolite | Effect | Molecular target | Proposed consequences | Ref. |
|---|---|---|---|---|
| **2HG** | Inhibition | KDM | Histone methylation, blocked MyoD-mediated differentiation, mTOR activation | 45–49 |
| **2HG** | Inhibition | TET | DNA methylation | 46,50 |
| **2HG** | Inhibition | PHD | HIF-1α induction | 46,60 |
| **2HG** | Activation | PHD | HIF-1α reduction | 61 |
| **2HG** | Inhibition | Collagen prolyl and lysine hydroxylase | Impaired collagen maturation | 60 |
| **2HG** | Inhibition | 2OG-dependent AlkB homolog (ALKBH) | Impaired DNA repair | 62,63 |
| **2HG** | Inhibition | Fat mass and obesity-associated protein (FTO) | RNA methylation, suppression of MYC/CEBPA-associated pathways | 64,65 |
| **2HG** | Inhibition | ATP synthase | Mitochondrial respiration and mTOR signalling reduction | 66 |
| **2HG** | Binding | DNA methyltransferase 1 (DNMT1) | RIP3 downregulation | 67 |
| **2HG** | Binding | BCAT transaminases | Impaired glutamate biosynthesis | 68 |
| **Succinate** | Inhibition | KDM | Histone methylation | 69–71 |
| **Succinate** | Inhibition | TET | DNA methylation | 29 |
| **Succinate** | Inhibition | PHD | HIF-1α induction | 72–74 |
| **Fumarate** | Inhibition | KDM | Histone methylation | 70,75 |
| **Fumarate** | Inhibition | TET | DNA methylation | 70 |
| **Fumarate** | Inhibition | PHD | HIF-1α induction | 73,74,76 |

**Table 1.1.** The multiple cellular targets and pathways potentially affected by the accumulation of 2HG, succinate and fumarate. The interaction targets of these metabolites extend beyond metabolic enzymes to many 2OG-dependent dioxygenases due to structural similarity with 2OG, resulting in diverse cellular consequences. Mixed evidence is found on whether mTOR and HIF-1α are activated by 2HG.

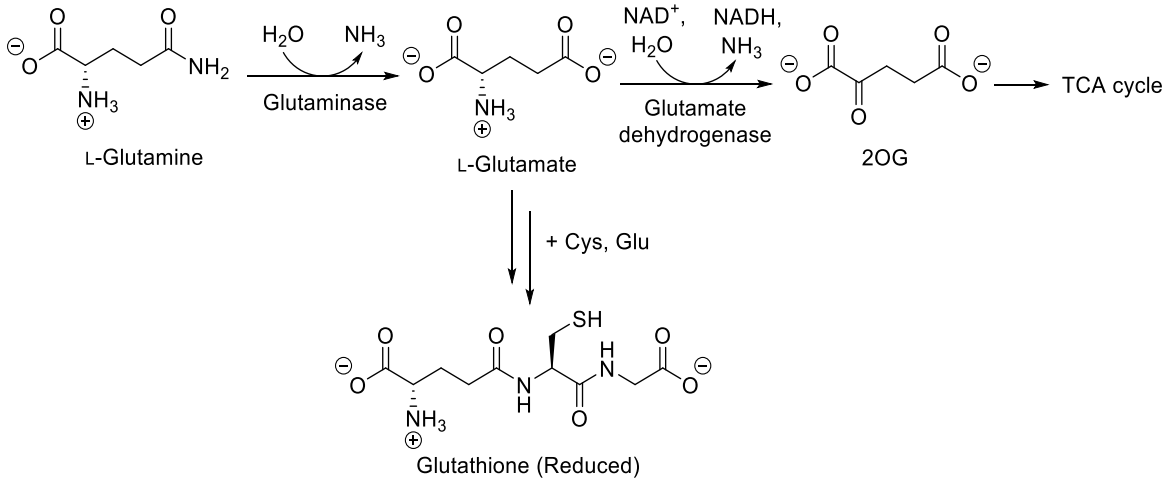
### 1.2.2 Depletion of NADPH and oxidative damage

In addition to the role of IDH1 in producing 2OG required by many cytoplasmic and nuclear 2OG-dependent dioxygenases, IDH1 is an important source of NADPH in the cytoplasm. IDH2 represents the major pathway for mitochondrial NADPH generation[77]. In GBM, IDH is reported to be responsible for 65% of the total NADPH production capacity[78]. NADPH is a reducing agent that maintains cellular redox balance, protects cells from oxidative damage, and is required for fatty acid biosynthesis and the regeneration of reduced glutathione (GSH)[77,79].

Mutations in *IDH* genes result in a reduction in the NADPH/$NADP^+$ ratio. This is because mutant IDH not only loses the wildtype activity to produce NADPH, but also consumes NADPH in its enzymatic conversion of 2OG to 2HG[60,78,80]. One study suggested that the R132H IDH1 variant reduced normal NADPH production by 38% in GBM tissue samples[78]. Consumption of NADPH for 2HG synthesis is reported to decrease NADPH-dependent fatty acid synthesis, thereby increasing pentose phosphate pathways to support the NADPH demands, and sensitising IDH1 mutant cells to oxidative stress[81]. Furthermore, depletion of NADPH also impairs the regeneration of GSH, a ubiquitous antioxidant which protects cells from oxidative stress by neutralising reactive oxygen species (ROS). As a result, GSH is found at lower levels in both R132H IDH1 overexpressing glioma cells[80] and knock-in mice[60]. Reduction in NADPH and GSH levels can result in oxidative damage, which may cause mutations in DNA, ultimately leading to tumorigenesis. Perturbed redox homeostasis has been reported to promote tumour cell survival in IDH1-mutant gliomas[82].

The reduction in GSH can be further exacerbated by the depletion of glutamine[83]. Tumour cells derive most of their energy from aerobic glycolysis of glucose to lactate without entering the TCA cycle[84]. The progression of lower grade glioma to the more aggressive phenotypes has been correlated to increased lactate formation, in a manner linked to loss of DNA methylation in glycolytic genes[85]. Glutamine, being the most abundant amino acid in humans, serves as an additional energy source to meet the high metabolic demands of tumour cells[86,87]. Glutamine can be converted to glutamate and then to 2OG to replenish TCA cycle intermediates[88] (**Scheme 1.2**). Isotope-labelling

experiments indicated that D-2HG produced by mutant IDH1/2 is derived not only from glucose, but also from glutamine via the intermediate glutamate[11,81]. Glutamate is also a substrate used in the biosynthesis of GSH[89] (**Scheme 1.2**). Reduced glutamate levels, as observed in R132H IDH1-expressing cells, implicates a further reduction in GSH, potentially leading to oxidative damage.




**Scheme 1.2**. Conversion of L-glutamine to L-glutamate and subsequently to 2OG to enter the TCA cycle. Glutamate is also a substrate to synthesise reduced glutathione.

### 1.2.3 2OG availability and regulation of HIF

Besides the KDMs and the TETs, the HIF-α prolyl hydroxylases (PHDs) are also 2OG dependent dioxygenases. The PHDs mediate cellular response to hypoxia[90]. Under normal oxygen levels, the PHDs catalyse the prolyl-hydroxylation of transcription factors, the HIFs, using 2OG and $O_2$ as (co)substrates, and $Fe^{2+}$ as a cofactor (**Figure 1.5**). Hydroxylated HIF is ubiquitinated by the von Hippel–Lindau (VHL) E3 ubiquitin ligase complex and targeted for efficient proteasomal degradation. Under hypoxic conditions, low availability of $O_2$ slows PHD-catalysed hydroxylation of HIF-α. The so stabilised HIF-α translocates to the nucleus and initiates transcription of target genes, for instance, in angiogenesis, that works to ameliorate the effects of hypoxia, but which may also promote tumour progression[90].

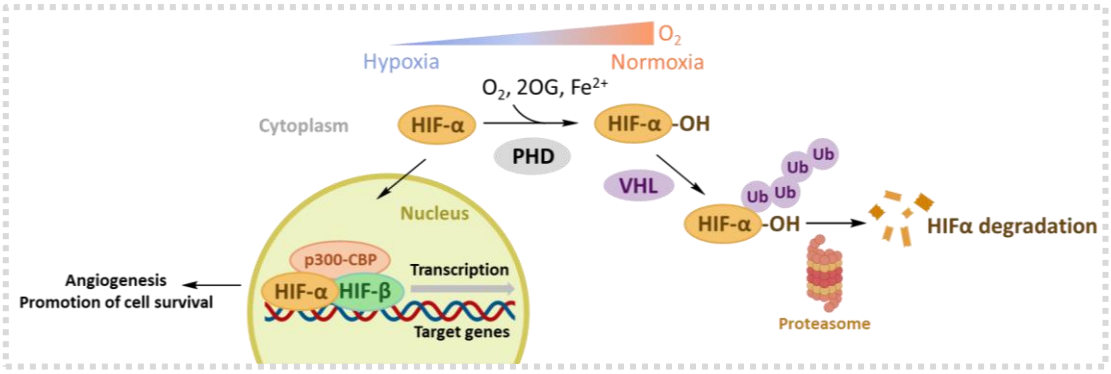



**Figure 1.5**. Schematic representation of the HIF system. Under normoxic conditions, hypoxia-inducible factors (HIF-α) are hydroxylated by the HIF prolyl hydroxylases (PHD). Hydroxylated α-subunit of the HIF is recognised by VHL E3 ubiquitin ligase complex and subsequently ubiquitinated, leading to its proteasomal degradation. Under hypoxic conditions, HIF-α is stabilised, translocates to the nucleus and binds to HIF-β and p300-CBP (a transcriptional coactivator) to initiate transcription of HIF target genes.

Stabilisation of HIF can also be attributed to decreased availability of 2OG. As mentioned in **Section 1.2.2**, although mutant IDH consumes 2OG, 2OG stocks can likely be replenished from glutamine[83]. This implies that there is a continuous source of 2OG for its conversion to 2HG by mutant IDH, and that the decrease in 2OG levels may not be coupled to the drastic increase in 2HG levels.

Accordingly, there is mixed evidence on HIF activity in IDH mutant gliomas. Some studies show no correlation between HIF expression and IDH mutant gliomas[91,92]; others show either upregulation[60,93] or downregulation[61] of HIF-1α in cells expressing mutant IDH1, possibly due to the variable $O_2$ availability in different studies. It is proposed that the microvascular proliferation featured in GBM is in part due to the activation of HIF[94]. In a counter-intuitive mechanism for downregulation of HIF, PHD catalysis is proposed to be coupled to oxidation of D-2HG, *i.e.* D-2HG behaves as a PHD agonist rather than an inhibitor[61,95]. Note that the $IC_{50}$ of D-2HG for PHD2 is high at 7.3 mM[45], and D-2HG concentration in IDH mutant glioma is 5–35 mM[11]. One possible reason for the agonist activity of 2HG is its non-enzymatic conversion to 2OG[96], although this is unlikely to occur at sufficient levels. Although HIF is usually viewed as a oncogene (or proto-oncogene) that is predicted to be activated in cancers[97], multiple studies suggest its tumour suppressor role, especially in glioma[98,99] and leukemic[100] cells. For example, inhibition of HIF reduces angiogenesis but enhances tumour growth in glioma cells, partly due to a reduction in tumour cell apoptosis[98]. The expression levels of many HIF

target genes are also decreased in IDH mutant gliomas[101,102]. Collectively, these findings raise the possibility that activation of HIF via PHD inhibition or other mechanisms may impair mutant IDH tumour growth[61].

### 1.2.4 Other downstream alterations

Assuming IDH mutation is a driver to initiate IDH mutant cancer, mutant IDH inhibitors may be effective in treating the disease at early stage. As tumour malignancy progresses, the metabolic landscape within the tumour microenvironment constantly evolves in a complex manner that may trigger other genotypic and phenotypic alterations to support tumour growth. It has been reported that alterations in known oncogenes, *PIK3CA*, *KRAS*, *AKT* or *PTEN*, and amplification of *PDGFRA*, *MET* or *N-MYC*, found in IDH1 mutant glioma patients during disease progression, are associated with shorter survival[103]. Targeted inhibition of some of these alterations decreases tumour cell proliferation[103]. Genomic analyses also reveal that activation in signalling pathways, including MYC and RTK-RAS-PI3K, enhances IDH1 mutant glioma progression. In IDH2 mutant AML, co-occurring mutations in the RAS pathway contribute to the therapeutic resistance to an IDH2 inhibitor, Enasidenib, despite its potent suppression of 2HG[104]. Inhibition of MYC pathways reduces the viability of IDH2 mutant AML cells[105]. Overall, multiple reports and reviews have suggested that combination therapy, such as demethylating agents to correct DNA hypermethylation or vaccines to stimulate immunity to ameliorate 2HG-mediated immunosuppression[106], may improve therapeutic outcomes[6,107,108].

## 1.3 Controversies and complexities

### 1.3.1 Variable clinical outcomes in gliomas and AML

To date, targeted treatment for AML has achieved marked success with two FDA approvals of mutant IDH1 (Ivosidenib)[109] and IDH2 (Enasidenib)[110] inhibitors. By contrast, although IDH mutations have stronger association with gliomas, there has been a lack of glioma patient responses to IDH1/2 inhibitors[111]. Two possible reasons are outlined below.

Firstly, blood-brain barrier (BBB) presents a major challenge for drug delivery in general, with 98% of small-molecule drugs being unable to enter the brain[112]. Unfortunately, there is not yet a rational way in medicinal chemistry to design brain-penetrant drugs. Ivosidenib, Enasidenib and Vorasidenib (pan mutant IDH1/2 inhibitor) have been shown to cross the BBB in rodent models[113–115]. However, rodent models are very often not predictive of human responses and clinical conditions, partly due to the complex transporters and efflux pumps in the brain, and different metabolic pathways of the drug as exemplified by Enasidenib[115].

Secondly, as discussed in **Section 1.2.4**, other oncogenic drivers besides mutant IDH may cooperate or dominate as glioma progresses. Although it is straightforward to block 2HG production by IDH inhibition, epigenetic changes driven by mutant IDH can be less easily reversed especially in tissue types like the central nervous system (CNS)[108,116]. Three separate studies demonstrated that inhibition of mutant IDH1 suppresses 2HG levels but does not attenuate tumour growth in glioma[117–119]. In addition, although two studies showed that inhibitors of DNA methylation, Decitabine and 5-azacytidine, are able to reduce DNA methylation, induce cellular differentiation and reduce cell growth in IDH mutant gliomas[120,121], clinical trials have not shown conclusive benefit[122,123]. Interestingly, Johannessen *et al.* suggested that continuous mutant IDH1 activity is not required to maintain the glioma phenotype[116]. It is likely that other oncogenic drivers are present to sustain disease progression. As such, inhibiting IDH alone might have minimal therapeutic benefit.

### 1.3.2 Causation or correlation?

It is important to understand whether the relationship between the mutations of metabolic genes and tumorigenesis is causative or correlative, and in this context, whether IDH mutations truly cause cancer by driving early tumorigenic processes. Analysis of the databases of genetic variations demonstrates a high degree of correlation between *IDH1* mutations and pathogenic phenotypes: no variants of IDH were found among the healthy population (database: gnomAD) while a variety of IDH1 variants were found in the pathogenic population (databases: HGMD and ClinVar)[124]. In addition, *IDH1* was identified as one of the cancer driver genes from analysis of genomic data[125].

Nevertheless, the complexity in the cellular network also suggests the possibility of multiple genes driving tumorigenesis. Indeed, several *in vivo* evidence demonstrated that mutant IDH1 alone is insufficient for glioma development. Two studies showed that although increased levels of 2HG and DNA methylation as well as repression of the tumour-associated immune system occur as a result of expressing R132H IDH1 in mice, no gliomas were observed, even in combination with TP53 and/or CDKN2A loss[126,127]. It was reported that in order to induce gliomagenesis in mouse models, R132H IDH1 needs to cooperate with PDGFA and loss of tumour suppressors CDKN2A, ATRX and PTEN[128]. Low-grade astrocytoma, a form of grade II glioma, carries mutations in IDH1 concurrently with P53 and ATRX loss[129]. Similar to IDH1 mutations, loss of P53 or ATRX alone did not result in brain tumour formation[130–132]. Overall, these findings demonstrated that R132H IDH1 correlates with glioma, but the actual cause of tumorigenesis may require multiple genetic alterations, besides IDH mutations, possibly in a defined order.

### 1.3.3 Improved survival in glioma with IDH1 mutations

One interesting observation is that glioma patients with *IDH1/2* gene mutations are associated with an increase in overall survival compared to those with wt *IDH* genes[24,25,78,133–135]. Consistent with human gliomas, mouse models expressing R132H IDH1 show increased 2HG production, DNA methylation, survival rate, and reduced infiltration of immune cells[127]. By contrast, wt IDH1 gliomas are associated with high

levels of chemokines and interleukins that stimulate infiltration of immune cells, which is linked to poor prognosis in many cancer types[127,136]. Other studies attribute the better prognosis of IDH mutant gliomas to the higher sensitivity of IDH mutant tumours to chemotherapy[80] and radiotherapy[137]. Cells expressing R132H IDH1 are found to be more sensitive to conventional chemotherapy drugs, temozolomide and cisplatin, possibly due to the R132H IDH1-induced depletion of NADPH and GSH as well as increased ROS generation as discussed in **Section 1.2.2**.

### 1.3.4 Beyond targeting inhibition of IDH mutants

Drug development strategies employed for IDH malignancies have followed a typical workflow by identification and validation of a target *e.g.* mutant IDH in glioma and AML, and then finding inhibitors of mutant IDH. Preclinical studies have provided proof of concept that targeted inhibition of mutant IDH yields therapeutic benefit by promoting cellular differentiation in both gliomas and AML[138,139]. Unfortunately, the first two FDA-approved mutant IDH1/2 inhibitors for AML treatment not only face drug resistance as manifested by a second-site mutation of the enzyme[140], but are also associated with differentiation syndrome, a life-threatening side effect[141].

The better prognosis associated with *IDH1* gene mutations in glioma patients seems to suggest that in addition to the tumour-promoting effects, mutant IDH may mediate growth inhibition at the same time. This puts into question whether inhibiting mutant IDH should be the only therapeutic approach. Elevated 2HG levels and redox stress generated by mutant IDH have been conventionally considered to be oncogenic: 2HG inhibits many 2OG-dependent dioxygenases while redox stress promotes oxidative damage (**Section 1.2**). The following attempts to offer an alternative perspective on the roles of 2HG and ROS.

#### 1.3.4.1 Alternative roles of 2HG and ROS

The potency of IDH1/2 inhibitors is frequently tested by measuring levels of the putative 'oncometabolite' 2HG, based on the underlying assumption that 2HG facilitates oncogenic transformation and blocking its production abrogates tumour growth[6,138]. In contrast to the common belief, recent evidence highlights the role of 2HG as a tumour

suppressor that prevents tumour progression after its initiation. D-2HG can inhibit the oncogenic activity of FTO, leading to RNA methylation and suppression of relevant pathways to prevent cancer proliferation[65]. D-2HG also inhibits ATP synthase and mTOR signalling, thereby inhibiting growth of R132H IDH1-expressing cells[66]. These potential anti-tumorigenic effects of 2HG may partly explain the low incidence of IDH mutations in primary GBM, and the better prognosis observed in IDH mutant gliomas where 2HG levels are higher than in wt IDH gliomas.

The role of ROS in tumorigenesis is a double-edged sword. ROS can initiate cell transformation by causing mutations in DNA, whereas in already transformed cells, a high level of ROS can induce apoptosis through various signalling pathways, thereby suppressing tumour growth[142,143]. In fact, many chemotherapy (including treatment of GBM[144]) and radiotherapy kill cancer cells, not by increasing antioxidant levels, but by augmenting ROS stress[145]. Increasing ROS generation has been shown to reverse chemoresistance to temozolomide in gliomas[146]. In IDH1 mutant cells, enhanced oxidative DNA damage decreases cell proliferation by blocking NRF2 which is responsible for transcription of antioxidant [147]. In this case, increased levels of ROS sensitise IDH1 mutant cells to chemotherapy[147]. Overall, increasing ROS levels *i.e.* pro-ROS may be an alternative therapeutic approach to treat IDH mutant cancers.

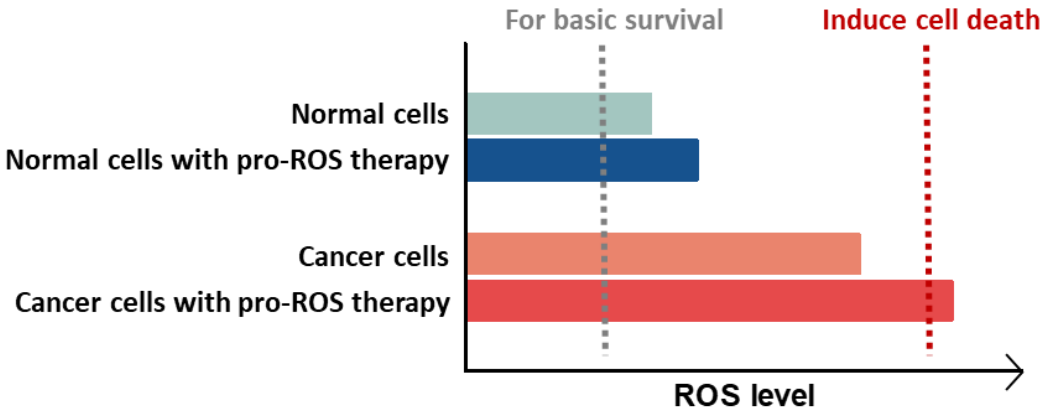



**Figure 1.6**. Illustration of threshold theory for pro-ROS approach, adapted from Wang *et al.*[148]. A certain level of ROS is required for basic cell survival (grey dotted line), but highly elevated ROS above a cellular tolerance threshold induces cell death (red dotted line). For cancer cells that have significantly more ROS (light red) than normal cells (light blue), further increasing ROS via the pro-ROS approach can induce cell death of cancer cells (red). Normal cells have a profound antioxidant system to cope with additional ROS so remain unaffected (dark blue). These result in the selective killing of cancer cells.

It is probably important to understand when to employ an anti-ROS or a pro-ROS strategy. Wang *et al.* proposed a 'threshold theory' as illustrated in **Figure 1.6**[148]. It recognises that the decision for controlling cancer cells by decreasing or increasing ROS depends on the magnitude of ROS levels: cancer cells with modestly increased ROS are suitable for reducing ROS to alleviate oxidative stress, whilst those with highly elevated ROS are suitable for increasing ROS further to trigger cell death.

Current evidence on the level of ROS in IDH1 mutant tumour is controversial. ROS are reported to be either higher[80,149–151], lower[60] or unaffected[61,152] in mutant IDH1/2 cells or mouse models compared to the wt counterparts. These could be due to some studies measuring steady-state conditions, using an insensitive ROS marker (CM-$H_2$DCFDA)[153,154], the effects being compartmentalised[9], and/or the models failing to mimic certain defective mechanisms in human cancers.

Should 2HG and ROS generated by mutant IDH play a tumour suppressing role in IDH mutant cancers under certain conditions, inhibiting mutant IDH might worsen the disease.

#### 1.3.4.2 Targeting wildtype IDH1

Nearly all reported cancer-linked *IDH* gene mutations are heterozygous[13,25,155]. This should theoretically result in a mixture of wt homodimer, mutant homodimer and wt/mutant heterodimer of IDH within cancer cells. The actual distribution of these species has not been determined. Both the mutant homodimer and the wt/mutant heterodimer of IDH1 can generate 2HG[156,157], suggesting a dominant effect of the mutant allele over the wt allele[158]. One study proposed that mutant IDH1, but not mutant IDH2, depends on the heterodimerisation with the wt allele for 2HG production, as the wt IDH subunit can supply 2OG as the substrate for the mutant subunit[159]. It has been suggested that the differing dependence of 2HG production on wt IDH activity is because 2OG is limiting in cytoplasm for 2HG production by IDH1, but not in mitochondria for the case of IDH2[159]. For heterozygous IDH1 mutant tumours, a significantly lower 2HG level is found in gliomas that undergo loss of the wildtype *IDH1* allele[155]. It follows that inhibiting the remaining wt *IDH1* allele to reduce local 2OG availability may alleviate pro-tumour effects of IDH1 mutations.

Separate studies have been conducted on IDH1 deficiency that may be useful in predicting the consequences of inhibiting wt IDH1[79,160,161]. IDH1-deficient mice showed a reduced 2OG level which attenuates 2OG-dependent transamination of glucogenic amino acids[160]. Upon treatment with lipopolysaccharide which induces ROS, IDH1 knockout mice showed a lower NADPH/$NADP^+$ ratio, higher levels of ROS and inflammatory cytokines, and were more susceptible to oxidative damage than the untreated group[161]. Cellular studies also demonstrated that IDH1 deficient cells have reduced defence against oxidative stress[79]. This is where a pro-ROS strategy (**Section 1.3.4.1**) might be adopted. Nonetheless, under the standard laboratory conditions, the IDH1 knockout mice have normal development and fertility, implying that inhibiting wt IDH1 activity is tolerable for survival[161].

Disrupting the TCA cycle can serve as a promising approach for cancer treatment. A pioneering example of inhibiting TCA cycle enzymes for therapeutic benefit is the inhibition of 2OG dehydrogenase complex (OGDHC) which converts 2OG to succinyl CoA[162]. Inactivating OGDHC disrupts the TCA cycle, attenuates cell growth, induces apoptosis, and most importantly, is sufficient to delay tumour initiation without affecting normal development in zebrafish[162]. An inhibitor of OGDHC, CPI-613, is in phase 2 clinical trials for treating pancreatic cancer[163]. In gastric cancer, overexpressed HNK4α sustains the oncogenic metabolism by regulating wt IDH1, implicating the clinical relevance of drugs targeting wt IDH1[164]. In non-small cell lung cancer, wt IDH1 is upregulated and associated with poor prognosis[165]. In GBM, wt IDH1 is also found to be overexpressed and to promote tumour growth[166]. Tumour cells may depend on wt IDH for its NADPH generation to maintain redox homeostasis and support fatty acid biosynthesis for survival, thus inhibiting wt IDH may be a promising therapeutic strategy[167].

The choice of whether to optimally use wt-selective or pan-wt/mutant IDH1 inhibitors for cancer treatment possibly depends on several unpredictable factors, including whether co-inhibition of wt and mutant IDH1 is overly disruptive, whether the effects of mutant IDH1 is truly adverse at all stages of cancer, and how efficient 2OG is supplied by the alternative source, GDH. In IDH mutant-free cancers, specific targeting of wt IDH1 might be achieved either by exploiting its overexpression at the tumour site, or through

a targeted delivery system to the tumour site. In IDH mutant cancers, particularly gliomas, a targeted delivery carrier may be hindered by the blood brain barrier. One possible approach would be to inhibit the wt subunit of the wt/mutant heterodimer. It is not conclusive whether existing inhibitors inhibit the wt subunit of the heterodimer due to limitations in the assay design. For instance, inhibition of mutant IDH2 by Enasidenib in the oxidative conversion of isocitrate is measured by formation of NADPH[168]. In a wt/mutant heterodimer, a decrease in NADPH could be due to either inhibition of wt activity, or active wt but fast consumption of NADPH by the mutant. The latter may be ruled out if low mutant activity is shown in a counter screen, although free 2OG in assay buffer may not represent the locally high concentrations of 2OG provided by the wt subunit. In another instance, inhibition of heterodimeric mutant IDH1 by GSK321 is measured by 2HG levels[169]. The inhibition of the wt subunit is even more difficult to be determined as a decrease in 2HG could be a result of three possible scenarios: (a) active wt subunit and inactive mutant subunit; (b) inactive wt subunit and active mutant subunit; (c) inactive wt subunit and inactive mutant subunit.

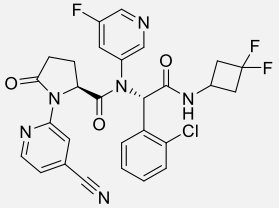
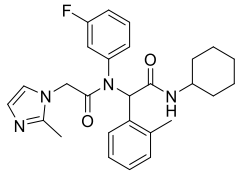
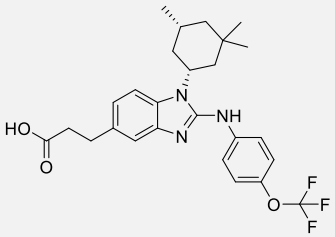
#### 1.3.4.3 Targeting other enzymes

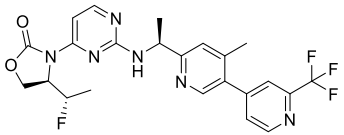
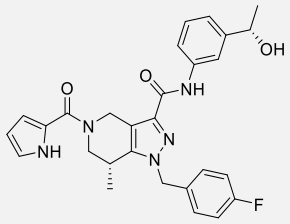
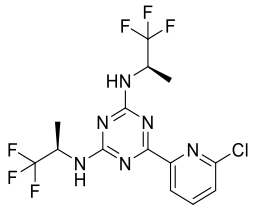
As simply reversing the IDH mutant phenotype by reducing elevated 2HG levels does not always bring therapeutic benefit (**Section 1.3.1**), combination therapy or targeted therapy against other enzymes to treat IDH mutant malignancies have been proposed. These exploit the profound cellular consequences associated with millimolar levels (5–35 mM[11]) of D-2HG in IDH mutant tumours. As mentioned in **Section 1.3.3**, IDH mutant gliomas have increased sensitivity to chemotherapy[80], promoting the utility of many other anticancer drugs. Combination therapy involving inhibitors of both IDH mutant and FTO whose overexpression promotes tumour growth[170] could also have beneficial outcomes that awaits validation[65]. One review focused on combination therapy comprising of an IDH mutant inhibitor and a DNA methyltransferase (DNMT) inhibitor to synergistically remove the DNA hypermethylation phenotype. The approach demonstrated efficacy in reducing DNA methylation, inducing cellular differentiation and inhibiting tumour growth in preclinical studies, but showed no definitive benefits in clinical studies, possibly because the 'epigenetic memory' of IDH mutant tumours is not limited to DNA methylation[6]. The limited clinical efficacy suggests that investigating

combinatorial application of inhibitors of other epigenetic regulators involved in RNA and histone methylation for instance, may be worthwhile. IDH1/2 mutant cells have also been found to have 2HG-mediated deficiency in DNA repair, which confers sensitivity to inhibitors of poly(adenosine 5'-diphosphate-ribose) polymerase (PARP) which is involved in DNA repair pathways. PARP inhibitors were reported to selectively kill R132H IDH1 cells and inhibit growth of R132H IDH1 tumour xenografts[111]. Additionally, IDH1/2 mutant AML cells were also reported to be sensitive to PARP inhibitors[171]. Notably, such vulnerability to PARP inhibitors in IDH mutant cells is reversed by IDH mutant inhibitors[111,171].

## 1.4 Therapeutic advances with mutant IDH1/2 inhibitors

Multiple drug discovery campaigns targeting mutant IDH1/2 were initiated following the identification of *IDH* gene mutations in gliomas and AML. Pharmaceutical companies involved include, but are not limited to, Agios, Bayer, GSK, Merck, Novartis and Sanofi. **Table 1.2** summarises some leading mutant IDH1/2 inhibitors with their structural and potency data. Surprisingly, all inhibitors with available crystal structure data are 'allosteric', binding at the dimer interface of IDH1/2 variants. Most of the inhibitors shown are under clinical development. AGI-5198 is a pioneering compound by Agios Pharmaceuticals; its subsequent optimisation led to Ivosidenib which is the first-in-class mutant IDH1 inhibitor[113]. GlaxoSmithKline (GSK) developed GSK321, which has poor pharmacokinetic properties and was optimised to give GSK864[169]. The low selectivity of the GSK series between wt and mutant IDH1 likely hindered its clinical development. Vorasidenib is the only reported inhibitor that targets both IDH1 and IDH2[114]. Notably, Ivosidenib[109] and Enasidenib[110], targeting mutant IDH1 and IDH2 respectively, have been approved by FDA for the treatment of AML.

| Inhibitor | Structure | Target mutant | X-ray crystal structures | Biochemical $IC_{50}$ | Cellular $IC_{50}$ |
|---|---|---|---|---|---|
| **Ivosidenib (AG-120) (Agios)** |  | IDH1 | NIL<br><br>Analogue ML309 (PDB 5K11[172]) Cryo-EM: One inhibitor binding at the dimer interface of R132C IDH1 | R132H IDH1: 12 nM; 0.04 µM<br>R132C IDH1 : 13 nM; 0.05 µM<br>R132G IDH1: 8 nM<br>R132L IDH1: 13 nM<br>R132S IDH1: 12 nM<br>wt/R132H IDH1: 12 nM<br>wt IDH1: 71 nM; 4.26 µM<br>wt IDH2: >30 µM<br>Ref[113,173] | U87 (R132H IDH1): 19 nM<br>HT1080 (R132C IDH1): 8 nM<br>COR-L105 (R132C IDH1): 15 nM<br>HCCC-9810 (R132S IDH1): 12 nM<br>Ref[113] |
| **AGI-5198 (Agios)** |  | IDH1 | NIL<br><br>Analogue ML309 (PDB 5K11[172]) Cryo-EM: One inhibitor binding at the dimer interface of R132C IDH1 | R132H IDH1: 0.07 µM; 0.39 µM<br>R132C IDH1: 0.16 µM; 1.28 µM<br>wt IDH1: >100 µM; >30 µM<br>wt IDH2: >100 µM; >30 µM<br>R140Q IDH2: >100 µM<br>R172K IDH2: >100 µM<br>Ref[138,173,174] | U87 (R132H IDH1): 0.07 µM; 0.04 µM<br>THP-1 (R132H IDH1): 0.05 µM<br>HT1080 (R132C IDH1): 0.48 µM<br>Ref[173,174] |
| **BAY-1436032 (Bayer)** |  | IDH1 | Analogue compound 1 (PDB 5LGE[118]): One inhibitor binding at dimer interface of R132H IDH1 | R132H IDH1: 15 nM<br>R132C IDH1: 15 nM<br>wt IDH1: 20 µM<br>wt IDH2: >100 µM<br>Ref[118] | LN229 (R132H IDH1): 73 nM<br>HCT116 (R132H IDH1): 47 nM<br>NCH551b (R132H IDH1): 13 nM<br>HT1080 (R132C IDH1): 135 nM<br>Mouse hematopoietic:<br>R132H IDH1: 60 nM<br>R132C IDH1: 45 nM<br>Human AML patient-derived:<br>R132H IDH1: 5 nM<br>R132C IDH1: 5 nM<br>R132G IDH1: 4 nM<br>R132L IDH1: 3 nM |

| | | | | | |
|---|---|---|---|---|---|
| | | | | | R132S IDH1: 16 nM<br>Ref[118,175] |
| **IDH305 (Novartis)** |  | IDH1 | PDB 6B0Z[176]<br>Three inhibitors binding at dimer interface of R132H IDH1<br><br>Analogue IDH889 (PDB 5TQH[177]): two inhibitors binding at dimer interface of R132H IDH1 | R132H IDH1: 0.018/0.027 μM<br>R132C IDH1: 0.028 μM<br>wt IDH1: 6.14 μM<br>Ref[176] | HCT116 (R132H IDH1): 24 nM<br>HCT116 (R140Q IDH2): 3.8 μM<br>HCT116 (R172K IDH2): 10 μM<br>Ref[176] |
| **GSK321 (GlaxoSmithKline)** |  | IDH1 | PDB 5DE1[169]<br>Two inhibitors binding at dimer interface of R132H IDH1 | R132H IDH1: 4.6 nM<br>R132C IDH1: 3.8 nM<br>R132G IDH1: 2.9 nM<br>wt IDH1: 46 nM<br>R140Q IDH2: 1358 nM<br>R172S IDH2: 1034 nM<br>wt IDH2: 496 nM<br>Ref[169] | HT1080 (R132C IDH1): 85 nM<br>Ref[169] |
| **Vorasidenib (AG-881) (Agios)** |  | IDH1/2 | PDB 6ADG[178]<br>One inhibitor binding at dimer interface of R132H IDH1<br><br>PDB 6ADI[178]<br>One inhibitor binding at dimer interface of R140Q IDH2 | R132H IDH1: 6/8 nM; 31.9 nM<br>R132C IDH1: 19 nM<br>R132G IDH1: 17 nM<br>R132L IDH1: 34 nM<br>R132S IDH1: 6 nM<br>wt/R132H IDH1: 4 nM; 0.6 nM<br>R140Q IDH2: 12/118 nM; 31.7 nM<br>R172K IDH2: 32/94 nM<br>wt/R140Q IDH2: 32/251 nM | HCT116 (R132H IDH1): 3 nM<br>TF-1 (R132H IDH1): 3.2 nM<br>TS603 (R132H IDH1): 0.25 nM<br>HCT116 (R132C IDH1): 22 nM<br>COR-L105(R132C IDH1): 3.8 nM<br>HT1080 (R132C IDH1): 4 nM<br>JJ012 (R132G IDH1): 6.6 nM<br>HCCC-9810 (R132S IDH1): 0.845 nM<br>TF-1 (R140Q IDH2): 14 nM |

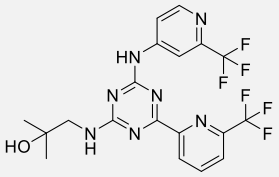
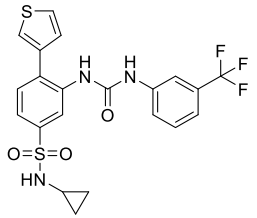
| | | | | | |
|---|---|---|---|---|---|
| | | | | wt/R172K IDH2: 8/49 nM<br>Ref[114,178] | U87 (R140Q IDH2): 7.1 nM<br>HCT116 (R172K IDH2): 130 nM<br>Ref[114] |
| **Enasidenib (AG-221) (Agios)** |  | IDH2 | PDB 5I96[179]<br>One inhibitor binding at dimer interface of R140Q IDH2 | R140Q IDH2: 0.1/0.32 μM; 0.77 μM; 0.009 μM<br>wt/R140Q IDH2: 0.03/0.31 μM<br>R172K IDH2: 0.2/0.4 μM; 0.21 μM<br>wt/R172K IDH2: 0.01/0.11 μM<br>R172S IDH2: 0.155 μM<br>wt IDH2: 1.8/40 μM; 34 μM<br>R132H IDH1: 48/78 μM; 4.95 μM<br>wt/R132H IDH1: 0.677 μM<br>wt IDH1: 0.45/1.12 μM<br>Ref[114,115,179] | TF-1 (R140Q IDH2): 0.02 μM; 0.012 μM<br>U87 (R140Q IDH2): 0.01 μM; 0.012 μM<br>HCT116 (R172K IDH2): 0.53 μM<br>TF-1 (R172K IDH2): 0.98 μM<br>U87 (R172K IDH2): 1.59 μM; 1.4 μM<br>SW1353 (R172S IDH2): 2.1 μM<br>U87 (R132H IDH1): >3 μM<br>HT1080 (R132C IDH1): >3 μM<br>Ref[115,179] |
| **AGI-6780 (Agios)** |  | IDH2 | PDB 4JA8[139]<br>One inhibitor binding at dimer interface of R140Q IDH2 | R140Q IDH2: 23/170 nM<br>wt/R140Q IDH2: 4/120 nM<br>wt IDH2: 190/2700 nM<br>R132H IDH1: 11 μM<br>wt IDH1: >100 μM<br>Ref[139] | TF-1 (R140Q IDH2): 18 nM<br>U87 (R140Q IDH2): 11 nM<br>U87 (R132H IDH1): >100 μM<br>Ref[139] |

**Table 1.2**. Summary of selected IDH1 and IDH2 inhibitors, with their chemical structures, binding stoichiometry and location observed from reported X-ray crystal structures, and biochemical and cellular $IC_{50}$ values. Note: "/" in $IC_{50}$ values refers to measurements from different incubation time under the same study while ";" separates reported values from different studies. "wt/mutant" refers to heterodimer and the rest represents homodimer.

## 1.5 Overview of the thesis

The work on IDH described in this thesis can be categorised into two parts: the first half is dedicated to studying the structures and mechanisms of wt and mutant IDH1, while the second half is dedicated to the inhibition of mutant IDH1. The overall aim is to increase the understanding of the basic mechanisms of IDH1 and thereby enable the identification of a new class of (mutant) IDH inhibitors for the treatment of IDH malignancies.

As a new project in the Schofield group, the work began with biochemical and biophysical characterisation of IDH1 and its representative variant, R132H IDH1, as described in **Chapter 2**. $^{1}$H NMR spectroscopy was employed to monitor biochemical reactions, in addition to the commonly used spectrophotometric assays. Binding and structural studies were carried out by complementary biophysical techniques, including non-denaturing mass spectrometry (MS), differential scanning fluorimetry (DSF), isothermal titration calorimetry (ITC), NMR spectroscopy and circular dichroism (CD) spectroscopy. The results provided foundations to the work described in **Chapter 3**, which answered an important question: why are all the reported mutant IDH inhibitors allosteric? During this process, it was found that metal ions play key roles in both substrate binding and inhibition mechanisms of IDH1. In the work described in **Chapter 4**, NMR spectroscopy, specifically diffusion-ordered spectroscopy (DOSY), was employed to further explore the interactions and structures of metabolites with metal ions under physiological conditions. This work uncovered new information on small molecule-metal ion complexes distinct from the reported X-ray crystal structures[180].

A comprehensive comparison of a diverse set of mutant IDH inhibitors is presented in **Chapter 5**, as previously their $IC_{50}$ values have been reported from independent studies and their binding data is very limited. Understanding how the existing inhibitors work will likely be useful in designing new inhibitors to overcome the recently emerged drug resistance. Three novel approaches to IDH inhibition are described thereafter: (a) targeted degradation by proteolysis targeting chimera (PROTAC) of which its cellular effects on R132H IDH1 degradation were verified

qualitatively by western blot, (b) covalent inhibition (in collaboration with Evotec) in **Chapter 6**, and (c) the use of substrate (2OG) analogues in **Chapter 7**.

The conclusions in **Chapter 8** summarise the insights from all the research described. New approaches to antibody-assisted targeted drug delivery systems are discussed in **Appendix**. Work on a proof-of-concept study employing biophysical techniques such as biolayer interferometry (BLI) and AlphaScreen™ is described. If successful, the approach outlined could be applicable to many other diseases beyond IDH mutant cancers.

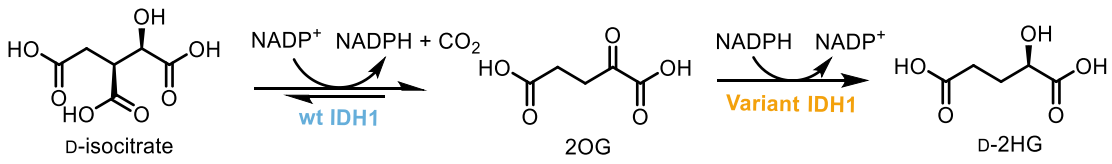
# CHAPTER 2.

# BASIC CHARACTERISATION OF WT IDH1 AND R132H IDH1

The main purpose of the work described in this chapter was to characterise wt IDH1 and R132H IDH1 using biochemical and biophysical methods. The work involved optimisation of conditions specific to IDH1 in different assays, with the optimised conditions being presented. The results enabled a better understanding of wt IDH1 and R132H IDH1 catalysis and opened up areas of research that were pursued in subsequent chapters.

## 2.1 Kinetic comparison of wt IDH1 and R132H IDH1

Most reported biochemical assays for IDH1 are based on end-point or continuous measurements of changes in (a) the absorbance of NADPH (340 nm, extinction coefficient ε= 6.22 $mM^{-1}$ $cm^{-1}$)[158,169,181,182], (b) the fluorescence of NADPH (excitation 340 nm, emission 460 nm)[183], (c) the fluorescence of resorufin (excitation 525–544 nm, emission 580–590 nm)[139,169,173,181,183] (product of diaphorase catalysed conversion of resazurin and NADPH, which constitutes an indirect/coupled assay), or (d) the measurement of 2HG production by MS[169]. The work described in this thesis employs the NADPH absorbance-based assays to monitor the turnover of wt IDH1 and R132H IDH1, by observing changes in the absorbance of NADPH at 340 nm continuously over 15 min. This assay enables the determination of the reactions' initial rates over the linear range of the reaction profile.




**Scheme 2.1**. Enzymatic reactions catalysed by wt IDH1 and variant IDH1. Isocitrate conversion to 2OG is measured by formation of NADPH whilst 2OG conversion to isocitrate or 2HG is measured by depletion of NADPH, as measured by absorbance-based assays.

In order to define standard assay conditions, the kinetics of four reactions catalysed by IDH1 (**Scheme 2.1**) were examined: (a) oxidative decarboxylation of isocitrate to 2OG as catalysed by wt IDH1, *i.e.* the forward reaction catalysed by wt IDH1; (b) oxidative

decarboxylation of isocitrate to 2OG as catalysed by R132H IDH1; (c) reduction of 2OG to isocitrate as catalysed by wt IDH1, *i.e.* the reverse reaction by wt IDH1; and (d) reduction of 2OG to 2HG as catalysed by R132H IDH1, *i.e.* the neomorphic reaction by R132H IDH1. Kinetic parameters[184], *i.e.* Michaelis–Menten constants ($K_M$), maximal reaction rate ($V_{max}$) and catalytic rate constant or turnover number ($k_{cat}$) were determined (**Table 2.1**). Within the standard conditions, the concentration of each (co)substrate was set to at least twice its $K_M$ to ensure achievement of $V_{max}$ conditions. Enzyme concentrations were optimised to define the linear range of a given reaction within 15 min. Buffer components and pH were selected based on literature conditions[169,183]. The final standard assay conditions are presented in **Table 2.2**.

| **Oxidative (isocitrate to 2OG)** | | | |
|---|---|---|---|
| | | **wt** | **R132H** |
| **Isocitrate** | $K_M$ (μM) | 38 ± 6 | 257 ± 50 |
| | $V_{max}$ (nM $s^{-1}$) | 216 ± 8 | 36 ± 2 |
| | $k_{cat}/K_M$ ($s^{-1}$ $\mu M^{-1}$) | 1.3 ± 0.3 | (3.9 ± 1.1) × $10^{-4}$ |
| **$NADP^+$** | $K_M$ (μM) | 27 ± 2 | 10 ± 1 |
| | $V_{max}$ (nM $s^{-1}$) | 246 ± 4 | 40 ± 1 |
| | $k_{cat}/K_M$ ($s^{-1}$ $\mu M^{-1}$) | 1.9 ±0.3 | (1.0 ± 0.2) × $10^{-2}$ |
| **$MgCl_2$** | $K_M$ (μM) | 36 ± 4 | 171 ± 23 |
| | $V_{max}$ (nM $s^{-1}$) | 214 ± 5 | 45 ± 2 |
| | $k_{cat}/K_M$ ($s^{-1}$ $\mu M^{-1}$) | 1.4 ± 0.3 | (5.8 ± 1.4) × $10^{-4}$ |
| | $k_{cat}$ ($s^{-1}$) | 50 ± 4 | 0.10 ± 0.01 |

| **Reductive (2OG to isocitrate by wt IDH1, or 2HG by R132H IDH1)** | | | |
|---|---|---|---|
| | | **wt** | **R132H** |
| **2OG** | $K_M$ (μM) | (1.1 ± 0.3) × $10^3$ | 652 ± 116 |
| | $V_{max}$ (nM $s^{-1}$) | 200 ± 16 | 236 ± 10 |
| | $k_{cat}/K_M$ ($s^{-1}$ $\mu M^{-1}$) | (1.9 ± 0.6) × $10^{-3}$ | (9.4 ± 2.7) × $10^{-4}$ |
| **NADPH** | $K_M$ (μM) | 115 ± 19 | 15 ± 2 |
| | $V_{max}$ (nM $s^{-1}$) | 221 ± 15 | 276 ± 10 |
| | $k_{cat}/K_M$ ($s^{-1}$ $\mu M^{-1}$) | (1.8 ± 0.4) × $10^{-2}$ | (4.1 ± 1.0) × $10^{-2}$ |
| **$MgCl_2$** | $K_M$ (μM) | † | (4.4 ± 0.7) × $10^3$ |
| | $V_{max}$ (nM $s^{-1}$) | | 224 ± 10 |
| | $k_{cat}/K_M$ ($s^{-1}$ $\mu M^{-1}$) | | (1.4 ± 0.4) × $10^{-4}$ |
| | $k_{cat}$ ($s^{-1}$) | 2.1± 0.1 | 0.61 ± 0.07 |

**Table 2.1.** A summary of kinetic parameters for the oxidative and reductive reactions catalysed by wt IDH1 and R132H IDH1. The $K_M$ value for each (co)substrate was determined by varying its concentration while maintaining the concentrations of the other components at the standard conditions. Due to instrumental detection limits, the $K_M$ values for $NADP^+$ or NADPH could not be accurately determined at concentrations <10 μM. †Partial conversion was observed at 0 mM $MgCl_2$, as confirmed by $^1H$ NMR (700 MHz) spectroscopy (data not shown). Original plots are presented in **Figures S2.1** and **S2.2**.

| Isocitrate to 2OG | | | | 2OG to isocitrate | | 2OG to 2HG | |
|---|---|---|---|---|---|---|---|
| **wt** | 4.5 nM | **R132H** | 400 nM | **wt** | 100 nM | **R132H** | 400 nM |
| **Isocitrate** | 150 µM | **Isocitrate** | 1.5 mM | **2OG** | 15 mM | **2OG** | 1.5 mM |
| **$NADP^+$** | 75 µM | **$NADP^+$** | 75 µM | **NADPH** | 500 µM | **NADPH** | 50 µM |
| | | | | **$NaHCO_3$*** | 100 mM | | |

**Table 2.2**. Standard assay conditions in buffer containing 100 mM Tris-HCl, 10 mM $MgCl_2$, 0.005% (v/v) Tween 20, 0.1 mg/mL BSA and 0.2 mM DTT, pH 8.0. *$NaHCO_3$ (100 mM, ~2.3 mM $CO_2$ at pH 8, actual pH may vary)[181] was added as a source of $CO_2$.

The $K_M$ corresponds to the concentration of substrate when the reaction velocity reaches half of its $V_{max}$. A low $K_M$ indicates that the enzyme requires only a small amount of substrate to reach maximum reaction rate[184]. Albeit not a direct measurement of binding affinity, $K_M$ can be used to estimate the binding affinity of the substrate to the enzyme, providing $k_2 << k_{-1}$ (an assumption that is not always valid) (**Scheme 2.2**). This estimation allows evaluation of substrate binding preference. The overall catalytic efficiency is often judged by comparison of $k_{cat}/K_M$ values, where $k_{cat}$ (catalytic rate constant) is defined as the number of substrate molecules each enzyme site can turn over per unit time and is calculated by $V_{max}$/enzyme concentration.

$$\text{Enzyme + Substrate} \underset{k_{-1}}{\overset{k_1}{\rightleftharpoons}} \text{Enzyme-substrate complex} \xrightarrow{k_2} \text{Enzyme + Product} \qquad K_M = \frac{k_{-1} + k_2}{k_1}$$

**Scheme 2.2.** A representation of the Michaelis-Menten model for enzyme kinetics. If the rate of product formation, $k_2$, is very slow (the rate-determining step) compared to $k_{-1}$, $K_M$ approximates to $\frac{k_{-1}}{k_1}$, which is the dissociation constant, $K_D$.

Comparing the $K_M$ values for the oxidative decarboxylation of isocitrate (**Table 2.1**), R132H IDH1 has a lower affinity for isocitrate (a DL-mixture was used unless otherwise stated, as has been the practice previously[138,158,181]) ($K_M$= 257 µM) compared to wt IDH1 ($K_M$= 38 µM). The lower preference of R132H IDH1 for isocitrate compared to wt IDH1 is consistent with the reported kinetic data[11,158,181]. The $k_{cat}/K_M$ of R132H IDH1 for isocitrate ($3.9 \times 10^{-4}$ $s^{-1}$ $\mu M^{-1}$) is over 3000× lower than that of wt IDH1 (1.3 $s^{-1}$ $\mu M^{-1}$), also consistent with reported values[158]. These observations partly account for the reduced ability of R132H IDH1 to convert isocitrate to 2OG.

However, gaps remain in understanding the neomorphic function of R132H IDH1. An unexpectedly high $K_M$ of 652 µM for 2OG was observed for R132H IDH1 in the reductive reaction (**Table 2.1**). High $K_M$ values for 2OG have been previously reported, at 965 µM

for the R132H IDH1 homodimer[11] and 700 μM for the wt/R132H heterodimer[185]. Accordingly, the $k_{cat}/K_M$ of R132H IDH1 for 2OG is low at $9.4 \times 10^{-4}$ $s^{-1}$ $\mu M^{-1}$, only slightly over twofold higher than that of R132H IDH1 for isocitrate conversion ($3.9 \times 10^{-4}$ $s^{-1}$ $\mu M^{-1}$). This suggests that R132H IDH1 converts 2OG to 2HG at a comparable catalytic efficiency as it does for the isocitrate to 2OG reaction.

In reality, the catalytic efficiency of isocitrate to 2OG conversion catalysed by R132H IDH1 may be higher than what was observed. This is because any 2OG produced from isocitrate is likely a transient intermediate which undergoes further reduction by R132H IDH1 to 2HG. The conversion of isocitrate to 2HG as catalysed by R132H IDH1 was validated by reaction monitoring using $^1$H NMR spectroscopy (**Figure 2.1**). Cofactor $NADP^+$ is converted to NADPH initially in the conversion of isocitrate to 2OG. However, as R132H IDH1 also catalyses the conversion of 2OG to 2HG, NADPH is consumed to generate $NADP^+$, whilst 2OG formed from isocitrate is converted to 2HG. Consequently, the levels of $NADP^+$, NADPH and 2OG equilibrate to their initial levels, and the conversion of isocitrate to 2HG can proceed without a net consumption of the cofactors, NADP(H). As a result, the apparent catalytic rate and efficiency for the isocitrate to 2OG conversion by R132H IDH1 are low as the product 2OG is constantly consumed, even though R132H IDH1 could possibly catalyse isocitrate to 2OG at a comparable efficiency to wt IDH1.

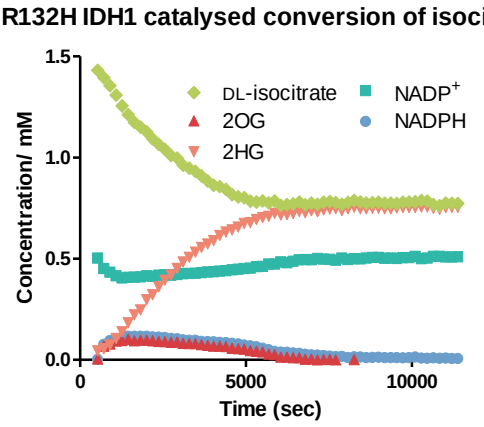



**Figure 2.1**. Conversion of DL-isocitrate and $NADP^+$ catalysed by R132H IDH1, as monitored by $^1$H NMR (excitation sculpting suppression with perfect-echo, 700 MHz) spectroscopy. Buffer: 50 mM Tris-$D_{11}$-HCl pH 7.5 in 90% $H_2O$/ 10% $D_2O$ (v/v). The conditions are 2 μM R132H IDH1, 1.5 mM DL-isocitrate, 500 μM $NADP^+$ and 10 mM $MgCl_2$.

Previous studies have suggested complexity in the structural reasons underlying how the single R132H substitution leads to the gained 2OG reduction activity. It has been proposed that movement of Y139 compensates the increased negative charge at the C-2 centre of 2OG during hydride transfer from NADPH[158], and that the increased binding

strength of NADPH enables relatively efficient reduction of 2OG to 2HG[181]. The latter proposal is consistent with the observation that the $K_M$ of R132H IDH1 for NADPH (15 µM) is about 8 times lower than that of wt IDH1 (115 µM). However, it should be noted that the kinetic parameters for wt IDH1 and R132H IDH1 are measured with formation of different reduced products *i.e.* isocitrate for wt IDH1 and 2HG for R132H IDH1. The conversion of 2OG to 2HG by wt IDH1 could not be measured under the tested conditions, *i.e.* no substantial consumption of NADPH was observed with wt IDH1.

Overall, at saturating conditions, R132H IDH1 catalyses the neomorphic reaction (2OG to 2HG, $k_{cat}$= 0.61 $s^{-1}$) about 6 times faster than the normal reaction (isocitrate to 2OG, $k_{cat}$= 0.10 $s^{-1}$). However, these $k_{cat}$ values for R132H IDH1 are two orders of magnitudes lower than that of the normal isocitrate conversion catalysed by wt IDH1 ($k_{cat}$= 50 $s^{-1}$). This implies that whilst the R132H substitution confers IDH1 a neomorphic function, it also impairs the general catalytic efficiency of the enzyme.

## 2.2 Structural comparison of wt and R132H IDH1

To rationalise observations in the kinetic parameters, reported X-ray crystal structures of wt IDH1[12] and R132H IDH1[11] were compared (**Figure 2.2**). Crystal structures show that both wt and R132H IDH1 are dimeric with an individual active site present in each monomer. Each active site in the crystal structure binds (a) a cofactor ($NADP^+$ for wt IDH1, and NADPH for R132H IDH1) as a hydride acceptor/donor, (b) a substrate (isocitrate for wt IDH1, and 2OG for R132H IDH1) to donate or accept the hydride (plus decarboxylation for isocitrate) leading to its conversion, and (c) a metal ion (an inactive $Ca^{2+}$ shown) which coordinates to the substrate and is required for enzymatic activity (**Section 2.4.3**). In the reverse wt reaction, $CO_2$ (or a $CO_2$ precursor ion) must also bind to the active site. Notably, IDH inhibitors, including those in clinical use/trials, bind at the dimer interface region, which links the two active sites in the dimer, instead of competing with the substrate or NADP(H) at the active site.

The crystallographic analyses[11,12] reveal that a nitrogen atom on the guanidinium group of R132 in wt IDH1 is positioned to form a hydrogen bond with an oxygen atom of the 2-carboxylic acid group on isocitrate (3.2 Å). The R132H substitution reduces the length

of the basic side chain (and likely its p$K_a$), in a manner that may diminish this hydrogen bond, consistent with the reduced ability of R132H IDH1 to convert isocitrate to 2OG.

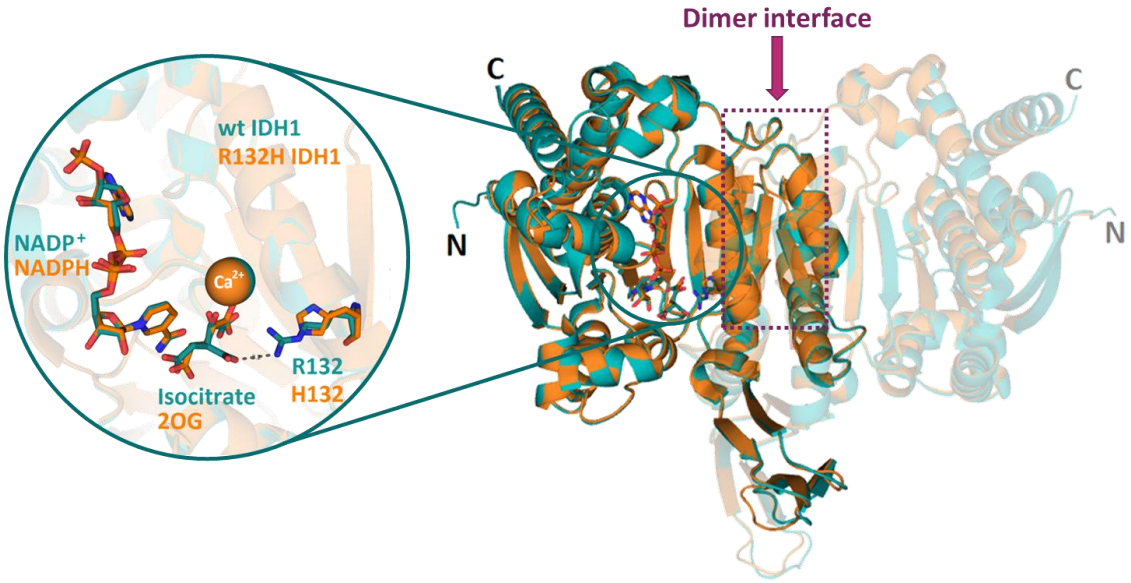



**Figure 2.2**. Active site and overall view of superimposed ribbon models of X-ray crystal structures of wt IDH1 (cyan, PDB 1T0L)[12] and R132H IDH1 (orange, PDB 3INM)[11], with the active site region expanded. Both wt and R132H IDH1 are dimeric; in each case one monomer is differentiated by a different transparency level. The active site in each monomer binds a cofactor ($NADP^+$ for wt IDH1 and NADPH for R132H IDH1), a substrate (isocitrate for wt IDH1 and 2OG for R132H IDH1) and a metal ion ($Ca^{2+}$ shown for both wt and R132H IDH1) which coordinates to the substrate. The dimer interface where most mutant IDH1 inhibitors bind is indicated by the purple dotted region. Note the proximity of the dimer interface to both active sites in the dimer.

The effect of the R132 substitution on the biophysical properties of IDH1 was then investigated. The reported X-ray crystal structures[11,12] of wt IDH1 and R132H IDH1 have near-identical overall structures with a backbone root mean square deviation (RMSD) of 0.35 Å over 767 $C_\alpha$ atoms (**Figure 2.2**). Secondary structure analyses of wt IDH1 and R132H IDH1 as measured by CD spectroscopy indicate closely related folds (**Figure 2.3**). The thermal stabilities of wt IDH1 ($T_m$= 52.0 °C) and R132H IDH1 ($T_m$= 50.8 °C) as measured by DSF are also similar, suggesting that the substitution does not significantly destabilise the enzyme. The small difference in thermal stabilities of wt IDH1 and R132H IDH1 observed in this work is consistent with reported values that were measured by CD (49.1 °C for wt IDH1 and 49.7 °C for R132H IDH1)[186].

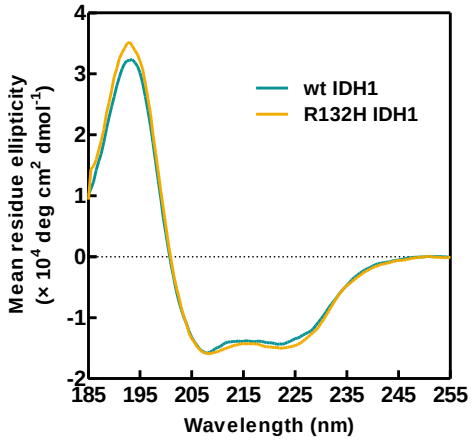



**Figure 2.3.** Both wt and R132H IDH1 have similar secondary structures. CD spectra of wt IDH1 and R132H IDH1 in cyan and orange respectively, both at 0.2 mg/mL in 10 mM sodium phosphate, pH 7.5. Both wt and R132H IDH1 contain well-defined β-pleated sheets indicated by the positive band between 185 and 200 nm, as well as α-helices indicated by the negative band between 205 to 230 nm.

Non-denaturing electrospray ionisation mass spectrometry (ESI-MS), a non-solution phase technique which retains non-covalent interactions, shows that wt IDH1 and R132H IDH1 both exist as dimers (**Figure 2.4**), consistent with the observations in solid phase by X-ray crystallography[11,12]. The observed masses reveal that each wt IDH1 and R132H IDH1 dimer is bound with two copurifying NADP(H) as the predominant native state. Unfortunately, the non-denaturing MS method employed cannot resolve the small mass difference of 1 Da between $NADP^+$ and NADPH. Thus, the exact redox state of the copurifying cofactor was determined by NMR spectroscopy (**Figure 2.5**), as protons from nicotinamide ring of $NADP^+$ have higher chemical shifts (at ~8–9 ppm) than those of NADPH. However, molecules bound tightly to the protein cannot be observed by NMR, due to their slow tumbling rate which leads to faster relaxation of transverse magnetisation (short $T_2$) and line broadening[187]. Therefore, wt IDH1 or R132H IDH1 protein was heated in an NMR tube to reveal the signals from the released cofactors. Signals from both wt IDH1 and R132H IDH1 after heating were compared with standard solutions of $NADP^+$ or NADPH, and matched with the NADPH standard. The conclusion that NADPH is the copurified cofactor in recombinant wt IDH1 differs from one study that reports 1:2 $NADP^+$:NADPH mixture in wt IDH1[181], but is consistent with another study which compares the retention time of NADPH with a standard using HPLC[188].

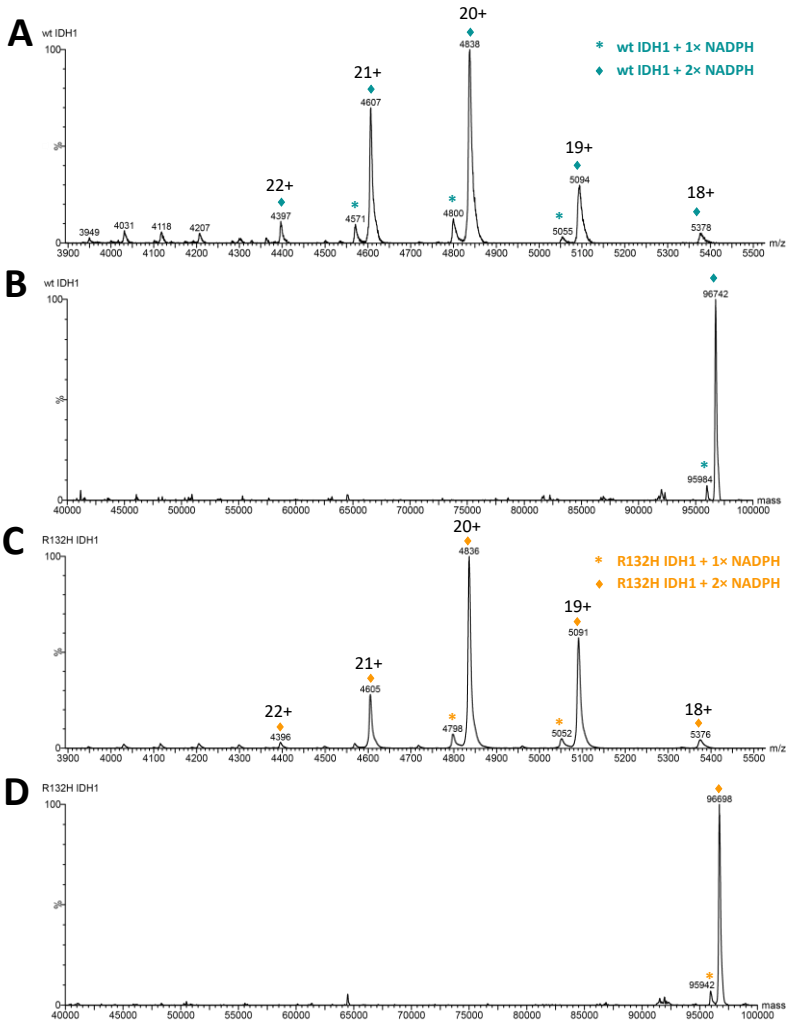



**Figure 2.4.** Raw (charge state distribution of $18^+$ to $22^+$) and deconvoluted non-denaturing electrospray ionisation mass spectra of 50 µM wt IDH1 (**A** and **B**) and R132H IDH1 (**C** and **D**) showing a dimer complexed with two copurifying NADPH molecules. Cone voltage= 200 V. Theoretical mass of monomeric wt IDH1 or R132H IDH1= 47.7 kDa. The observed mass of 96.7 kDa corresponds to the theoretical dimer protein mass without an *N*-terminal Met + 2× NADPH (MW 745).

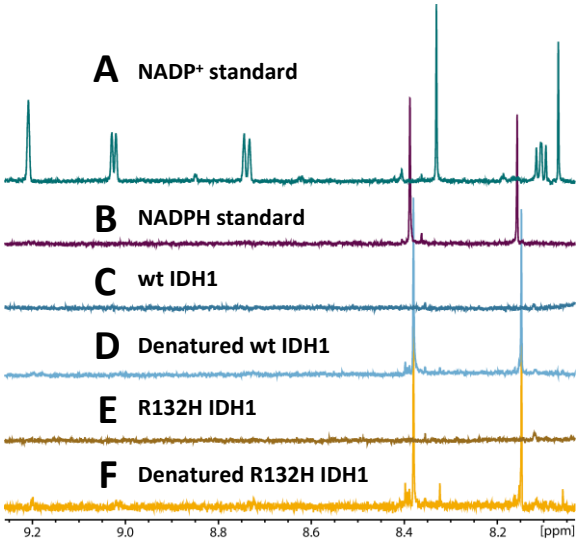



**Figure 2.5**. Both wt and R132H IDH1 copurify with the cofactor, NADPH. $^{1}$H NMR (CPMG-edited, 700 MHz) spectra to identify the copurifying cofactor in wt IDH1 and R132H IDH1. See Experimental Methods: Nuclear Magnetic Resonance for method details. (**A**) $NADP^+$ (50 µM) in $D_2O$. (**B**) NADPH (50 µM) in $D_2O$. (**C**) wt IDH1 (50 µM) in $D_2O$. Neither $NADP^+$ nor NADPH was observed as the cofactor is tightly bound to the protein. (**D**) wt IDH1 denatured by heating (**C**) at 90 °C for 30 s, then centrifuged to remove the precipitated protein. The supernatant contains the released cofactor, NADPH. (**E**) R132H IDH1 (50 µM) in $D_2O$. Neither $NADP^+$ nor NADPH was observed as the cofactor is tightly bound to the protein. (**F**) R132H IDH1 denatured by heating (**E**) at 90 °C for 30 s, then centrifuged to remove the precipitated protein. The supernatant contains the released cofactor, NADPH.

## 2.3 Binding studies of (co)substrates to IDH1

Initial binding studies of isocitrate, 2OG, 2HG, $NADP^+$ and NADPH to wt IDH1 and R132H IDH1 were carried out using DSF. Thermal stabilisation of IDH1 by addition of their (co)substrates was investigated using DSF. Both wt and R132H IDH1 were stabilised by addition of $NADP^+$ in a dose-dependent manner (1.2–6.4 °C for wt IDH1 and 1.7–5.3 °C for R132H IDH1 at 0.125–4 mM) (**Figure 2.6D** and **2.7D**). NADPH also stabilised both proteins, with the thermal stabilisation reaching a maximum (7.3 °C for wt IDH1 and 8.7 °C for R132H IDH1) at ~1 mM NADPH (**Figure 2.6E** and **2.7E**). By contrast, no thermal stabilisation of wt IDH1 and R132H IDH1 was observed by the addition of 2OG or 2HG (**Figure 2.6B**, **2.6C**, **2.7B** and **2.7C**). Notably, the significant stabilisation of 16 °C of wt IDH1 by isocitrate (4 mM, **Figure 2.6A**) was not observed for R132H IDH1 (**Figure 2.7A**). The lack of stabilisation of R132H IDH1 by isocitrate suggests that isocitrate is a weak binder for R132H IDH1, which is consistent with observation based on the $K_M$ values (**Section 2.1.2**), where R132H IDH1 has a significantly lower preference for isocitrate.

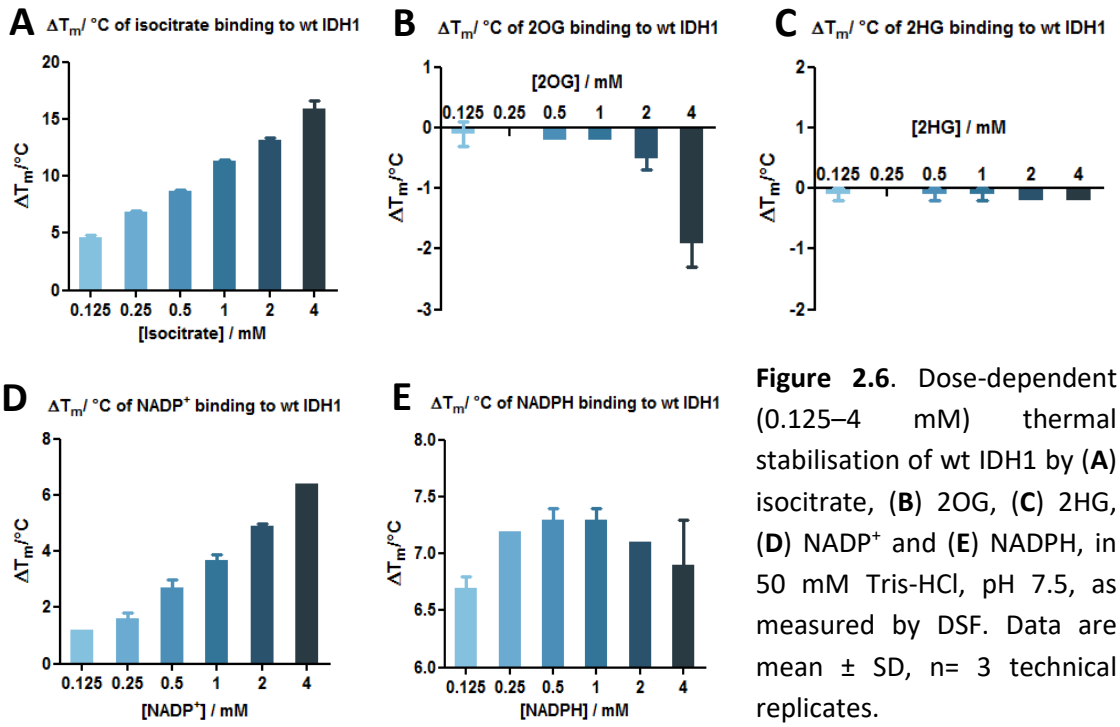



**Figure 2.6**. Dose-dependent (0.125–4 mM) thermal stabilisation of wt IDH1 by (**A**) isocitrate, (**B**) 2OG, (**C**) 2HG, (**D**) $NADP^+$ and (**E**) NADPH, in 50 mM Tris-HCl, pH 7.5, as measured by DSF. Data are mean ± SD, n= 3 technical replicates.

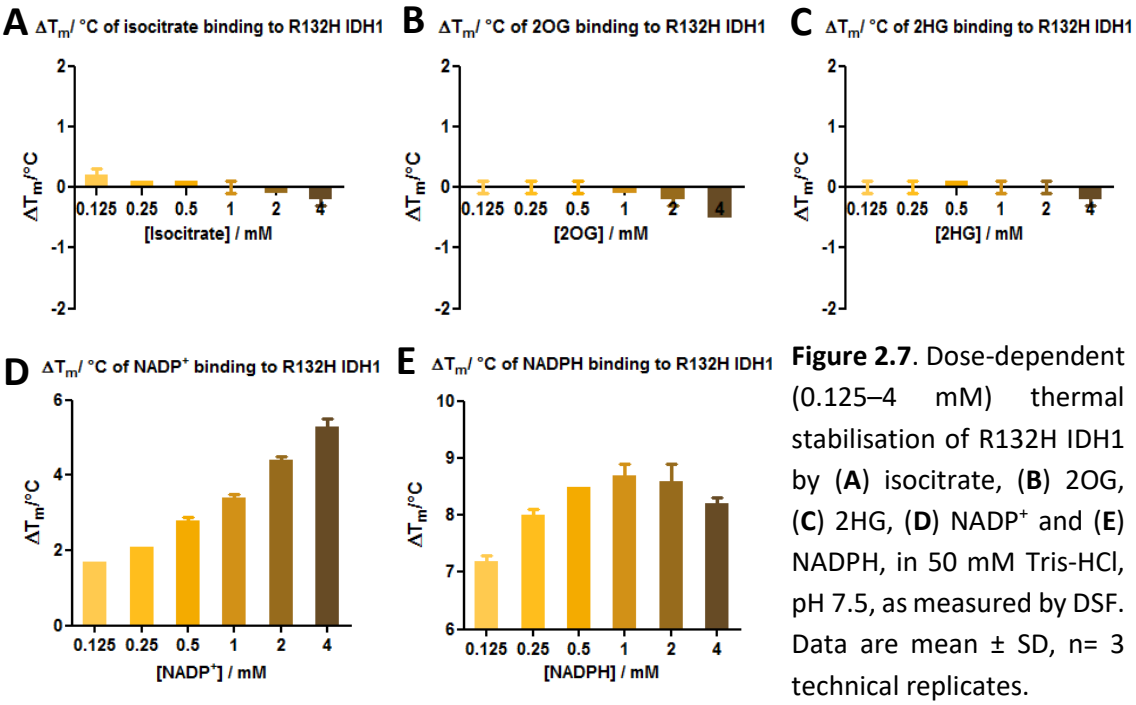



**Figure 2.7**. Dose-dependent (0.125–4 mM) thermal stabilisation of R132H IDH1 by (**A**) isocitrate, (**B**) 2OG, (**C**) 2HG, (**D**) $NADP^+$ and (**E**) NADPH, in 50 mM Tris-HCl, pH 7.5, as measured by DSF. Data are mean ± SD, n= 3 technical replicates.

ITC studies were then conducted to validate the results of the DSF studies on the binding of (co)substrates to wt IDH1 and R132H IDH1. The results with all (co)substrates, *i.e.* with isocitrate, 2OG, $NADP^+$, NADPH and 2HG, imply a lack of or very weak binding to wt IDH1 and R132H IDH1 in the absence of metal ions (**Table S2.3**). The apparent lack of

binding of isocitrate, 2OG and 2HG to R132H IDH1, as well as 2OG and 2HG to wt IDH1, is consistent with the DSF results (**Figures 2.6** and **2.7**). The lack of binding of $NADP^+$ and NADPH to wt IDH1 and R132H IDH1 can be explained by the fact that the protein is 'pre-occupied' with copurifying NADPH as revealed by non-denaturing MS (**Section 2.2**).

### 2.3.1 Role of $Mg^{2+}$ ions in IDH1 catalysis- an unexpected observation

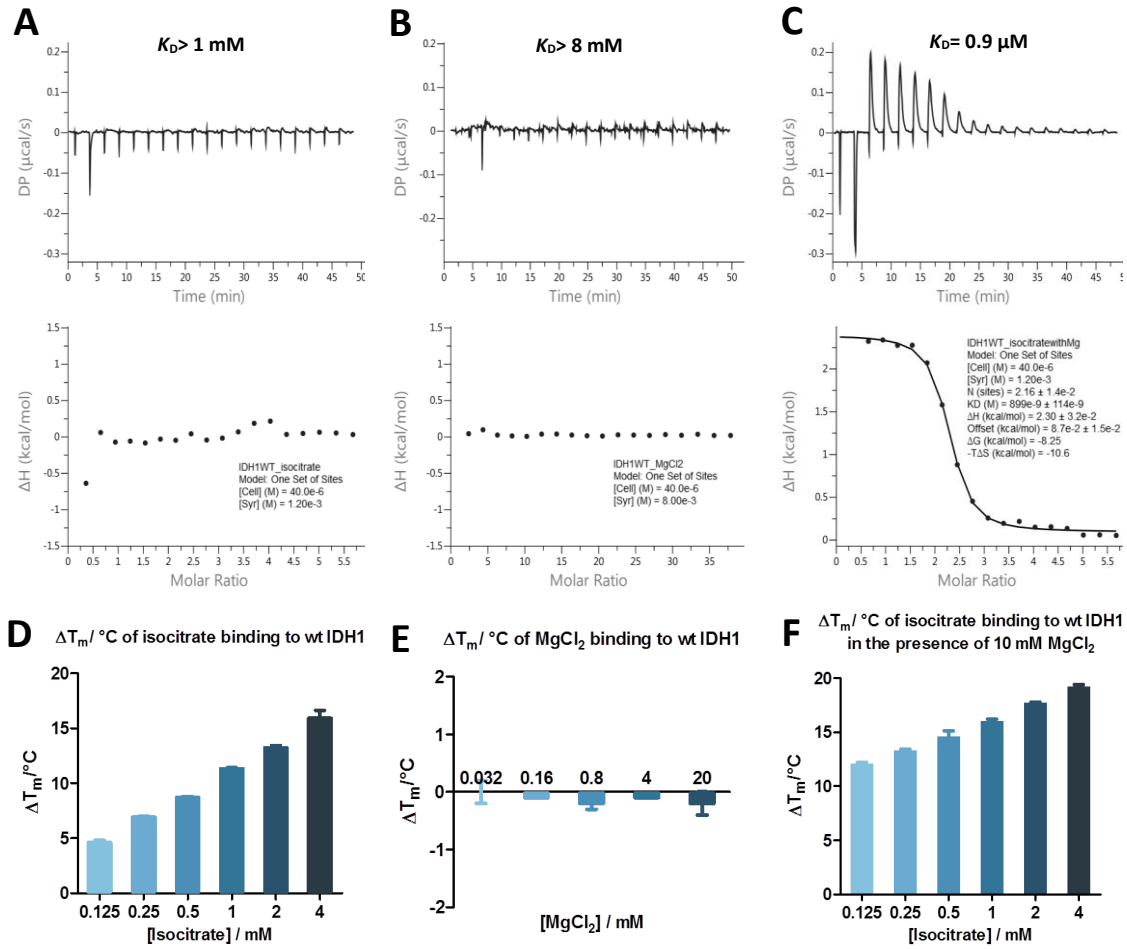



**Figure 2.8**. ITC analysis of (**A**) isocitrate (1.2 mM), (**B**) $MgCl_2$ (8 mM) and (**C**) isocitrate (1.2 mM) in the presence of $MgCl_2$ (5 mM), titrating against wt IDH1 (40 µM), in 50 mM Tris-HCl, pH 7.5. Isocitrate or $MgCl_2$ binding to wt IDH1 is very weak at $K_D$ > 1 mM and > 8 mM respectively, whilst isocitrate-$Mg^{2+}$ binding is strong at $K_D$= 0.9 µM. Stoichiometry of isocitrate with respect to wt IDH1, N=2 as DL-isocitrate is used but presumably only D-isocitrate binds to wt IDH1.
Dose-dependent (0.125–4 mM) thermal stabilisation of wt IDH1 by (**D**) isocitrate, (**E**) $MgCl_2$ and (**F**) isocitrate in the presence of $MgCl_2$, in 50 mM Tris-HCl, pH 7.5, as measured by DSF. Data are mean ± SD, n= 3 technical replicates. Thermal stabilisation of wt IDH1 by isocitrate is enhanced by the presence of 10 mM $MgCl_2$. $MgCl_2$ (0.032-20 mM) itself induces no significant thermal shift of wt IDH1.
See Experimental Methods: Isothermal Titration Calorimetry and Differential Scanning Fluorimetry for method details.

Interestingly, the ITC results show that neither isocitrate ($K_D$> 1 mM) nor $Mg^{2+}$ ($K_D$> 8 mM) binds tightly to wt IDH1 when added alone, but isocitrate binds to wt IDH1 with low micromolar binding affinity ($K_D$= 0.9 µM) in the presence of $MgCl_2$ (5 mM) (**Figure 2.8 A**–**C**). This suggests that the isocitrate-$Mg^{2+}$ complex may be the preferred substrate for wt IDH1. The enhancement of isocitrate binding to wt IDH1 by $Mg^{2+}$ was further supported by DSF analyses. Isocitrate alone stabilises wt IDH1 in a dose dependent manner (4.6–16 °C at 0.125–4 mM isocitrate) (**Figure 2.8D**). The presence of $Mg^{2+}$ (10 mM) enhances the thermal stabilisation of wt IDH1 by isocitrate (12–19 °C at 0.125–4 mM isocitrate) (**Figure 2.8F**). $Mg^{2+}$ was shown to have no thermally stabilising effect on wt IDH1 over a wide range of $Mg^{2+}$ concentrations (0.032–20 mM) (**Figure 2.8E**), thereby excluding the possibility that the enhancement of thermal stabilisation is caused directly by $Mg^{2+}$ binding to wt IDH1. These observations prompted detailed biophysical studies on the role of metal ions in IDH1 / IDH1 variant catalysis through the use of NMR spectroscopy and MS, which are described in **Chapter 3**.

## 2.4 (Co)substrates requirement of IDH1

### 2.4.1 D-isocitrate is the substrate for wt IDH1

The racemic DL-isocitrate mixture was typically used in studies with wt IDH1. To investigate which stereoisomer of isocitrate is converted by wt IDH1, the wt IDH1 catalysed reaction was monitored over time by $^1$H NMR (700 MHz) spectroscopy which shows how reactants and products, *i.e.* isocitrate, 2OG, $NADP^+$ and NADPH, change with time. D-isocitrate is commercially available, but L-isocitrate is unfortunately not available to carry out direct reaction monitoring with L-isocitrate. The results demonstrate that D-isocitrate (400 µM) is fully converted by wt IDH1 (**Figure 2.9A**) whereas the DL-isocitrate mixture (400 µM) was only half converted even after prolonged incubation (**Figure 2.9B**). This observation implies that D-isocitrate is selectively converted to 2OG in a mixture of DL-isocitrate by wt IDH1. The conversion rates of D-isocitrate (200 µM) alone or in the presence of equimolar L-isocitrate (as in the case of 400 µM DL-isocitrate mixture) are similar (**Figure 2.9B, 2.9D** and **2.9E**). These observations suggest that L-isocitrate is neither a substrate nor an inhibitor of wt IDH1. It is also worth noting that omitting $Mg^{2+}$ ions abolished the activity of wt IDH1 in catalysing isocitrate to 2OG, as no changes in

reactants and products levels were observed in the absence of $MgCl_2$, again highlighting the importance of $Mg^{2+}$ ions in IDH1 catalysis (**Figure 2.9C**).

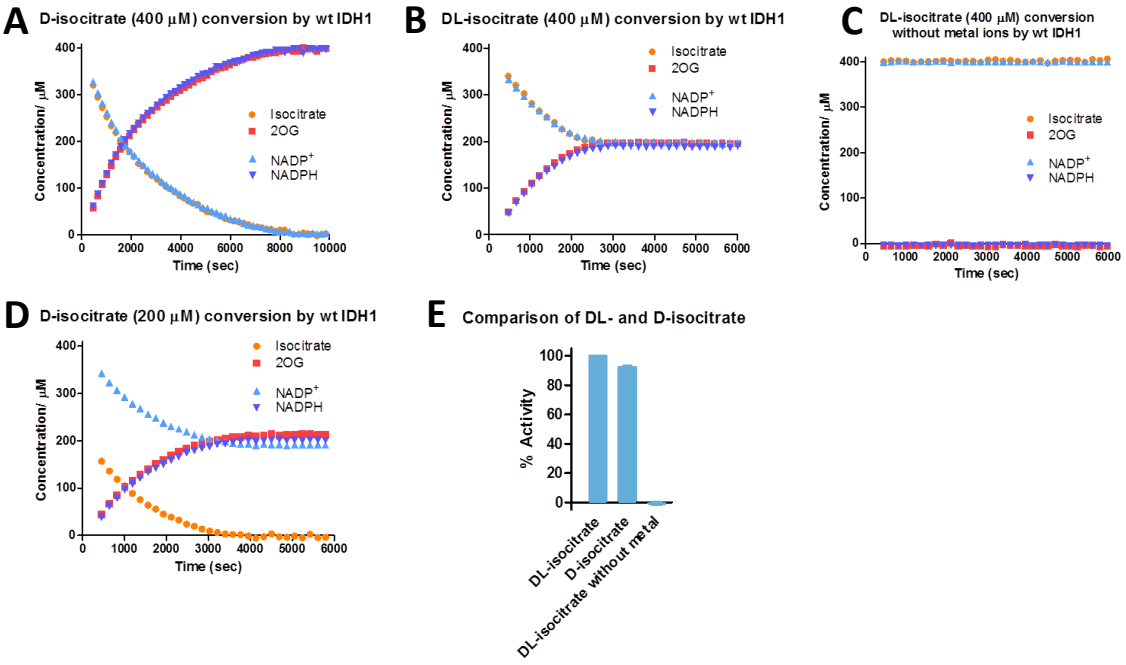



**Figure 2.9**. Conversion of DL-/ D-isocitrate and $NADP^+$ to 2OG and NADPH as catalysed by wt IDH1, as monitored by $^1H$ NMR (excitation sculpting suppression with perfect-echo, 700 MHz). The % activity is determined based on mean NMR signals of isocitrate, 2OG, $NADP^+$ and NADPH, ± SEM. Buffer: 50 mM Tris-$D_{11}$-HCl, pH 7.5 in 90% $H_2O$/ 10% $D_2O$ (v/v). The signal intensities of D-isocitrate and DL-isocitrate were normalised prior to reaction monitoring, as DL-isocitrate contains an unknown water content in the commercial product. (**A**) D-isocitrate was fully converted to 2OG. (**B**) DL-isocitrate underwent ~50% conversion, suggesting that only D-isocitrate was consumed. (**C**) No conversion of DL-isocitrate was observed in the absence of $MgCl_2$. (**E**) Comparing (**B**) and (**D**) which contain the same effective concentrations of D-isocitrate (200 mM), the rates of wt IDH1 (95 nM $s^{-1}$ as the 100% reference) catalysed conversion of DL-isocitrate and D-isocitrate to 2OG are similar, implying that IDH1 catalysis is not inhibited by L-isocitrate.

### 2.4.2 Phosphate group in NADP(H) is key in cofactors binding to IDH1

Among the three human isoforms of IDH, IDH1 and 2 use $NADP^+$ (NADPH for variant IDH1/2), whilst IDH3 uses $NAD^+$ as the cofactor. It was therefore of interest to investigate whether $NAD^+$ and NADH can act as alternative cofactors for wt IDH1 and R132H IDH1 respectively. Absorbance-based assays indicated that by removing the third phosphate group from $NADP^+$ or NADPH, *i.e.* by conducting assays with $NAD^+$/NADH, wt IDH1 and R132H IDH1 become completely inactive (**Figure 2.10A** and **2.10B**). This is consistent with the reported crystal structures that show the oxygen atoms of the

phosphate group forming key hydrogen bonding and ionic interactions with the nitrogen atoms of three amino acid residues (Q257, K260 and H315) of IDH1 (**Figure 2.10C**).

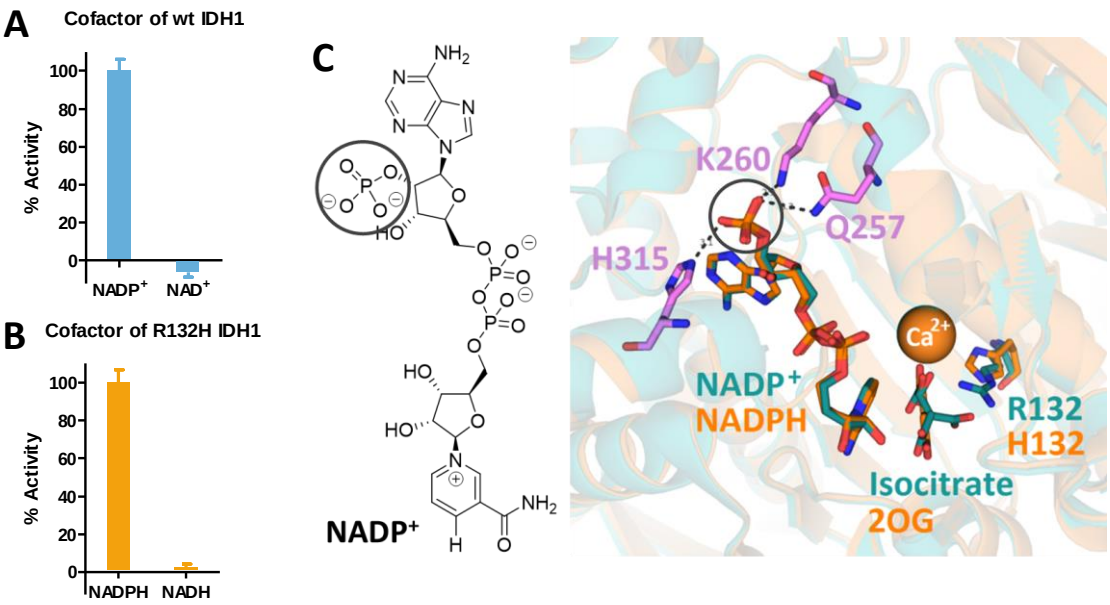



**Figure 2.10**. (**A**) Activity of wt IDH1 (0.25 µM $s^{-1}$ as the 100% reference) with $NADP^+$ or $NAD^+$ (75 µM for both) as the cofactor and (**B**) Activity of R132H IDH1 (0.18 µM $s^{-1}$ as the 100% reference) with NADPH or NADH (50 µM for both) as the cofactor, as measured by absorbance-based assays. The rest of the conditions follow the standard assay conditions. Data are mean ± SD, n= 3 technical replicates. (**C**) Active site view of superimposed X-ray crystal structures of wt IDH1 (cyan, PDB 1T0L)[12] and R132H IDH1 (orange, PDB 3INM)[11]. The phosphate group of NADP(H), which is absent in NAD(H), is circled in black.

Binding studies of $NAD^+$ and NADH to wt IDH1 and R132H IDH1 were also carried out using DSF and NMR spectroscopy. As shown in **Section 2.2**, copurifying NADPH was present for both wt and R132H IDH1 in all binding studies. The DSF results demonstrate that compared to the natural cofactors $NADP^+$ and NADPH (see **Figure 2.6D, 2.6E, 2.7D** and **2.7E**), wt IDH1 and R132H IDH1 are weakly stabilised by the addition of NADH (up to 1.8 °C for wt IDH1 and up to 2.6 °C for R132H IDH1) and show no thermal stabilisation by $NAD^+$ (**Figure 2.11**). In addition, NMR spectroscopy showed that both $NAD^+$ and NADH bind more strongly to wt IDH1 than to R132H IDH1, and that NADH binds more strongly to both forms of IDH1 than $NAD^+$ does (**Figure 2.12**). A ~10-fold molar excess of $NAD^+$ and NADH (500 µM) with respect to the native copurifying cofactor was each added to wt IDH1 and R132H IDH1, to compete with the copurifying cofactor, NADPH. NADPH was not displaced by NAD(H) as its NMR signal as free ligand in solution was not observed

(data not shown), suggesting that the strong binding of NADPH to wt IDH1 and R132H IDH1 could be attributed to its extra phosphate group shown in **Figure 2.10C**.

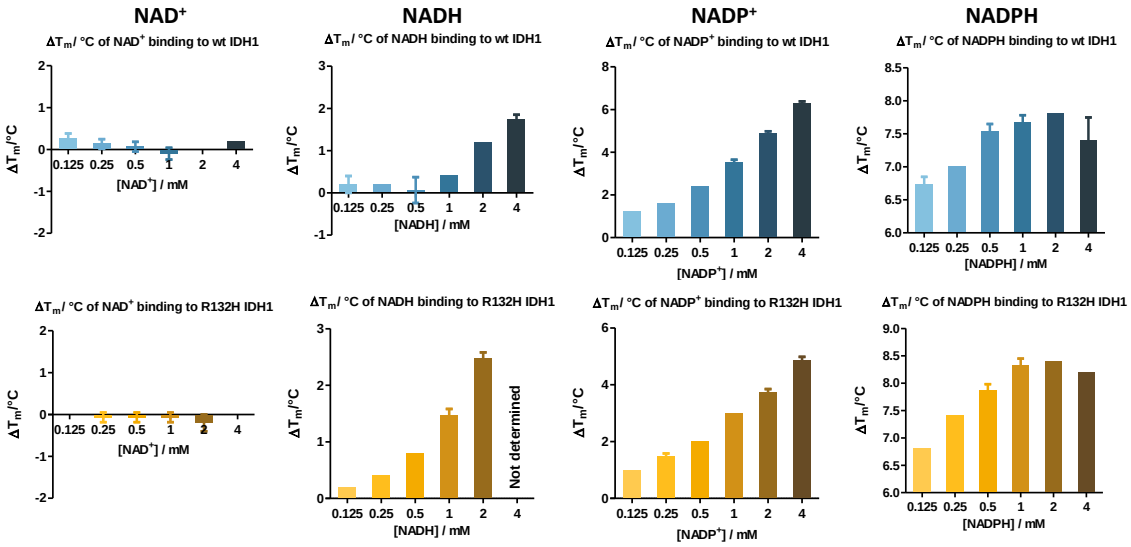



**Figure 2.11**. Dose-dependent (0.125–4 mM) thermal shift results of wt IDH1 (top row) and R132H IDH1 (bottom row) by cofactors (from left to right) $NAD^+$, NADH, $NADP^+$ and NADPH, in 50 mM Tris-HCl, pH 7.5, as measured by DSF. Data are mean ± SD, n= 3 technical replicates. Rank order of thermal stabilisation: NADPH > $NADP^+$ > NADH > $NAD^+$. The minimal stabilising effects of $NAD^+$ and NADH on wt IDH1 and R132H IDH1 are likely due to the missing phosphate group.

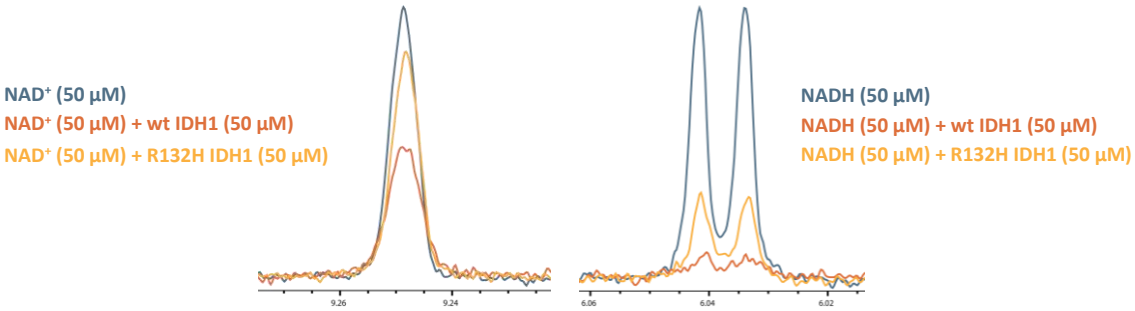



**Figure 2.12**. $^1H$ NMR (CPMG-edited, 700 MHz) binding analyses of 50 µM $NAD^+$ (left) and NADH (right) binding to equimolar wt IDH1 (orange) or R132H IDH1 (yellow-orange). Buffer: 50 mM Tris-$D_{11}$-HCl, pH 7.5 in 90% $H_2O$/ 10% $D_2O$ (v/v). Both $NAD^+$ and NADH bind more strongly to wt IDH1 than to R132H IDH1, and NADH binds more strongly to wt IDH1 and R132H IDH1 than $NAD^+$ does.

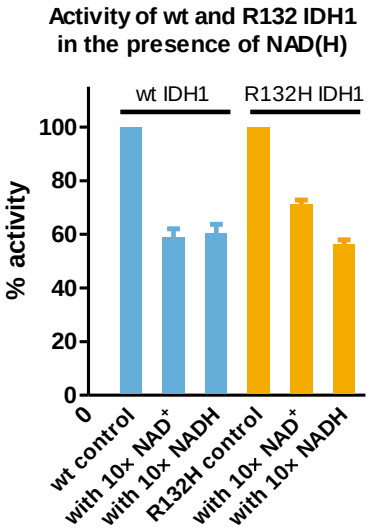



**Figure 2.13**. Activity of wt IDH1 (blue) and R132H IDH1 (orange) in the presence or absence of a 10× molar excess of $NAD^+$ or NADH compared to the native cofactor $NADP^+$ or NADPH, as measured by $^1H$ NMR (excitation sculpting suppression with perfect-echo, 700 MHz). The % activity is determined based on mean NMR signals of 2OG, isocitrate/2HG, $NADP^+$ and NADPH, and is calculated using the (treated/control) × 100% ± SEM. Buffer: 50 mM Tris-$D_{11}$-HCl, pH 7.5 in 90% $H_2O$/ 10% $D_2O$ (v/v). wt IDH1 activity (70 nM $s^{-1}$ as the 100% reference) is measured by isocitrate conversion to 2OG, using 6 nM wt IDH1, 550 µM DL-isocitrate, 600 µM $NADP^+$, 10 mM $MgCl_2$, ± 6 mM $NAD^+$ or NADH. R132H IDH1 activity (0.15 µM $s^{-1}$ as the 100% reference) is measured by 2OG conversion to 2HG, using 600 nM R132H IDH1, 0.5 mM 2OG, 0.5 mM NADPH, 10 mM $MgCl_2$, ± 5 mM $NAD^+$ or NADH.

The effect of NAD(H) on activity of wt IDH1 and R132H IDH1 was also examined. Due to the intrinsic absorbance of NADH being indistinguishable from that of NADPH, NMR spectroscopy instead of an absorbance-based assay was employed for reaction monitoring. At a 10× molar excess of NAD(H) than the native cofactor for wt IDH1 or R132H IDH1, around 40% inhibition of IDH1 activity is observed (**Figure 2.13**). Although $NAD^+$ and NADH bind to IDH1 more poorly than $NADP^+$ and NADH do, at sufficiently high concentrations, NAD(H) appear to act as inhibitors. Thus, competitive inhibition strategies employing analogues of NADP(H) may be viable.

### 2.4.3 $Mg^{2+}$ and $Mn^{2+}$ are active metal ions for IDH1

Following the unexpected results on the role of $Mg^{2+}$ ions in isocitrate binding to wt IDH1, it was of interest to investigate binding of other metal ions to wt IDH1 and R132H IDH1. Besides $Mg^{2+}$ and $Mn^{2+}$ ions that are commonly used in most IDH1 studies[11,38,158,181,183], the effects of a range of monovalent and divalent metal ions on the activities of wt IDH1 and R132H IDH1, relative to the maximum velocities effected by $Mg^{2+}$, were examined by absorbance-based assays. Of all the metal ions tested, $Mg^{2+}$ and $Mn^{2+}$ are the only two metal ions able to promote efficient IDH1 catalysis with similar activities at a concentration of 10 mM (**Figure 2.14**). DSF studies showed that wt IDH1 has the greatest thermal stabilisation by the addition of $Ca^{2+}$ (3.2 °C) and $Mn^{2+}$ (2.9 °C), with $Mg^{2+}$ having a less stabilising effect. This observation is consistent with use

of the catalytically inactive $Ca^{2+}$ to mimic $Mg^{2+}$ in X-ray crystallography of IDH1 (**Figure 2.2**)[11,12]. However, given that $Ca^{2+}$ has been reported to inhibit the binding of $Mn^{2+}$ and $Mg^{2+}$ to wt IDH1[189], the result shows subtle differences in divalent metal ions binding and their effects on wt IDH1 catalysis. Notably, $Mg^{2+}$, $Mn^{2+}$ and $Ca^{2+}$ all apparently destabilise R132H IDH1, with $Ca^{2+}$ having the least destabilising effect (-1.2 °C) (**Figure 2.15**). The differences in the effects of divalent metal ion on wt IDH1 and R132H IDH1 again hint at subtle differences between the two enzymes in the way they bind bivalent metal ions.

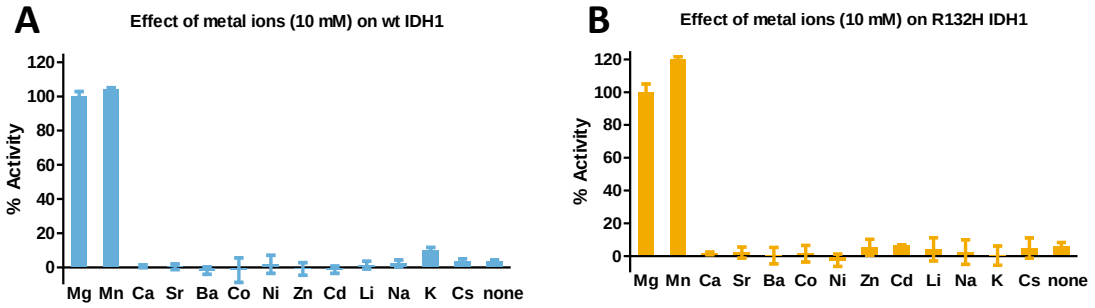



**Figure 2.14**. Activities of wt IDH1 and R132H IDH1 with different metal ions. Effect of metal ions (10 mM) on catalysis by (**A**) wt IDH1 and (**B**) R132H IDH1, as measured by absorbance-based assays. Data are mean ± SD, n= 3 technical replicates. Standard assay conditions as defined in **Table 2.2** were used with a replacement of $MgCl_2$ with other metal ions. Chloride salts were used in all cases. Activities were normalised to that observed with $MgCl_2$ (71 nM $s^{-1}$ for wt IDH1 (2 nM); 29 nM $s^{-1}$ for R132H IDH1 (30 nM)). The absorbance values from a no-enzyme control were subtracted from the raw data for $CoCl_2$ due to intrinsic absorbance of $Co^{2+}$ in solution.

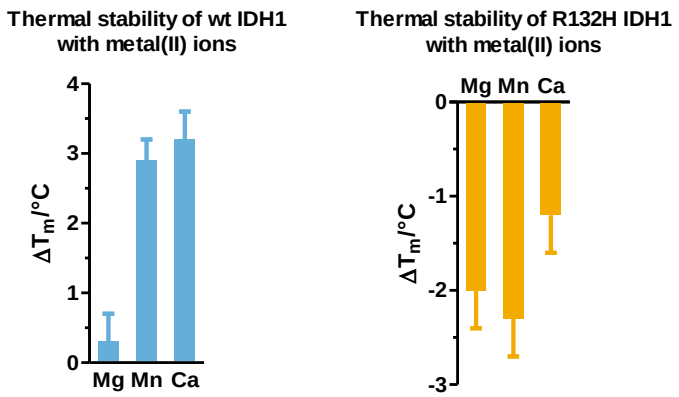
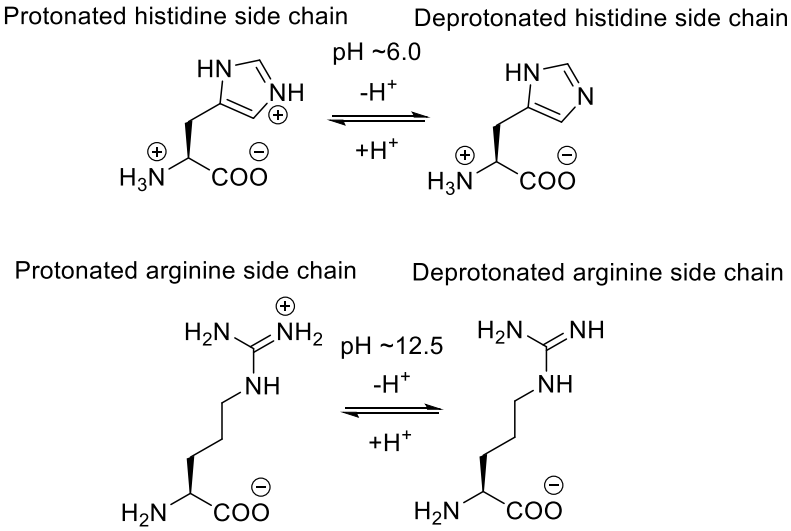



**Figure 2.15**. Thermal stability of wt (left) and R132H (right) IDH1 with different metal ions (5 mM), in 50 mM Tris-HCl, pH 7.5, as measured by DSF. Data are mean ± SD, n= 3 technical replicates. In general, these metal ions appear to stabilise wt IDH1 but destabilise R132H IDH1.

## 2.5 Effect of pH on IDH1 activity

It is intriguing to consider the natural selection of arginine-to-histidine as the predominant substitution for IDH1. Chemically, side chains of arginine and histidine are

both basic, however with different p$K_a$: ~6.0 for histidine and ~12.5 for arginine in solution (**Scheme 2.3**). This implicates that at physiological pH, the histidine side chain is substantially not protonated (*i.e.* not positively charged), whereas the arginine side chain is almost always protonated (*i.e.* positively charged). The equilibrium may be shifted to deprotonated histidine even further in cancer cells where the intracellular pH ($pH_i$) is higher at ~7.5–7.6[190,191] than in normal cells (pH ~7.2) (**Table 2.3**). (Note that this does not exclude the possibility of slightly varying local pH inside the protein microenvironment.) As a result, the R132H substitution potentially leads to loss of not only hydrogen bonding but also ionic interaction.




**Scheme 2.3**. Protonation states of the histidine and arginine side chains in solution at pH below and above their p$K_a$ values respectively.

| | Normal cells | Cancer cells |
|---|---|---|
| Intracellular pH (pHi) | 7.2 | 7.5–7.6 |
| Extracellular pH (pHe) | 7.4 | 6.7–7.1 |

**Table 2.3**. Intracellular and extracellular pH in normal and cancer cells[190,191]. Note that the pH gradient across the cell membrane is reversed in cancer cells compared to normal cells.

Besides IDH mutations in gliomas and AML, R to H substitutions are also enriched in multiple cancer types including colorectal, stomach and pancreatic cancers[192], with the highest overall frequency of occurrence compared to other mutations[193]. A model study using an R776H variant of the epidermal growth factor receptor (EGFR) suggests that the protonation state of histidine is pH sensitive within a narrow range of pH 7.3–7.6[191]. Raising $pH_i$ increases the mutant activity whilst lowering $pH_i$ reduces cancer cell proliferation and the tumorigenic effects of R to H mutations[191]. Thus, R to H

substitutions may confer the variant enzymes with an adaptive advantage to the more alkaline cancer cells.

Inspired by this proposal, both wt and R132H IDH1 activities were tested at different pHs. One aim was to see if it was possible to revert R132H IDH1 back to its wt function *i.e.* to find a pH for R132H IDH1 with decreased neomorphic activity and increased wt activity. A wide pH range from 3.0 to 10.5 in intervals of 0.5 pH units was tested using the appropriate buffer systems (**Figure 2.16**). Protein degradation, as observed by its precipitation at pH 3.0–4.0, likely occurred at extreme pH conditions and interfered with the results. Hence, only results from pH 5.5 to 9.0 are reported **(Figure 2.17**).

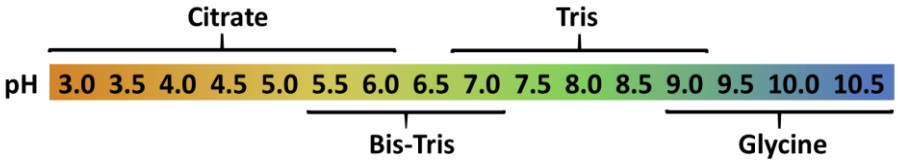



**Figure 2.16**. Buffer systems with different buffering ranges used for pH screening of IDH1 activity. At least one pH point is shared by two buffer systems to take account of different buffer component effects on IDH1 activity.

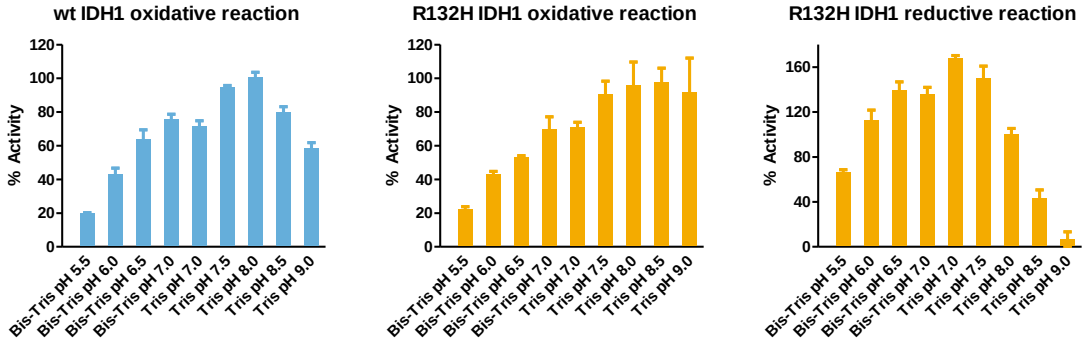



**Figure 2.17**. wt IDH1 and R132H IDH1 activity from pH 5.5 to 9.0 using Bis-Tris or Tris buffer system, as measured by absorbance-based assays. Data are mean ± SD, n= 3 technical replicates. wt IDH1 and R132H IDH1 oxidative reaction refers to the conversion of isocitrate to 2OG. R132H IDH1 reduction reactions refers to conversion of 2OG to 2HG. wt IDH1 reductive reaction of 2OG to isocitrate is not presented as varying $CO_2$ concentrations released by $NaHCO_3$ at different pH interfered with enzymatic activity. All other reagents were used at standard conditions as defined in **Table 2.2**. The % activity is calculated from initial linear slope of the reaction profile, using that at pH 8.0 which is used in standard assays as the 100% reference (0.15 µM $s^{-1}$ for wt IDH1 (3 nM) oxidative; 48 nM $s^{-1}$ for R132H IDH1 (1 µM) oxidative; 97 nM $s^{-1}$ for R132H IDH1 (200 nM) reductive).

Most reported IDH activity assays are conducted at pH 7.5 or 8.0. The results in **Figure 2.17** showed that the oxidative activity of wt IDH1 (isocitrate to 2OG) is the highest at pH 8.0 with a decrease past pH 8.0, whilst the oxidative activity of R132H IDH1 (isocitrate to 2OG) is the highest at pH 8.0–8.5 and the maximum activity is sustained even to pH 9.0. By contrast, the R132H IDH1 reductive activity (2OG to 2HG) is the highest at pH 7.0, with a drastic drop beyond pH 7.5 and minimal activity at pH 9.0. In addition, reported MS analysis revealed that wt IDH1 exhibits minimal change with pH (tested at pH 6.0 and 7.4) in 2HG production[194]. Overall, these suggest that at high pH values (*e.g.* pH 9.0), the neomorphic activity of R132H IDH1 leading to 2HG production can be significantly reduced without compromising its 'wildtype' oxidative activity. This knowledge may be relevant to the role of IDH variants in cancer and further highlights differences between catalysis by wt IDH1 and the R132H variant.

## 2.6 Preliminary inhibitor screening against IDH1

Given the key role of IDHs in 2OG production and the proposed role of elevated 2HG arising from cancer associated IDH variants in inhibiting 2OG-dependent dioxygenases, it was of interest to pursue 2OG-dependent dioxygenase inhibitors as IDH inhibitors. Inhibitors of some 2OG-dependent dioxygenases, compounds related to metabolism and cellular pathways of IDH1, as well as antibiotics (**Table 2.4**) were thus screened at 250× molar excess of enzyme concentration *i.e.* 1.125 μM and 100 μM against wt IDH1 and R132H IDH1 respectively (**Figure 2.18**). TCA cycle intermediates and 2OG analogues such as *N*-oxalylglycine (NOG) were also screened, and the results are separately presented in **Chapter 7**.

In general, there is no potent inhibition of wt IDH1 or R132H IDH1 by inhibitors of 2OG-dependent dioxygenases, including the PHD inhibitors in clinical trials. This is perhaps unsurprising since most of the reported IDH inhibitors are allosteric inhibitors without structural resemblance to 2OG. Glutamate dehydrogenase (GDH) inhibitors, such as bithionol and hexachlorophene, inhibit R132H IDH1, but not wt IDH1 at the tested concentrations. However, these compounds may have a non-specific inhibition mechanism, as close to full inhibition was also observed for wt IDH1 at 100 μM bithionol and hexachlorophene (data not shown). Notably, ebselen[195] fully inhibits both wt and

R132H IDH1. Preliminary data showed that the inhibition of R132H IDH1 by ebselen is time-dependent, suggesting that ebselen could be behaving as a covalent inhibitor, as observed for ebselen with other enzymes (via cysteine modifications)[196,197]. This leads to a detailed investigation of both selective and non-selective covalent inhibitors of R132H IDH1, as described in **Chapter 6**.

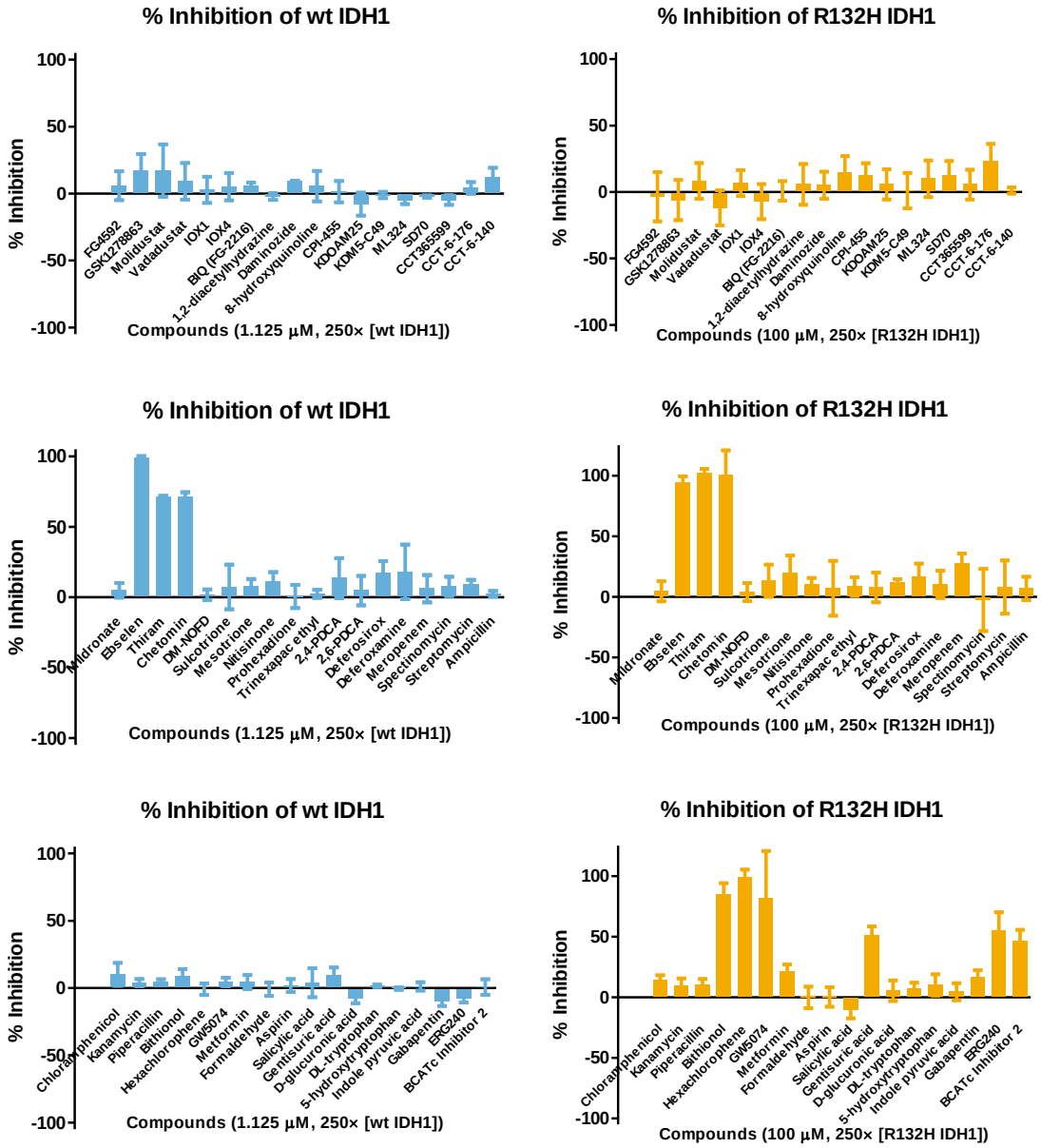
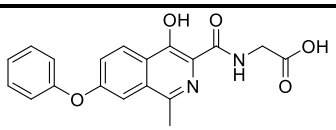
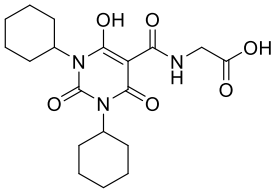
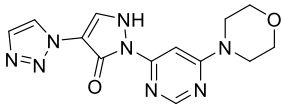
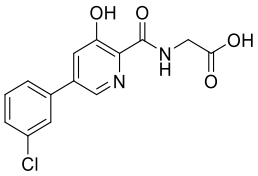
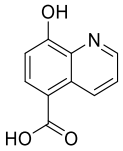
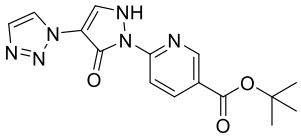
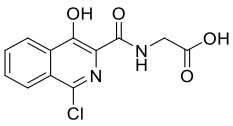
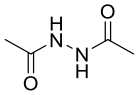
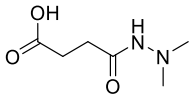
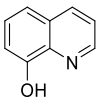
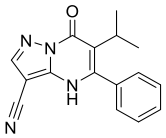
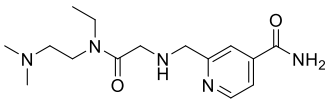
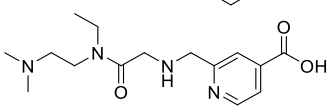
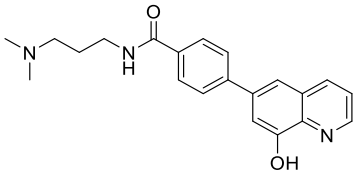
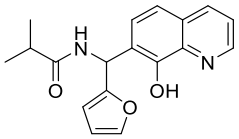
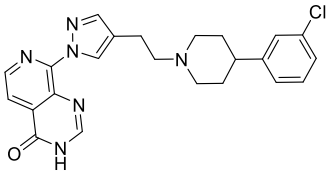
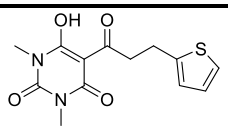
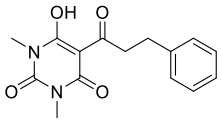
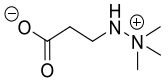
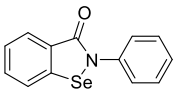
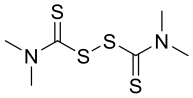
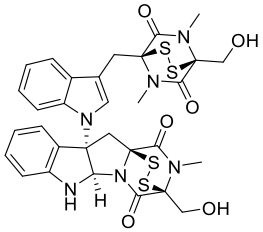
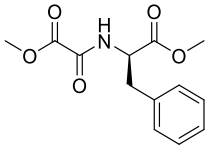
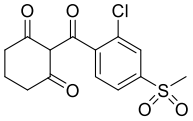
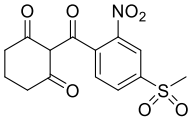
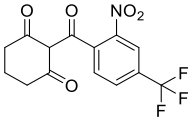
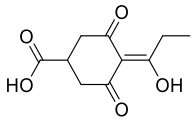
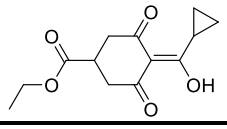
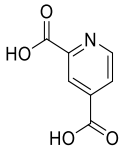
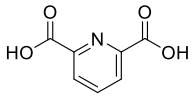
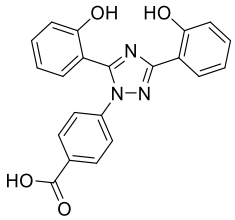
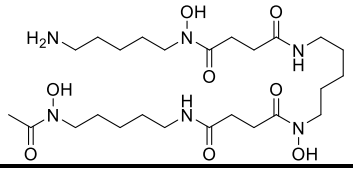
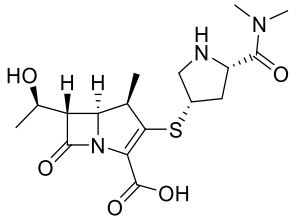
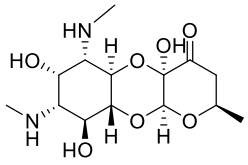
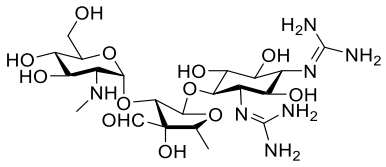
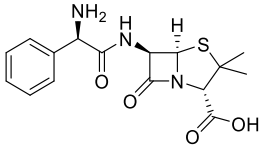
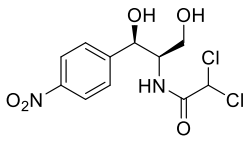
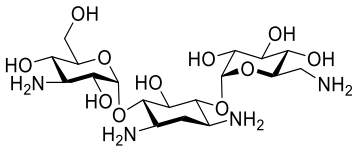
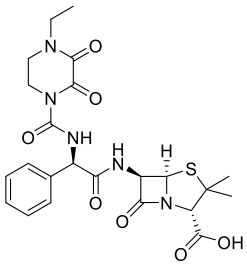
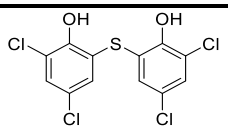
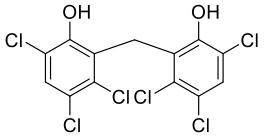
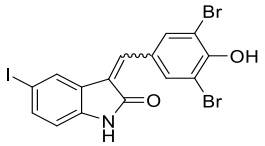
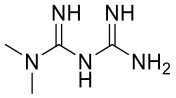
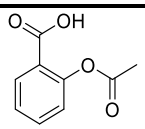
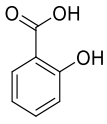
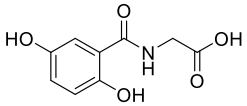
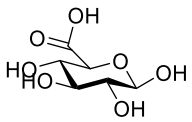
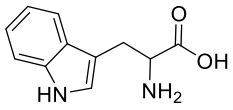
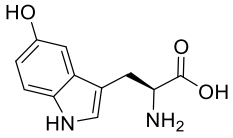



**Figure 2.18**. Percentage inhibition of compounds screened against wt IDH1 and R132H IDH1, as measured by absorbance-based assays. Data are mean ± SD, n= 3 technical replicates. The wt activity is measured by oxidative conversion of isocitrate to 2OG whilst R132H IDH1 activity is measured by reductive conversion of 2OG to 2HG. All compounds were tested at 250× the enzyme concentration.

| Category | Compound | Structure |
|---|---|---|
| **PHD inhibitors**<br><br>The PHDs are 2OG-dependent dioxygenase that modify the HIF transcription factors (see **Section 1.2.3**). Note that FG4592 is approved for clinical use for the treatment of anaemia and other PHD inhibitors are in clinical trials. | FG4592 |  |
| | GSK1278863 |  |
| | Molidustat |  |
| | Vadadustat |  |
| | IOX1 |  |
| | IOX4 |  |
| | BIQ (FG-2216) |  |
| | 1,2-diacetylhydrazine |  |
| **JmjC KDM inhibitors**<br><br>The JmjC KDMs are 2OG-dependent histone demethylases (see **Section 1.2.1**). | Daminozide |  |
| | 8-hydroxyquinoline |  |
| | CPI-455 |  |
| | KDOAM25 |  |
| | KDM5-C49 |  |

| | | |
|---|---|---|
| | ML324 |  |
| | SD70 |  |
| | CCT365599[198] |  |
| **2-oxoglutarate and iron-dependent oxygenase domain containing 1 (OGFOD) inhibitors**<br><br>OGFOD is a 2OG-dependent oxygenase[199]. | CCT-6-176 |  |
| | CCT-6-140 |  |
| **γ-Butyrobetaine hydroxylase (BBOX)**<br><br>BBOX is a 2OG-dependent oxygenase[195]. | Mildronate (Meldonium) |  |
| | Ebselen |  |
| | Thiram |  |
| **Hypoxia-inducible factor (HIF) inhibitor**<br><br>HIF contains motifs of 2OG-dependent oxygenase[200]. | Chetomin |  |
| **Factor-inhibiting HIF (FIH) inhibitor**<br><br>FIH is a 2OG-dependent oxygenase. | Dimethyl *N*-oxalyl-D-phenylalanine (DM-NOFD), prodrug of NOFD |  |
| **4-Hydroxyphenylpyruvate dioxygenase (HPPD) inhibitors**<br><br>HPPD is a '2OG oxygenase like' 2-oxo acid oxygenase[201]. | Sulcotrione |  |
| | Mesotrione |  |
| | Nitisinone |  |

| | | |
|---|---|---|
| | Prohexadione |  |
| | Trinexapac ethyl |  |
| **Metal Chelators**<br><br>$Mg^{2+}$ is present at 10 mM in the assay buffer as $K_M$ of $MgCl_2$ in the reductive reaction by R132H IDH1 is 4.4 ± 0.7 mM (**Table 1**). Metal chelators were expected to have little effect on IDH1 when tested at <10 mM. | 2,4-PDCA |  |
| | 2,6-PDCA |  |
| | Deferosirox |  |
| | Deferoxamine |  |
| **Antibiotics**<br><br>YcfD ribosomal 2OG-dependent oxygenase is inhibited by chloramphenicol (unpublished results from the Schofield group). | Meropenem |  |
| | Spectinomycin |  |
| | Streptomycin |  |
| | Ampicillin |  |
| | Chloramphenicol |  |

| | | |
|---|---|---|
| | Kanamycin |  |
| | Piperacillin |  |
| **Glutamate dehydrogenase (GDH) inhibitors**<br><br>GDH catalyses the conversion of glutamate to 2OG using $NAD(P)^+$. The product and the cofactor are the same as wt IDH. | Bithionol |  |
| | Hexachlorophene |  |
| | GW5074 |  |
| **Diabetes drug**<br><br>To elucidate the mechanism of action of metformin | Metformin |  |
| **Alkylating agent**<br><br>To explore covalent modifications on IDH | Formaldehyde |  |
| **Aspirin and its metabolites**<br><br>To explore the possible links between inflammation and IDH mutations | Aspirin (Acetylsalicylic acid) |  |
| | Salicylic acid |  |
| | Gentisuric acid (GUA) |  |
| | D-glucuronic acid |  |
| **Tryptophan and its metabolites**<br><br>Tryptophan metabolism was deregulated for cancer cells with mutated *IDH* genes[202]. | DL-Tryptophan |  |
| | 5-hydroxytryptophan |  |

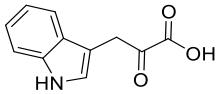
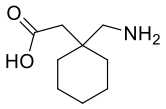
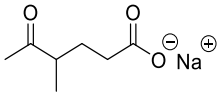
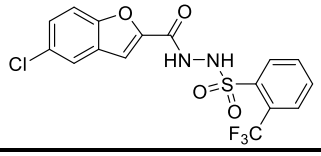
| | | |
|---|---|---|
| | Indole pyruvic acid |  |
| **Branched-chain amino acid transferase-1 (BCAT 1) inhibitor**<br><br>BCAT1 is an enzyme which regulates glutamate synthesis and is upregulated in IDH mutant cells[203]. | Gabapentin (Neurontin) |  |
| | ERG240 (4-methyl-5-oxohexanoic acid) |  |
| | BCATc Inhibitor 2 |  |

**Table 2.4**. A list of compounds screened against wt IDH1 and R132H IDH1, presented with their structures and biological/inhibitory relevance.

## 2.7 Summary

Biochemical comparison of wt IDH1 and R132H IDH1 reveals distinct differences in their $K_M$ values, particularly for isocitrate, providing an explanation for the lower preference of R132H IDH1 for isocitrate as the substrate compared to wt IDH1. Both wt and R132H IDH1 also manifested differences in their pH dependences, notably for the R132H variant with respect to its acceptance of isocitrate versus 2OG as a substrate. The copurifying cofactor NADPH has high binding affinity to both wt IDH1 and the R132H variant, evident from both its low $K_M$ value and high degree of thermal stabilisation of the enzymes. Despite the differences in enzyme kinetics, both wt and R132H IDH1 share similar overall structures. Binding studies highlighted the importance of metal ion cofactors in substrate binding by IDH1, with subtle differences being observed between the effects of divalent metal ions on wt IDH1 and the R132H variant. Interestingly the results implied that the combination of $Mg^{2+}$ and isocitrate was important in wt IDH1 catalysis, an observation pursued in **Chapter 3**. Preliminary inhibitor screening identified covalent inhibitors as an area of research to be further investigated, as described in **Chapter 6**.

## 2.8 Supplementary Figures

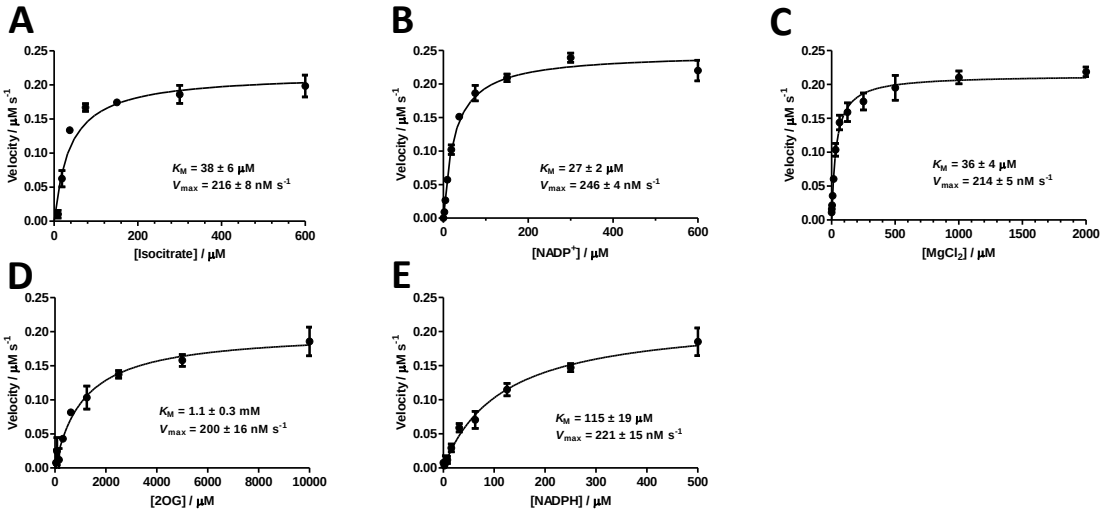



**Figure S2.1.** Dependence of reaction rates (monitored by NADPH formation/depletion by absorbance-based assays) on different concentrations of (co)substrates (**A**) DL-isocitrate, (**B**) $NADP^+$ and (**C**) $MgCl_2$ in the oxidative reaction (isocitrate to 2OG), as well as (**D**) 2OG and (**E**) NADPH in the reductive reaction (2OG to isocitrate) by wt IDH1. The error bars represent mean ± SEM, n= 3 technical replicates. The calculated $K_M$ and $V_{max}$ values are reported as mean ± SEM from the data fit. Buffer is 100 mM Tris-HCl, 10 mM $MgCl_2$, 0.005% (v/v) Tween 20, 0.1 mg/mL BSA and 0.2 mM DTT, pH 8.0. 10 mM $MgCl_2$ is excluded in the kinetic parameters determination of $MgCl_2$. Kinetic parameters for $MgCl_2$ in the reductive reaction (2OG to isocitrate) by wt IDH1 could not be reliably determined as the reaction occurs even at 0 mM $MgCl_2$.

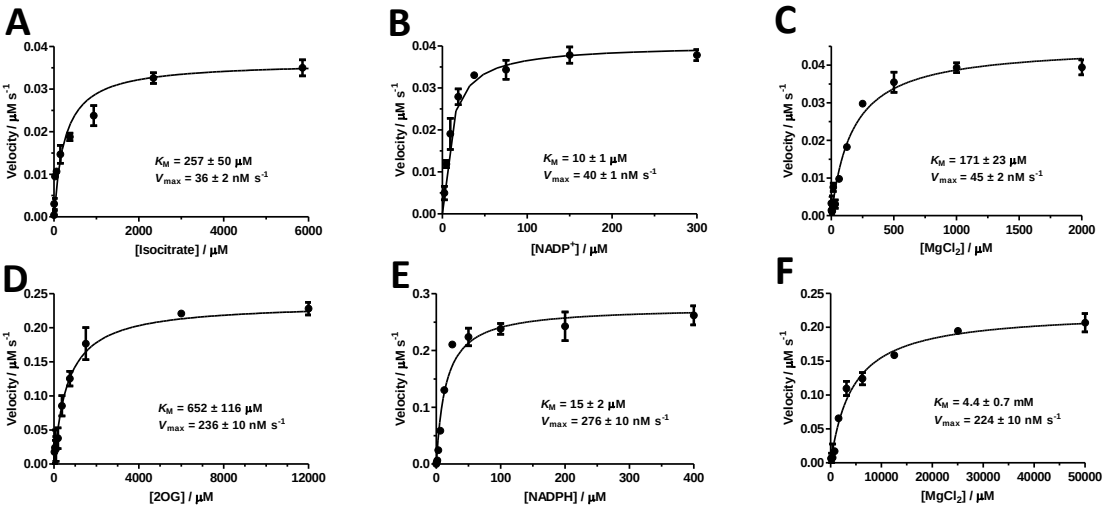



**Figure S2.2.** Dependence of reaction rates (monitored by NADPH formation/depletion by absorbance-based assays) on different concentrations of (co)substrates (**A**) DL-isocitrate, (**B**) $NADP^+$ and (**C**) $MgCl_2$ in the oxidative reaction (isocitrate to 2OG), as well as (**D**) 2OG, (**E**) NADPH and (**F**) $MgCl_2$ in the reductive reaction (2OG to 2HG) by R132H IDH1. The error bars represent mean ± SEM, n= 3 technical replicates. The calculated $K_M$ and $V_{max}$ values are reported as mean ± SEM from the data fit. Buffer is 100 mM Tris-HCl, 10 mM $MgCl_2$, 0.005% (v/v) Tween 20, 0.1 mg/mL BSA and 0.2 mM DTT, pH 8.0. 10 mM $MgCl_2$ is excluded in the kinetic parameters determination of $MgCl_2$.

| Cell | Titrant | [Titrant]/ μM | Additive | Observations |
|---|---|---|---|---|
| **wt IDH1 (40 μM)** | Isocitrate | 400 | | Very weak binding |
| **wt IDH1 (40 μM)** | Isocitrate | 1200 | | Very weak binding |
| **wt IDH1 (40 μM)** | Isocitrate | 1200 | Mg | Binding, $K_D$= 1 μM, N= 2.15. Reproducible, $K_D$= 1 μM, N= 2.25 |
| **wt IDH1 (40 μM)** | 2OG | 800 | Mg | Weak binding |
| **wt IDH1 (40 μM)** | $MgCl_2$ | 800 | | No binding |
| **wt IDH1 (40 μM)** | $NADP^+$ | 400 | | First peak only |
| **wt IDH1 (40 μM)** | $NADP^+$ | 1200 | | First two peaks only |
| **wt IDH1 (40 μM)** | $NADP^+$ | 800 | Mg | First peak only |
| **wt IDH1 (40 μM)** | NADPH | 800 | Mg | First peak only |
| **wt IDH1 (40 μM)** | 2HG | 1200 | Mg | No binding |
| **wt IDH1 (40 μM)** | $MgCl_2$ | 8000 | | First peak only |
| **wt IDH1 (40 μM)** | $CaCl_2$ | 8000 | | Weak binding |
| **R132H IDH1 (40 μM)** | Isocitrate | 800 | | No binding |
| **R132H IDH1 (40 μM)** | Isocitrate | 800 | Mg | No binding |
| **R132H IDH1 (40 μM)** | Isocitrate | 1200 | Mg | No binding |
| **R132H IDH1 (40 μM)** | 2OG | 400 | | No binding |
| **R132H IDH1 (40 μM)** | 2OG | 10000 | | No binding |
| **R132H IDH1 (40 μM)** | 2OG | 400 | Mg | No binding |
| **R132H IDH1 (40 μM)** | 2OG | 8000 | Mg | No binding |
| **R132H IDH1 (40 μM)** | NOG | 800 | Mg | Weak binding |
| **R132H IDH1 (40 μM)** | $NADP^+$ | 400 | | First peak only |
| **R132H IDH1 (40 μM)** | $NADP^+$ | 1200 | | First two peaks only |
| **R132H IDH1 (40 μM)** | $NADP^+$ | 800 | Mg | First peak only |
| **R132H IDH1 (40 μM)** | NADPH | 400 | | First peak only |
| **R132H IDH1 (40 μM)** | NADPH | 800 | Mg | First two peaks only |
| **R132H IDH1 (40 μM)** | 2HG | 1200 | Mg | No/weak binding, first peak only |
| **R132H IDH1 (40 μM)** | $MgCl_2$ | 800 | | No binding |
| **R132H IDH1 (40 μM)** | $MgCl_2$ | 8000 | | No binding |
| **Buffer** | NADPH | 400 | | First peak only |
| **Buffer** | $NADP^+$ | 1200 | | No effect |
| **Buffer** | Isocitrate | 1200 | | No effect |
| **Buffer** | Isocitrate | 1200 | Mg | No effect |
| **Buffer** | Isocitrate | 4000 | Mg | Weak binding likely due to isocitrate binding to Mg |
| **Buffer** | Isocitrate | 8000 | Mg | Binding likely due to isocitrate binding to Mg |
| **Buffer** | 2OG | 8000 | Mg | No effect |
| **Isocitrate (500 μM)** | $MgCl_2$ | 5000 | | Binding, $K_D$= 2.69 mM |
| **2OG (500 μM)** | $MgCl_2$ | 5000 | | No binding |

**Table S2.3**. ITC results summary. Buffer: 50 mM Tris-HCl, pH 7.5; 'Mg' refers to 50 mM Tris-HCl and 5 mM $MgCl_2$, pH 7.5. 'First peak only' and 'First two peaks only' refers to signals at the first (and second) injection(s) but no further significant signals for the subsequent injections. 'Weak binding' suggests a weak binding pattern but $K_D$ could not be extracted. N is the stoichiometry of titrant with respect to protein (N= 2 as DL-isocitrate was used)

# CHAPTER 3.

# METAL IONS PLAY A KEY ROLE IN THE ALLOSTERIC INHIBITION OF R132H IDH1

Binding studies of (co)substrates to wt IDH1 by ITC as described in **Chapter 2** showed that neither isocitrate nor $Mg^{2+}$ alone binds tightly to wt IDH1, implying that an isocitrate-$Mg^{2+}$ complex may be the preferred substrate for wt IDH1 instead. This proposal is consistent with the reported kinetic studies which concluded that either the isocitrate-$Mg^{2+}$ [204] or isocitrate-$Mn^{2+}$ [205] complex is the actual substrate for NADP-dependent porcine heart IDH2. Thus, isocitrate forms a complex with $Mg^{2+}$ before binding to the enzyme, instead of isocitrate or $Mg^{2+}$ individually binding to the enzyme. Additionally, upon careful re-examination of the kinetic parameters of wt IDH1 and R132H IDH1 (**Chapter 2**), profound differences in metal ion dependencies are observed: the $K_M$ of $Mg^{2+}$ for wt IDH1 is significantly lower than that for R132H IDH1. These results highlight the importance of metal ions in the catalysis and the inhibition of wt IDH1 and the R132H variant. The work described in this chapter seeks to further investigate the role of metal ions in IDH catalysis in detail. Although there are classical studies on metal ions used by wt IDH2 from porcine heart[205,206], few recent studies are reported on this topic, particularly with respect to IDH inhibition.

## 3.1 Metal ions in biology

Metal ions are fundamentally important in biology. ~70% of all enzymes bind metal ions for structural stabilisation and function[207]. $Na^+$, $K^+$, $Mg^{2+}$ and $Ca^{2+}$ are widely found in all life forms[208], with $Mg^{2+}$ and $K^+$ being the most abundant metal ions in cells[209]. $Mg^{2+}$ plays an important role in binding to nucleic acids and stabilising their structures[210]. Differences in $Mg^{2+}$ levels are reported in diseases such as diabetes[211]. $Ca^{2+}$, a ubiquitous second messenger, is involved in signalling and regulation of numerous cellular processes[212]. $Mn^{2+}$ and less commonly, $Ni^{2+}$ and $Co^{2+}$, can be used as surrogates for $Mg^{2+}$, due to their relatively similar size and chemistry. $Mn^{2+}$ can replace $Mg^{2+}$ in many enzymes that use MgATP as the substrate, resulting in similar or sometimes higher enzymatic activity[209]. $Ca^{2+}$ is generally a poor substitute for $Mg^{2+}$, likely due to its

significantly larger ionic radius. These findings provide a plausible explanation for the observations in **Section 2.4.3** and literature reports[11,158] that both wt IDH1 and its R132H variant are active with either $Mg^{2+}$ or $Mn^{2+}$ in IDH1 catalysed reactions.

## 3.2 Biochemical studies of metal ions for IDH1

Many reported kinetic studies on human IDH1[11,38,158,181,183,185] lack a comprehensive characterisation of metal ions in the oxidative and reductive reactions by wt and mutant IDH1. In **Table 2.1**, a striking 120-fold difference in $K_M$ for $MgCl_2$ was observed between the R132H IDH1 catalysed reduction of 2OG to 2HG (4.4 mM) and the wt IDH1 catalysed oxidation of isocitrate to 2OG (36 µM). Similarly, one study reports a 300-fold difference in $K_M$ for $MgCl_2$ between the reductive reaction of R132H IDH1 (6.3 mM) and the oxidative reaction of wt IDH1 (19 µM)[183]. Furthermore, the $k_{cat}/K_M$ for $MgCl_2$ in the reductive reaction of R132H IDH1 ($1.4 \times 10^{-4}$ $s^{-1}$ $\mu M^{-1}$) is 10,000× lower than that in the oxidative reaction of wt IDH1 (1.4 $s^{-1}$ $\mu M^{-1}$), suggesting a profound difference in the catalytic efficiency of R132H IDH1 and wt IDH1 in their respective reactions using $MgCl_2$. The high $K_M$ for $MgCl_2$ observed for R132H IDH1 may be a consequence of its regulatory segment (residues 271–286) being only partially ordered and therefore cannot coordinate $Mg^{2+}$ with high affinity[213].

Besides $Mg^{2+}$, $Mn^{2+}$ is also an active metal ion for IDH1 catalysis. The same set of kinetic parameters was determined to compare the effects of metal ions on IDH1 catalysis. On substituting $Mn^{2+}$ for $Mg^{2+}$ (**Table 3.1**), the difference between $K_M$ for $MnCl_2$ in the R132H IDH1 catalysed reductive reaction and that in the wt IDH1 catalysed oxidative reaction becomes as large as 210-fold. Accordingly, the $k_{cat}/K_M$ for $MnCl_2$ in the reductive reaction of R132H IDH1 ($2.5 \times 10^{-3}$ $s^{-1}$ $\mu M^{-1}$) is 16400× lower than that in the oxidative reaction of wt IDH1 (41 $s^{-1}$ $\mu M^{-1}$). In general, reactions are faster with $Mn^{2+}$ than with $Mg^{2+}$, with a greater rate enhancement being observed for R132H IDH1 compared to wt IDH1: $k_{cat}$ of R132H IDH1 catalysed oxidation using $MnCl_2$ is 8 times faster than that using $MgCl_2$, whilst $k_{cat}$ of R132H IDH1 catalysed reduction using $MnCl_2$ is 1.7 times faster than that using $MgCl_2$. $K_M$ for $MnCl_2$ is 18 times smaller than that for $MgCl_2$ in the oxidative reaction by wt IDH1 and 10 times smaller for the reductive reaction by R132H IDH1. This finding shares similarity with prior literature where $Mg^{2+}$ has a $K_M$ 11 times greater than

that of $Mn^{2+}$ in the oxidative reaction by wt porcine heart IDH2[205]. These results suggest that R132H IDH1 prefers $MnCl_2$ to $MgCl_2$ in its catalysis. In the cellular context, $Mg^{2+}$ is likely to be more abundant than $Mn^{2+}$ [209]. In fact, from the preliminary data, $Mg^{2+}$, but not $Mn^{2+}$, was detected by inductively coupled plasma mass spectrometry (ICP-MS) for the mammalian wt IDH1 and R132H IDH1 cell (HEK293, obtained from co-worker Ilaria Pettinati) extracts.

| **Oxidative (Isocitrate to 2OG)** | | | |
|---|---|---|---|
| | | **wt** | **R132H** |
| **Isocitrate** | $K_M$ (μM) | 35 ± 4 | 219 ± 35 |
| | $V_{max}$ (nM $s^{-1}$) | 313 ± 8 | 355 ± 22 |
| | $k_{cat}/K_M$ ($s^{-1}$ $\mu M^{-1}$) | 2.3 ± 0.6 | (3.6 ± 0.9) × $10^{-3}$ |
| **$NADP^+$** | $K_M$ (μM) | 27 ± 3 | 80 ± 8 |
| | $V_{max}$ (nM $s^{-1}$) | 358 ± 7 | 302 ± 9 |
| | $k_{cat}/K_M$ ($s^{-1}$ $\mu M^{-1}$) | 3.0 ± 0.7 | (9.8 ± 2.0) × $10^{-3}$ |
| **$MnCl_2$** | $K_M$ (μM) | 2.0 ± 0.3 | (1.64 ± 0.01) × $10^3$ |
| | $V_{max}$ (nM $s^{-1}$) | 416 ± 13 | 290± 12 |
| | $k_{cat}/K_M$ ($s^{-1}$ $\mu M^{-1}$) | 41 ± 12 | (4.8 ± 0.5) × $10^{-4}$ |
| | $k_{cat}$ ($s^{-1}$) | 81 ± 11 | 0.78 ± 0.08 |

| **Reductive (2OG to isocitrate by wt, or 2HG by R132H)** | | | |
|---|---|---|---|
| | | **wt** | **R132H** |
| **2OG** | $K_M$ (μM) | | 175 ± 26 |
| | $V_{max}$ (nM $s^{-1}$) | | 390 ± 16 |
| | $k_{cat}/K_M$ ($s^{-1}$ $\mu M^{-1}$) | | (5.9 ± 1.2) × $10^{-3}$ |
| **NADPH** | $K_M$ (μM) | | 32 ± 5 |
| | $V_{max}$ (nM $s^{-1}$) | ‡ | 433 ± 18 |
| | $k_{cat}/K_M$ ($s^{-1}$ $\mu M^{-1}$) | | (3.3 ± 0.7) × $10^{-2}$ |
| **$MnCl_2$** | $K_M$ (μM) | | 422 ± 67 |
| | $V_{max}$ (nM $s^{-1}$) | | 421 ± 18 |
| | $k_{cat}/K_M$ ($s^{-1}$ $\mu M^{-1}$) | | (2.5 ± 0.5) × $10^{-3}$ |
| | $k_{cat}$ ($s^{-1}$) | | 1.04 ± 0.05 |

**Table 3.1.** Effects of $Mn^{2+}$ ions on the kinetic parameters for the oxidative and reductive reactions catalysed by wt IDH1 and R132H IDH1, respectively. The $K_M$ value of each (co)substrate was determined by varying its concentration while maintaining the concentrations of the other components at the standard conditions. Due to instrumental detection limits, the $K_M$ values for $NADP^+$ or NADPH could not be accurately determined at concentrations <10 μM. ‡Not measured due to formation of insoluble $MnCO_3$ salt from $MnCl_2$ and $NaHCO_3$. Original plots are presented in **Figures S3.1** and **S3.2**.

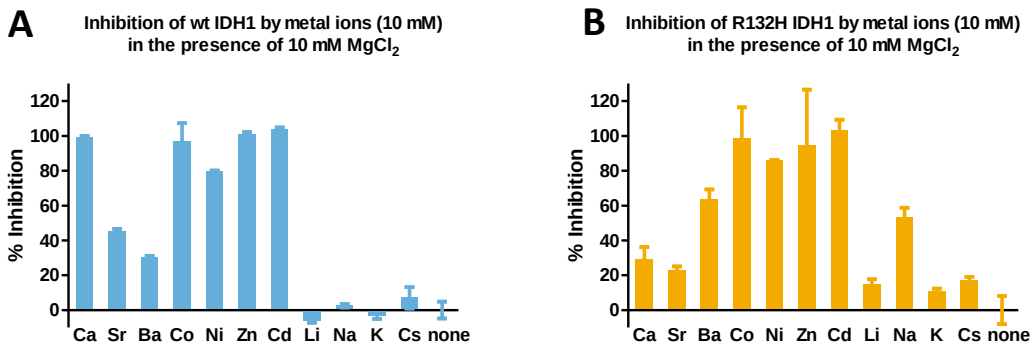
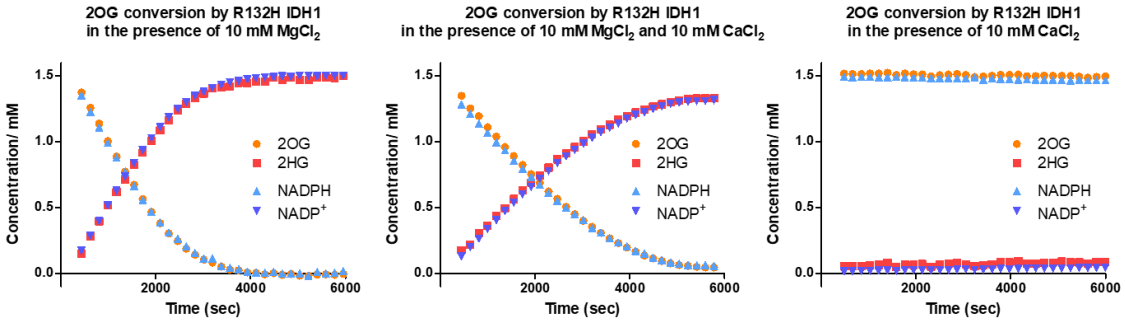



**Figure 3.1**. Inhibition of (**A**) wt IDH1 and (**B**) R132H IDH1 by catalytically inactive metal ions (10 mM) in the presence of 10 mM $MgCl_2$, as measured by absorbance-based assays. Data are mean ± SD, n= 3 technical replicates. Chloride salts were used in all cases. See Experimental Methods: Biochemical assays for general assay conditions. Activities were normalised to that observed with $MgCl_2$. Enzymatic inhibition uses no-metal as the 0% inhibition reference. A no-enzyme control was subtracted from the raw data for $CoCl_2$ due to intrinsic absorbance of $Co^{2+}$ in buffer. In general, inhibition was observed with other divalent metal ions and no activity with monovalent metal ions.

$Mg^{2+}$ and $Mn^{2+}$ are the only two active metal ions amongst those tested, as determined by absorbance-based assays (**Section 2.4.3**). Since metal ions with no measurable activity can either exert no effect or inhibit the enzyme, inhibitory effects of the inactive metal ions were tested in the presence of equal concentrations of the active metal $Mg^{2+}$ (10 mM) (**Figure 3.1**). Alkaline earth metals, $Ca^{2+}$, $Sr^{2+}$ and $Ba^{2+}$, inhibit both wt and R132H IDH1. The inhibition of R132H IDH1 by $Ca^{2+}$ was confirmed by NMR spectroscopy (**Figure 3.2**), consistent with results from absorbance-based assays. $Ca^{2+}$ and $Sr^{2+}$ were previously found to be competitive inhibitors of active $Mn^{2+}$ against porcine heart IDH2[205]. $Ca^{2+}$ binds to the active site as observed in reported X-ray crystal structures of human wt IDH1 and R132H IDH1[11,12]. **Figure 3.1A** shows that the percentage inhibition of alkaline earth metals decreases with an increase in ionic radius for wt IDH1, indicating the decreased ability of these metal ions to bind in the active site. Inhibition of R132H IDH1 by $Ca^{2+}$ and $Sr^{2+}$ is less pronounced compared to $Ba^{2+}$. Divalent transition metals ($Co^{2+}$, $Ni^{2+}$) and post-transition metals ($Zn^{2+}$, $Cd^{2+}$) show very strong inhibitory effects against both enzymes. However, it is inconclusive that they act through direct inhibition. $Cd^{2+}$, for instance, was observed to cause protein precipitation of IDH1 in NMR experiments. Monovalent metal ions ($Li^+$, $Na^+$, $K^+$ and $Cs^+$) show no effect against wt IDH1. $Na^+$ unexpectedly shows 53% inhibition for R132H IDH1 (**Figure 3.1B**). Presumably it does not act by binding at the active site due to its inability to be

coordinated by the substrates in the same manner as the divalent metal ions. In the R132H IDH1 crystal structure, $Na^+$ binds to an oxygen of the phosphate group on NADPH furthest away from the active site near the protein surface (**Figure 3.3**). More precise information on the free intracellular metal concentrations is needed to allow a meaningful assessment of the metal ion that serves as the principal activator or inhibitor of IDH1 *in vivo*.



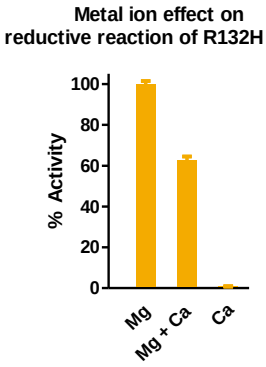




**Figure 3.2**. $Ca^{2+}$ is not catalytically active for R132H IDH1 catalysed reduction of 2OG to 2HG and inhibits R132H IDH1. The % activity of R132H IDH1 catalysed conversion of 2OG to 2HG with 10 mM $MgCl_2$ (0.59 µM $s^{-1}$ as the 100% reference), 10 mM $MgCl_2$ and 10 mM $CaCl_2$ (showing ~40% inhibition of R132H IDH1 activity), and 10 mM $CaCl_2$ (showing no activity of R132H IDH1), as monitored by $^1H$ NMR (excitation sculpting suppression with perfect-echo, 700 MHz). The % activity is determined based on mean NMR signals of 2OG, 2HG, $NADP^+$ and NADPH, ± SEM. Buffer: 50 mM Tris-$D_{11}$-HCl, pH 7.5 in 90% $H_2O$/ 10% $D_2O$ (v/v).

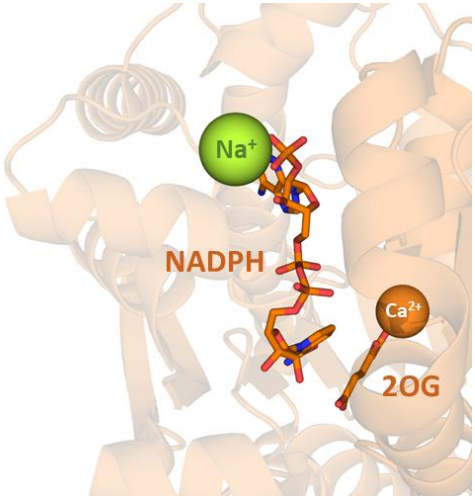



**Figure 3.3**. View of X-ray crystal structure of R132H IDH1 (PDB 3INM)[11] showing that a $Na^+$ ion (shown in green) binds to the phosphate group of NADPH near the surface of R132H IDH1.

## 3.3 Effect of metal ions on substrate binding to IDH1

### 3.3.1 Binding of isocitrate to wt IDH1

Following binding studies of isocitrate to wt IDH1 in the presence of $Mg^{2+}$ (**Section 2.3**), similar ITC experiments were performed with $Mn^{2+}$ and $Ca^{2+}$. Unexpectedly, both the catalytically active $Mn^{2+}$ and the inactive $Ca^{2+}$ promote binding of isocitrate to wt IDH1, with a $K_D$ of 1.30 µM and 1.79 µM respectively (**Figure 3.4**). This could not account for the loss of IDH1 enzymatic activity with $Ca^{2+}$.

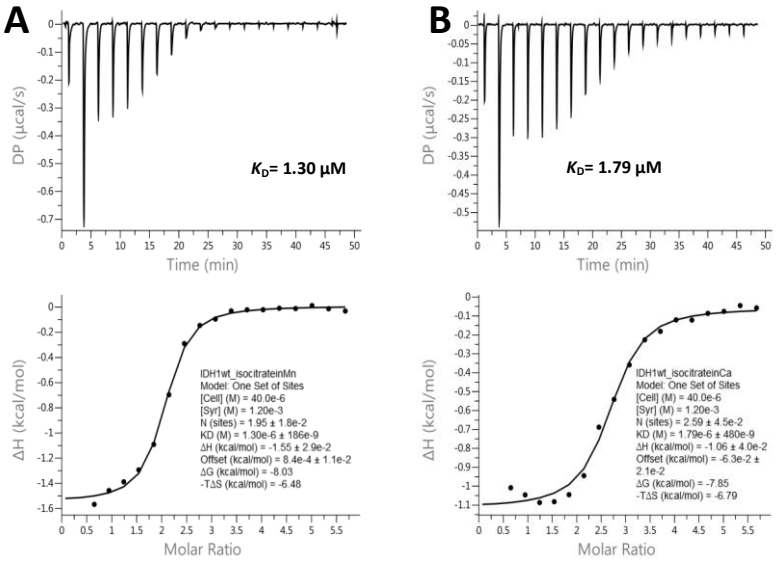



**Figure 3.4**. ITC analysis of DL-isocitrate binding to wt IDH1 in the presence of 5 mM (**A**) $MnCl_2$ and (**B**) $CaCl_2$, in 50 mM Tris-HCl, pH 7.5. See Experimental Methods: Isothermal Titration Calorimetry for method details. Isocitrate binds to wt IDH1 with low micromolar affinity in the presence of $Mn^{2+}$ or $Ca^{2+}$.

Differences in the apparent $K_D$ could reflect differences either in the intrinsic affinity of isocitrate-metal ion complex to the enzyme, or in the binding between isocitrate and the metal ions. Consequently, the $K_D$ of metal ions to isocitrate was evaluated by ITC (**Table 3.2**). Interestingly, binding was observed for catalytically active $Mg^{2+}$ and $Mn^{2+}$, whereas no binding was observed for catalytically inactive $Ca^{2+}$, $Sr^{2+}$ and $Ba^{2+}$. Transition and post-transition metals also have very different $K_D$ values but their activity data (**Figure 3.1**) require further examination before identifying a correlation. The $K_D$ values likely also have a correlation with the ionic radii and consequently the bond distance between the metal ions and oxygen atoms of isocitrate, as metal ions with ionic radii ≥95 pm and M–O distance ≥2.30 Å (*i.e.* $Cd^{2+}$, $Ca^{2+}$, $Sr^{2+}$ and $Ba^{2+}$) showed no binding to

isocitrate. Based on the available evidence, it is hypothesised that direct binding between isocitrate and metal ions may be necessary for IDH enzymatic activity.

| | $Mg^{2+}$ | $Mn^{2+}$ | $Ca^{2+}$ | $Sr^{2+}$ | $Ba^{2+}$ | $Co^{2+}$ | $Ni^{2+}$ | $Zn^{2+}$ | $Cd^{2+}$ |
|---|---|---|---|---|---|---|---|---|---|
| **$K_D$ / mM** | 1.50 | 0.56 | > 10 | >10 | > 10 | 0.14 | 0.066 | 0.061 | > 10 |
| **Ionic radii / pm**[214] | 72 | 83 | 100 | 118 | 135 | 75 | 69 | 74 | 95 |
| **M–O distance / Å**[215] | 2.10 | 2.20 | 2.46 | 2.62 | 2.82 | 2.08 | 2.06 | 2.08 | 2.30 |

**Table 3.2**. Dissociation constants ($K_D$) of divalent metal ions binding to isocitrate as measured by ITC. Ionic radii of metal ions[214] assume 2+ charge state, coordination number of 6, and a high spin, where applicable. M–O distance[215] is the bond distance between the metal ion and oxygen in $H_2O$. See Experimental Methods: Isothermal Titration Calorimetry for method details. See **Figure S3.3** for ITC graphs.

Non-denaturing MS was employed to study how $Mg^{2+}$ affects isocitrate binding to wt IDH1. Addition of D-isocitrate to wt IDH1 without $Mg^{2+}$ demonstrated weak binding of isocitrate to wt IDH1 (**Figure 3.5C**). A mixture of wt IDH1 and D-isocitrate (wt IDH1: D-isocitrate= 1: 4) revealed peaks of protein bound with zero, one or two isocitrate molecules, in decreasing abundance. Addition of $Mg^{2+}$ (wt IDH1: D-isocitrate: $Mg^{2+}$= 1: 4: 4) significantly increases the abundance of two-isocitrate bound protein (**Figure 3.5D**), indicating strengthening of isocitrate binding to wt IDH1 by $Mg^{2+}$.

$^1H$ NMR (700 MHz) measurements demonstrated that D-isocitrate was selectively converted to 2OG in a mixture of DL-isocitrate by wt IDH1, and L-isocitrate was neither a substrate nor an inhibitor of wt IDH1 (**Section 2.4.1**). Subsequent binding studies of DL-isocitrate and D-isocitrate to wt IDH1 by $^1H$ NMR (700 MHz) were conducted. Binding events can be detected by spectral line broadening of the small molecule due to its slower tumbling rate and fast transverse relaxation rate upon binding to protein[216]. In the absence of $Mg^{2+}$, DL-isocitrate binds to wt IDH1 (0.5 and 1 molar equivalent with respect to isocitrate) partially (**Figure 3.6A**), whereas D-isocitrate binds to wt IDH1 fully as observed by the complete broadening of the isocitrate signals (**Figure 3.6B**). This implies that the remaining isocitrate signals in **Figure 3.6A** belong to L-isocitrate, which does not bind appreciably to wt IDH1. Direct binding studies with L-isocitrate were not conducted due to its commercial unavailability.

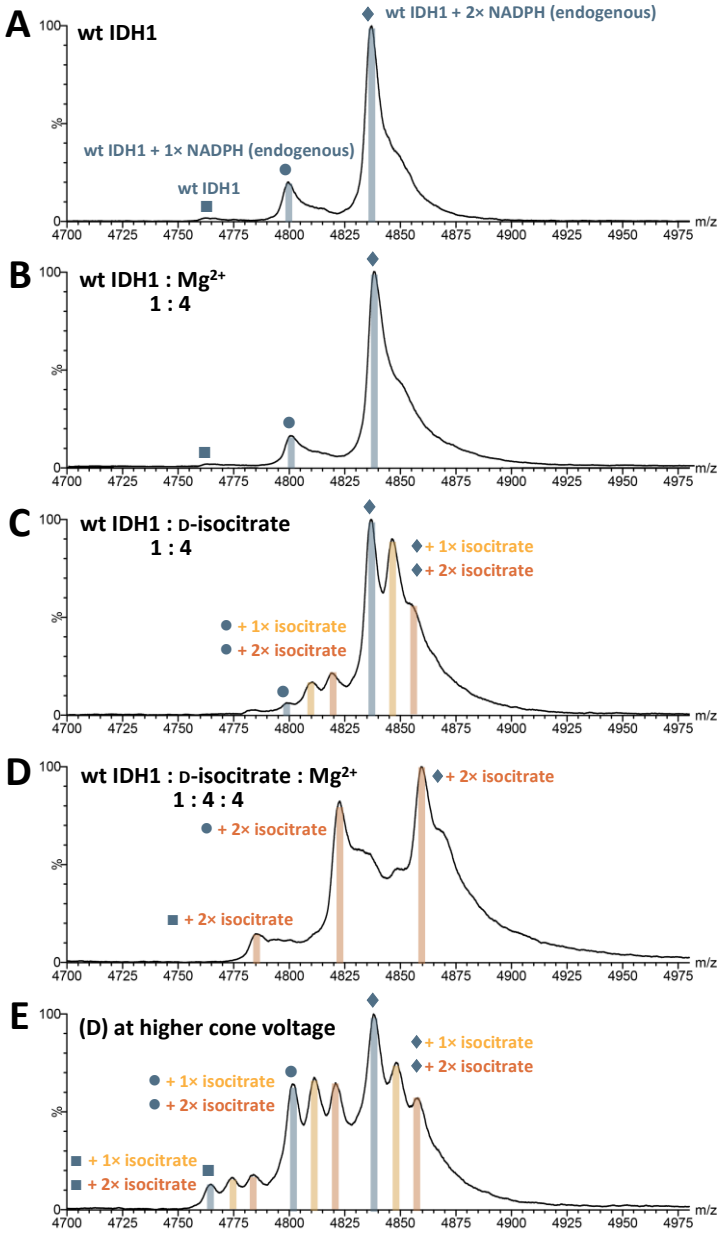



**Figure 3.5**. Isocitrate binding to wt IDH1 is enhanced by $Mg^{2+}$ ions. Mass spectrometric analysis (non-denaturing) of wt IDH1 binding to D-isocitrate and/or $Mg^{2+}$ ions. Data for the m/z= $20^{+}$ charge state are shown. Cone voltage= 100 V unless otherwise stated. Buffer: 200 mM ammonium acetate, pH 7.5. See Experimental Methods: Protein non-denaturing MS for method details. (**A**) wt IDH1 (50 µM) exists as a dimer with two NADPH molecules bound. (**B**) wt IDH1: $MgCl_2$= 50 µM: 200 µM; note the protein peak shifts rightward with the change in singly charged mass being + ~9 Da, < 1× Mg (MW= 24), likely reflecting non-specific binding. (**C**) wt IDH1: D-isocitrate= 50 µM: 200 µM, showing the binding of first and (weak) second isocitrate molecules (MW= 192) to wt IDH1. (**D**) wt IDH1: D-isocitrate: $MgCl_2$= 50 µM: 200 µM: 200 µM. The presence of $Mg^{2+}$ shifts the equilibrium towards more binding with isocitrate as wt IDH1 with two isocitrate molecules bound becoming predominant. (**E**), as (**D**), but with a higher cone voltage of 200 V that induces partial in-source dissociation of bound ligands; protein with a single isocitrate molecule bound is observed.

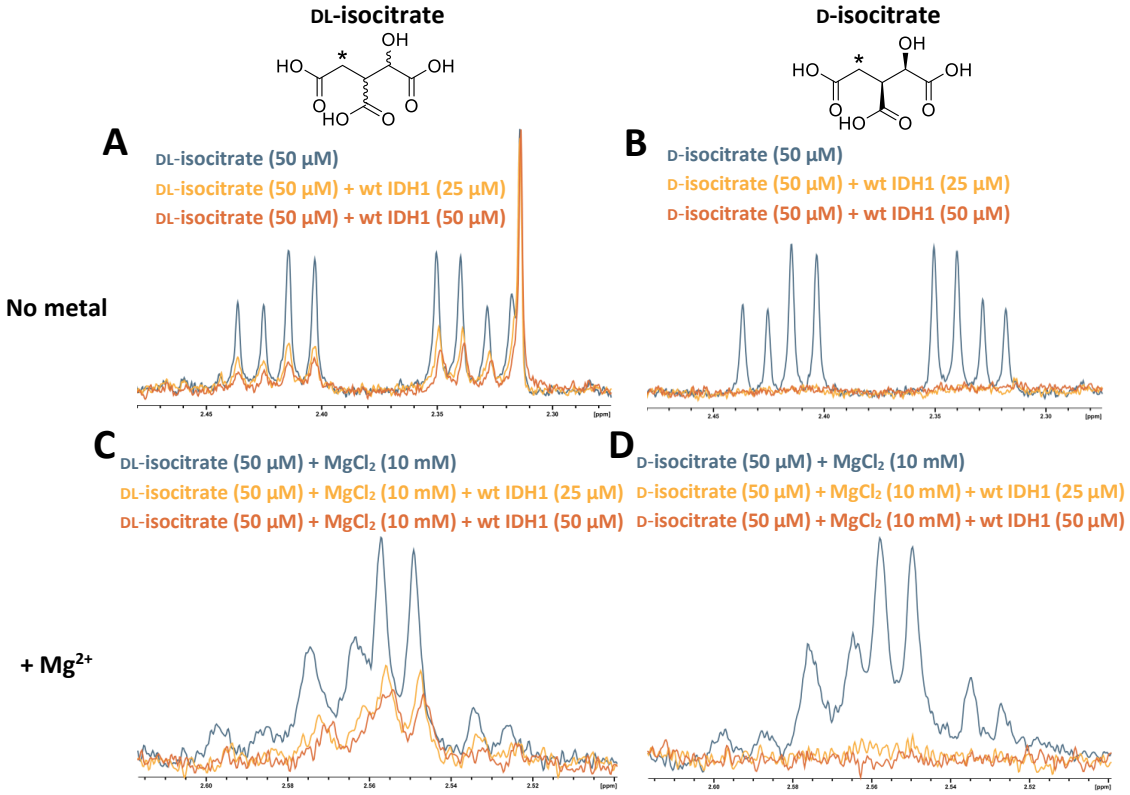



**Figure 3.6**. D-isocitrate binds to wt IDH1 more strongly than L-isocitrate. $^{1}$H NMR (CPMG-edited, 700 MHz) binding analyses of (**A**) DL-isocitrate or (**B**) D-isocitrate binding to wt IDH1 in the absence of metal ions, and (**C**) DL-isocitrate or (**D**) D-isocitrate binding to wt IDH1 (0.5 and 1 molar equivalent to isocitrate) in the presence of $MgCl_2$. Buffer: 50 mM Tris-$D_{11}$-HCl, pH 7.5 in 90% $H_2O$/ 10% $D_2O$ (v/v). Blue: substrate or substrate-metal complex. Yellow-orange: substrate or substrate-metal complex with 0.5 molar equivalent protein. Orange: substrate or substrate-metal complex with equimolar protein. See Experimental Methods: Nuclear Magnetic Resonance for method details. The peak at 2.32 ppm in (**A**) is due to an impurity in the commercial product.

Upon addition of 10 mM $Mg^{2+}$ ions to the mixture of isocitrate and wt IDH1 (**Figures 3.6C** and **3.6D**), the extent of binding for both DL-isocitrate and D-isocitrate to wt IDH1 with $Mg^{2+}$ was observed to be similar to those without $Mg^{2+}$. In this case, D-isocitrate is likely already tightly bound to wt IDH1 in the absence of $Mg^{2+}$ (**Figures 3.6A** and **3.6B**) and hence any enhancement would not be visible.

### 3.3.2 Binding of weakly bound ligands to IDH1

Whilst D-isocitrate binds strongly to wt IDH1, kinetic studies (**Section 2.1**) and binding studies using DSF and ITC (**Section 2.3**) showed that isocitrate has a low binding affinity for R132H IDH1. $^{1}$H NMR (700 MHz) confirmed the weak binding of D-isocitrate to R132H IDH1 as addition of R132H IDH1 (0.5 and 1 molar equivalent to isocitrate) had little to no effect on D-isocitrate signal intensities (**Figure 3.7A**). However, the binding of isocitrate to R132H IDH1 can be enhanced by metal ions such as $Ca^{2+}$ (**Figure 3.7B**).

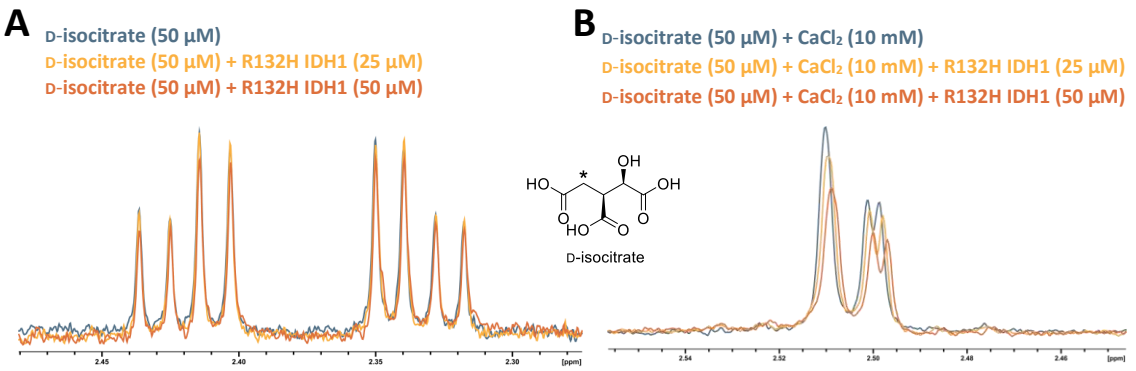



**Figure 3.7**. Binding of isocitrate to R132H IDH1 is enhanced by $CaCl_2$. $^{1}$H NMR (CPMG-edited, 700 MHz) binding analyses of D-isocitrate and R132H IDH1. (**A**) In the absence of $CaCl_2$, no binding was observed. (**B**) The addition of $CaCl_2$ enhances the binding due to an observable decrease in the signal intensities of isocitrate. Buffer: 50 mM Tris-$D_{11}$-HCl, pH 7.5 in 90% $H_2O$/ 10% $D_2O$ (v/v). Blue: substrate or substrate-metal complex. Yellow-orange: substrate or substrate-metal complex with 0.5 molar equivalent protein. Orange: substrate or substrate-metal complex with equimolar protein. See Experimental Methods: Nuclear Magnetic Resonance for method details.

2OG is a weaker binder to wt IDH1 compared to isocitrate. NMR analyses demonstrated that 2OG binds to wt IDH1 (0.5 and 1 molar equivalent to isocitrate) partially (**Figure 3.8A**). Addition of $CaCl_2$ (10 mM) allows complete binding of 2OG to wt IDH1 (**Figure 3.8C**). A similar enhancement of 2OG binding to R132H IDH1 was observed where no binding of 2OG to R132H IDH1 was detected without $Ca^{2+}$ (**Figure 3.8B**), but partial binding was achieved after $Ca^{2+}$ addition (**Figure 3.8D**). Non-denaturing MS measurements provided similar observations. Both 2OG and the surrogate substrate, *N*-oxalylglycine (NOG), bind weakly to R132H IDH1. However, the addition of $Mg^{2+}$ improves the binding of NOG to R132H IDH1 (**Figure 3.9**). The combination of 2OG and $Mg^{2+}$ was avoided in all binding studies, as conversion of 2OG to 2HG was observed due to the presence of copurifying NADPH in both wt and R132H IDH1 (**Figure 3.10**).

2HG has the weakest affinity to wt IDH1 or R132H IDH1 compared to isocitrate and 2OG, because it does not bind to both enzymes without metal ions, as observed by $^{1}$H NMR (700 MHz) (**Figures 3.11A** and **3.11B**), as well as by ITC and DSF measurements (**Section 2.3**). Metal ions such as $Mg^{2+}$ and $Ca^{2+}$ enhance 2HG binding to wt IDH1 but not to R132H IDH1 (**Figure 3.11 C–F**).

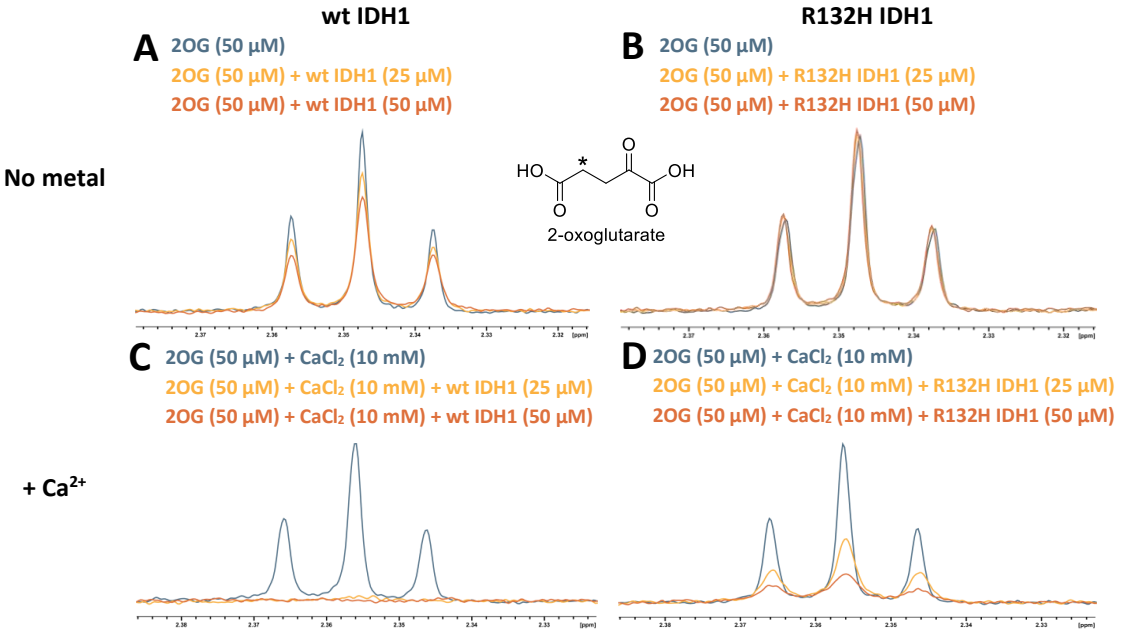



**Figure 3.8**. Binding of 2OG to R132H IDH1 is enhanced by $Ca^{2+}$. $^{1}$H NMR (CPMG-edited, 700 MHz) binding analyses of 2OG binding to (**A**) wt IDH1 (0.5 and 1 molar equivalent to 2OG) or (**B**) R132H IDH1 (0.5 and 1 molar equivalent to 2OG) in the absence of metal ions, as well as 2OG binding to (**C**) wt IDH1 or (**D**) R132H IDH1 in the presence of 10 mM $CaCl_2$. Buffer: 50 mM Tris-$D_{11}$-HCl, pH 7.5 in 90% $H_2O$/ 10% $D_2O$ (v/v). Blue: substrate or substrate-metal complex. Yellow-orange: substrate or substrate-metal complex with 0.5 molar equivalent protein. Orange: substrate or substrate-metal complex with equimolar protein. See Experimental Methods: Nuclear Magnetic Resonance for method details. $CaCl_2$ enhances the binding of 2OG to both wt and R132H IDH1. 2OG is a better binder to wt IDH1 than R132H IDH1 with or without $Ca^{2+}$.

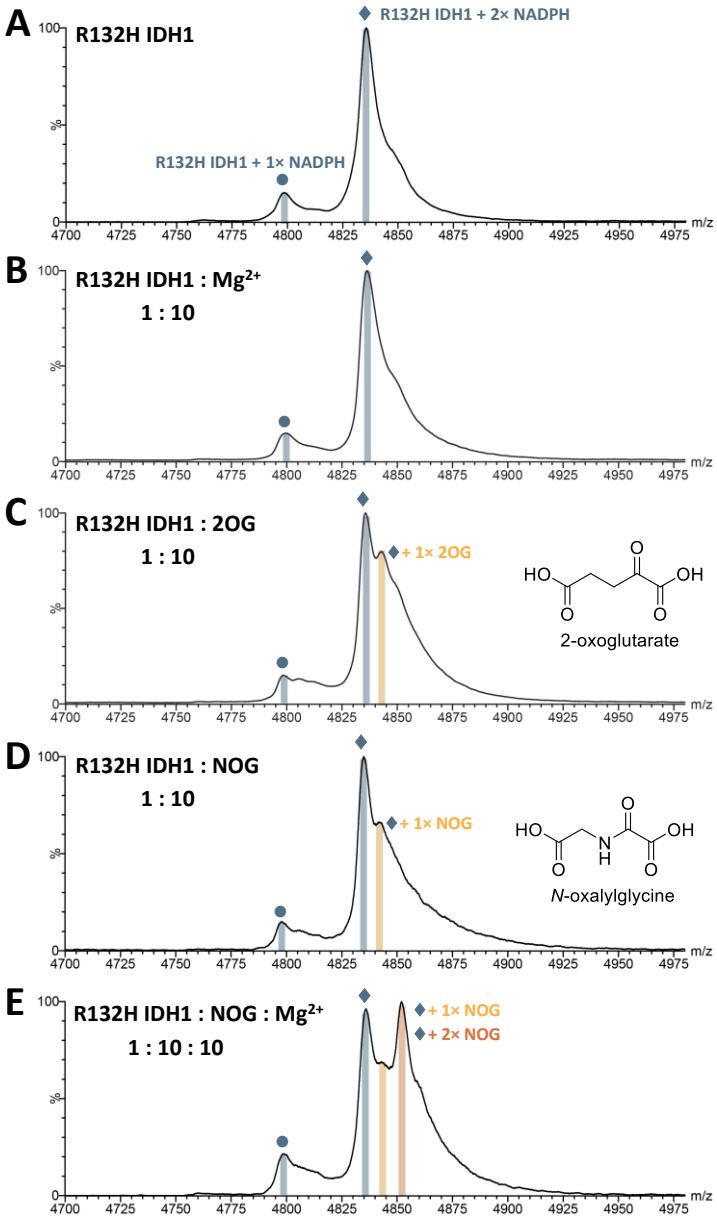



**Figure 3.9**. $Mg^{2+}$ enhances binding of NOG, a 2OG analogue, to R132H IDH1. Mass spectrometric analysis (non-denaturing) of R132H IDH1 binding to 2OG or NOG. Data for the m/z= $20^{+}$ charge state are shown. Cone voltage= 100 V. Buffer: 200 mM ammonium acetate, pH 7.5. See Experimental Methods: Protein non-denaturing MS for method details. (**A**) R132H IDH1 (50 µM) is a dimer with two copurifying NADPH molecules bound. (**B**) R132H IDH1: $MgCl_2$= 50 µM: 500 µM. On addition of a 10× molar excess of $MgCl_2$, the protein mass increases slightly, likely due to non-specific binding of $Mg^{2+}$ ions. (**C**) R132H IDH1: 2OG= 50 µM: 500 µM showing weak binding of one 2OG molecule to IDH1 dimer. (**D**) R132H IDH1: NOG= 50 µM: 500 µM indicating weak binding of one NOG molecule to IDH1 dimer, similar to (**C**). (**E**) R132H IDH1: NOG: $MgCl_2$= 50 µM: 500 µM: 500 µM. Addition of $Mg^{2+}$ leads to the complexation of IDH1 dimer with two NOG molecules. The combination of R132H IDH1: 2OG: $MgCl_2$ enables catalysis and hence was not investigated.

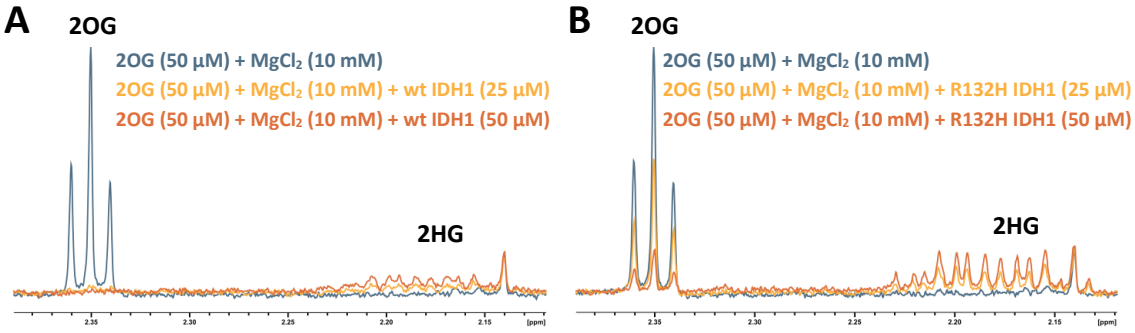



**Figure 3.10**. The combination of 2OG and $Mg^{2+}$ in IDH1 binding studies enables catalysis. $^{1}H$ NMR (CPMG-edited, 700 MHz) binding analyses of 2OG binding to (**A**) wt IDH1 and (**B**) R132H IDH1 in the presence of 10 mM $Mg^{2+}$. Buffer: 50 mM Tris-$D_{11}$-HCl, pH 7.5 in 90% $H_2O$/ 10% $D_2O$ (v/v). Blue: substrate or substrate-metal complex. Yellow-orange: substrate or substrate-metal complex with 0.5 molar equivalent protein. Orange: substrate or substrate-metal complex with equimolar protein. See Experimental Methods: Nuclear Magnetic Resonance for method details. Disappearance of the 2OG signal is attributed partly to its conversion to 2HG so the combination of 2OG and $Mg^{2+}$ cannot be used for binding analyses.

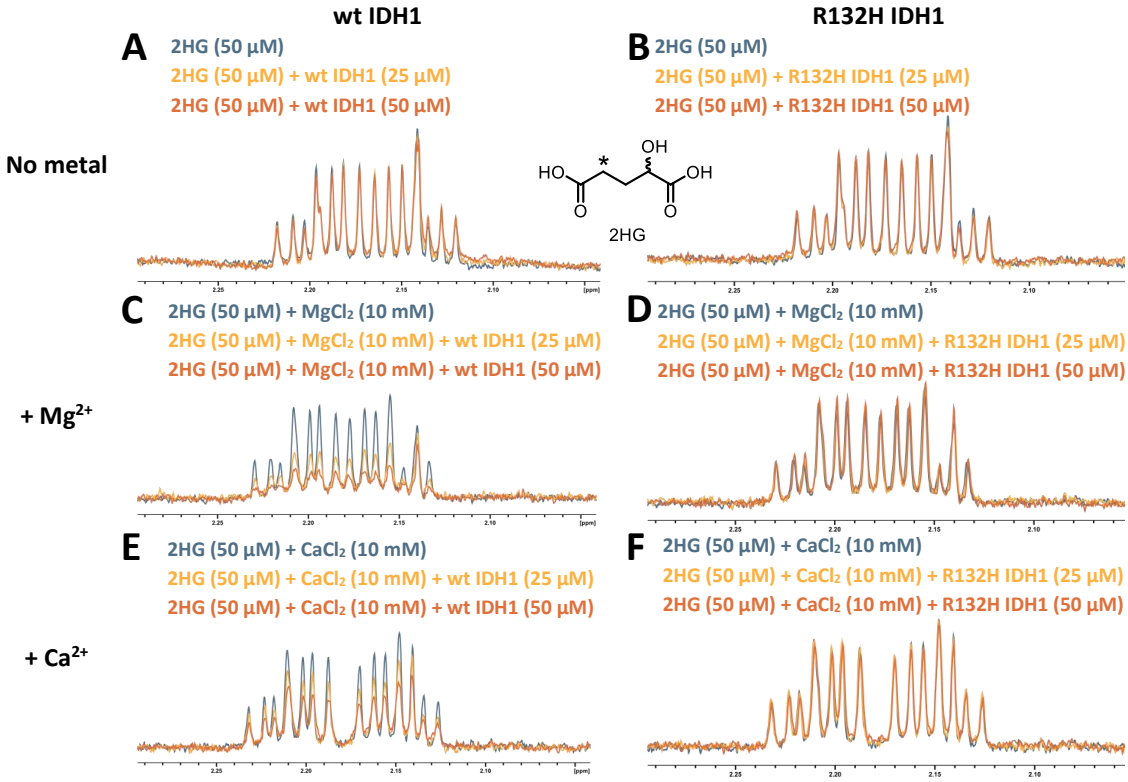



**Figure 3.11**. Metal ions ($MgCl_2$ and $CaCl_2$) enable 2HG binding to wt IDH1. $^{1}H$ NMR (CPMG-edited, 700 MHz) binding analyses of 2HG binding to (**A**, **C**, **E**) wt IDH1 and (**B**, **D**, **F**) R132H IDH1 in the absence of metal ions, in the presence of $Mg^{2+}$ (10 mM) and $Ca^{2+}$ (10 mM) respectively. Buffer: 50 mM Tris-$D_{11}$-HCl, pH 7.5 in 90% $H_2O$/ 10% $D_2O$ (v/v). Blue: substrate or substrate-metal complex. Yellow-orange: substrate or substrate-metal complex with 0.5 molar equivalent protein. Orange: substrate or substrate-metal complex with equimolar protein. See Experimental Methods: Nuclear Magnetic Resonance for method details.

## 3.4 Competition studies of IDH1 substrates and inhibitors

### 3.4.1 Binding of isocitrate and inhibitors to wt IDH1 is mutually exclusive

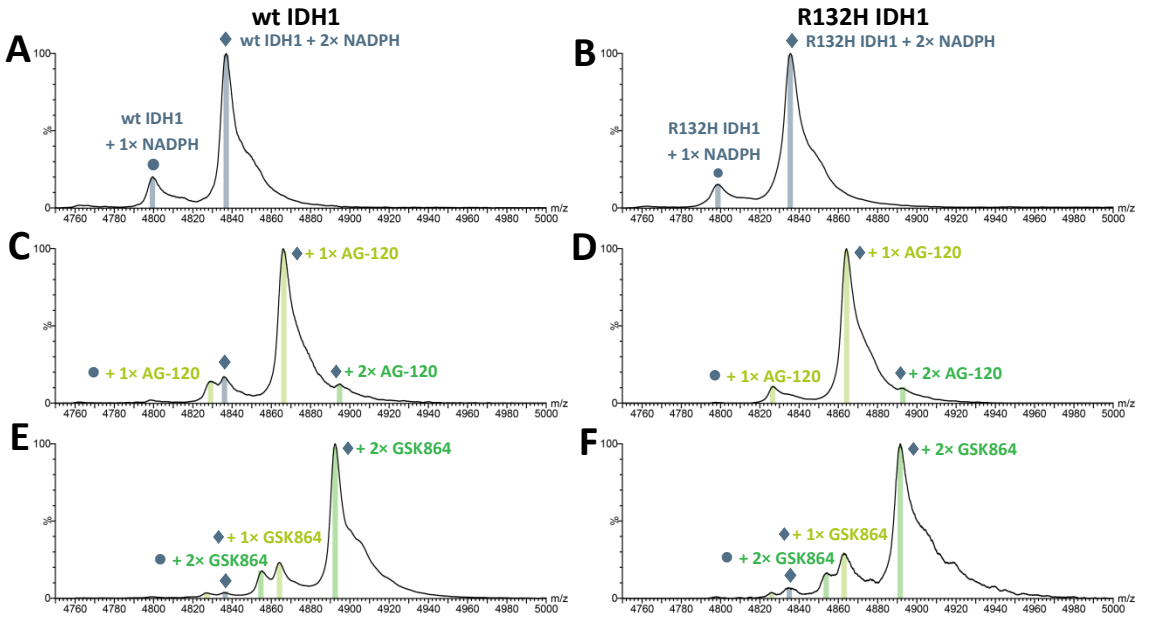



**Figure 3.12**. Binding of R132H IDH1 inhibitors to wt IDH1 and R132H IDH1. MS analyses (non-denaturing) of wt IDH1 and R132H IDH1 with or without inhibitors. Data for the m/z= $20^{+}$ charge state are shown. Cone voltage= 100 V. Buffer: 200 mM ammonium acetate, pH 7.5. See Experimental Methods: Protein non-denaturing MS for method details. (**A**) wt IDH1 (50 µM) and (**B**) R132H IDH1 (50 µM) with two copurifying NADPH molecules bound. AG-120 (MW= 583.0, $IC_{50}$ against R132H IDH1= 4.9 ± 0.3 nM) binds to (**C**) wt IDH1 and (**D**) R132H IDH1 with a stoichiometry of 1 inhibitor per IDH1 dimer, IDH1: AG-120= 50 µM: 200 µM. Excess AG-120 above the chosen concentration does not promote further binding of second AG-120 molecule. GSK864 (MW= 558.6, $IC_{50}$ against R132H IDH1= 20 ± 1 nM) binds to (**E**) wt IDH1 and (**F**) R132H IDH1 with a stoichiometry of 2 inhibitors per IDH1 dimer, IDH1: GSK864= 50 µM: 400 µM to saturate binding of GSK864 to IDH1 without inducing compound precipitation.

After demonstrating that metal ions assist the binding of substrates to IDH1, competition binding experiments of substrate and inhibitors of IDH1 were carried out. AG-120 (Ivosidenib) and GSK864, both of which have different scaffolds and binding stoichiometries with IDH1, are used as representative inhibitors in this work. AG-120 is FDA-approved[109] but there is no reported X-ray crystal structure for it in complex with an IDH. Non-denaturing MS analyses revealed that AG-120 binds to wt IDH1 and R132H IDH1 with a stoichiometry of 1 inhibitor per IDH1 dimer (**Figures 3.12C** and **3.12D**). By contrast, GSK864 binds to wt IDH1 and R132H IDH1 with a stoichiometry of 2 inhibitors per IDH1 dimer (**Figures 3.12E** and **3.12F**). The stoichiometry is consistent with the reported X-ray crystal structure of a closely related analogue, GSK321[169].

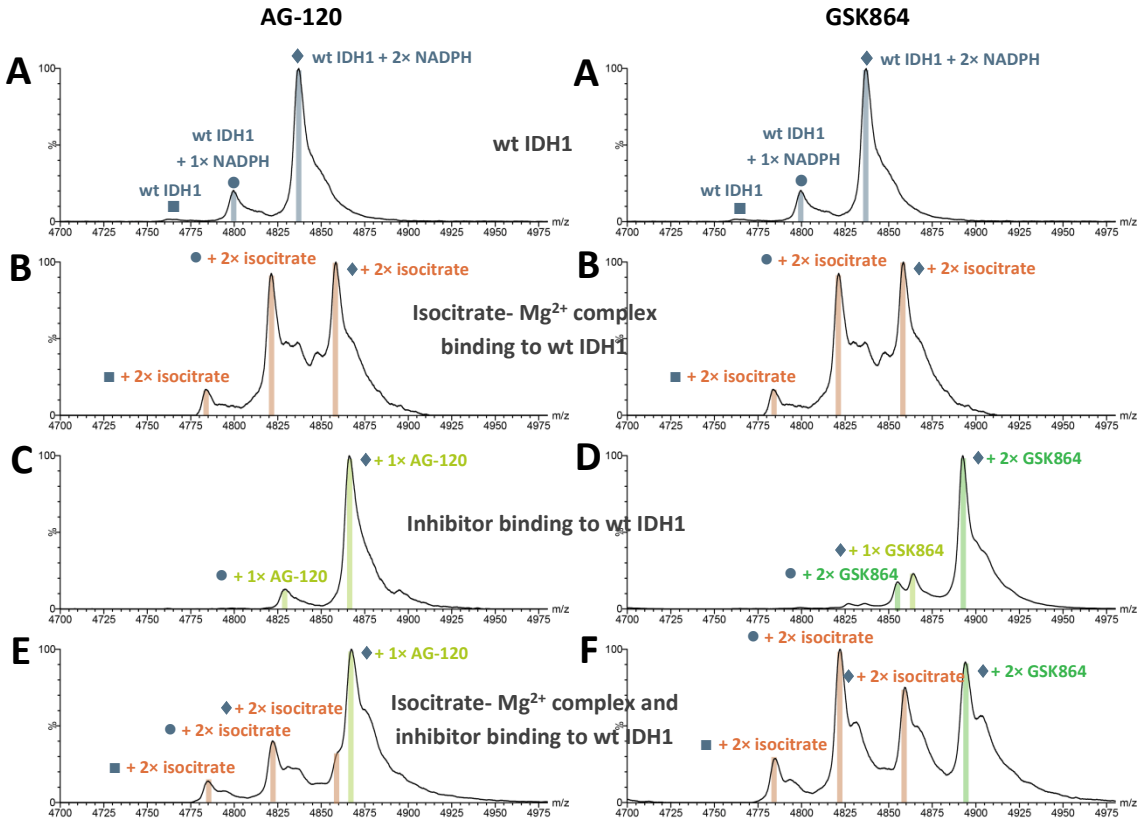



**Figure 3.13**. Isocitrate-$Mg^{2+}$ binding to wt IDH1 is not diminished by R132H IDH1 inhibitors. Mass spectrometric analysis (non-denaturing) of competition experiments with wt IDH1. Data for the m/z= $20^{+}$ charge state are shown. Cone voltage= 100 V. Buffer: 200 mM ammonium acetate, pH 7.5. See Experimental Methods: Protein non-denaturing MS for method details. (**A**) wt IDH1 (50 µM) protein only. (**B**) wt IDH1: D-isocitrate: $Mg^{2+}$= 50 µM: 200 µM: 200 µM showing two isocitrate molecules bound to wt IDH1 dimer. (**C**) wt IDH1: AG-120= 50 µM: 200 µM showing one AG-120 bound to wt IDH1. (**D**) wt IDH1: GSK864= 50 µM: 400 µM showing two GSK864 bound to wt IDH1. (**E**) wt IDH1: D-isocitrate: $Mg^{2+}$: AG-120= 50 µM: 200 µM: 200 µM: 200 µM reflecting a superposition of spectra (**B**) and (**C**). (**F**) wt IDH1: D-isocitrate: $Mg^{2+}$: GSK864= 50 µM: 200 µM: 200 µM: 400 µM reflecting a superposition of spectra (**B**) and (**D**). In (**E**) and (**F**), wt IDH1 bound with both isocitrate-$Mg^{2+}$ and R132H IDH1 inhibitor is not observed, indicating that wt IDH1 binds to either isocitrate-$Mg^{2+}$ complex or inhibitor, but not both simultaneously. Note: addition of $Mg^{2+}$ does not affect inhibitor binding (**Figure S3.4B**).

The D-isocitrate-$Mg^{2+}$ complex was allowed to compete with AG-120 or GSK864 for binding to wt IDH1. Interestingly, in both cases the resulting mass spectra (**Figures 3.13E** and **3.13F**) reflect a superposition of the spectra of wt IDH1 with two isocitrate molecules (**Figure 3.13B**) and wt IDH1 with the respective inhibitor (**Figures 3.13C** and **3.13D**). There is no peak corresponding to wt IDH1 binding to both isocitrate and inhibitor. It is inferred from published X-ray[169] and cryo-EM[172] structures of IDH1 complexes with analogues of GSK864 and AG-120, respectively, that these inhibitors

bind near the dimer interface whereas isocitrate binds at the active site. The results demonstrate that although occupying different binding sites, IDH1 inhibitors and isocitrate cannot co-exist on the protein simultaneously. In other words, the binding of isocitrate and the inhibitor is mutually exclusive. Importantly, even in the presence of the inhibitors, isocitrate-$Mg^{2+}$ binding to wt IDH1 is still observed as indicated by observation of the protein with two isocitrate molecules bound.

### 3.4.2 Metal ions help isocitrate but not 2OG to stay bound to IDH1

After demonstrating that isocitrate cannot bind simultaneously with inhibitors to wt IDH1, the effect of inhibitors on substrate binding to wt IDH1 and R132H IDH1, with and without metal ions, was investigated by $^1$H NMR (700 MHz). How the inhibitor influences D-isocitrate binding to wt IDH1 was first examined. Using a lower enzyme concentration (D-isocitrate: wt IDH1= 8: 1), a partially broadened D-isocitrate signal was used as the basis for subsequent comparisons. Addition of inhibitors results in an incomplete recovery of the D-isocitrate signals, indicating that some, but not all, of the bound D-isocitrate molecules are displaced by the inhibitors (**Figures 3.14A** and **3.14B**).

The same experiments of isocitrate binding to wt IDH1 were then conducted with metal ions. In the presence of $Mg^{2+}$ or $Ca^{2+}$, D-isocitrate binds partially to wt IDH1, similar to the case without metal ions. However, no isocitrate is displaced from wt IDH1 upon addition of inhibitors in the presence of metal ions (**Figures 3.14 C–F**), indicating that the metal ions help isocitrate to bind tightly to wt IDH1. ITC, non-denaturing MS and NMR spectroscopy have shown that $Mg^{2+}$ alone has no substantial effect on the binding of inhibitors to IDH1 (**Figure S3.4**).

Parallel investigations on the effect of inhibitor on 2OG binding to R132H IDH1 were then conducted. As shown in **Figure 3.8B**, 2OG is a weak binder so such investigations are difficult in the absence of metal ions. Again, the combination of 2OG and $Mg^{2+}$ was avoided in binding studies, as it is catalytically active due to the presence of copurifying NADPH present in R132H IDH1. $Ca^{2+}$ was added to enhance binding of 2OG to R132H IDH1, to the extent comparable to isocitrate binding to wt IDH1 in **Figures 3.14A** and **3.14B**. Addition of inhibitors, however, displaces most of the 2OG molecules (**Figures**

**3.15A** and **3.15B**). Experiments with NOG and $Mg^{2+}$ gave similar results (**Figures 3.15C** and **3.15D**).

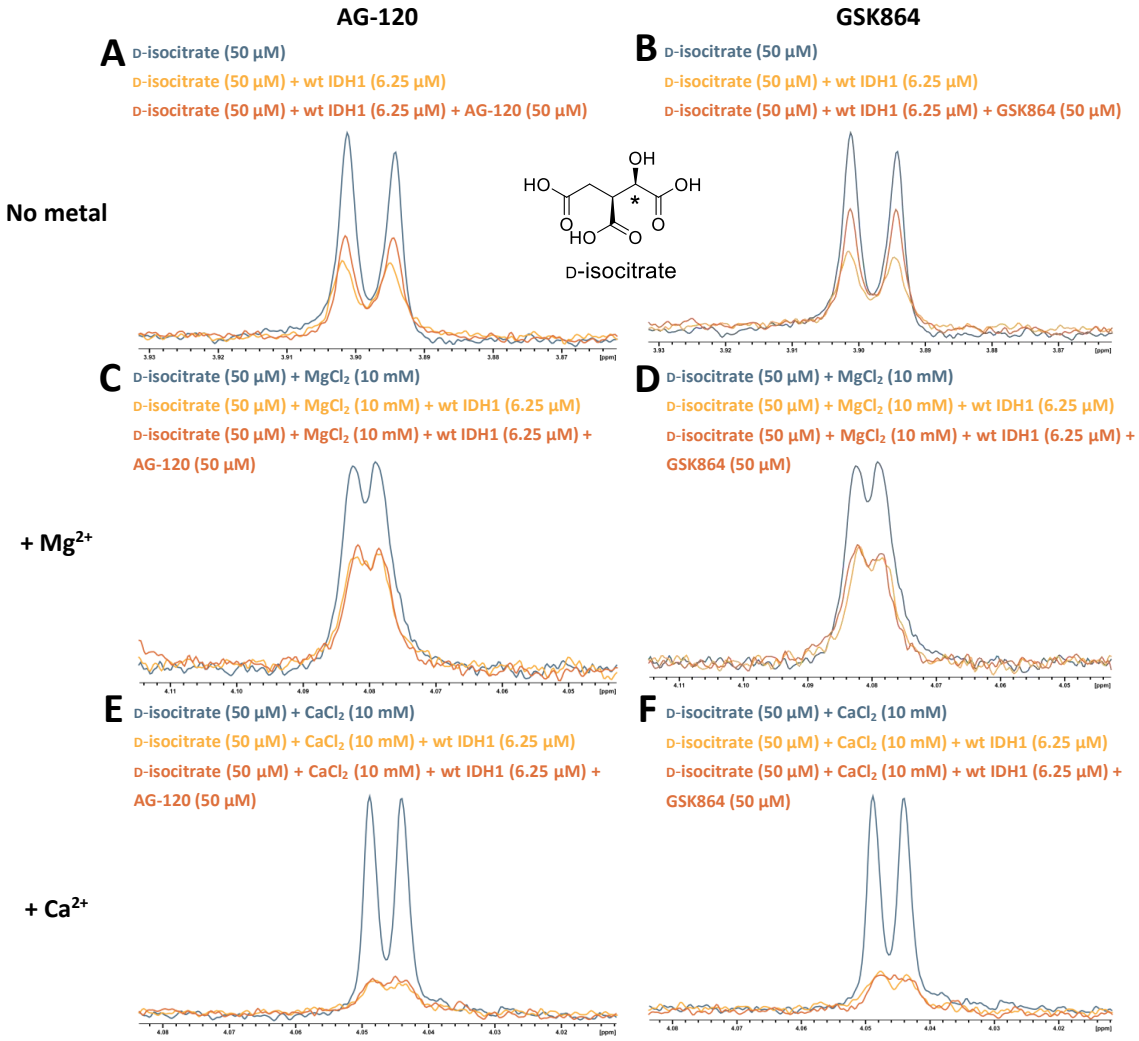



**Figure 3.14**. R132H IDH1 inhibitors are unable to displace isocitrate from wt IDH1 in the presence of metal ions. $^{1}H$ NMR (CPMG-edited, 700 MHz) binding analyses of D-isocitrate binding to wt IDH1 upon competition with inhibitors. Buffer: 50 mM Tris-$D_{11}$-HCl, pH 7.5 in 90% $H_2O$/ 10% $D_2O$ (v/v). (**A**) D-isocitrate binding to wt IDH1 (D-isocitrate: wt IDH1= 8:1) in the presence of inhibitor AG-120 but without metal ions. (**B**) Same as (**A**), but with inhibitor GSK864. D-isocitrate is partially displaced by the inhibitor in the absence of any metal ions. (**C**) and (**D**): Same as (**A**) and (**B**), but in the presence of 10 mM $MgCl_2$. (**E**) and (**F**): Same as (**A**) and (**B**), but in the presence of 10 mM $CaCl_2$. Blue: substrate or substrate-metal complex. Yellow-orange: substrate or substrate-metal complex with 0.125 molar equivalent protein. Orange: substrate or substrate-metal complex with 0.125 molar equivalent protein and equimolar inhibitor. See Experimental Methods: Nuclear Magnetic Resonance for method details. D-isocitrate is displaced by R132H IDH1 inhibitors without metal ions but is not displaced by the inhibitors in the presence of metal ions $MgCl_2$ or $CaCl_2$.

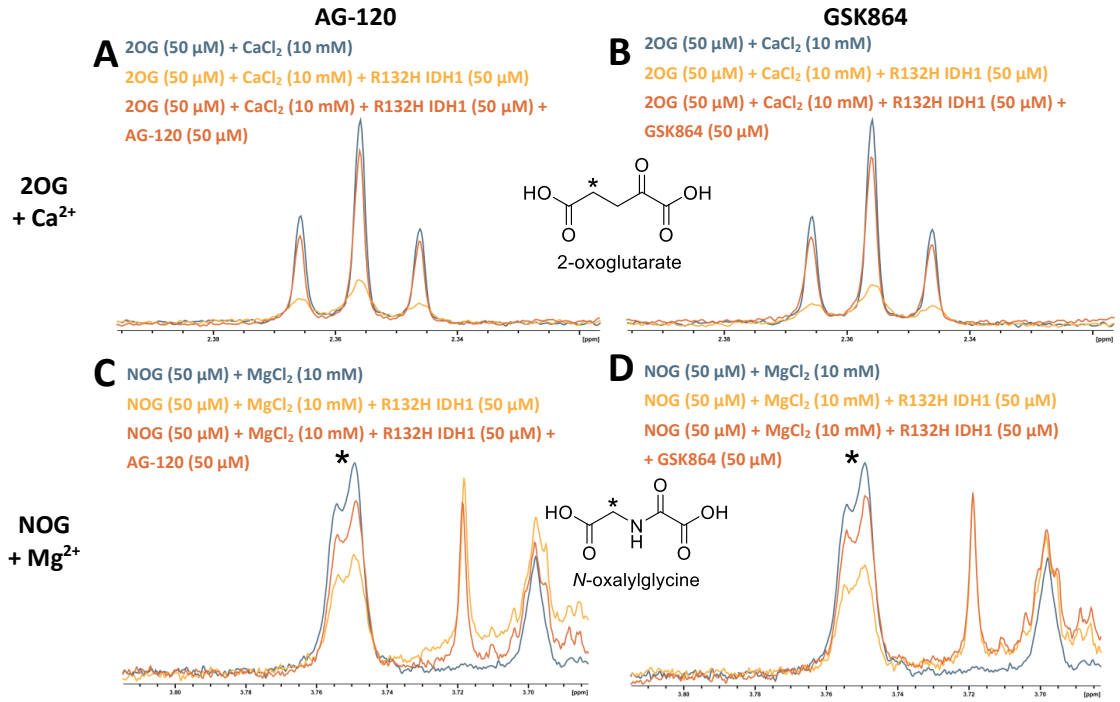



**Figure 3.15**. R132H IDH1 inhibitors displace 2OG from R132H IDH1. $^{1}$H NMR (CPMG-edited, 700 MHz) binding analyses of 2OG binding to R132H IDH1 upon competition with inhibitors. Buffer: 50 mM Tris-$D_{11}$-HCl, pH 7.5 in 90% $H_2O$/ 10% $D_2O$ (v/v). (**A**) 2OG binding to R132H IDH1 (2OG: R132H IDH1= 1:1) in the presence of of 10 mM $CaCl_2$ and inhibitor AG-120. (**B**) Same as (**A**), but with inhibitor GSK864. (**C**) and (**D**): Same as (**A**) and (**B**), but replacing 2OG and $CaCl_2$ with NOG and $MgCl_2$. Blue: substrate or substrate-metal complex. Yellow-orange: substrate or substrate-metal complex with equimolar protein. Orange: substrate or substrate-metal complex with equimolar protein and inhibitor. See Experimental Methods: Nuclear Magnetic Resonance for method details. 2OG or its surrogate NOG is displaced by inhibitor in the presence of metal ions.

The results suggest that in the presence of $Mg^{2+}$ or $Ca^{2+}$, AG-120 or GSK864 can displace 2OG/NOG from R132H IDH1, but not D-isocitrate from wt IDH1. Overall, it suggests that metal ions help to stabilise the binding of isocitrate to wt IDH1 upon addition of inhibitors.

The presence of metal ions may account for the wt/mutant selectivity of IDH1 inhibitors. In the cellular context, the concentration of free cytosolic $Mg^{2+}$, which represents only a small fraction of the total $Mg^{2+}$, was reported to be 0.25–1 mM[217,218] and in particular, 0.3 mM for human brain[219]. The concentrations of $Mg^{2+}$ may deviate in a diseased state, especially with IDH1 mutations. An MRI study showed elevated free intracellular $Mg^{2+}$ in brain tumours compared to normal brain tissue[219]. In addition, another MS study reported that the concentration of total Mg in brain tumour cells is twice that of normal brain tissue[220]. Assuming that the $K_M$ of $Mg^{2+}$ (36 µM) for wt IDH1 is lower than the

cellular level of $Mg^{2+}$, $Mg^{2+}$ should be tightly bound to help isocitrate stay in place. In comparison, 2OG can be displaced by the inhibitor from R132H IDH1 relatively easily even in the presence of metal ions. This could be attributed to the weaker binding affinity of 2OG to R132H IDH1, exacerbated by the fact that $K_M$ of $Mg^{2+}$ (4.4 mM) for R132H IDH1 is higher than the concentration of free cytosolic $Mg^{2+}$. It is plausible that R132H IDH1 inhibitors are selective for the IDH1 variants as they can displace 2OG from R132H IDH1 more readily than displacing isocitrate from wt IDH1.

### 3.4.3 Inhibitors displace metal ions from R132H IDH1

Competition binding experiments involving substrate and inhibitors on R132H IDH1 were conducted using non-denaturing MS. One molecule of 2OG binds weakly to the R132H IDH1 dimer when used at a 10× molar excess of protein concentration (**Figure 3.16D**). Note that this does not reflect the actual binding stoichiometry due to the relatively weak binding affinity of 2OG to R132H IDH1. A similar 2OG binding pattern was obtained when an inhibitor, AG-120 (**Figure 3.16E**) or GSK864 (**Figure 3.16F**), was introduced to the mixture. It can be concluded that both 2OG and these inhibitors can bind to R132H IDH1 in the absence of metal ions. In addition, the binding of inhibitor to R132H IDH1 does not affect the binding of 2OG to R132H IDH1, and vice versa. For competition studies in the presence of metal ions, the surrogate substrate, NOG, and $Mg^{2+}$ were chosen to avoid any enzymatic reactions. One molecule of NOG binds to the R132H IDH1 dimer at a 10× molar excess relative to the protein concentration without $Mg^{2+}$ (**Figure 3.16G**). Similar to the case of 2OG, this does not reflect the actual binding stoichiometry due to the relatively weak binding affinity of NOG to R132H IDH1, and addition of inhibitors merely shifts the spectrum by the mass of the inhibitor without affecting NOG binding to R132H IDH1 (**Figures 3.16H** and **3.16I**). Addition of $MgCl_2$ results in two molecules of NOG bound per R132H IDH1 dimer as $Mg^{2+}$ enhances substrate binding to R132H IDH1 (**Figure 3.16J**).

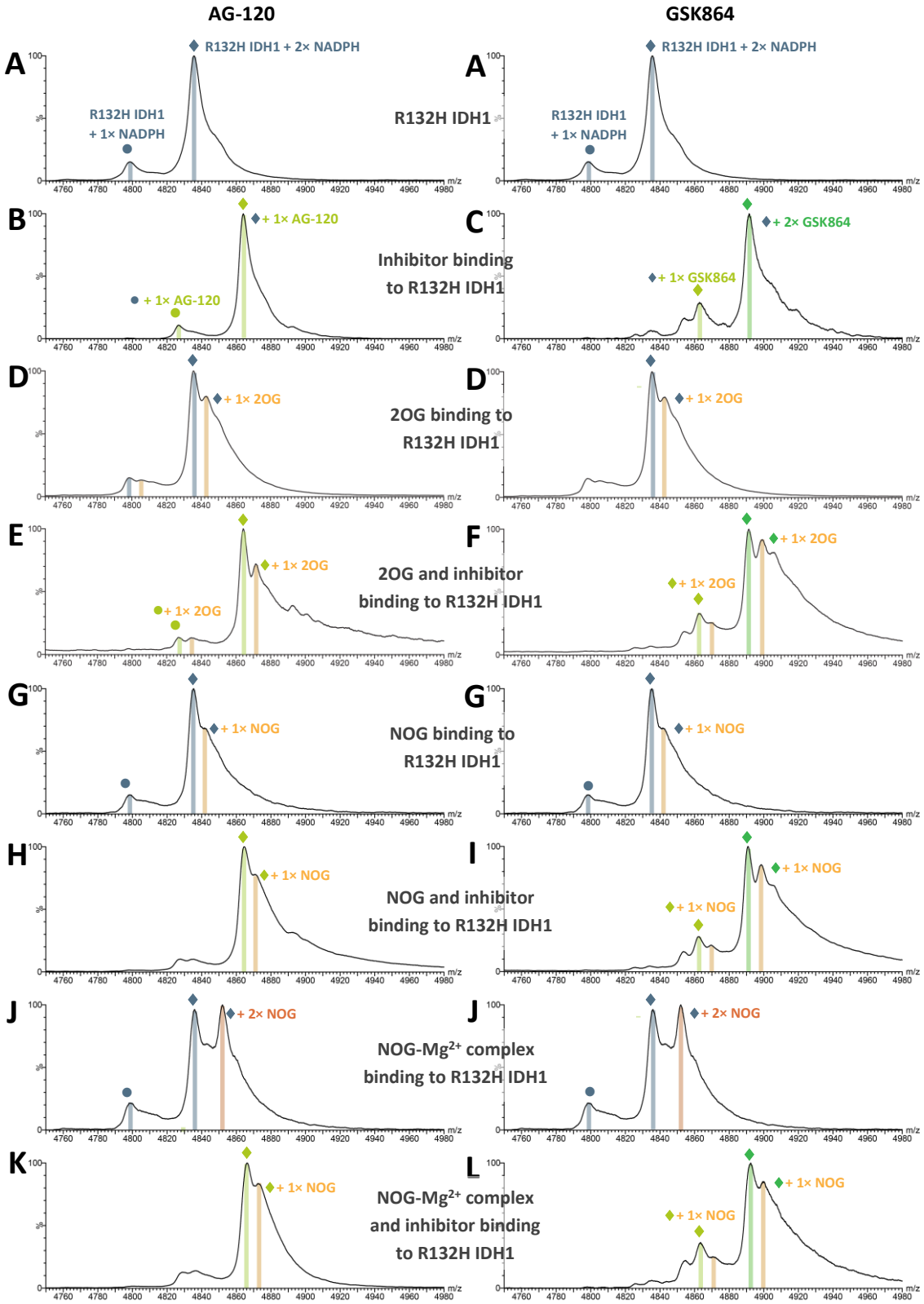



**Figure 3.16**. NOG-$Mg^{2+}$ binding to R132H IDH1 is diminished by R132H IDH1 inhibitors. Mass spectrometric analysis (non-denaturing) of competition experiments with R132H IDH1. Data for the m/z= $20^{+}$ charge state are shown. Cone voltage= 100 V. Buffer: 200 mM ammonium acetate, pH 7.5. See Experimental Methods: Protein non-denaturing MS for method details. (**A**) R132H IDH1 (50 µM) protein only. (**B**) R132H IDH1: AG-120= 50 µM: 200 µM showing one AG-120

molecule bound per R132H IDH1 dimer. (**C**) R132H IDH1: GSK864= 50 μM: 400 μM showing two GSK864 molecules bound per R132H IDH1 dimer. (**D**) R132H IDH1: 2OG= 50 μM: 500 μM showing one 2OG molecule bound per R132H IDH1 dimer. (**E**) R132H IDH1: 2OG: AG-120= 50 μM: 500 μM: 200 μM, reflecting a shift of protein peak (**D**) by the mass of AG-120 without affecting 2OG binding to R132H IDH1, in the absence of metal ions. (**F**) R132H IDH1: 2OG: GSK864= 50 μM: 500 μM: 400 μM, similar to (**E**), binding of GSK864 to R132H IDH1 does not affect 2OG binding to R132H IDH1, in the absence of metal ions. (**G**) R132H IDH1: NOG= 50 μM: 500 μM showing one NOG molecule binding to R132H IDH1 as indicated by the shoulder peak. (**H**) R132H IDH1: NOG: AG-120= 50 μM: 500 μM: 200 μM, reflecting a shift of protein peaks in (**G**) by the mass of AG-120 without affecting NOG binding, in the absence of metal ions. This is similar to the 2OG case. (**I**) R132H IDH1: NOG: GSK864= 50 μM: 500 μM: 400 μM, similar to (**H**), binding of GSK864 to R132H IDH1 does not affect NOG binding to R132H IDH1, in the absence of metal ions. (**J**) R132H IDH1: NOG: $MgCl_2$= 50 μM: 500 μM: 500 μM, showing two NOG molecules bound to R132H IDH1. The addition of $Mg^{2+}$ significantly enhances the binding of NOG to R132H IDH1. (**K**) R132H IDH1: NOG: $MgCl_2$: AG-120= 50 μM: 500 μM: 500 μM: 200 μM. Instead of shifting the spectrum by the mass of the inhibitor without affecting binding of NOG, it resembles a spectrum similar to (**H**) in which only one NOG molecule is bound to R132H IDH1. (**L**) R132H IDH1: NOG: $MgCl_2$: GSK864= 50 μM: 500 μM: 500 μM: 400 μM. Similar to (**K**), two-NOG bound peak is depleted when inhibitor competes with NOG-$Mg^{2+}$ complex, showing only one NOG bound to R132H IDH1. This resemblance of spectrum to (**I**) without any metal ions suggests that inhibitor displaces $Mg^{2+}$.

By contrast with the previous competition experiments that have no metal ions, addition of inhibitors to the NOG-$Mg^{2+}$ mixture results in not only a shift of the spectrum by the mass of the inhibitor, but also a depletion of the 2× NOG bound protein peak (**Figures 3.16K** and **3.16L**). In fact, the spectra of the NOG-$Mg^{2+}$-inhibitor mixtures (**Figures 3.16K** and **3.16L**) resemble those without $Mg^{2+}$ added (**Figures 3.16H** and **3.16I**). It can be inferred that the inhibitor displaces the $Mg^{2+}$ ion that is important in assisting binding of the substrate or surrogate substrate. It has also been shown that $Mg^{2+}$ does not directly affect inhibitor binding to IDH1, as no significant differences were observed in the binding affinity of inhibitor to wt IDH1 or R132H IDH1 with or without $Mg^{2+}$, as measured by non-denaturing MS, ITC and NMR spectroscopy (**Figure S3.4**).

Non-denaturing MS analyses demonstrated that the binding of substrate, 2OG, or surrogate substrate, NOG, was not affected by the addition of inhibitors to R132H IDH1, in the absence of metal ions. This result is contrary to the conclusion from the kinetic studies[169,173] which suggested that R132H IDH1 inhibitors are competitive with 2OG. The disagreement is within expectation as kinetic studies are inevitably conducted in the presence of catalytically active metal ion, but binding studies can be designed with or without metal ions. NOG binding was weakened upon addition of inhibitor in the

presence of $Mg^{2+}$, to an extent similar to that of NOG binding without $Mg^{2+}$. The results provide evidence to support the hypothesis that R132H IDH1 inhibitors are competitive with $Mg^{2+}$ that is important for 2OG binding, instead of being competitive with 2OG directly.

### 3.4.4 Metal ions affect efficacy of R132H IDH1 inhibitors

Based on the biophysical results from NMR spectroscopy and non-denaturing MS, IDH1 R132H inhibitors likely work by displacing the catalytically active metal ion that is important for 2OG binding. It follows that increasing metal concentration should make R132H IDH1 more resilient to inhibition, leading to less effective inhibition of R132H IDH1 by its inhibitors. Biochemical studies were conducted to test relative inhibition of three inhibitors, AGI-5198, GSK864 and AG-120, under various $MgCl_2$ concentrations. The results (**Figure 3.17**) revealed that % inhibition of R132H IDH1 by its inhibitors decreases with increasing $Mg^{2+}$, particularly over the range of 2.5–20 mM $MgCl_2$, coinciding with $K_M$ of $MgCl_2$ for R132H IDH1 (4.4 mM). The weakening of inhibition by $Mg^{2+}$ is consistent with the hypothesis that R132H IDH1 inhibitors are competitive with the metal ions.

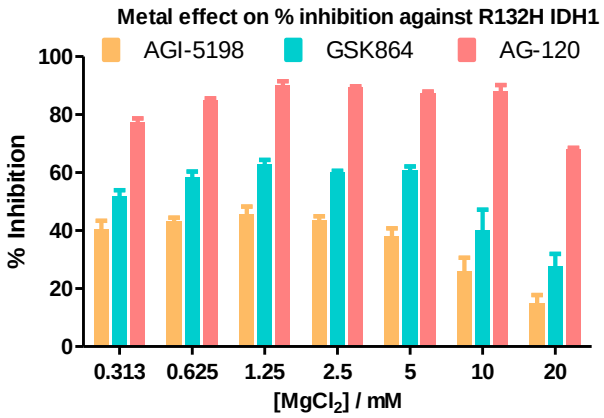



**Figure 3.17**. Relative inhibition of R132H IDH1 by mutant IDH1 inhibitors is weakened with increasing $MgCl_2$ concentrations. The % inhibition of R132H IDH1 (300 nM) by AGI-5198, GSK864 (different scaffold and binding stoichiometry from AGI-5198) and AG-120 (similar scaffold to AGI-5198 but more potent) (all at 100 nM) under different $MgCl_2$ concentrations (0.313–20 mM), as determined by absorbance-based assays. Data are mean ± SD, n= 3 technical replicates. The % inhibition is calculated by (1 – activity with inhibitor/activity with DMSO control) × 100%. Buffer: 100 mM Tris-HCl, 0.005% (v/v) Tween 20, 0.1 mg/mL BSA and 0.2 mM DTT, pH 8.0. See Experimental Methods: Biochemical assays for general assay conditions.

## 3.5 Mode of inhibition of R132H IDH1 inhibitors

Historically, it is more common for enzyme inhibitors to bind competitively at the same site as the endogenous ligand, as supported by a review of 85 drugs approved by FDA between 2001 and 2004, where 80% of the drugs are active site binding substrate competitors[221]. However, nearly all potent ($IC_{50}$< 100 nM) R132H IDH1 inhibitors with reported X-ray crystal structures are allosteric and bind at the dimer interface instead of the active site of the enzyme, despite being apparently structurally diverse[118,169,172,176,213]. Such an unusual observation implies undetermined processes at play during substrate and inhibitor binding to IDH1.

During the investigation on the mechanism of inhibition of R132H IDH1 inhibitors, non-denaturing MS showed that addition of inhibitors to the mixture of substrate and enzyme in all cases does not displace the endogenous NADPH in wt IDH1 or R132H IDH1, consistent with the conclusion from kinetic studies[169,173] that inhibitors are non-competitive with respect to the cofactor, NADPH.

On the basis of Lineweaver-Burk analyses, reported biochemical studies concluded that GSK321, an inhibitor with an $IC_{50}$ of 4.6 nM against R132H IDH1, is competitive with the substrate 2OG[169]. In another instance, ML309 and AGI-5198, inhibitors with different scaffold from the GSK series, were reported to be competitive for 2OG using inhibition studies under various 2OG concentrations[173]. These studies neglected the roles of metal ions in R132H IDH1.

Nonetheless, other studies highlighted the importance of metal ions in the inhibition mechanisms of R132H IDH1 inhibitors. Steady-state kinetic studies demonstrated that an allosteric inhibitor with a bis-imidazole phenol structure (PDB 4UMX) is competitive with $Mg^{2+}$ [183]. It was reasoned that the phenol group of the inhibitor binding at the dimer interface makes direct contact with Asp279 which in turn is responsible for binding the catalytically essential divalent metal ion[183]. A more recent study by surface plasmon resonance (SPR) also revealed that depletion of $Mg^{2+}$ in wt IDH1 enables a mutant-selective inhibitor, IDH125, to bind to the enzyme due to destabilisation of the regulatory segment (residues 271–286)[213]. This suggests that $Mg^{2+}$ is important for stabilising the regulatory segment and resisting R132H IDH1 inhibitors

binding to wt IDH1, thereby making the inhibitor mutant selective. These two studies, together with the kinetic data presented in this work, are consistent in finding a >100-fold difference in the $K_M$ of $Mg^{2+}$ between wt IDH1 and R132H IDH1.

In a review by Golub *et al.*, the modes of inhibition by various IDH1 and IDH2 inhibitors are summarised as follows: Ivosidenib competes for binding with the enzyme's essential cofactor, $Mg^{2+}$, thereby preventing the formation of a catalytically active site; others including GSK321, BAY-1436032, IDH305, Vorasidenib, Enasidenib and AGI-6780 bind at the dimer interface to cause steric hindrance that locks the enzyme in an open, inactive conformation[6]. A unified explanation to account for all these observations is that the inhibitors are competitive with $Mg^{2+}$, leading to the displacement of the substrate 2OG. The substrate isocitrate (likely as a complex with $Mg^{2+}$) is required to lock wt IDH into the closed conformation[12]. Consequently, without the substrate (isocitrate or 2OG), the protein is in the open conformation, consistent with observations in crystal structures of R132H IDH1 with its inhibitors[213]. Combined with evidence from previous structural studies[169,183,213], the proposed allosteric inhibition mechanism is that mutant IDH inhibitors bind to a regulatory α-helix (residues 271–286) at the dimer interface and disrupts binding of a divalent metal ion that also coordinates to the α-helix (**Figure 3.18**). Since the metal ion coordinates to substrate and assists in substrate binding for enzymatic conversion, the displacement of the metal ion due to the presence of the allosteric inhibitors consequently inhibits substrate binding and conversion. Future therapeutic agents of IDH1 could be rationally designed by targeting modulation of the binding of divalent metal ions to IDH1.

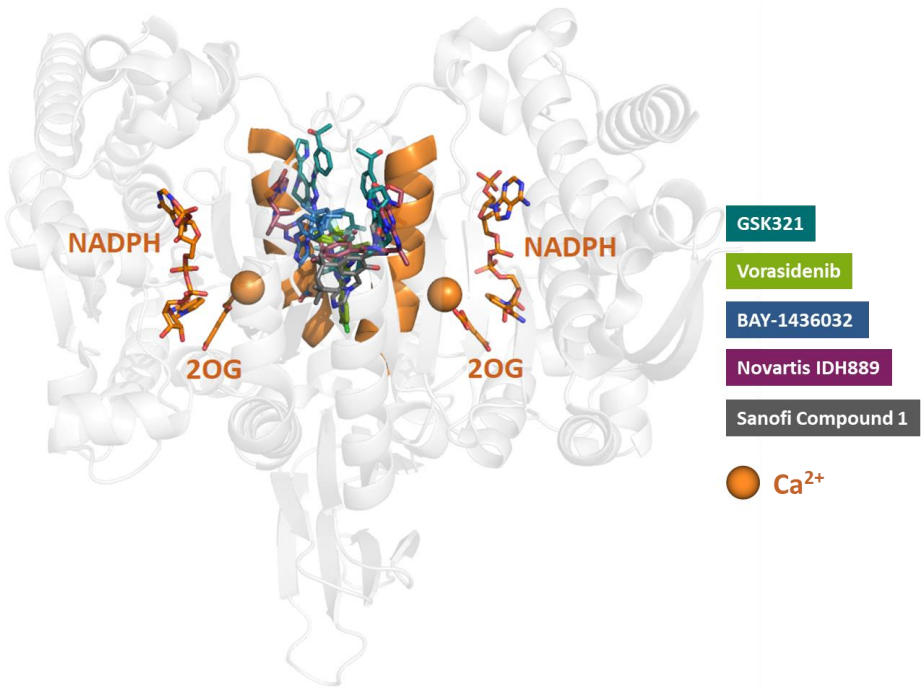



**Figure 3.18**. Active site (occupied by (co)substrates) and dimer interface (occupied by inhibitors) of R132H IDH1 are spatially linked through a proposed regulatory α-helix segment, which forms one face of the active site. X-ray crystal structure view of R132H IDH1 (translucent light grey, PDB 3INM)[11] with its cofactor (NADPH), substrate (2OG), metal ion ($Ca^{2+}$ shown) and an α-helix segment (residues 271–286) with which both the metal ion and inhibitors interact, all shown in orange. This is superimposed with the binding modes of four inhibitors at the dimer interface: GSK321 (blue-green, PDB 5DE1)[169], Vorasidenib (green, PDB 6ADP)[178], BAY-1436032 (navy, PDB 5LGE)[118], Novartis IDH889 (purple, PDB 5TQH)[177] and Sanofi 1 (dark grey, PDB 4UMX)[183]. The proposed allosteric mechanism for R132H IDH1 inhibitors is that their binding results in conformational changes involving the inhibitor-α helix-$Mg^{2+}$-substrate complex.

## 3.6 Summary

Biochemical studies demonstrated that wt IDH1 and R132H IDH1 have greater preference and catalytic rates with $MnCl_2$ compared to $MgCl_2$. Catalytically inactive divalent metal ions such as $Ca^{2+}$ inhibit wt IDH1 and R132H IDH1. Interestingly, isocitrate binds to wt IDH1 in the presence of $Mg^{2+}$, $Mn^{2+}$ or $Ca^{2+}$, as measured by ITC. However, isocitrate does not bind to $Ca^{2+}$, possibly explaining why $Ca^{2+}$ is catalytically inactive for IDH1.

Detailed biophysical analyses using non-denaturing MS and $^1$H NMR spectroscopy revealed key roles of metal ions in regulating substrate and inhibitor binding to wt IDH1 and R132H IDH1. Divalent metal ions including $Mg^{2+}$ substantially enhance isocitrate binding to wt IDH1 and 2OG/NOG binding to R132H IDH1. Competition binding experiments of substrates and inhibitors to wt IDH1 and R132H IDH1 were performed to rationalise mutant selectivity of R132H IDH1 inhibitors. Non-denaturing MS showed that in the presence of metal ions, binding of isocitrate and inhibitor to wt IDH1 is mutually exclusive and that isocitrate binding is not reduced by the inhibitor. $^1$H NMR studies also demonstrated that isocitrate is not displaced by the R132H IDH1 inhibitors in the presence of $Mg^{2+}$ or $Ca^{2+}$. The allosteric R132H IDH1 inhibitors weaken the binding of the divalent metal ion complexes required for catalysis, presumably through interaction with a regulatory α-helix segment. Weakening of the inhibition of R132H IDH1 by its inhibitors through increasing $Mg^{2+}$ concentrations was validated in biochemical assays. Collectively, the work described in this chapter revealed an interaction cascade of inhibitor-α-helix-$Mg^{2+}$-substrate for IDH1, emphasising on the underappreciated feature of metal ions in the inhibition mechanism and the broader human physiology.

## 3.7 Supplementary Figures

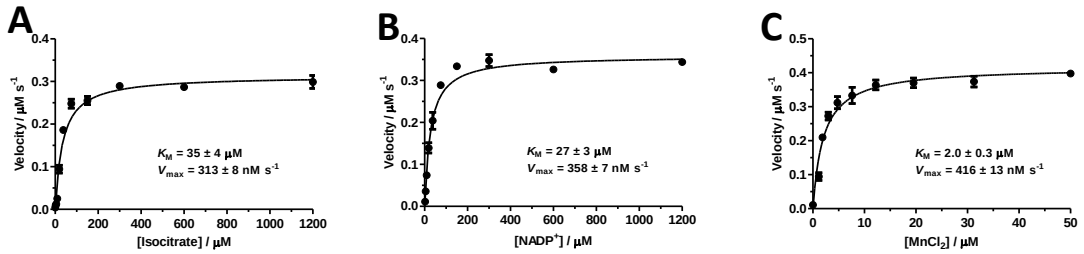



**Figure S3.1.** Dependence of reaction rates (monitored by NADPH formation/depletion by absorbance-based assays) on different concentrations of (co)substrates (**A**) DL-isocitrate, (**B**) $NADP^+$ and (**C**) $MnCl_2$ in the oxidative reaction (isocitrate to 2OG) by wt IDH1. The error bars represent mean ± SEM, n= 3 technical replicates. The calculated $K_M$ and $V_{max}$ values are reported as mean ± SEM from the data fit. Buffer is 100 mM Tris-HCl, 10 mM $MnCl_2$, 0.005% (v/v) Tween 20, 0.1 mg/mL BSA and 0.2 mM DTT, pH 8.0. 10 mM $MnCl_2$ is excluded in the kinetic parameters determination of $MnCl_2$. Kinetic parameters for reductive reaction (2OG to isocitrate) by wt IDH1 were not determined as $MnCl_2$ forms insoluble carbonate salt with $NaHCO_3$ in the reaction mixture.

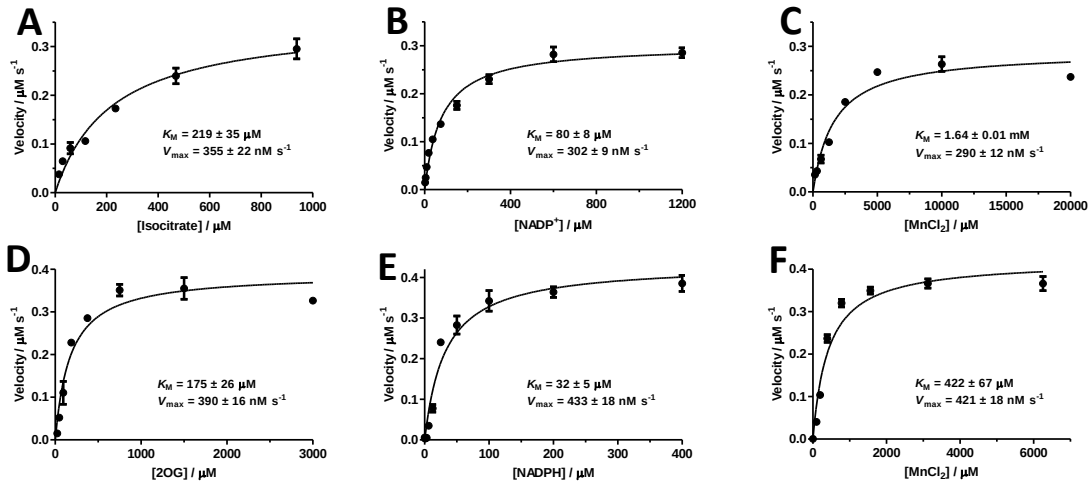



**Figure S3.2.** Dependence of reaction rates (monitored by NADPH formation/depletion by absorbance-based assays) on different concentrations of (co)substrates (**A**) DL-isocitrate, (**B**) $NADP^+$ and (**C**) $MnCl_2$ in the oxidative reaction (isocitrate to 2OG), as well as (**D**) 2OG, (**E**) NADPH and (**F**) $MnCl_2$ in the reductive reaction (2OG to 2HG) by R132H IDH1. The error bars represent mean ± SEM, n= 3 technical replicates. Buffer is 100 mM Tris-HCl, 10 mM $MnCl_2$, 0.005% (v/v) Tween 20, 0.1 mg/mL BSA and 0.2 mM DTT, pH 8.0. 10 mM $MnCl_2$ is excluded in the kinetic parameters determination of $MnCl_2$.

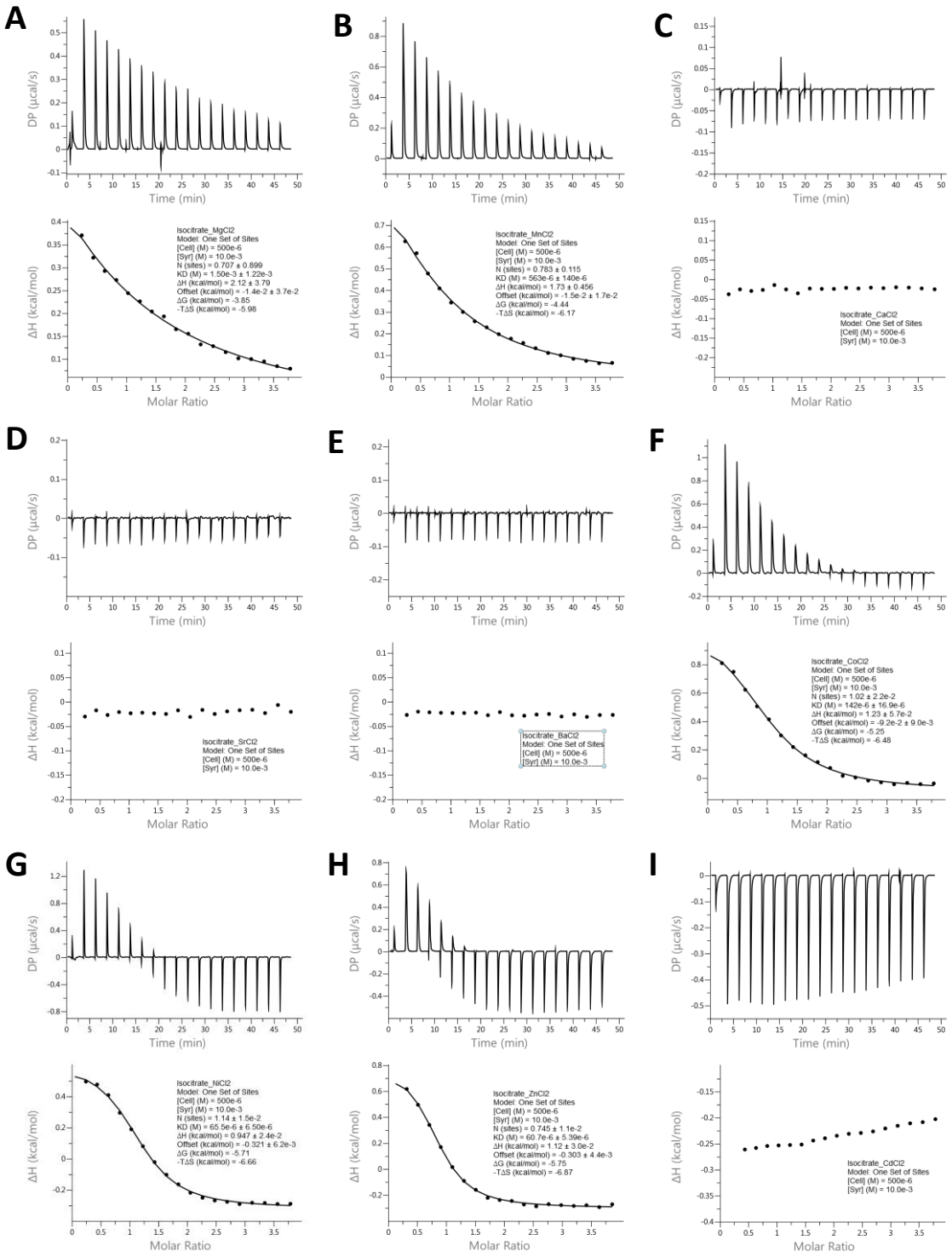
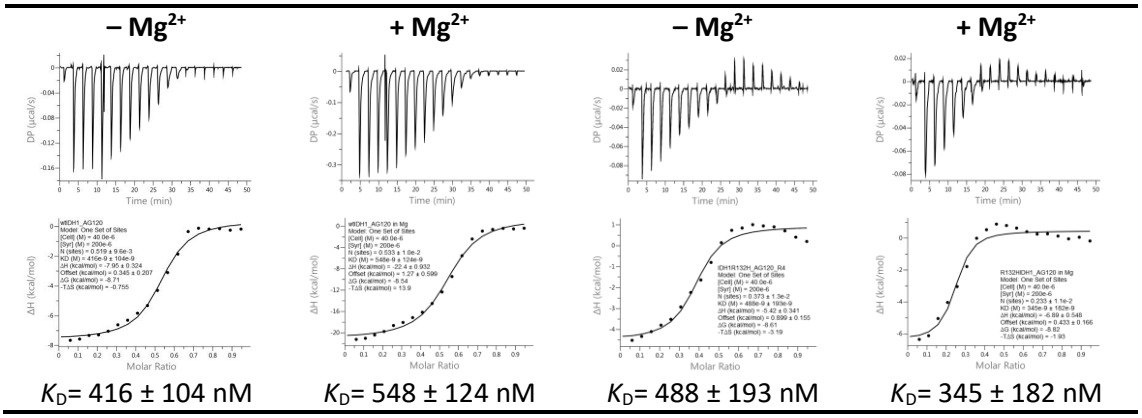
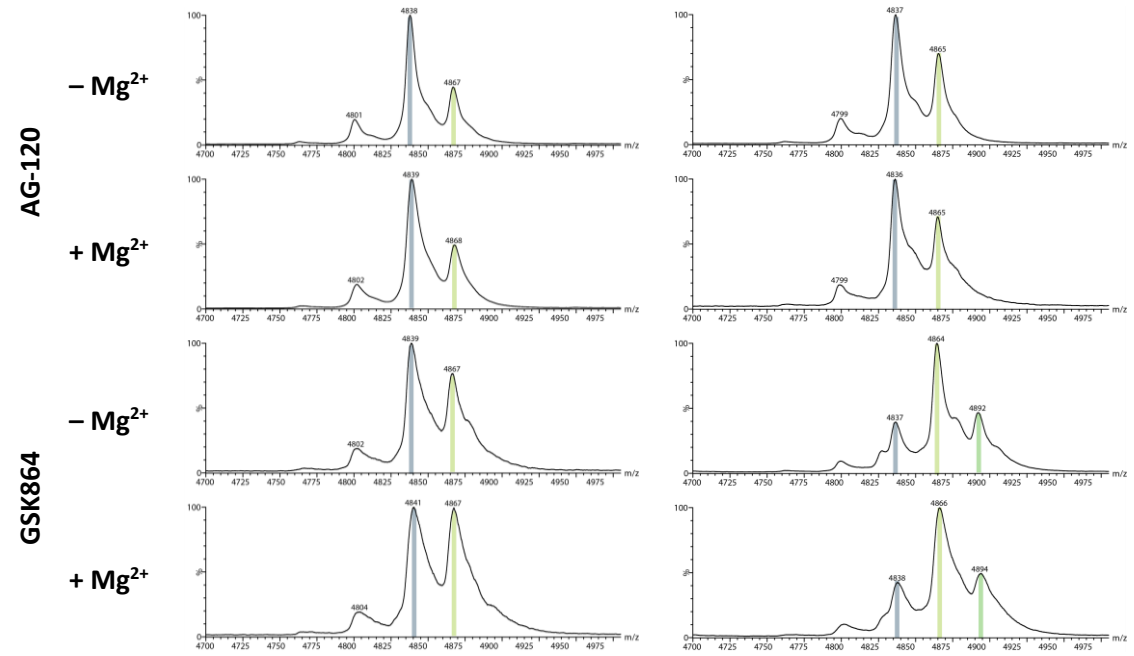



**Figure S3.3**. ITC graphs of metal ions (10 mM) binding to DL-isocitrate (500 µM) in 50 mM Tris-HCl, pH 7.5. See Experimental Methods: Isothermal Titration Calorimetry for method details. Metal ions: (**A**) $MgCl_2$, (**B**) $MnCl_2$, (**C**) $CaCl_2$, (**D**) $SrCl_2$, (**E**) $BaCl_2$, (**F**) $CoCl_2$, (**G**) $NiCl_2$, (**H**) $ZnCl_2$, (**I**) $CdCl_2$. Rank order of binding affinity to isocitrate: $ZnCl_2$ (strongest)> $NiCl_2$ > $CoCl_2$ > $MnCl_2$ > $MgCl_2$; no detectable binding for $CaCl_2$, $SrCl_2$, $BaCl_2$ and $CdCl_2$.

**A**


wt IDH1
R132H IDH1
– Mg2+
+ Mg2+
– Mg2+
+ Mg2+
DP (µcal/s)
Time (min)
ΔH (kcal/mol)
Molar Ratio
KD= 416 ± 104 nM
KD= 548 ± 124 nM
KD= 488 ± 193 nM
KD= 345 ± 182 nM

**B**


wt IDH1
R132H IDH1
AG-120
GSK864
– Mg2+
+ Mg2+
– Mg2+
+ Mg2+
m/z

**C**

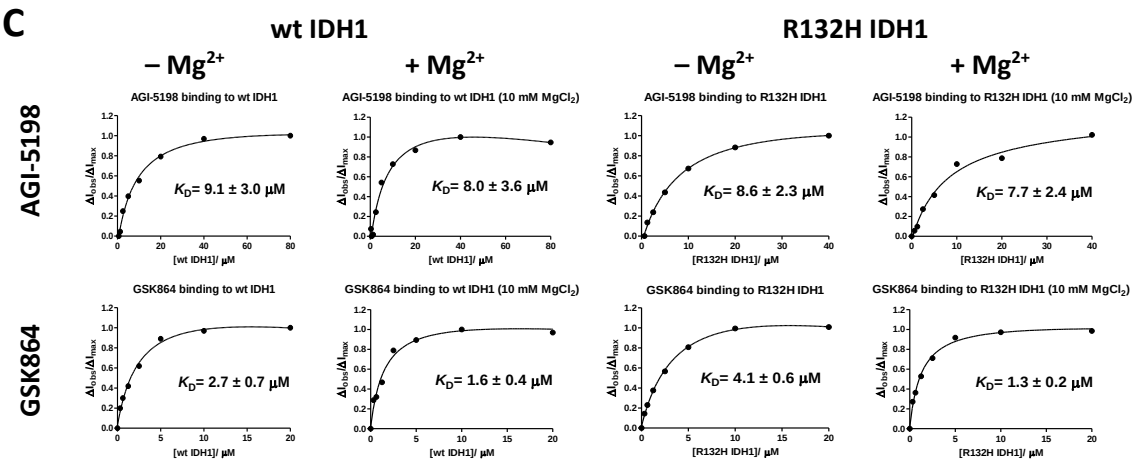

wt IDH1
R132H IDH1
– Mg2+
+ Mg2+
– Mg2+
+ Mg2+
AGI-5198
GSK864
AGI-5198 binding to wt IDH1
AGI-5198 binding to wt IDH1 (10 mM MgCl2)
AGI-5198 binding to R132H IDH1
AGI-5198 binding to R132H IDH1 (10 mM MgCl2)
GSK864 binding to wt IDH1
GSK864 binding to wt IDH1 (10 mM MgCl2)
GSK864 binding to R132H IDH1
GSK864 binding to R132H IDH1 (10 mM MgCl2)
KD= 9.1 ± 3.0 µM
KD= 8.0 ± 3.6 µM
KD= 8.6 ± 2.3 µM
KD= 7.7 ± 2.4 µM
KD= 2.7 ± 0.7 µM
KD= 1.6 ± 0.4 µM
KD= 4.1 ± 0.6 µM
KD= 1.3 ± 0.2 µM
[wt IDH1]/ µM
[R132H IDH1]/ µM

**Figure S3.4**. (**A**) $K_D$ values for the binding of AG-120 to wt IDH1/R132H IDH1 are similar with or without $MgCl_2$. ITC analysis of Ivosidenib (200 μM) titrating against wt IDH1 or R132H IDH1 (40 μM), in 50 mM Tris-HCl, pH 7.5, ± 5 mM $MgCl_2$. See Experimental Methods: Isothermal Titration Calorimetry for method details.

(**B**) Binding pattern of AG-120/GSK864 binding to wt IDH1/R132H IDH1 are similar with or without $MgCl_2$. MS analyses (non-denaturing) of binding of AG-120 or GSK864 to wt IDH1 or R132H IDH1, ± $MgCl_2$. Data for the m/z= $20^+$ charge state are shown. Cone voltage= 100 V. Buffer: 200 mM ammonium acetate, pH 7.5. See Experimental Methods: Protein non-denaturing MS for method details. For clarity, only 2× NADPH bound protein peaks are annotated. Samples for wt IDH1 contain 50 μM wt IDH1, 12.5 μM AG-120 or 25 μM GSK864, ± 200 μM $MgCl_2$. Samples for R132H IDH1 contain 50 μM R132H IDH1, 12.5 μM AG-120 or 50 μM GSK864, ± 500 μM $MgCl_2$.

(**C**) $K_D$ values for the binding of AGI-5198/GSK864 to wt IDH1/R132H IDH1 are similar with or without $MgCl_2$. $K_D$ of AGI-5198 or GSK864 against wt IDH1 or R132H IDH1, ± $MgCl_2$ (10 mM), determined by $^1$H NMR (CPMG-edited, 700 MHz) spectroscopy. See Experimental Methods: Nuclear Magnetic Resonance for method details. The intensity of the inhibitor peak(s) shown was monitored. Graphs of $\Delta I_{obs}/\Delta I_{max}$ against [protein]/uM are fitted using GraphPad Prism to get $K_D$. $\Delta I_{obs}/\Delta I_{max}=(I_{max}-I_{obs})/(I_{max}-I_{min})$ where $I_{max}$ is the maximum inhibitor peak intensity observed when no protein is added, $I_{obs}$ is the observed inhibitor peak intensity at a particular protein concentration, and $I_{min}$ is the minimum inhibitor peak intensity (typically ~0) when the binding is fully saturated.

# CHAPTER 4.

# STUDIES ON METABOLITE-METAL ION COMPLEXES USING DOSY

As described in **Chapters 2** and **3**, work with biophysical techniques demonstrated the enhancement of isocitrate binding to wt IDH1 by metal ions, highlighting the potential importance of metal ions in forming complexes with TCA cycle intermediates and metabolites. The binding of metal ions to adenosine triphosphate (ATP) has been intensely studied due to its important biological role[222–225]. However, current evidence on the structure of divalent metal ions to TCA cycle intermediates, such as isocitrate-$Mg^{2+}$ complex is limited. As described in this chapter, various NMR techniques, in particular DOSY, were employed to provide insights in the solution-state structures of isocitrate-$Mg^{2+}$ and other metabolite-metal ion complexes. The recent advances in DOSY[226] have enabled the prediction of the molecular weights (MWs) of small molecule-metal ion complexes based on their diffusion coefficients.

## 4.1 A more 'symmetrical' isocitrate

$^1$H NMR (600 MHz) measurements of isocitrate in $D_2O$ reveal a typical ABX coupling pattern for the C-4 $H_A$ and $H_B$ protons (X is $H_C$ in this case) as shown in **Figure 4.1**. These proton signals were used to monitor changes in isocitrate levels in NMR reaction monitoring. Intriguingly, in experiments with $Mg^{2+}$ present in the mixture, the signals converge towards a simpler AX coupling pattern (**Figure 3.6**). This change in coupling pattern indicates a different conformational state for isocitrate upon its coordination by $Mg^{2+}$.

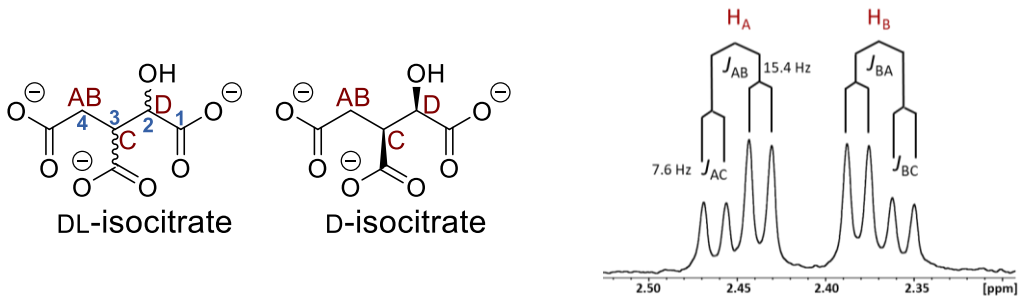



**Figure 4.1**. Structures of DL-isocitrate and D-isocitrate with NMR detectable protons ($H_A$, $H_B$, $H_C$ and $H_D$) in red, and the carbon positions in blue (left); ABX coupling observed in $^1$H NMR (600 MHz) spectrum of isocitrate (right). See **Figure 4.2** 'DL-isocitrate only' for full spectrum.

To fully characterise how the coupling pattern of isocitrate protons changes with addition of different concentrations of $Mg^{2+}$, DL-isocitrate was titrated against $Mg^{2+}$, with analysis by $^{1}H$ NMR (600 MHz) spectroscopy (**Figure 4.2**). The DL-isocitrate concentration was fixed at 1 mM, which is likely close to a physiologically relevant value[227] and which enables a good signal-to-noise ratio. The $MgCl_2$ concentrations were varied based on the DL-isocitrate:$MgCl_2$= 32:1 to 1:32, *i.e.* from 31.25 µM to 32 mM. As shown in **Figure 4.2**, the ABX coupling pattern for $H_A$ and $H_B$ of DL-isocitrate without $Mg^{2+}$ converges to a doublet (an apparent AX coupling) at DL-isocitrate:$MgCl_2$= 1:1. At higher $Mg^{2+}$ concentrations, however, the apparent AX coupling pattern reverts to an ABX coupling pattern. Interestingly, the chemical shifts of $H_A$, $H_B$, $H_D$ (and $H_C$ to a smaller extent) also move to the lower field (leftward shift) with the greatest rate of change around DL-isocitrate:$MgCl_2$= 1:1 (**Figure 4.2**).

$^{13}C$ NMR measurements showed significant changes to the chemical shifts for the carbon resonances of all three carboxyl groups, suggesting that their chemical environments are affected by $Mg^{2+}$ coordination (**Figure 4.3**). In the $^{13}C$ NMR studies, due to a lower abundance of $^{13}C$ compared to $^{1}H$, 100 mM instead of 1 mM DL-isocitrate was used to ensure a good signal:noise ratio whilst keeping the relative ratio with $MgCl_2$ the same.

It was noted that with the change in the absolute concentrations of DL-isocitrate and $MgCl_2$, the trend in the $^{1}H$ coupling pattern using the 100 mM DL-isocitrate:$MgCl_2$ mixture was similar, but not identical, to that at 1 mM (**Figure 4.3**). Given the changes in the coupling patterns and chemical shifts observed when using different ratios of DL-isocitrate:$MgCl_2$, it was proposed that DL-isocitrate is in a dynamic equilibrium with another distinct conformation at equimolar $MgCl_2$. The apparent AX coupling pattern observed at DL-isocitrate:$MgCl_2$= 1:1 suggests that under this condition $H_A$ and $H_B$ of DL-isocitrate are in the same chemical environment, despite the presence of an adjacent chiral carbon to which $H_C$ is attached.

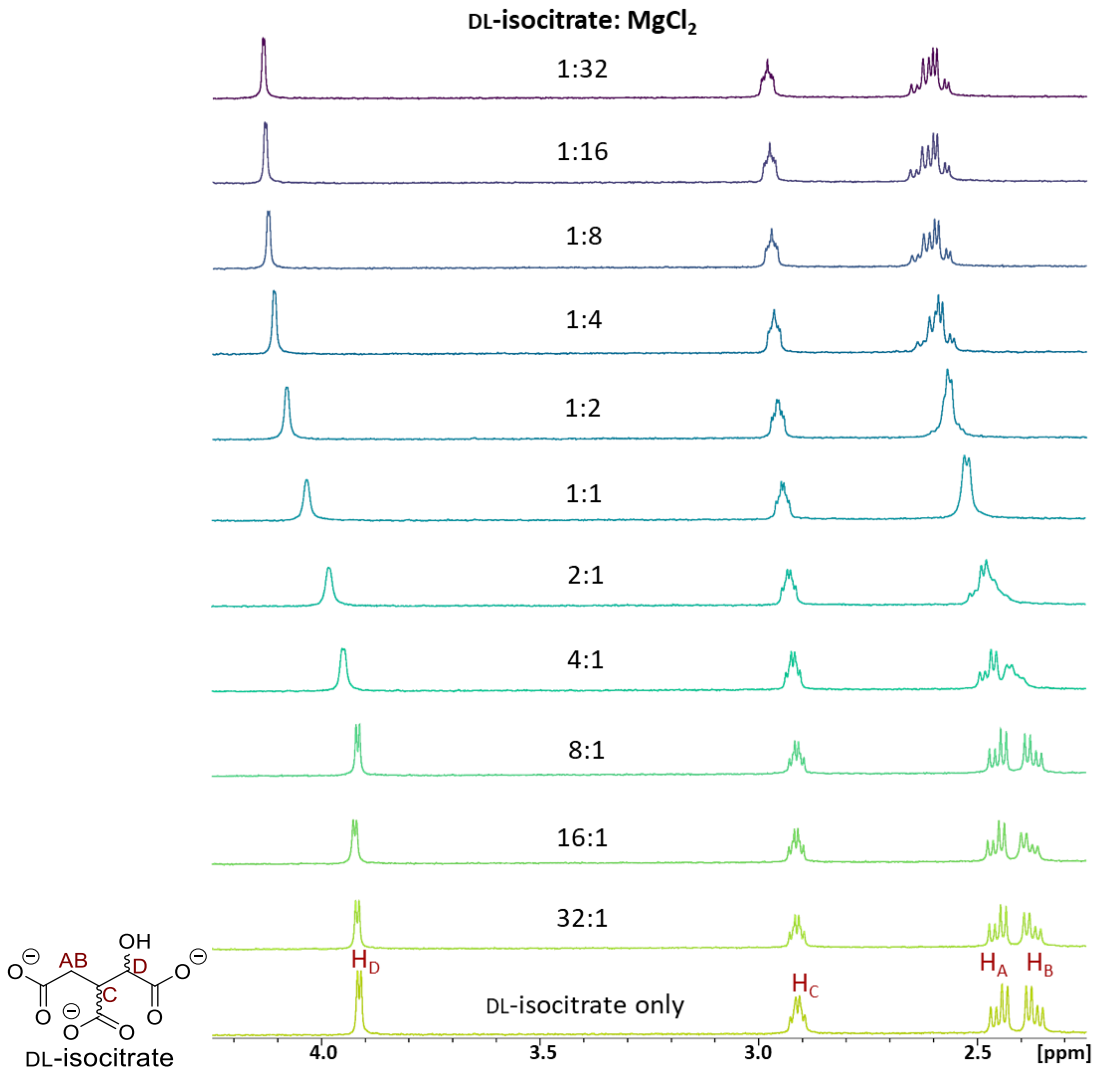



**Figure 4.2**. $^{1}H$ NMR (600 MHz) spectra of DL-isocitrate with $MgCl_2$ in $D_2O$. The DL-isocitrate concentration is fixed at 1 mM whilst the $MgCl_2$ concentrations are increased from 31.25 µM to 32 mM with two-fold step changes. No significant change in pH across the samples was detected by pH paper.

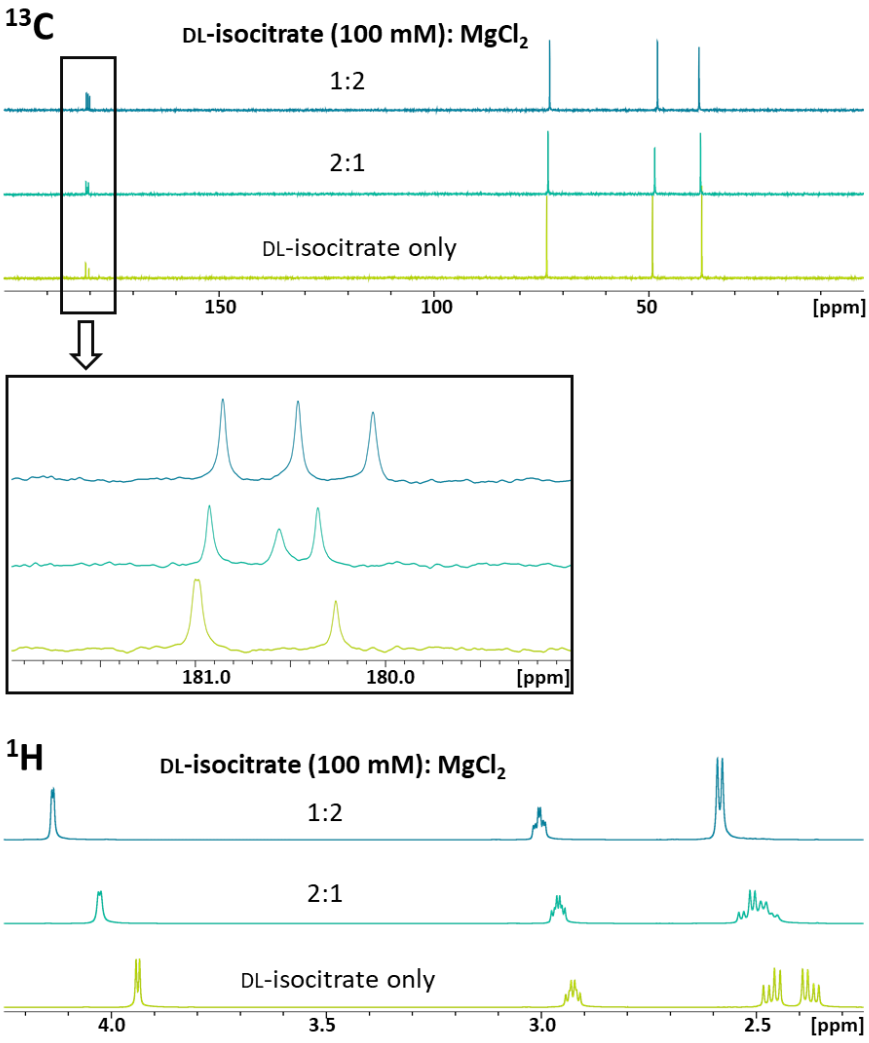



**Figure 4.3**. $^{13}C$ NMR (600 MHz) spectra of 100 mM DL-isocitrate with 0, 50 or 200 mM $MgCl_2$ in $D_2O$. The carboxyl region (black box) is expanded for clarity. The corresponding $^{1}H$ NMR (600 MHz) spectra are also presented.

As DL-isocitrate is racemic, the first step in elucidating the conformation of the isocitrate-$Mg^{2+}$ complex was to compare the $^{1}H$ NMR spectra for DL-isocitrate titrated with $Mg^{2+}$ with those using the single enantiomer, D-isocitrate. Initially, no change in the ABX coupling pattern of D-isocitrate with addition of $Mg^{2+}$ was observed. This observation was later realised to be caused by different pHs in the DL-isocitrate-$MgCl_2$ and D-isocitrate-$MgCl_2$ mixtures. DL-Isocitrate is supplied as a trisodium salt that gives a neutral solution (pH ~7 by pH paper), whereas D-isocitrate is supplied as a monopotassium salt that give an acidic solution acidic (pH ~4 by pH paper). Presumably $Mg^{2+}$ coordinates to the negatively charged $COO^{-}$ groups of isocitrate, hence a lower pH means more protonated COOH that may hinder $Mg^{2+}$ coordination to isocitrate. Subsequently, the

pH of D-isocitrate was adjusted to 7 by addition of two molar equivalents of NaOH with respect to D-isocitrate. The ionic strength (concentrations of sodium and potassium ions) and the effective concentrations of DL-isocitrate and D-isocitrate were also adjusted to enable a fair comparison of their NMR spectra. **Figure 4.4** shows the $^{1}$H NMR (600 MHz) spectra of D-isocitrate with $MgCl_2$ varying from D-isocitrate:$MgCl_2$= 4:1 to 1:4. The resultant NMR spectra are identical to those of DL-isocitrate, suggesting that $Mg^{2+}$ coordination to isocitrate cannot distinguish between the two enantiomers of isocitrate.

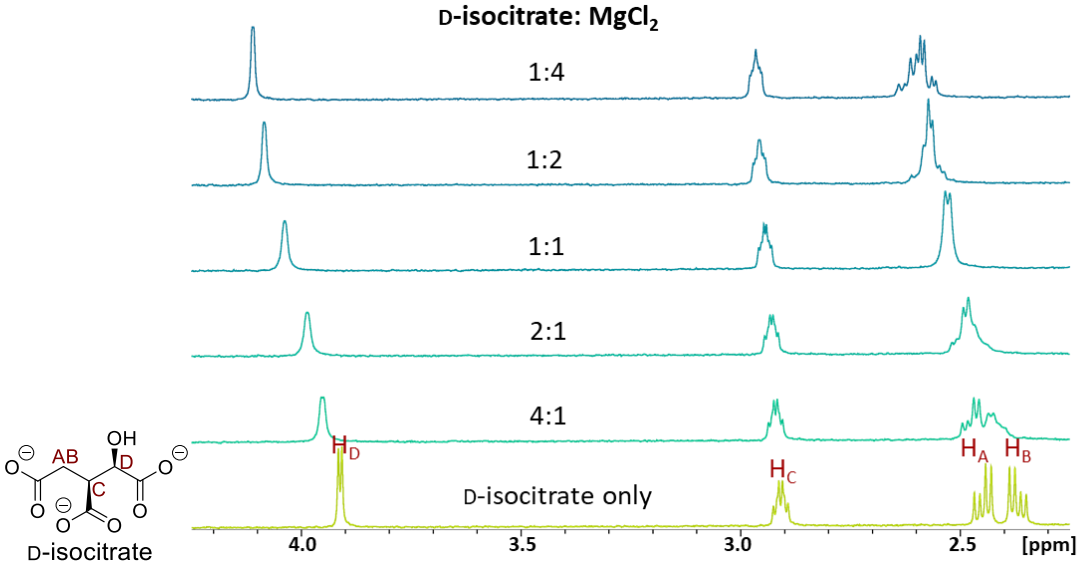



**Figure 4.4**. $^{1}$H NMR (600 MHz) spectra of D-isocitrate with $MgCl_2$ in $D_2O$. The D-isocitrate concentration is fixed at 1 mM whilst the $MgCl_2$ concentrations are increased from 0.25 mM to 4 mM with two-fold step changes. No significant change in pH across the samples was detected by pH paper.

The results reveal that there is no detectable difference in $Mg^{2+}$ coordination to D-isocitrate or DL-isocitrate, likely ruling out the possibility of the formation of a mixed D- and L-isocitrate complex under the current experimental conditions. To account for the apparent AX coupling pattern observed for the $H_A$ and $H_B$ protons, a conformational model is proposed below using D-isocitrate only for simplicity. The simpler peak pattern for equimolar D-isocitrate (or DL-isocitrate) and $Mg^{2+}$ implies a more 'symmetrical' isocitrate structure, such as the one shown in **Figure 4.5**, than for isocitrate alone. When all the three carboxylate groups of isocitrate are brought together by coordination to a $Mg^{2+}$ ion, $H_A$ and $H_B$ can orientate between $H_C$, experiencing similar chemical environments and hence resulting in a simpler apparent AX coupling pattern. To support the validity of the proposed conformation, Nuclear Overhauser Effect Spectroscopy

(NOESY) studies were conducted on the same set of $Mg^{2+}$ titration samples to provide information about spatial orientations of the protons of isocitrate. An intensity graph of relative NOE intensities of the protons of DL-isocitrate against $MgCl_2$ concentration (**Figure 4.6**) was plotted by co-worker, Mohammadali Foroozandeh. Although NOE data may not be conclusive in general, it is useful as a secondary validation. Notably, the NOE of $H_A$ and $H_B$ to $H_C$ is greatest at DL-isocitrate:$MgCl_2$= 1:1, implying that $H_A$ and $H_B$ are the closest to $H_C$, consistent with the conformation proposed in **Figure 4.5**.

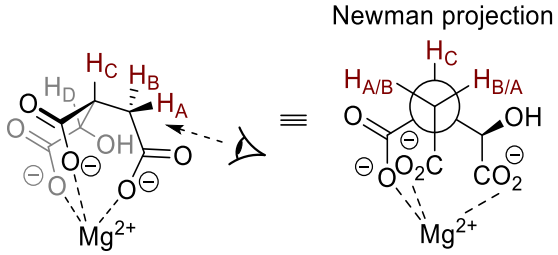



**Figure 4.5**. Proposed conformation of D-isocitrate-$Mg^{2+}$ complex, with Newman projection highlighting that $H_A$ and $H_B$ of D-isocitrate is between $H_C$.

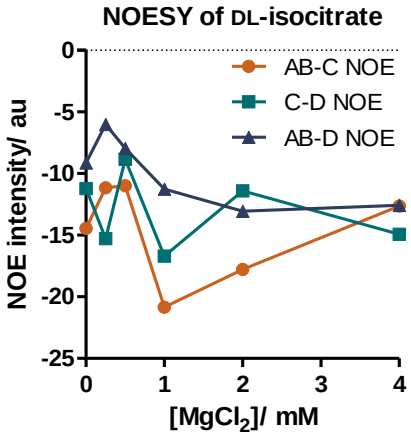



**Figure 4.6**. $^1H$-$^1H$ NOESY (600 MHz) results of DL-isocitrate titrated with $MgCl_2$, presented as NOE intensities between the protons of DL-isocitrate against $MgCl_2$ concentration. The DL-isocitrate concentration is fixed at 1 mM, whilst the $MgCl_2$ concentrations are varied from isocitrate:$MgCl_2$= 4:1 to 1:4, in $D_2O$ at 298 K. Correlations between the isocitrate protons are presented as the NOE of $H_A$ and $H_B$ to $H_C$ (orange), $H_C$ to $H_D$ (cyan), and $H_A$ and $H_B$ to $H_D$ (navy).

It should be noted that the use of equimolar isocitrate and $MgCl_2$ does not necessarily mean that the stoichiometry of isocitrate and $Mg^{2+}$ in the isocitrate-$Mg^{2+}$ complex is 1:1. The proposed conformation (**Figure 4.5**) assumes that the isocitrate-$Mg^{2+}$ complex is monomeric, instead of a oligomer or polymer of isocitrate:$Mg^{2+}$= n:n. The latter possibility considerably expands the potential scope and complexity of structural considerations. The model in **Figure 4.5** also does not explain the reappearance of ABX coupling at $MgCl_2$ concentrations above isocitrate:$MgCl_2$= 1:2, an observation which suggests other forms of isocitrate-$Mg^{2+}$ complexes may occur. DOSY was thus employed to find solutions to these problems.

## 4.2 DOSY

Somewhat unexpectedly, given its biological importance, there are no reported structures of the isocitrate-$Mg^{2+}$ complex or of other isocitrate-metal ion complexes. However, an X-ray crystal structure of a related complex, *i.e.* that of citrate-$Mn^{2+}$, has been reported[180]. Citrate is converted to isocitrate via *cis*-aconitate by aconitase in the TCA cycle[228]. The structure of citrate differs from isocitrate in the position of the hydroxyl group (**Figure 4.7**). $Mn^{2+}$ is often a substitute for $Mg^{2+}$ in biological processes, as mentioned in **Section 3.1**. In the reported structure of citrate-$Mn^{2+}$ (**Figure 4.8**), two molecules of citrate coordinate to an octahedral $Mn^{2+}$ ion through the carboxyl group at C-1 as well as the carboxyl and hydroxyl groups at C-3 of citrate. Such octahedral geometry is perhaps what might be anticipated for isocitrate- and citrate-metal ion complexes. However, X-ray crystallography is a solid phase technique often employing saturating conditions of reagents in crystallisation, which may not represent the structure in solution. Based on UV-vis and infrared spectral studies, another study proposed that citrate may form a dimeric citrate complex with two bridging metal ions, or a monomeric citrate complex with one metal ion (**Figure 4.9**)[229].

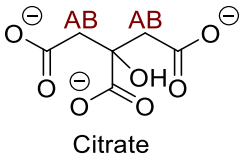



**Figure 4.7**. Structure of citrate with NMR detectable protons, $H_A$ and $H_B$, labelled in red.

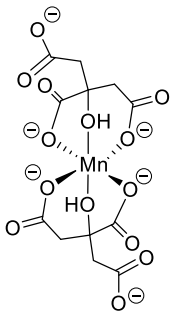



**Figure 4.8**. Structure of $[Mn(C_6H_5O_7)_2]^{4-}$ anion, as reported by Matzapetakis *et al.*[180]

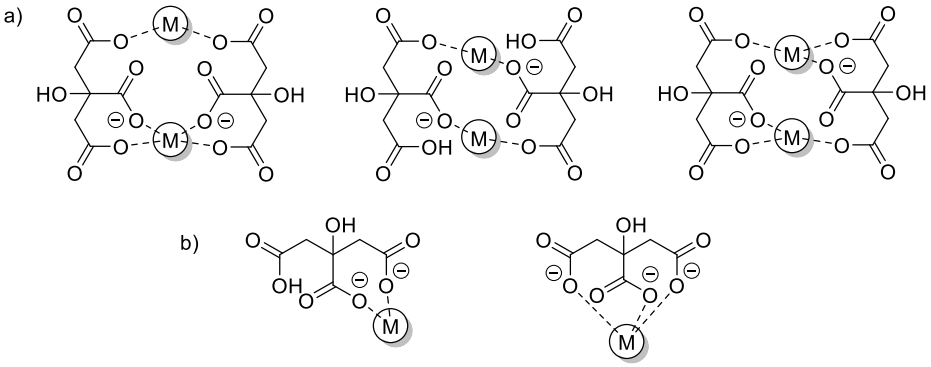



**Figure 4.9**. Proposed models of citrate-metal ion complexes as (a) dimeric and (b) monomeric, based on UV-vis and infrared spectral studies, by Zabiszak *et al*.[229]

Due to the inconclusive results from X-ray crystallography, UV-vis and infrared spectroscopies, DOSY NMR experiments[230] were employed to investigate the structure of the isocitrate-$Mg^{2+}$ complex. In DOSY NMR experiments, a pulsed field gradient (PFG) is applied so that molecules along the NMR tube experience different local magnetic fields, destroying signals from the sample. A second PFG is applied to act in opposition to the first PFG to refocus the signal. If the molecules do not move between the two PFGs, the full signal is recovered. Conversely, diffusion causes some molecules to move away from where their signals can be refocused, resulting in a reduction in their signals. By incrementing the gradient strength, a diffusion profile is obtained to calculate the diffusion coefficient, *D*. Larger molecules diffuse more slowly and have a smaller diffusion coefficient compared to smaller molecules, and vice versa[230].

DOSY was initially used as a qualitative technique to distinguish different species in a mixture, and to predict the relative sizes of species, from their diffusion coefficients[230]. There has been recent improvement in using DOSY to predict the MW of small molecules. By using empirical data from over 600 independently acquired diffusion coefficients, a theoretical model using the Stokes–Einstein equation (**Equation 4.1**) was modified to the Stokes–Einstein Gierer–Wirtz Estimation (SEGWE), enabling quantitative prediction of molecular weights (MWs), with reasonable accuracy, from diffusion coefficients obtained with DOSY[226]. One caveat of DOSY-SEGWE is that it does not directly provide information on the solvation state or the shape of molecules/complexes.

$$D = \frac{\mathrm{k_B}T}{6\pi f \eta r}$$

**Equation 4.1**. The Stokes–Einstein equation. $D$ is diffusion coefficient, $\mathrm{k_B}$ is the Boltzmann's constant, $T$ is temperature, $f$ is the shape correction factor and is equal to 1 for a spherical particle, $\eta$ is solution viscosity and $r$ is the hydrodynamic radius of the solute particle. $D$ is proportional to $T$ and inversely proportional to $\eta$ and $r$.

DOSY and SEGWE were applied to investigate the MW of the isocitrate-$Mg^{2+}$ complex at different $MgCl_2$ concentrations, as illustrated in **Figure 4.10**. Diffusion coefficients, *D*, as measured by DOSY, are shown in the vertical axis whilst chemical shifts are shown in the horizontal axis. Samples of DL-isocitrate (1 mM) without $MgCl_2$ or titrated with $MgCl_2$ (0.125–8 mM) in $D_2O$ were analysed by DOSY. SEGWE was then used to predict the MW from the measured diffusion coefficients. In SEGWE calculations, the temperature is set

to 298 K as per NMR measurements, and the solvent is set to $D_2O$. The predicted MWs by DOSY and SEGWE in **Table 4.1** are reasonably accurate, since the MW of DL-isocitrate without any $MgCl_2$ is predicted to be 196, close to its theoretical MW of 192. The small deviation from the theoretical MW is likely due to limitations in the empirical dataset used in SEGWE.

The results (**Table 4.1**) suggest that when the DL-isocitrate:$MgCl_2$ ratio in solution is 1:1, there is approximately one $Mg^{2+}$ ion coordinating to one molecule of DL-isocitrate. This stoichiometry clearly differs from the two molecules of citrate coordinating to one $Mn^{2+}$ ion as observed in the reported X-ray crystal structure[180], or the two molecules of citrate bridged by two metal ions as proposed from the reported spectral studies[229]. The structure is consistent with the proposed structure in **Figure 4.5**. At higher $Mg^{2+}$ concentrations, *i.e.* DL-isocitrate: $MgCl_2$= 1:4, there are approximately two $Mg^{2+}$ ions coordinating to one molecule of DL-isocitrate. This complex could adopt one of the proposed structures shown in **Figure 4.11**. A non-integer coordination number, *e.g.* 0.4 when DL-isocitrate: $MgCl_2$= 2:1, may reflect an equilibrium between zero $Mg^{2+}$ and one $Mg^{2+}$ ion coordinating to the DL-isocitrate. There are no significant changes in the number of $Mg^{2+}$ ions coordinated to DL-isocitrate at DL-isocitrate: $MgCl_2$= 1:8 compared to 1:4, possibly because the system is saturated. It was considered that above 8 mM $MgCl_2$, the assumption of salt-free $D_2O$ used in SEGWE calculation is no longer valid due to the increased ionic strength and viscosity, potentially leading to less accurate prediction and the results were therefore excluded.

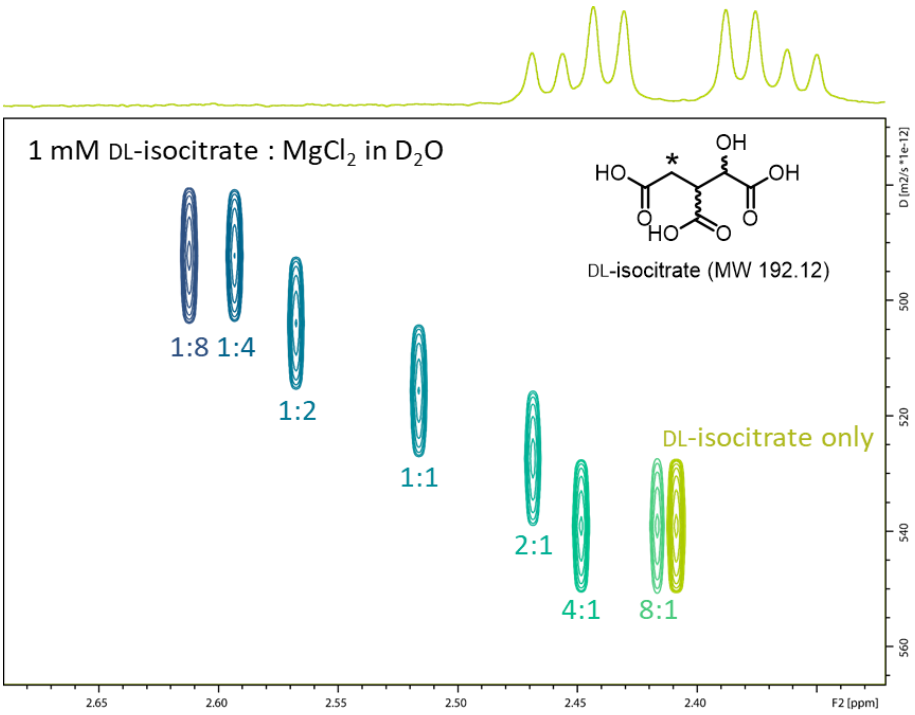



**Figure 4.10**. $^{1}$H DOSY (600 MHz) spectra of DL-isocitrate alone and DL-isocitrate:$MgCl_2$ at ratios from 8:1 to 1:8. The vertical axis shows the diffusion coefficient, *D*, in unit of $10^{-12}$ $m^2$ $s^{-1}$. The horizontal axis shows the centre of chemical shifts for $H_A$ and $H_B$ of isocitrate used to calculate the diffusion coefficients.

| DL-isocitrate:$MgCl_2$ | Diffusion coefficient/ $10^{-10}$ $m^2$ $s^{-1}$ | Predicted MW | No. of $Mg^{2+}$ |
|---|---|---|---|
| DL-isocitrate only | 5.39 | 196 | 0 |
| 8:1 | 5.39 | 196 | 0 |
| 4:1 | 5.39 | 196 | 0 |
| 2:1 | 5.27 | 206 | 0.4 |
| 1:1 | 5.16 | 217 | 0.9 |
| 1:2 | 5.04 | 228 | 1.3 |
| 1:4 | 4.92 | 241 | 1.9 |
| 1:8 | 4.92 | 241 | 1.9 |

**Table 4.1**. Predicted MWs from diffusion coefficients measured by DOSY, from samples of DL-isocitrate and $MgCl_2$ at different ratios in $D_2O$ at 298 K. The number of $Mg^{2+}$ ions coordinated to DL-isocitrate can be estimated by (MW calculated for the specific DL-isocitrate:$MgCl_2$ ratio – MW calculated for DL-isocitrate only) / MW of $Mg^{2+}$.

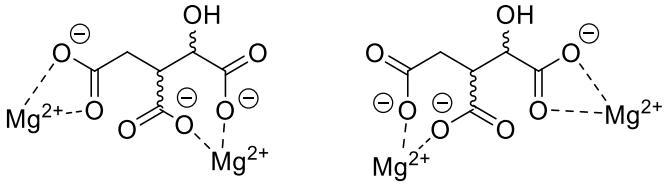



**Figure 4.11**. Possible structures of DL-isocitrate coordinated by two $Mg^{2+}$ ions, when DL-isocitrate:$MgCl_2$= 1:4 or 1:8.

MW prediction was similarly conducted for complexes of D-isocitrate and $MgCl_2$ (D-isocitrate:$MgCl_2$= 4:1 to 1:4) (**Figure 4.4**). The results (**Table 4.2**) showed the same trend as that for DL-isocitrate:$MgCl_2$ mixtures (**Table 4.1**), again confirming that $Mg^{2+}$ coordination to isocitrate is not affected by having both enantiomers of isocitrate being present.

| D-isocitrate:$MgCl_2$ | Diffusion coefficient/ $10^{-10}$ $m^2$ $s^{-1}$ | Predicted MW | No. of $Mg^{2+}$ |
|---|---|---|---|
| D-isocitrate only | 5.39 | 196 | 0 |
| 4:1 | 5.39 | 196 | 0 |
| 2:1 | 5.27 | 206 | 0.4 |
| 1:1 | 5.16 | 217 | 0.9 |
| 1:2 | 5.04 | 228 | 1.3 |
| 1:4 | 4.92 | 241 | 1.9 |

**Table 4.2**. Predicted MWs from diffusion coefficients measured by DOSY, from samples of D-isocitrate and $MgCl_2$ at different ratios in $D_2O$ at 298 K. The number of $Mg^{2+}$ ions coordinated to D-isocitrate can be estimated by (MW calculated for the specific D-isocitrate:$MgCl_2$ ratio – MW calculated for D-isocitrate only) / MW of $Mg^{2+}$.

## 4.3 Isocitrate with different metal ions

**Chapter 3** described the effects of different metal ions on IDH1 catalysis. As an extension of that study, it was of interest to investigate how isocitrate interacts with different metal ions by DOSY. Metal ions such as $Mn^{2+}$, $Co^{2+}$ and $Ni^{2+}$ are paramagnetic and are not suitable for NMR measurements. Thus, studies were carried out with $Ca^{2+}$ and $Zn^{2+}$ which are also biologically important metal ions.

**Figure 4.12** shows the $^1H$ NMR (600 MHz) spectra of DL-isocitrate with $CaCl_2$ at different ratios. Compared to the mixture of DL-isocitrate and $MgCl_2$ (**Figure 4.2**), the ABX coupling of isocitrate converges to the apparent AX coupling at a higher $Ca^{2+}$ concentration *i.e.* DL-isocitrate:$CaCl_2$= 1:2. Furthermore, the apparent AX coupling is maintained up to 32 mM $CaCl_2$ which is the highest $CaCl_2$ concentration tested, and does not revert back to an ABX coupling like that for the case of $Mg^{2+}$. MW prediction of the complexes formed (**Table 4.3**) show that approximately one $Ca^{2+}$ ion coordinates to one molecule of DL-isocitrate at DL-isocitrate:$CaCl_2$= 1:4. This may imply that $Ca^{2+}$ binds more weakly to isocitrate than $Mg^{2+}$ does, which is consistent with the ITC results in **Table 3.2**. In addition, it has been reported that $Ca^{2+}$-$H_2O$ exchange in aqueous ionic solution is

much faster than $Mg^{2+}$-$H_2O$ exchange[231]. Should this also apply to the binding between metal ions and isocitrate, the binding time of $Ca^{2+}$ to isocitrate would be shorter compared to $Mg^{2+}$, consistent with the observations summarised in **Table 4.3**, *i.e.* that $Ca^{2+}$ shows a smaller coordination number to isocitrate compared to $Mg^{2+}$ at the same metal ion concentrations.

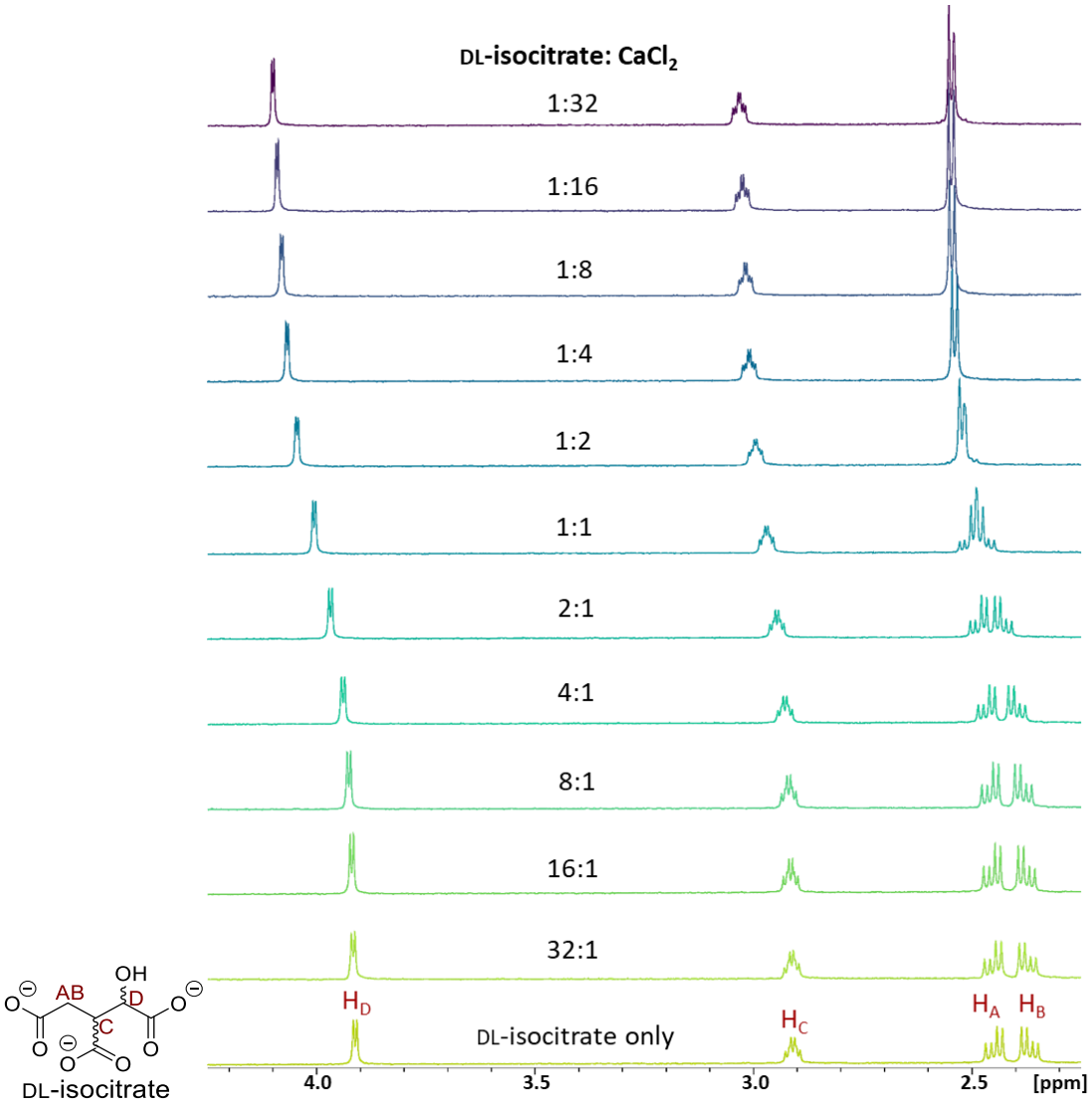



**Figure 4.12**. $^1$H NMR (600 MHz) spectra of DL-isocitrate with $CaCl_2$ in $D_2O$. The DL-isocitrate concentration is fixed at 1 mM whilst the $CaCl_2$ concentrations are increased from 31.25 µM to 32 mM with two-fold step changes. No significant change in pH across the samples was detected by pH paper.

| DL-isocitrate:$CaCl_2$ | Diffusion coefficient/ $10^{-10}$ $m^2$ $s^{-1}$ | Predicted MW | No. of $Ca^{2+}$ |
|---|---|---|---|
| DL-isocitrate only | 5.39 | 196 | 0 |
| 8:1 | 5.39 | 196 | 0 |
| 4:1 | 5.39 | 196 | 0 |
| 2:1 | 5.27 | 206 | 0.2 |
| 1:1 | 5.16 | 217 | 0.5 |
| 1:2 | 5.04 | 228 | 0.8 |
| 1:4 | 4.92 | 241 | 1.1 |
| 1:8 | 4.80 | 254 | 1.4 |

**Table 4.3**. Predicted MWs from diffusion coefficients measured by DOSY, from samples of DL-isocitrate and $CaCl_2$ at different ratios in $D_2O$ at 298 K. The number of $Ca^{2+}$ ions coordinated to DL-isocitrate can be estimated by (MW calculated for the specific DL-isocitrate:$CaCl_2$ ratio – MW calculated for DL-isocitrate only) / MW of $Ca^{2+}$.

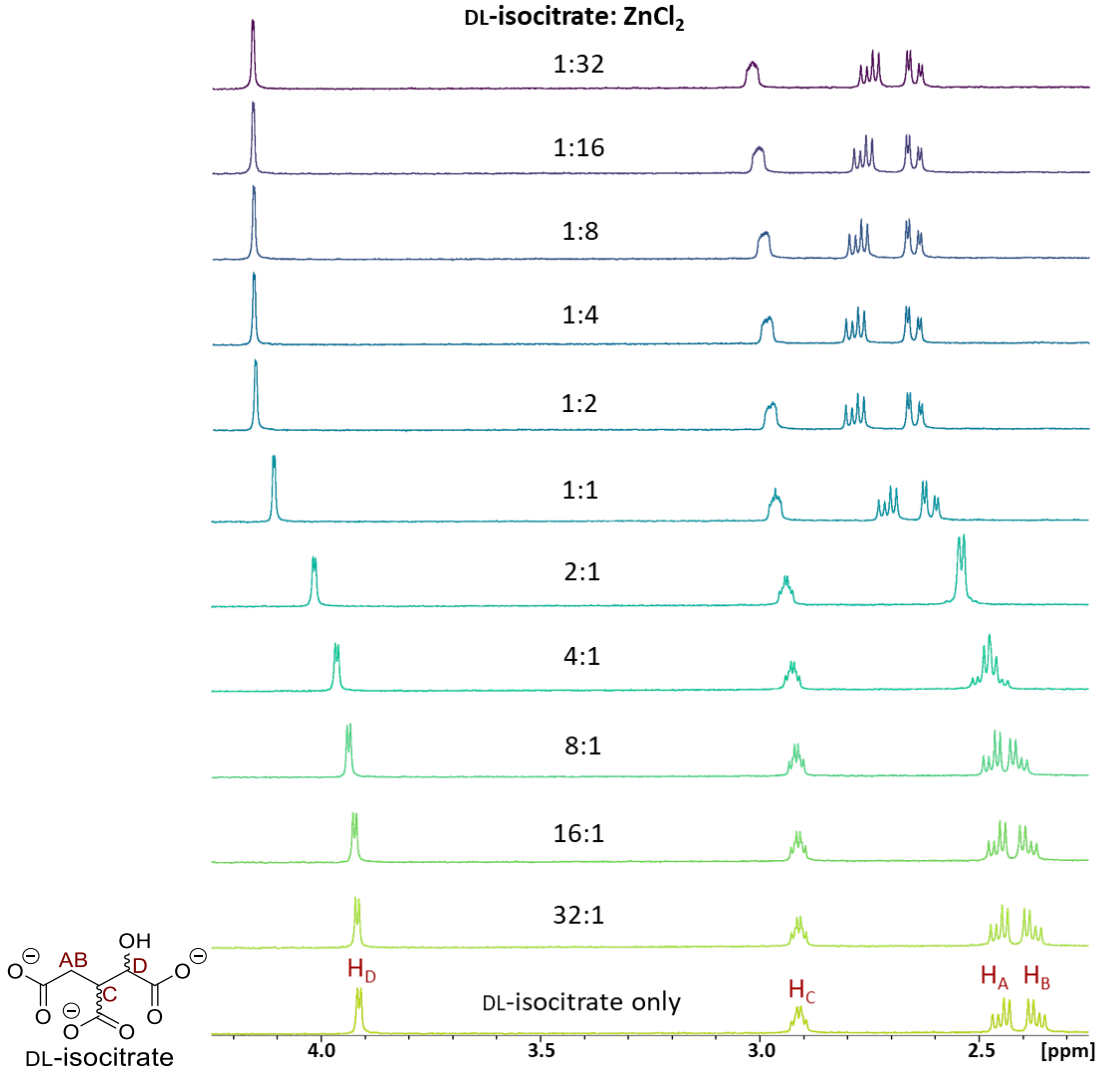



**Figure 4.13**. $^1H$ NMR (600 MHz) spectra of DL-isocitrate with $ZnCl_2$ in $D_2O$. The DL-isocitrate concentration is fixed at 1 mM whilst the $ZnCl_2$ concentrations are increased from 31.25 µM to 32 mM with two-fold step changes. No significant change in pH across the samples was detected by pH paper.

| DL-isocitrate:$ZnCl_2$ | Diffusion coefficient/ $10^{-10}$ $m^2$ $s^{-1}$ | Predicted MW | No. of $Zn^{2+}$ |
|---|---|---|---|
| DL-isocitrate only | 5.39 | 196 | 0 |
| 8:1 | 5.51 | 187 | -0.1 |
| 4:1 | 5.39 | 196 | 0 |
| 2:1 | 5.27 | 206 | 0.2 |
| 1:1 | 5.04 | 228 | 0.5 |
| 1:2 | 5.04 | 228 | 0.5 |
| 1:4 | 4.92 | 240 | 0.7 |
| 1:8 | 4.80 | 254 | 0.9 |

**Table 4.4**. Predicted MWs from diffusion coefficients measured by DOSY, from samples of DL-isocitrate and $ZnCl_2$ at different ratios in $D_2O$ at 298 K. The number of $Zn^{2+}$ ions coordinated to DL-isocitrate can be estimated by (MW calculated for the specific DL-isocitrate:$ZnCl_2$ ratio – MW calculated for DL-isocitrate only) / MW of $Zn^{2+}$.

The mixture of DL-isocitrate and $ZnCl_2$ was also investigated by DOSY. By contrast to the observations with $Ca^{2+}$ ions, the apparent AX coupling was observed to manifest at a relatively low $ZnCl_2$ concentration, *i.e.* DL-isocitrate:$ZnCl_2$= 2:1 (**Figure 4.13**), with reversion back to a distinct ABX coupling at higher concentrations of $ZnCl_2$. However, MW prediction by SEGWE (**Table 4.4**) shows that approximately one $Zn^{2+}$ ion coordinates to DL-isocitrate only when there is a large excess of $ZnCl_2$, *i.e.* DL-isocitrate:$ZnCl_2$= 1:8.

The overall results reveal that the interactions between isocitrate and the three metal ions investigated differ substantially. One caveat in comparing different metal ions using DOSY is that the results may be affected by the subtle pH changes caused by different metal ions. Comparing the trend of DL-isocitrate coordination by $Mg^{2+}$, $Ca^{2+}$ and $Zn^{2+}$ (**Figure 4.14**), $Mg^{2+}$ has the greatest ability to coordinate to DL-isocitrate. By contrast, in the case of $Ca^{2+}$ and $Zn^{2+}$, the evidence implies formation of a 1:1 complex at an isocitrate-metal ion ratio of 1:4 and 1:8, respectively.

In the case of $Ca^{2+}$, the apparent AX coupling pattern appears at a higher isocitrate-metal ion ratio of 1:4 (**Figure 4.12**) compared to the case of $Mg^{2+}$. This is consistent with the DOSY-SEGWE calculation which suggests that one $Ca^{2+}$ ion coordinating to isocitrate at an isocitrate-metal ion ratio of 1:4 (**Table 4.3**). The weaker coordination by $Ca^{2+}$ to DL-isocitrate might be attributed to its larger ionic radius (**Table 3.2**) and consequently fast exchange with DL-isocitrate.

There are some complications in the interpretation of the results for the isocitrate:$ZnCl_2$ mixtures. Compared to $Mg^{2+}$, $Zn^{2+}$ has a higher binding affinity to DL-isocitrate as measured by ITC (**Table 3.2**). Accordingly, $Zn^{2+}$ shows an early onset of the apparent AX coupling pattern at a lower isocitrate-metal ion ratio of 2:1 (**Figure 4.13**). The inconsistency arises as $Zn^{2+}$ was calculated to have the weakest coordination to DL-isocitrate by DOSY-SEGWE (**Table 4.4**). It should be noted that in SEGWE, the number of metal ions coordinated to isocitrate was calculated based on the atomic mass of the metals. However, $Mg^{2+}$ and $Zn^{2+}$ have similar ionic radii at 72 pm and 74 pm respectively[214]. Consequentially, the diffusion constants and the predicted MWs for both the $Mg^{2+}$ and $Zn^{2+}$ experiments are also very similar, because the Stokes–Einstein model only provides information (and prediction) based on the hydrodynamic radius of the complex but has no bearing on MW. This accounts for the similarity in results between $Mg^{2+}$ and $Zn^{2+}$ by ITC (**Table 3.2**) and the coupling patterns observed in their $^1H$ NMR spectra (**Figures 4.2** and **4.13**). In addition, $Zn^{2+}$ typically has a coordination number of 4, instead of 6 for $Mg^{2+}$ and $Ca^{2+}$ [232], potentially resulting in a different structure for the DL-isocitrate:$Zn^{2+}$ complex compared to that proposed for $Mg^{2+}$ (**Figure 4.5**).

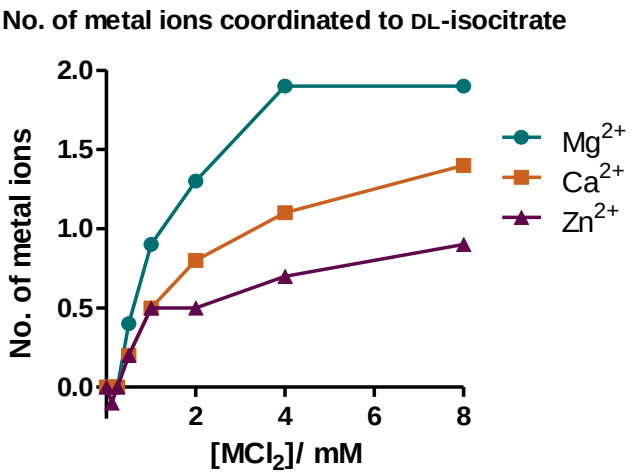



**Figure 4.14**. Graph showing the correlation between number of metal ions ($Mg^{2+}$ in cyan, $Ca^{2+}$ in orange and $Zn^{2+}$ in violet) coordinated to one molecule of DL-isocitrate and different metal ion concentrations, summarised based on the calculated DOSY-SEGWE results in **Tables 4.1**, **4.3** and **4.4**.

## 4.4 Other metabolites and metal ions

Many model studies on the structure of metabolites and metal ion complexes are based on citrate instead of isocitrate[180,229]. Citrate has been reported as a chelating agent for $Mg^{2+}$, $Ca^{2+}$, $Zn^{2+}$ and other metal ions, regulating many biological functions including that of the nervous sytem[233]. Interestingly, $Mg^{2+}$-citrate is sold as a health supplement to increase $Mg^{2+}$ intake[234].

DOSY experiments were thus conducted for titrations of citrate with $MgCl_2$, $CaCl_2$ and $ZnCl_2$ at different ratios. Since citrate does not have a chiral centre, the $^1H$ NMR spectra show only AB coupling (**Figure 4.15**). As the $MgCl_2$ concentration increases from 0 to 32 mM, the difference in the chemical shifts of the $H_A$ and $H_B$ protons of citrate increases from 0.09 ppm to 0.16 ppm, probably because the different chemical environment of $H_A$ and $H_B$ are reinforced by the constrained movement of citrate upon $Mg^{2+}$ coordination. The trend in the coordination of $Mg^{2+}$ to citrate (**Table 4.5**), which shows one $Mg^{2+}$ ion coordinating to one molecule of citrate at citrate:$MgCl_2$= 1:1, is similar to that of $Mg^{2+}$ to isocitrate despite a different position of the hydroxyl group, suggesting that the hydroxyl group may not be involved in $Mg^{2+}$ binding. This hypothesis is, however, contrary to the reported X-ray crystal structure of citrate-$Mn^{2+}$ (**Figure 4.8**)[180] where two carboxyl groups and one hydroxyl group of citrate are involved in metal coordination. Nonetheless, given that the hydroxyl group of citrate has been reported with a high pKa of 14.4 by $^{13}C$ NMR spectroscopy[235], unless restricted by unfavoured bond rotations, the three deprotonated carboxyl groups of citrate might preferentially coordinate to $Mg^{2+}$ in an approximately neutral aqueous environment.

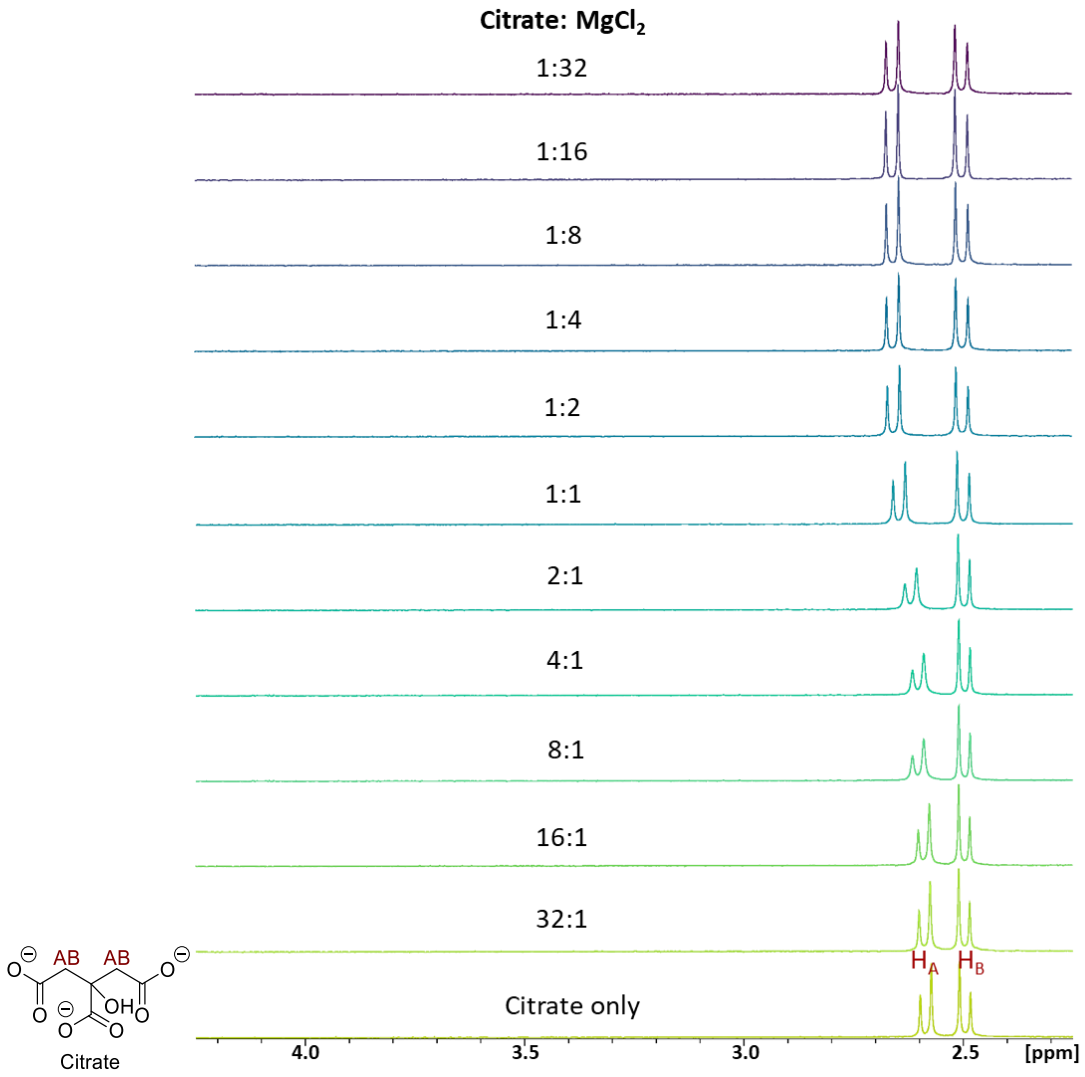



**Figure 4.15**. $^{1}$H NMR (600 MHz) spectra of citrate with $MgCl_2$ in $D_2O$. The citrate concentration is fixed at 1 mM whilst the $MgCl_2$ concentrations are increased from 31.25 µM to 32 mM with two-fold step changes.

| Citrate:$MgCl_2$ | Diffusion coefficient/ $10^{-10}$ $m^2$ $s^{-1}$ | Predicted MW | No. of $Mg^{2+}$ |
|---|---|---|---|
| Citrate only | 5.39 | 196 | 0 |
| 8:1 | 5.39 | 196 | 0 |
| 4:1 | 5.39 | 196 | 0 |
| 2:1 | 5.27 | 206 | 0.4 |
| 1:1 | 5.16 | 217 | 0.9 |
| 1:2 | 5.04 | 228 | 1.3 |
| 1:4 | 5.04 | 228 | 1.3 |
| 1:8 | 4.92 | 241 | 1.9 |

**Table 4.5**. Predicted MWs from diffusion coefficients measured by DOSY, from samples of citrate and $MgCl_2$ at different ratios in $D_2O$ at 298 K. The number of $Mg^{2+}$ ions coordinated to citrate can be estimated by (MW calculated for the specific citrate:$MgCl_2$ ratio – MW calculated for citrate only) / MW of $Mg^{2+}$.

Metal ions titrations against citrate were also conducted using $CaCl_2$ and $ZnCl_2$. As $CaCl_2$ and $ZnCl_2$ concentrations increase from 0 to 32 mM, the differences in the chemical shifts between $H_A$ and $H_B$ of citrate increase from 0.09 ppm to 0.19 ppm for $CaCl_2$ (**Figure 4.16**) and 0.17 ppm for $ZnCl_2$ (**Figure 4.17**), both of which are larger than the difference for $MgCl_2$ (**Figure 4.15**). The trend in the coordination of $Ca^{2+}$ (**Table 4.6**) or $Zn^{2+}$ (**Table 4.7**) to citrate is similar to the case of isocitrate (**Tables 4.3** and **4.4**), both of which achieved one metal ion coordinating to one molecule of citrate/isocitrate when metal ions are in excess of citrate/isocitrate, suggesting that the hydroxyl group may not be involved in $Ca^{2+}$ or $Zn^{2+}$ binding.

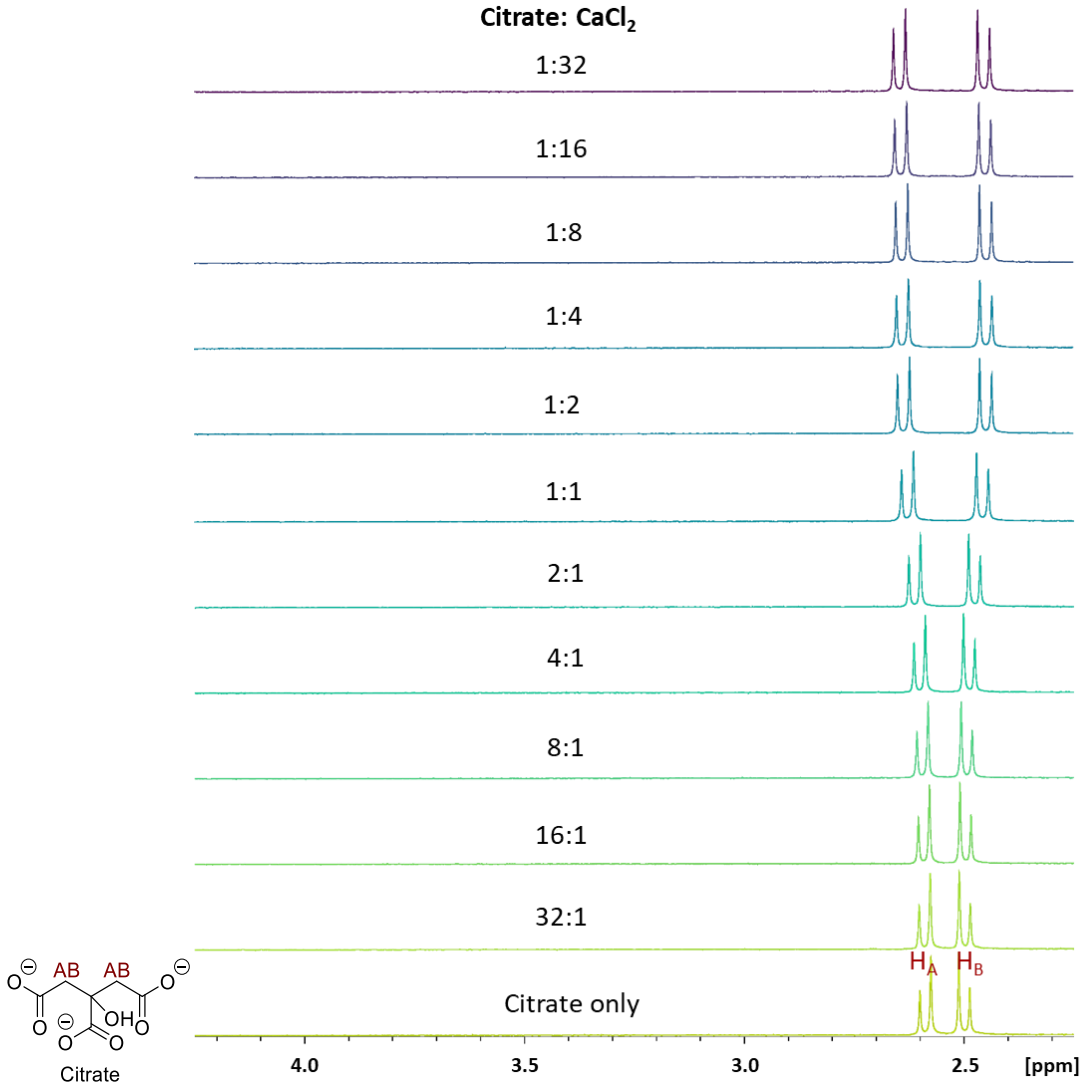



**Figure 4.16**. $^1H$ NMR (600 MHz) spectra of citrate with $CaCl_2$ in $D_2O$. The citrate concentration is fixed at 1 mM whilst the $CaCl_2$ concentrations are increased from 31.25 µM to 32 mM with two-fold step changes.

| Citrate:$CaCl_2$ | Diffusion coefficient/ $10^{-10}$ $m^2$ $s^{-1}$ | Predicted MW | No. of $Ca^{2+}$ |
|---|---|---|---|
| Citrate only | 5.39 | 196 | 0 |
| 8:1 | 5.39 | 196 | 0 |
| 4:1 | 5.39 | 196 | 0 |
| 2:1 | 5.27 | 206 | 0.2 |
| 1:1 | 5.04 | 228 | 0.8 |
| 1:2 | 5.04 | 228 | 0.8 |
| 1:4 | 4.92 | 241 | 1.1 |
| 1:8 | 4.92 | 241 | 1.1 |

**Table 4.6**. Predicted MWs from diffusion coefficients measured by DOSY, from samples of citrate and $CaCl_2$ at different ratios in $D_2O$ at 298 K. The number of $Ca^{2+}$ ions coordinated to citrate can be estimated by (MW calculated for the specific citrate:$CaCl_2$ ratio – MW calculated for citrate only) / MW of $Ca^{2+}$.

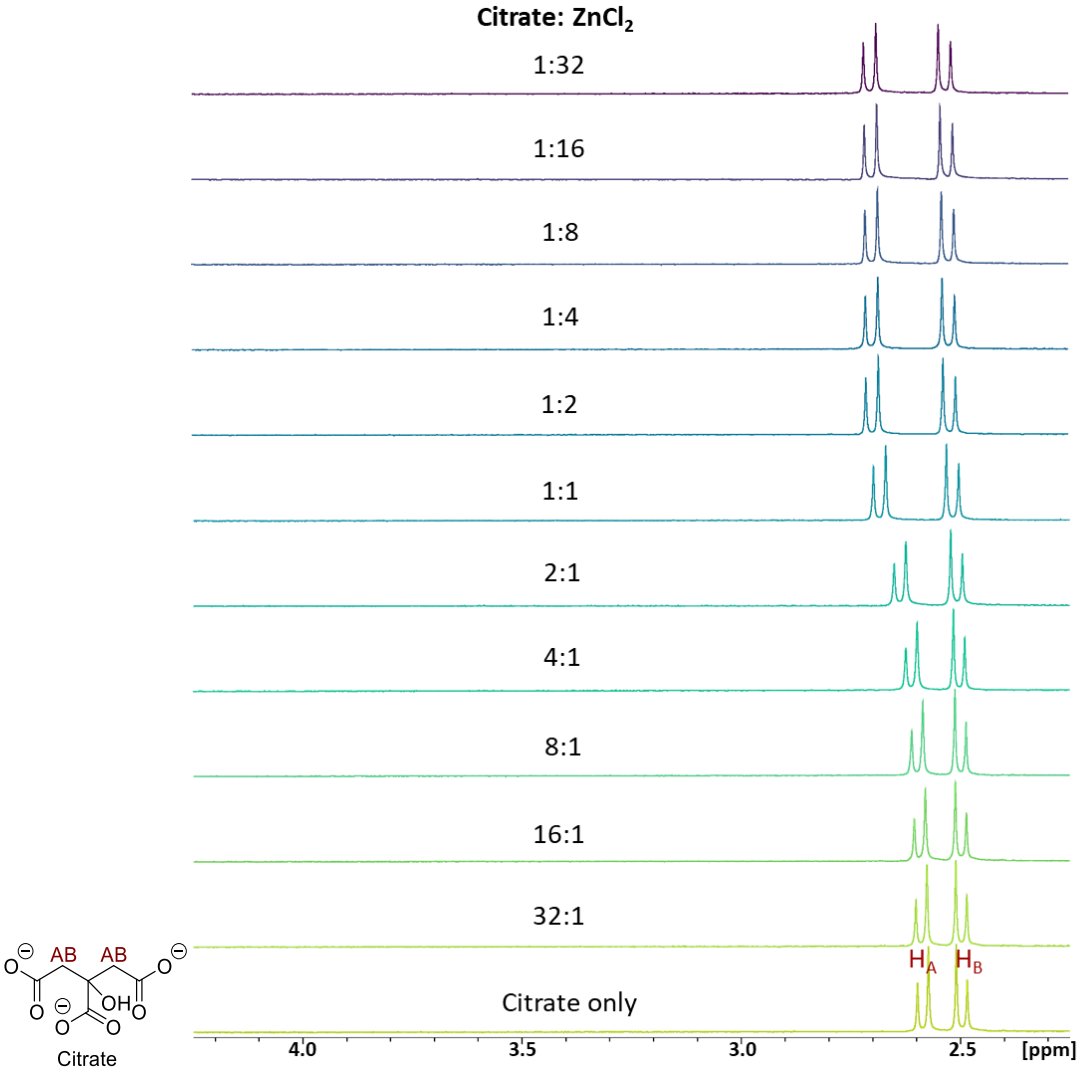



**Figure 4.17**. $^1H$ NMR (600 MHz) spectra of citrate with $ZnCl_2$ in $D_2O$. The citrate concentration is fixed at 1 mM whilst the $ZnCl_2$ concentrations are increased from 31.25 µM to 32 mM with two-fold step changes.

| Citrate:$ZnCl_2$ | Diffusion coefficient/ $10^{-10}$ $m^2$ $s^{-1}$ | Predicted MW | No. of $Zn^{2+}$ |
|---|---|---|---|
| Citrate only | 5.39 | 196 | 0 |
| 8:1 | 5.39 | 196 | 0 |
| 4:1 | 5.39 | 196 | 0 |
| 2:1 | 5.27 | 206 | 0.2 |
| 1:1 | 5.16 | 217 | 0.3 |
| 1:2 | 5.04 | 228 | 0.5 |
| 1:4 | 4.92 | 241 | 0.7 |
| 1:8 | 4.81 | 254 | 0.9 |

**Table 4.7**. Predicted MWs from diffusion coefficients measured by DOSY, from samples of citrate and $ZnCl_2$ at different ratios in $D_2O$ at 298 K. The number of $Zn^{2+}$ ions coordinated to citrate can be estimated by (MW calculated for the specific citrate:$ZnCl_2$ ratio – MW calculated for citrate only) / MW of $Zn^{2+}$.

The interactions of $Mg^{2+}$ with other metabolites relevant to IDH, *i.e.* 2OG and 2HG, were also explored by $^1$H NMR spectroscopy and DOSY. As shown in **Figure 4.18**, no significant changes in the $^1$H NMR spectra were observed at different ratios of 2OG and $MgCl_2$ (2OG:$MgCl_2$= 4:1 to 1:4). MW prediction (**Table 4.8**) suggests that less than one $Mg^{2+}$ ion coordinates to one molecule of 2OG even at 2OG:$MgCl_2$= 1:4. These results support the observations from ITC (**Table S2.3**), *i.e.* $Mg^{2+}$ only coordinates to 2OG very weakly. Note that the DOSY-SEGWE predicted MW of 2OG is 123, ~16% less than the theoretical MW of 146.

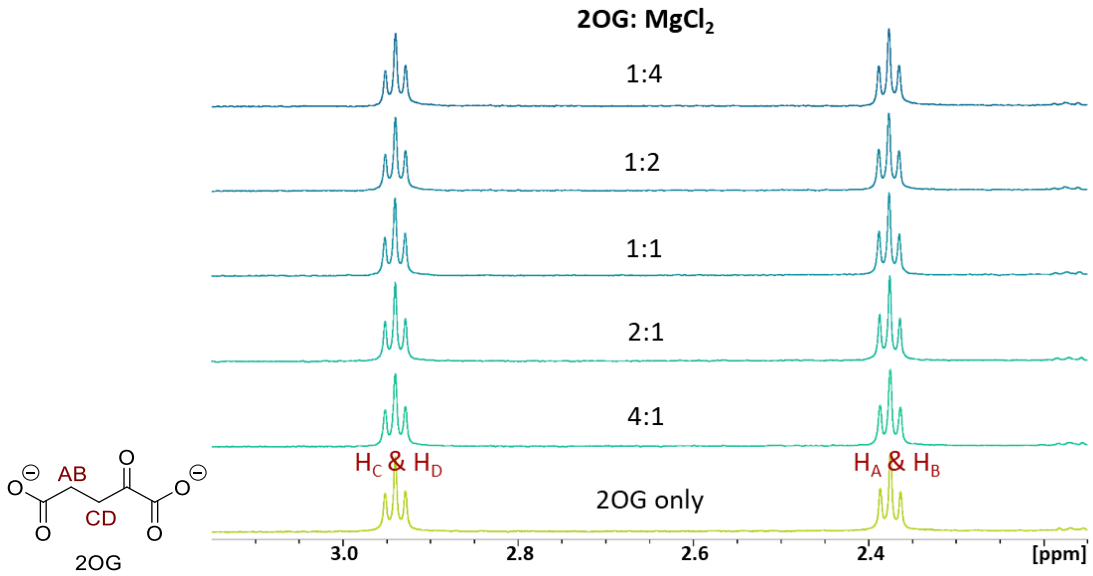



**Figure 4.18**. $^1$H NMR (600 MHz) spectra of 2OG with $MgCl_2$ in $D_2O$. The 2OG concentration is fixed at 1 mM whilst the $MgCl_2$ concentrations are increased from 0.25 mM to 4 mM with two-fold step changes.

| 2OG:$MgCl_2$ | Diffusion coefficient/ $10^{-10}$ $m^2$ $s^{-1}$ | Predicted MW | No. of $Mg^{2+}$ |
|---|---|---|---|
| 2OG only | 6.68 | 123 | 0 |
| 4:1 | 6.68 | 123 | 0 |
| 2:1 | 6.56 | 128 | 0.2 |
| 1:1 | 6.44 | 133 | 0.4 |
| 1:2 | 6.45 | 133 | 0.4 |
| 1:4 | 6.33 | 138 | 0.6 |

**Table 4.8**. Predicted MWs from diffusion coefficients measured by DOSY, from samples of 2OG and $MgCl_2$ at different ratios in $D_2O$ at 298 K. The number of $Mg^{2+}$ ions coordinated to 2OG can be estimated by (MW calculated for the specific 2OG:$MgCl_2$ ratio – MW calculated for 2OG only) / MW of $Mg^{2+}$.

Similar to the results with 2OG and $MgCl_2$, there are no significant changes in the $^1$H NMR spectra of DL-2HG and $MgCl_2$ at different ratios (2HG:$MgCl_2$= 4:1 to 1:4) (**Figure 4.19**). The MW prediction of 2HG from DOSY-SEGWE, *i.e.* 150, is close to its theoretical MW of 148 (**Table 4.9**). The predicted extent of $Mg^{2+}$ coordination to 2HG is greater than that for 2OG. DOSY-SEGWE predicts that approximately one $Mg^{2+}$ ion coordinates to one molecule of 2HG at 2HG:$MgCl_2$= 1:2 (**Table 4.9**), possibly because $Mg^{2+}$ can coordinate to the hydroxyl group and the carboxyl group on the adjacent carbon. However, $Mg^{2+}$ coordination to a hydroxyl group is likely to be weaker than to a carboxyl group as the hydroxyl group will be largely protonated at neutral pH[235]. Comparing the structure of 2HG with that of isocitrate, 2HG lacks the carboxyl group at the C-3 centre and is more weakly coordinated by $Mg^{2+}$, implying that the middle C-3 isocitrate carboxyl group is likely involved in $Mg^{2+}$ coordination, consistent with the proposed structure of the isocitrate-$Mg^{2+}$ complex in **Figure 4.5**.

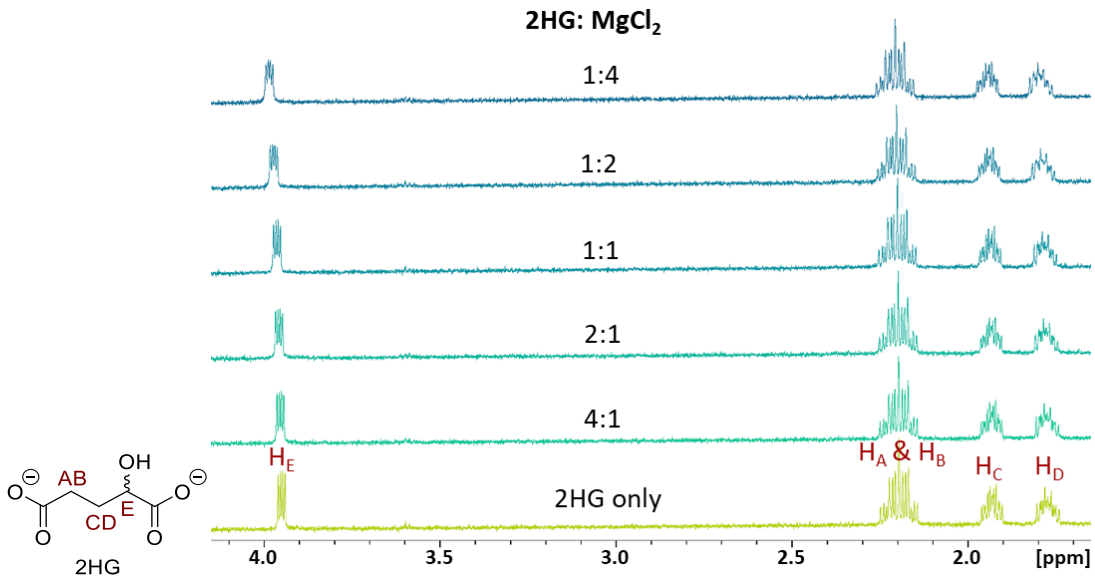



**Figure 4.19**. $^{1}$H NMR (600 MHz) spectra of DL-2HG with $MgCl_2$ in $D_2O$. The DL-2HG concentration is fixed at 1 mM whilst the $MgCl_2$ concentrations are increased from 0.25 mM to 4 mM with two-fold step changes.

| 2HG:$MgCl_2$ | Diffusion coefficient/ $10^{-10}$ $m^2$ $s^{-1}$ | Predicted MW | No. of $Mg^{2+}$ |
|---|---|---|---|
| 2HG only | 6.10 | 150 | 0 |
| 4:1 | 5.98 | 156 | 0.2 |
| 2:1 | 5.98 | 156 | 0.2 |
| 1:1 | 5.86 | 163 | 0.5 |
| 1:2 | 5.74 | 171 | 0.9 |
| 1:4 | 5.63 | 179 | 1.2 |

**Table 4.9**. Predicted MWs from diffusion coefficients measured by DOSY, from samples of 2HG and $MgCl_2$ at different ratios in $D_2O$ at 298 K. The number of $Mg^{2+}$ ions coordinated to 2HG can be estimated by (MW calculated for the specific 2HG:$MgCl_2$ ratio – MW calculated for 2HG only) / MW of $Mg^{2+}$.

It was also of interest to explore the interaction of $Mg^{2+}$ with other TCA cycle metabolites such as succinate and fumarate. Compared to the previously tested compounds (isocitrate, citrate, 2OG and 2HG), succinate and fumarate have a shorter carbon backbone with two terminal carboxyl groups and lack any carbonyl, carboxyl or hydroxyl groups on the alpha carbons. **Figures 4.20** and **4.21** show that no significant changes in the $^{1}$H signals of succinate and fumarate, respectively, are observed. In **Tables 4.10** and **4.11**, approximately 0.2 $Mg^{2+}$ ion coordinates to both succinate and fumarate, at equimolar concentrations of succinate/fumarate and $MgCl_2$. Less than one $Mg^{2+}$ ion coordinates to succinate and fumarate, respectively, when $MgCl_2$ is present at

a 4× molar excess of succinate/fumarate, suggesting a weak coordination of $Mg^{2+}$ to succinate and fumarate.

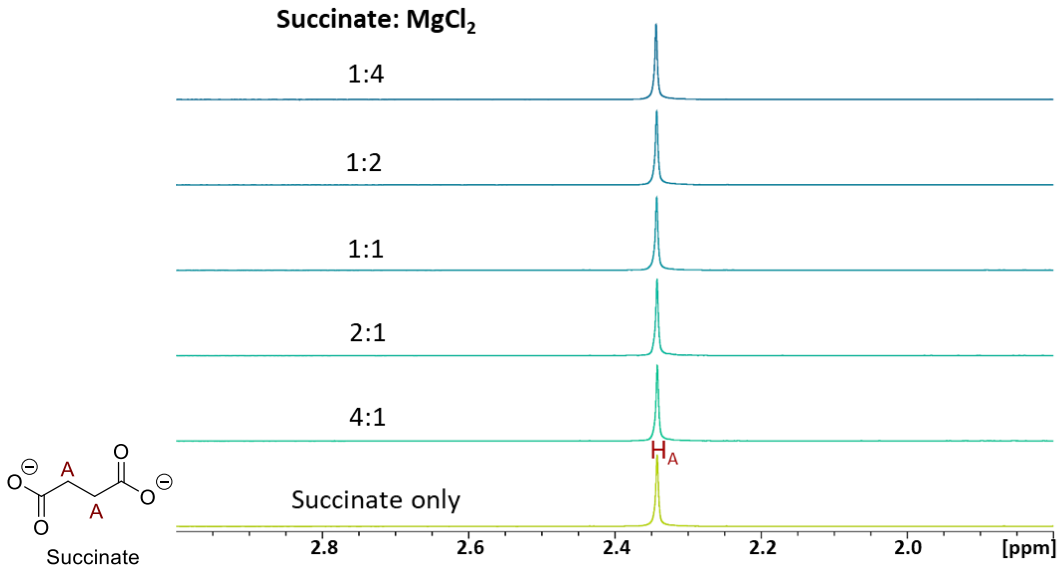



**Figure 4.20**. $^{1}H$ NMR (600 MHz) spectra of succinate with $MgCl_2$ in $D_2O$. The succinate concentration is fixed at 1 mM whilst the $MgCl_2$ concentrations are increased from 0.25 mM to 4 mM with two-fold step changes.

| Succinate:$MgCl_2$ | Diffusion coefficient/ $10^{-10}$ $m^2$ $s^{-1}$ | Predicted MW | No. of $Mg^{2+}$ |
|---|---|---|---|
| Succinate only | 6.56 | 129 | 0 |
| 4:1 | 6.56 | 129 | 0 |
| 2:1 | 6.45 | 134 | 0.2 |
| 1:1 | 6.45 | 134 | 0.2 |
| 1:2 | 6.33 | 139 | 0.4 |
| 1:4 | 6.21 | 145 | 0.7 |

**Table 4.10**. Predicted MWs from diffusion coefficients measured by DOSY, from samples of succinate and $MgCl_2$ at different ratios in $D_2O$ at 298 K. The number of $Mg^{2+}$ ions coordinated to succinate can be estimated by (MW calculated for the specific succinate:$MgCl_2$ ratio – MW calculated for succinate only) / MW of $Mg^{2+}$.

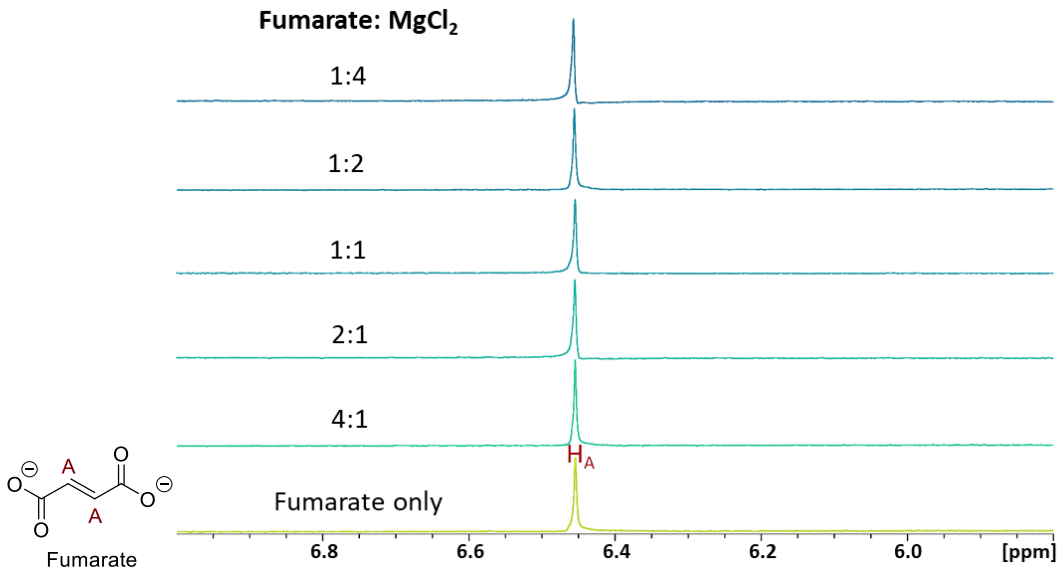



**Figure 4.21**. $^{1}$H NMR (600 MHz) spectra of fumarate with $MgCl_2$ in $D_2O$. The fumarate concentration is fixed at 1 mM whilst the $MgCl_2$ concentrations are increased from 0.25 mM to 4 mM with two-fold step changes.

| Fumarate:$MgCl_2$ | Diffusion coefficient/ $10^{-10}$ $m^2$ $s^{-1}$ | Predicted MW | No. of $Mg^{2+}$ |
|---|---|---|---|
| Fumarate only | 6.80 | 120 | 0 |
| 4:1 | 6.80 | 120 | 0 |
| 2:1 | 6.69 | 124 | 0.2 |
| 1:1 | 6.68 | 124 | 0.2 |
| 1:2 | 6.56 | 129 | 0.4 |
| 1:4 | 6.33 | 139 | 0.8 |

**Table 4.11**. Predicted MWs from diffusion coefficients measured by DOSY, from samples of fumarate and $MgCl_2$ at different ratios in $D_2O$ at 298 K. The number of $Mg^{2+}$ ions coordinated to fumarate can be estimated by (MW calculated for the specific fumarate:$MgCl_2$ ratio – MW calculated for fumarate only) / MW of $Mg^{2+}$.

Mixtures of isocitrate, citrate, 2OG and 2HG were then prepared with different concentrations of $MgCl_2$, in order to investigate whether $Mg^{2+}$ selectively coordinates to isocitrate and citrate in the presence of other metabolites. However, peaks of these species overlap on the $^{1}$H spectrum, resulting in less accurate diffusion coefficients. Further optimisation on the DOSY experiments of mixtures is required.

## 4.5 Variable temperature studies on the isocitrate-$Mg^{2+}$ complex

The effects of temperature on $Mg^{2+}$ coordination to isocitrate were then investigated by $^{1}H$ NMR spectroscopy. The temperature was varied from 278 K to 318 K in intervals of 10 K. Convection increases with temperature, leading to higher diffusion coefficients observed for both the DL-isocitrate and DL-isocitrate:$Mg^{2+}$ complexes (**Table 4.12**). The effects of convection are partially normalised by SEGWE, through changing its temperature parameter. An additional measure to normalise the effects of convection is to conduct two experiments, using samples of 1 mM DL-isocitrate with or without $MgCl_2$ at a given temperature, and calculate the difference in their MWs. For the sample containing DL-isocitrate only, all the proton peaks move to the lower field (leftward shift) as the temperature is increased (**Figure 4.22**), but their coupling patterns were unchanged. For the sample containing equimolar DL-isocitrate and $MgCl_2$, broader peaks were observed at lower temperatures *i.e.* 278 K and 288 K, likely due to slow exchange between $Mg^{2+}$ and isocitrate. At a higher temperature *e.g.* 318 K, the coupling pattern resembles that of DL-isocitrate:$MgCl_2$= 1:2 at 298 K (**Figure 4.2**), suggesting increased $Mg^{2+}$ coordination to isocitrate at higher temperature (318 K). This is confirmed by the MW calculation (**Table 4.12**) where approximately 1.5 $Mg^{2+}$ ion coordinates to one molecule of DL-isocitrate. Dissociation of the carboxyl groups of isocitrate to give $COO^{-}$ and $H^{+}$ likely increases with temperature, as more energy is present to overcome the strong O-H bond. Additionally, dissociation of the hydration shell surrounding $Mg^{2+}$ may also increase with temperature. The increased availability of $COO^{-}$ and less solvated $Mg^{2+}$ may have enhanced $Mg^{2+}$ coordination to isocitrate at higher temperatures. More robust validation is needed, for example, by expanding the dataset in SEGWE to provide more accurate MW prediction at different temperatures.

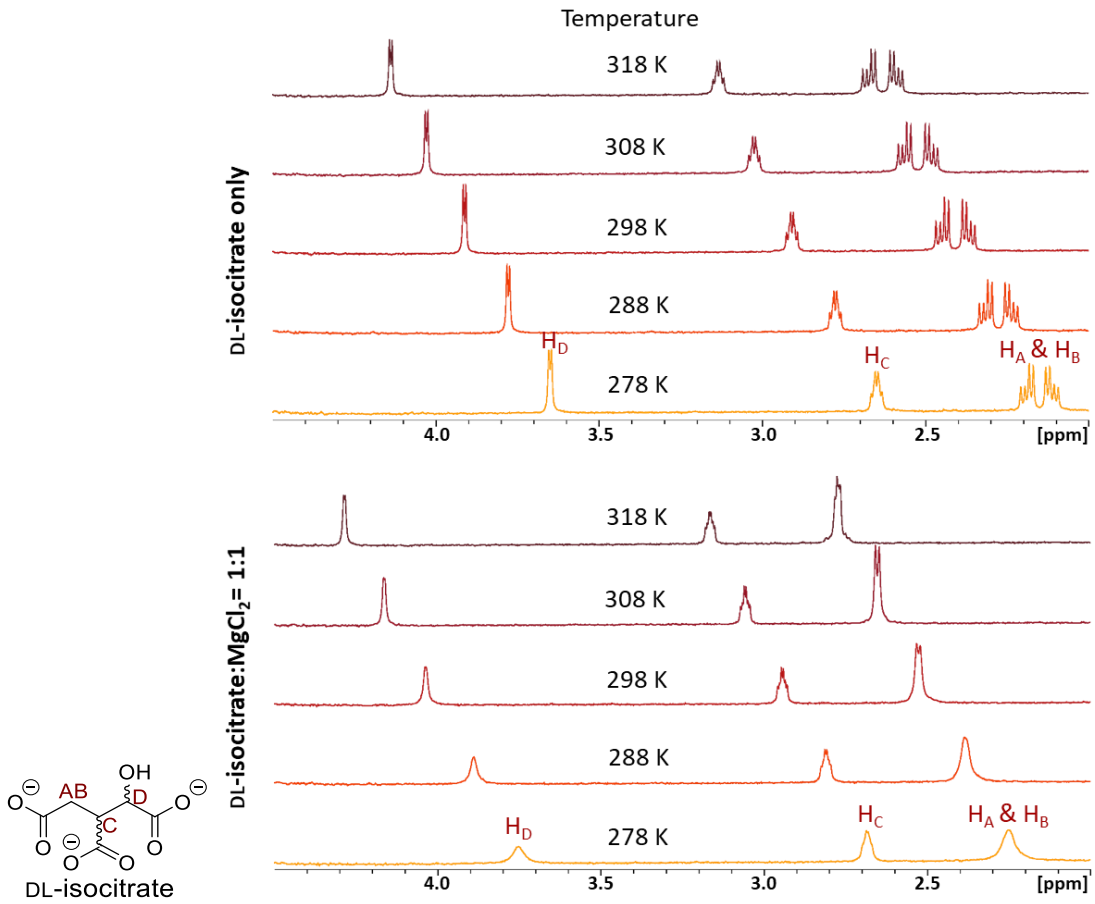



**Figure 4.22**. $^{1}$H NMR (600 MHz) spectra of 1 mM DL-isocitrate with or without 1 mM $MgCl_2$ in $D_2O$ at different temperatures 278–318 K.

| T/K | Diffusion coefficient/ $10^{-10}$ $m^2$ $s^{-1}$ | | Predicted MW | | No. of $Mg^{2+}$ |
|---|---|---|---|---|---|
| | DL-isocitrate only | DL-isocitrate:$MgCl_2$ =1:1 | DL-isocitrate only | DL-isocitrate:$MgCl_2$ =1:1 | |
| 278 | 2.81 | 2.70 | 205 | 225 | 0.8 |
| 288 | 3.98 | 3.75 | 195 | 223 | 1.2 |
| 298 | 5.39 | 5.16 | 196 | 217 | 0.9 |
| 308 | 7.03 | 6.56 | 206 | 240 | 1.4 |
| 318 | 8.90 | 8.32 | 222 | 258 | 1.5 |

**Table 4.12**. Predicted MWs from diffusion coefficients measured by DOSY, from a sample of 1 mM DL-isocitrate:$MgCl_2$= 1:1 at different temperatures 278–318 K. The number of $Mg^{2+}$ ions coordinated to DL-isocitrate can be estimated by (MW calculated for DL-isocitrate:$MgCl_2$= 1:1 – MW calculated for DL-isocitrate only) / MW of $Mg^{2+}$, at a particular temperature.

## 4.6 Summary

The intriguing coupling pattern change of isocitrate in the presence of $MgCl_2$ prompted investigations on the structure of isocitrate-$Mg^{2+}$ complex in the solution state, which is more physiologically relevant than solid-state crystal structures. Recent advances in MW prediction by DOSY NMR experiments enabled a series of experiments on metabolite-metal ion complexes. The proposed structure of one $Mg^{2+}$ ion coordinating to one molecule of isocitrate through its three carboxyl groups is consistent with results from $^{1}H$ and $^{13}C$ NMR spectroscopy, NOESY and DOSY, when $Mg^{2+}$ and isocitrate are present in equimolar ratio. The results from $^{1}H$ NMR spectroscopy and DOSY show that the $Mg^{2+}$ coordination does not distinguish between the enantiomers of isocitrate. Compared to $Mg^{2+}$, isocitrate is more weakly coordinated by $Ca^{2+}$, consistent with the $K_D$ measurements between metal ions and isocitrate by ITC in **Chapter 3**. Citrate behaves similarly to isocitrate in terms of metal ion coordination. However, 2OG, 2HG, fumarate and succinate are more weakly coordinated to $Mg^{2+}$ compared to isocitrate and citrate, suggesting that the three carboxyl groups of isocitrate or citrate are important for metal coordination. Variable temperature studies suggest that $Mg^{2+}$ coordination to isocitrate increases with temperature. Importantly, the results in this chapter provided new information on the small molecule-metal complex distinct from the published X-ray crystal structures that mostly suggested two ligands surrounding one metal ion.

# CHAPTER 5. INHIBITOR PROFILING OF IDH1

Multiple drug discovery campaigns targeting IDH1 and IDH2 variants have been initiated[6] following the identification of IDH1 mutations in glioblastoma by genomic sequencing in 2008[24]. These have led to inhibitors which now are either in use or under clinical development. Historically, it is more likely for enzyme inhibitors to bind competitively at the same site as the endogenous ligand, as supported by a review of 85 drugs approved by FDA between 2001 and 2004, where 80% of the drugs are active site binding substrate competitor[221]. However, the most potent ($IC_{50}$< 100 nM) R132H IDH1 inhibitors *e.g.* BAY-1436032 (Bayer), GSK321 (GSK), IDH305 (Novartis) and ML309 (Agios) as yielded from various high-throughput screens and subsequent optimisation to date, are all allosteric inhibitors not binding at the active site[118,169,172,176,213]; this is despite the structural diversity amongst these inhibitors. Ivosidenib and Enasidenib, which target mutant IDH1 and IDH2 respectively, have been FDA-approved for the treatment of AML within the last two years[109,110]. Unfortunately, drug resistance to them has emerged[140], potentially compromising the long-term efficacy of similar IDH mutant inhibitors. Although the majority of inhibitors demonstrated activities as described in their respective reports, there has been only one side-by-side biochemical comparison of the inhibition of mutant forms of IDH1 (mIDH1)[173], which was published during the course of my work. To characterise mIDH inhibitors in detail and compare inhibitors of mIDH1 and mIDH2, various biochemical and biophysical studies were employed to validate and supplement current literature data, and to study inhibitors binding to wt IDH1 and R132H IDH1. The results provide clues to the inhibition mechanism of IDH1 by the allosteric inhibitors and give useful information for the design of better therapeutics to treat IDH malignancies.

## 5.1 Biochemical characterisation of inhibitors of IDH variants

The inhibitory activities of eleven mIDH1 inhibitors, two mIDH2 inhibitors and one pan-mIDH1/2 inhibitor (**Figures 5.1**) was characterised using recombinant wt IDH1 and R132H IDH1. Ivosidenib (AG-120)[113], AGI-5198[138], Agios135[183] and ML309[236] were all developed by Agios and share a phenyl-glycine scaffold. Ivosidenib is FDA approved for the treatment of AML[109]. Novartis 224 and Novartis 556 are analogues of the clinical

candidate IDH305[176] developed by Novartis and have a pyrimidin-5-yl-oxazolidine-2-one scaffold. EVO894 was a generous gift from a collaborator, Evotec (Abingdon, UK), and shares a similar scaffold as the Novartis series, replacing pyrimidine with pyrrolopyrimidine. GSK864 (GSK) is similar to GSK321, but has better pharmacokinetic properties[169]. BAY-1436032[118], Sanofi 1[183] and SYC-435[237] provide additional distinct scaffolds to the set of mIDH1 inhibitors investigated in this work. mIDH2 inhibitors include AGI-6780[139] and Enasidenib (AG-221)[179]; the latter being notably the first mutant IDH inhibitor approved for the treatment of AML by FDA[110]. Lastly, Vorasidenib (AG-881) is the only reported inhibitor that targets both mIDH1 and mIDH2[114]. Several inhibitors were not commercially available at the time this work was undertaken, including FT-2102 (Forma)[238], IDH305 (Novartis, **Table 1.2**) and IDH889 (Novartis)[176].

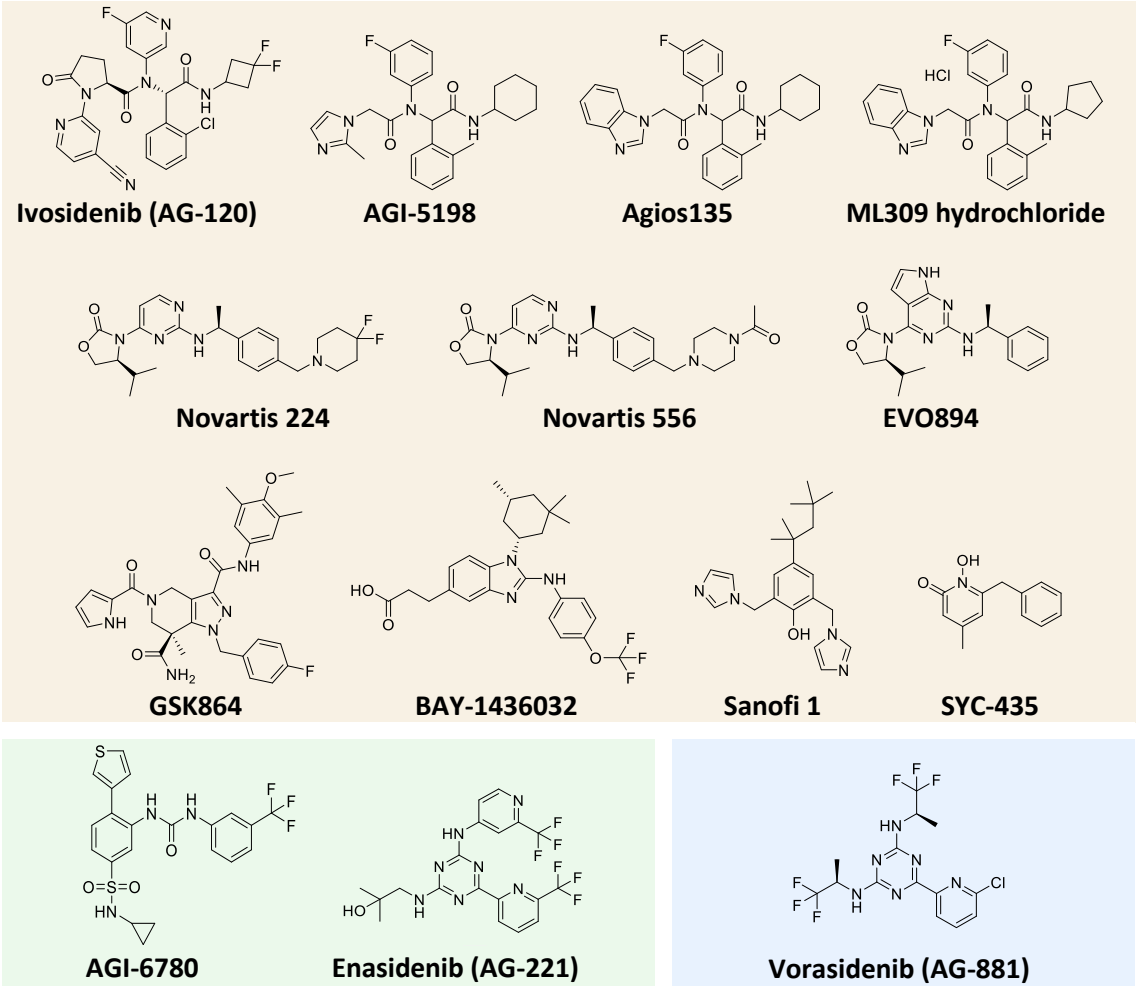



**Figure 5.1**. mIDH1 inhibitors (shaded in beige), mIDH2 inhibitors (shaded in green) and pan-mIDH1 and mIDH2 inhibitor (shaded in blue) used in this work.

### 5.1.1 Absorbance-based assays

Enzymatic activity was assessed by measuring the change in the absorbance of NADPH at 340 nm, using the standard assay conditions described in **Section 2.1**. The results for the inhibition of wt IDH1- and R132H IDH1- catalysed oxidative and reductive reactions by mIDH inhibitors are presented in **Figure 5.2**. **Figure 5.2D** shows the relative inhibition of the R132H IDH1 catalysed conversion of 2OG to 2HG. All mIDH1 inhibitors (tested at 25× the enzyme concentration) inhibit R132H IDH1 almost fully, except for Sanofi 1 which has 75% inhibition of R132H IDH1 and SYC-435 which does not inhibit R132H IDH1. Sanofi 1 was first reported with an $IC_{50}$ of 13 nM[183], but was later reported with a higher $IC_{50}$ of >13 µM by another group[173]; the latter value agrees better with my results. SYC-435 has a reported $IC_{50}$ of 190 nM against R132H IDH1[237] but demonstrates weak activity ($IC_{50}$ >10 µM) here. The pan-mIDH1 and mIDH2 inhibitor, Vorasidenib, shows 73% inhibition of R132H IDH1, *i.e.* it is less potent than most of the mIDH1 inhibitors tested. The mIDH2 inhibitors, AGI-6780 and Enasidenib, are not very selective for the mIDH2 isoform, as they show 32% and 21% inhibition of R132H IDH1, respectively. This suboptimal selectivity is expected given the reported $IC_{50}$ values of 11 µM[139] for AGI-6780 and 4.95/48/78 µM[114,179] for Enasidenib against R132H IDH1.

The inhibitors with >50% inhibition on R132H IDH1 catalysed conversion of 2OG to 2HG were further tested for their $IC_{50}$ values to compare their potency against R132H IDH1. For $IC_{50}$ determinations, the R132H IDH1 enzyme concentration in the absorbance-based assay was decreased from 400 nM to 30 nM to lower the measurement limit thereby giving more accurate $IC_{50}$ values. **Table 5.1** shows reported $IC_{50}$ values of mIDH inhibitors against R132H IDH1, as well as the $IC_{50}$ values measured in this work. The most potent inhibitors against R132H IDH1 are Ivosidenib ($IC_{50}$= 4.9 nM) and Novartis 224 ($IC_{50}$= 8.2 nM). This is consistent with the rank order by Urban *et al*. which generally gave higher $IC_{50}$ values, likely due to high enzyme concentrations used in the biochemical assays[173]. BAY-1436032, Agios135, GSK864, Vorasidenib and Novartis 556 are also potent with $IC_{50}$ values of ~20 nM, in close agreement with the reported values (**Table 5.1**). Notably, Vorasidenib did not show full inhibition when tested for the percentage inhibition of R132H IDH1 at 10 µM. A closer examination at the its $IC_{50}$ results (**Figure S5.1**) reveals that Vorasidenib inhibits R132H IDH1 to a maximum of ~75% and the graph

plateaus above ~400 nM of Vorasidenib. Sanofi 1, as expected from results in **Figure 5.2D**, displays a weak activity against R132H IDH1 ($IC_{50}$= 4.5 µM), consistent with the results of Urban *et al*.[173]

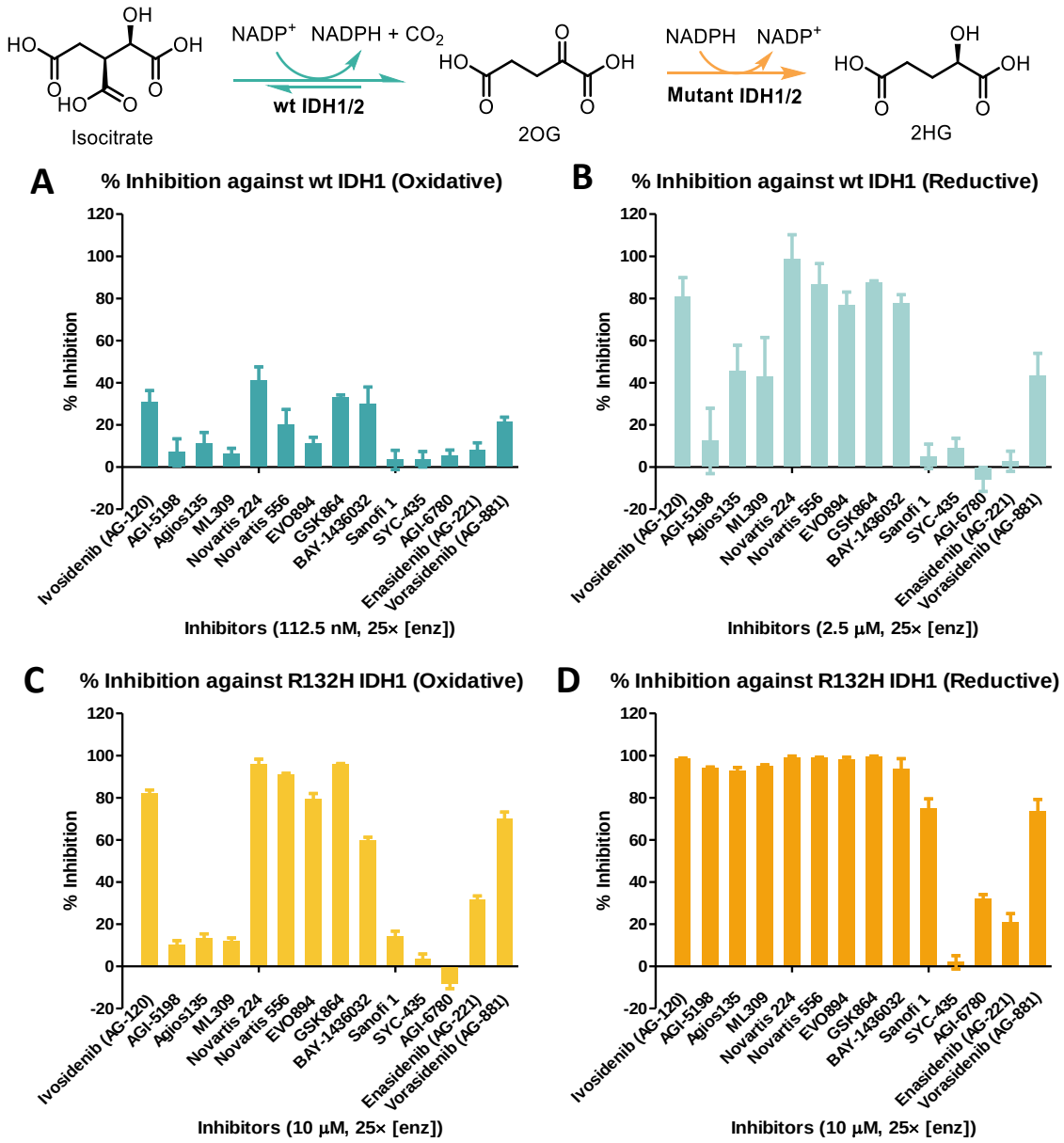



**Figure 5.2**. Inhibition of wt IDH1 and R132H IDH1 catalysed reactions by mIDH1 and mIDH2 inhibitors, as measured by absorbance-based assays. Data are mean ± SD, n= 3 technical replicates. The % inhibition is calculated by (1 – activity of (treated/DMSO control)) × 100%. See Experimental Methods: Biochemical assays for general assay conditions. The compounds were tested at 25× the enzyme concentrations used in the respective reactions. (**A**) The % inhibition of wt IDH1 catalysed conversion of isocitrate to 2OG. (**B**) The % inhibition of wt IDH1 catalysed conversion of 2OG to isocitrate. (**C**) The % inhibition of R132H IDH1 catalysed conversion of isocitrate to 2OG. (**D**) The % inhibition of R132H IDH1 catalysed conversion of 2OG to 2HG.

| | R132H IDH1 Inhibitors | $IC_{50}$/nM (reported) | $IC_{50}$/ nM (measured) |
|---|---|---|---|
| 1 | Ivosidenib (AG-120) | 12[113]; 40[173] | 4.9 ± 0.3 |
| 2 | Novartis 224 | 17[239]; 130[173] | 8.2 ± 0.7 |
| 3 | BAY-1436032 | 15[118] | 18 ± 2 |
| 4 | Agios135 | 42[183]; 380[173] | 18 ± 1 |
| 5 | GSK864 | 15[169]; 160[173] | 20 ± 1 |
| 6 | Vorasidenib (AG-881) | 6[114] | 21 ± 2 |
| 7 | Novartis 556 | <72[239]; 140[173] | 25 ± 1 |
| 8 | EVO894 | NA | 29 ± 2 |
| 9 | AGI-5198 | 70[138]; 390[173] | 61 ± 5 |
| 10 | ML309 HCl | 68[236]; 340[173] | 73 ± 6 |
| 11 | Sanofi 1 | 13[183]; 13.4 × $10^3$ [173] | (4.5 ± 1.5) × $10^3$ |

**Table 5.1**. Reported and measured $IC_{50}$ values of selected mIDH inhibitors (>50% inhibition when tested at 10 μM) against R132H IDH1. Measured $IC_{50}$ values are mean ± SD from three technical replicates. $IC_{50}$ graphs are presented in **Figure S5.1**.

A comparison between the relative inhibition of R132H IDH1 catalysed conversion of 2OG to 2HG (**Figure 5.2D**) and that of wt IDH1 catalysed conversion of isocitrate to 2OG (**Figure 5.2A**) provided information on the wt/mutant selectivity of mIDH inhibitors. Ivosidenib, Novartis 224, GSK864 and BAY-1436032 exhibit ≥30% inhibition of the wt IDH1 catalysed reaction, suggesting that they are not very selective for the IDH1 mutants. Poor wt/mutant selectivity of Ivosidenib and GSK864 have been reported with 30-fold[169] and 6-fold[113] differences, respectively, in the $IC_{50}$ values between wt IDH1 and R132H IDH1. BAY-1436032 has been reported with a 1300-fold difference in the $IC_{50}$ values against wt IDH1 and R132H IDH1[118], but this work shows that it may not be as selective.

**Figure 5.2B** shows the relative inhibition of mIDH inhibitors on the reverse reaction of wt IDH1, *i.e.* wt IDH1 catalysed conversion of 2OG to isocitrate. The observed inhibition trend resembles a cross between the forward reactions of wt IDH1 (**Figure 5.2A**) and R132H IDH1 (**Figure 5.2D**). In this reaction, wt IDH1 uses 2OG which is a substrate for IDH1 variant, so it is conceivable that wt IDH1 may adopt a conformation somewhere between wt forward reaction and mutant forward reaction.

**Figure 5.2C** shows the relative inhibition of mIDH inhibitors on the R132H IDH1 catalysed conversion of isocitrate to 2OG. Interestingly, AGI-5198, Agios135 and ML309 HCl display low inhibition on this reaction. As shown in **Figure 2.1**, any 2OG produced is further reduced by R132H IDH1 to 2HG. As two reactions *i.e.* isocitrate to 2OG and 2OG

to 2HG are intimately coupled, it is more complex to isolate and analyse the inhibition effects at play.

### 5.1.2 NMR reaction monitoring

To ascertain that the change in NADPH levels measured in the absorbance-based assays reflects activity of R132H IDH1, $^{1}$H NMR (700 MHz) spectroscopy was employed to monitor the inhibition of R132H IDH1 catalysed conversion of 2OG to 2HG by mIDH inhibitors (**Figure 5.3**). For all the inhibition experiments, the change in NADPH levels was coupled to the changes in other reactants (2OG) and products (2HG and $NADP^{+}$). AG-120, Novartis 224, GSK864, BAY-1436032 (all used at 20× molar excess of enzyme concentration) fully inhibited R132H IDH1 continuously over ~2.5 hr. AGI-5198 inhibits R132H IDH1 to a lesser extent, which can be explained by its higher $IC_{50}$ value (61 nM). Vorasidenib, despite having a low $IC_{50}$ value (20 nM), is the weakest inhibitor among all the inhibitors tested by NMR spectroscopy. As mentioned above, Vorasidenib cannot reach 100% inhibition of R132H IDH1 in biochemical assays, possibly explaining its lower than expected potency against R132H IDH1 as observed by NMR spectroscopy.

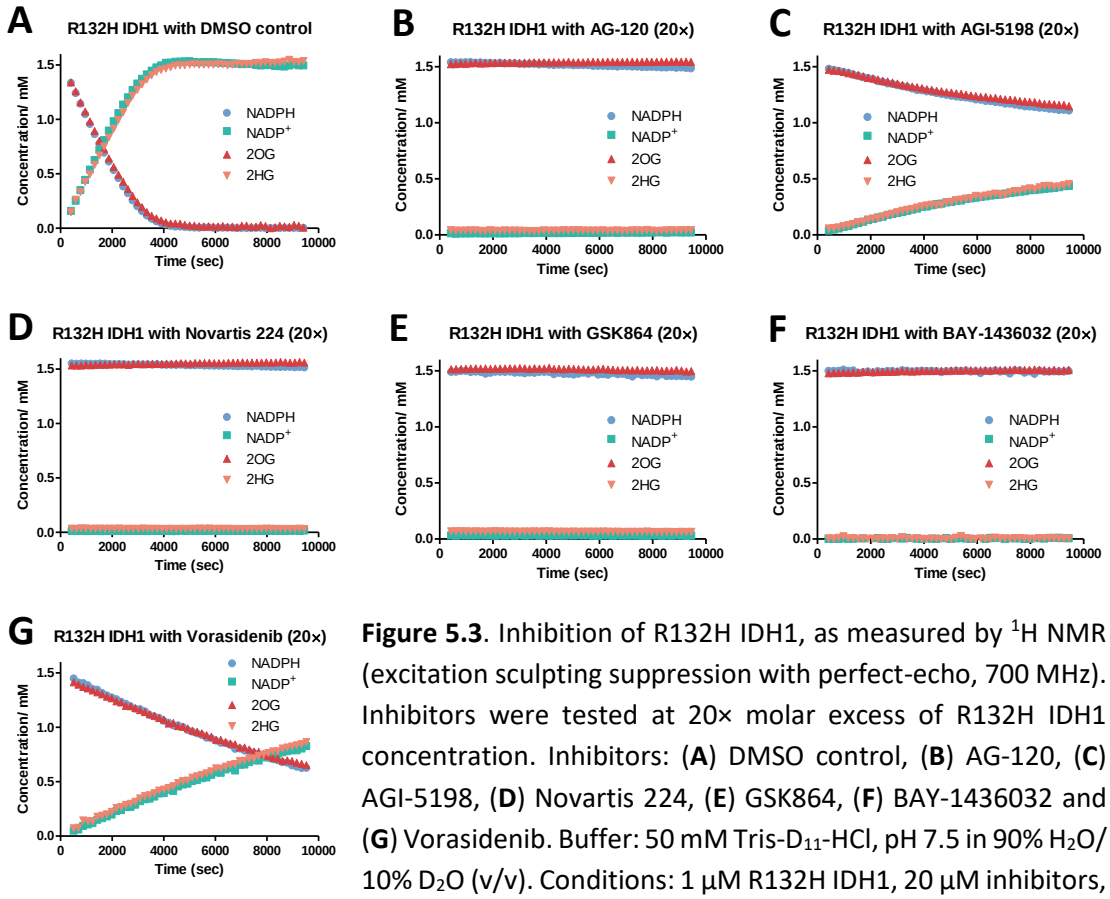



**Figure 5.3**. Inhibition of R132H IDH1, as measured by $^{1}$H NMR (excitation sculpting suppression with perfect-echo, 700 MHz). Inhibitors were tested at 20× molar excess of R132H IDH1 concentration. Inhibitors: (**A**) DMSO control, (**B**) AG-120, (**C**) AGI-5198, (**D**) Novartis 224, (**E**) GSK864, (**F**) BAY-1436032 and (**G**) Vorasidenib. Buffer: 50 mM Tris-$D_{11}$-HCl, pH 7.5 in 90% $H_2O$/ 10% $D_2O$ (v/v). Conditions: 1 µM R132H IDH1, 20 µM inhibitors, 1.5 mM 2OG, 1.5 mM NADPH and 10 mM $MgCl_2$.

## 5.2 Biophysical characterisation of inhibitors of IDH variants

The binding affinities of the reported mIDH inhibitors to IDH and its variants have not been previously determined. The following sections describe efforts towards studying and comparing the binding properties of mIDH inhibitors to wt IDH1 and R132H IDH1 with complementary biophysical techniques: DSF, ITC, CD, non-denaturing MS and NMR.

### 5.2.1 DSF analyses on IDH inhibition

DSF was used to investigate the thermal stabilisation of wt IDH1 or R132H IDH1 by the addition of inhibitors. The degree of thermal stabilisation can qualitatively reflect binding affinity of an inhibitor for a protein. Various concentrations of inhibitors from 3.125 to 100 µM were tested against wt IDH1 and R132H IDH1 (**Figure 5.4)**. The degree of thermal stabilisation of R132H IDH1 by the mIDH inhibitors approximately correlates with their inhibitory potency as measured by absorbance-based assays (**Table 5.1**). Inhibitors with nanomolar $IC_{50}$ values, including Novartis 224 ($\Delta T_m$= 11.7 °C), EVO894 ($\Delta T_m$= 11.5 °C), BAY-1436032 ($\Delta T_m$= 9.9 °C) and Ivosidenib ($\Delta T_m$= 8.5 °C), gave the strongest thermal stabilisation with R132H IDH1. mIDH1 inhibitors with high micromolar $IC_{50}$ values (Sanofi 1 and SYC-435), as well as IDH2 inhibitors (AGI-6780 and Enasidenib), do not stabilise R132H IDH1 significantly ($\Delta T_m$< 2 °C). Interestingly, although these mIDH inhibitors are at least partially mutant selective based on the turnover results (**Figure 5.2**), they stabilise wt IDH1 to a similar degree as R132H IDH1. To my knowledge, this is the first biophysical evidence that mIDH inhibitors appear to be non-selective with respect to binding to wt IDH1 and R132H IDH1.

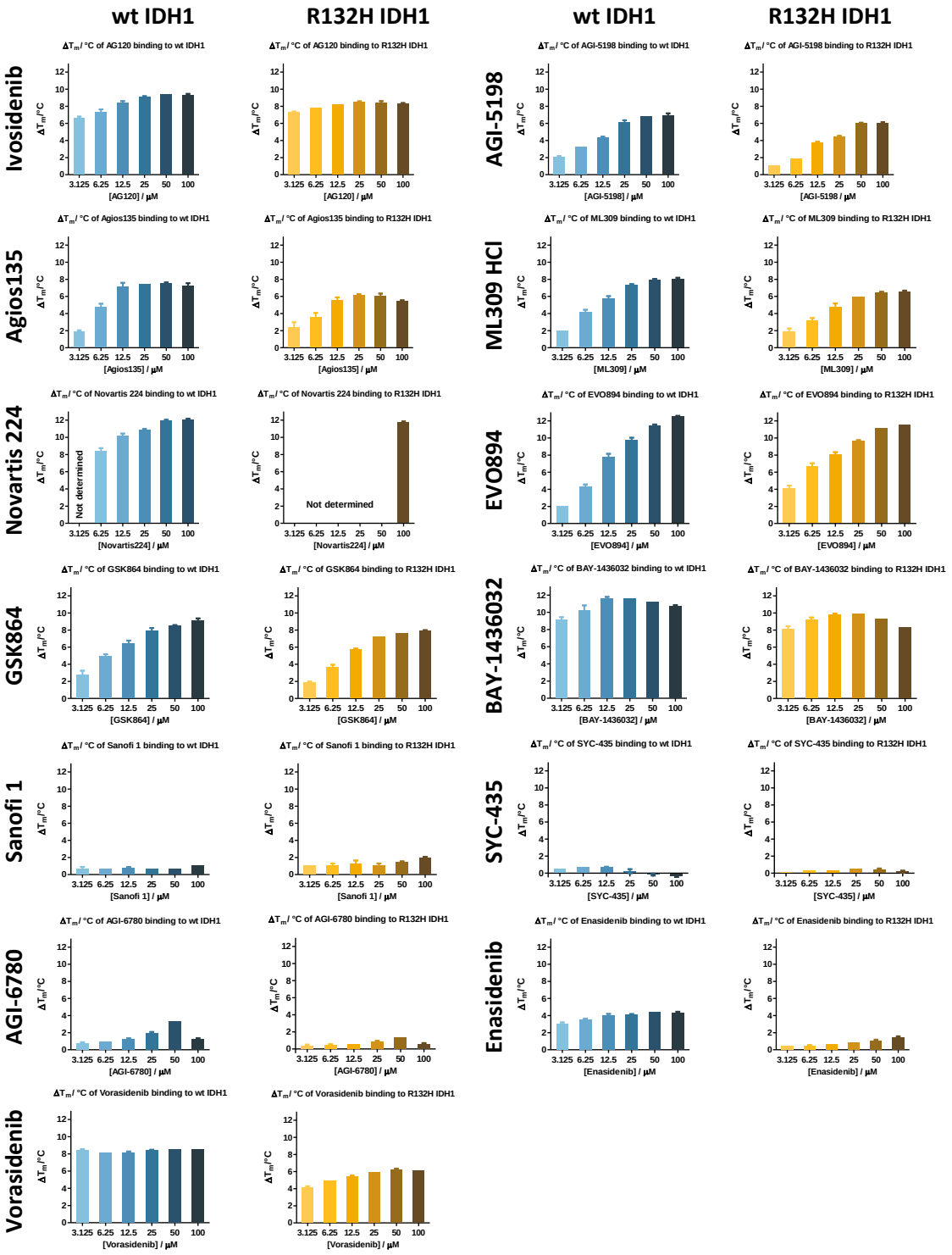



**Figure 5.4**. Dose-dependent thermal stabilisation of wt IDH1 (blue gradient) and R132H IDH1 (orange gradient) by reported mIDH inhibitors (3.125–100 µM), in 50 mM Tris-HCl, pH 7.5, as measured by DSF. Data are mean ± SD, n= 3 technical replicates. "Not determined": Novartis 224 and Novartis 556 interfere with the fluorescence signals, and hence partial or no results are presented respectively.

It should be noted that binding does not always correlate with inhibition. In this case, the discrepancy may also be a result of binding studies utilising apo-protein that is

deprived of (co)substrates. On the other hand, inhibition is often a dynamic process, in the case of IDHs involving the interplay of inhibitors and (co)substrates of IDH1; the interpretation of results is further complicated by the dimeric nature of IDHs. It has been suggested that while mIDH1 inhibitors can potentially bind to the same allosteric pockets of wt IDH1 and R132H IDH1, the wt/mutant selectivity of mIDH1 inhibitors arises from the greater stability of the regulatory segment (residues 271–286) in wt IDH1 than in R132H IDH1, particularly at physiological (cellular) $Mg^{2+}$ concentrations (~$10^2$-$10^3$× higher than the $K_M$ of $MgCl_2$ for wt IDH1, **Chapter 3**)[213]. The stable regulatory segment restricts the access of the inhibitor to the allosteric pocket in wt IDH1. As no difference was observed in the binding affinity of mIDH1 inhibitors to wt IDH1 and R132H IDH1 with or without $Mg^{2+}$ (**Chapter 3**), it was proposed that the inhibitor selectivity may not be due to only $Mg^{2+}$, but the substrate-$Mg^{2+}$ complex. Further experiments could be designed to mimic the conditions of the inhibition process by incorporating catalytically inactive substrate-metal ion complexes in the binding studies.

### 5.2.2 ITC analyses on IDH inhibition

ITC studies were then conducted to investigate the binding affinity of mIDH inhibitors to wt IDH1 and R132H IDH1. Eight inhibitors were tested, namely Ivosidenib, AGI-5198, Novartis 224, GSK864, BAY-1436032, Sanofi 1, Vorasidenib and Enasidenib. As expected, ITC showed no evidence for binding of Enansidenib, a mIDH2 inhibitor, to both wt IDH1 and R132H IDH1 (**Figure S5.2**). Surprisingly, no binding to wt IDH1 or R132H IDH1 was also observed for all other mIDH1 and pan-mIDH1/2 inhibitors (**Figure S5.2**), except for Ivosidenib which has the lowest $IC_{50}$ value (4.9 nM) of all mIDH inhibitors tested (**Table 5.1**). Other mIDH1 inhibitors may not be sufficiently potent in causing detectable heat changes during binding to IDH1. **Figure 5.5** shows that Ivosdenib binds to wt IDH1 and R132H IDH1 with similar nanomolar binding affinity of 416 nM and 488 nM respectively. This is consistent with the DSF results where mIDH1 inhibitors stabilise wt IDH1 and R132H IDH1 to a similar degree (**Section 5.2.1**). ITC analyses also provided the binding stoichiometry of Ivosidenib with respect to protein, N= 0.52 and 0.37 to wt IDH1 and R132H IDH1 respectively. This suggests that approximately one molecule of Ivosidenib binds to a protein dimer, which is consistent with the observations from non-denaturing MS studies (**Section 3.4.1**).

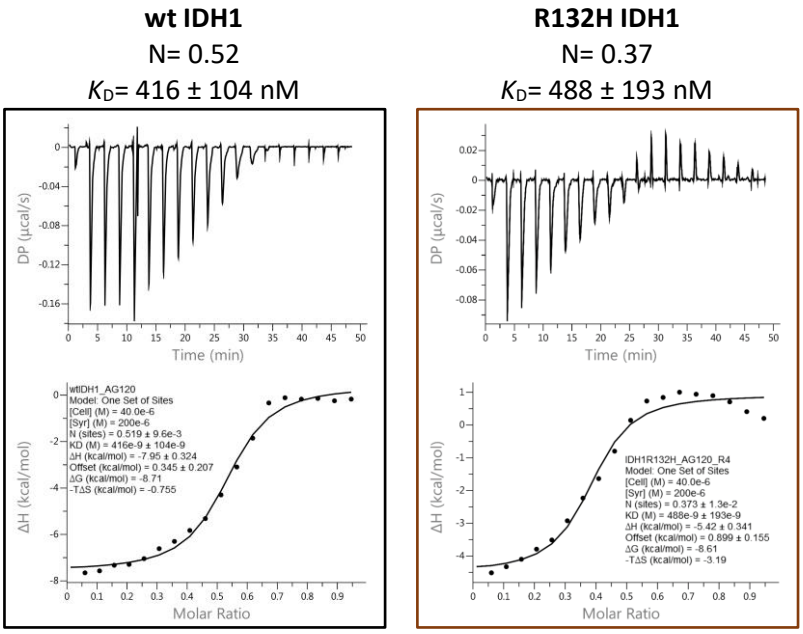



**Figure 5.5**. ITC analysis of Ivosidenib (200 µM) titrated against wt IDH1 or R132H IDH1 (40 µM), in 50 mM Tris-HCl, pH 7.5. The binding of Ivosidenib to both wt IDH1 and R132H IDH1 is strong at $K_D$= 416 nM and 488 nM respectively. See Experimental Methods: Isothermal Titration Calorimetry for method details.

### 5.2.3 Non-denaturing MS analyses on IDH inhibition

As ITC is not an optimal technique to characterise the $K_D$ of mIDH inhibitors to IDH1, non-denaturing MS was subsequently employed for $K_D$ measurements. In addition, the binding stoichiometry of the inhibitors to proteins can also be determined by non-denaturing MS, which provides faster and potentially more relevant solution state results than X-ray crystallography due to the use of non-saturating and 'native' conditions. A caveat is that the non-denaturing MS conditions still do not necessarily fully reflect the solution situations.

$K_D$ values and/or the stoichiometry of binding were determined for six mIDH inhibitors, *i.e.* Ivosidenib, AGI-5198, Novartis 224, GSK864, BAY-1436032 and Vorasidenib by non-denaturing MS. For all non-denaturing MS experiments, mIDH inhibitors were prepared as 10 mM MeOH stock solutions, as MeOH is more volatile than DMSO that may solvate the protein and produce broad signals. Prior to analysis, the IDH1 protein was buffer exchanged into 200 mM ammonium acetate, pH 7.5, which is a volatile solvent and provides solvation to the protein similar to that of physiological conditions[240].

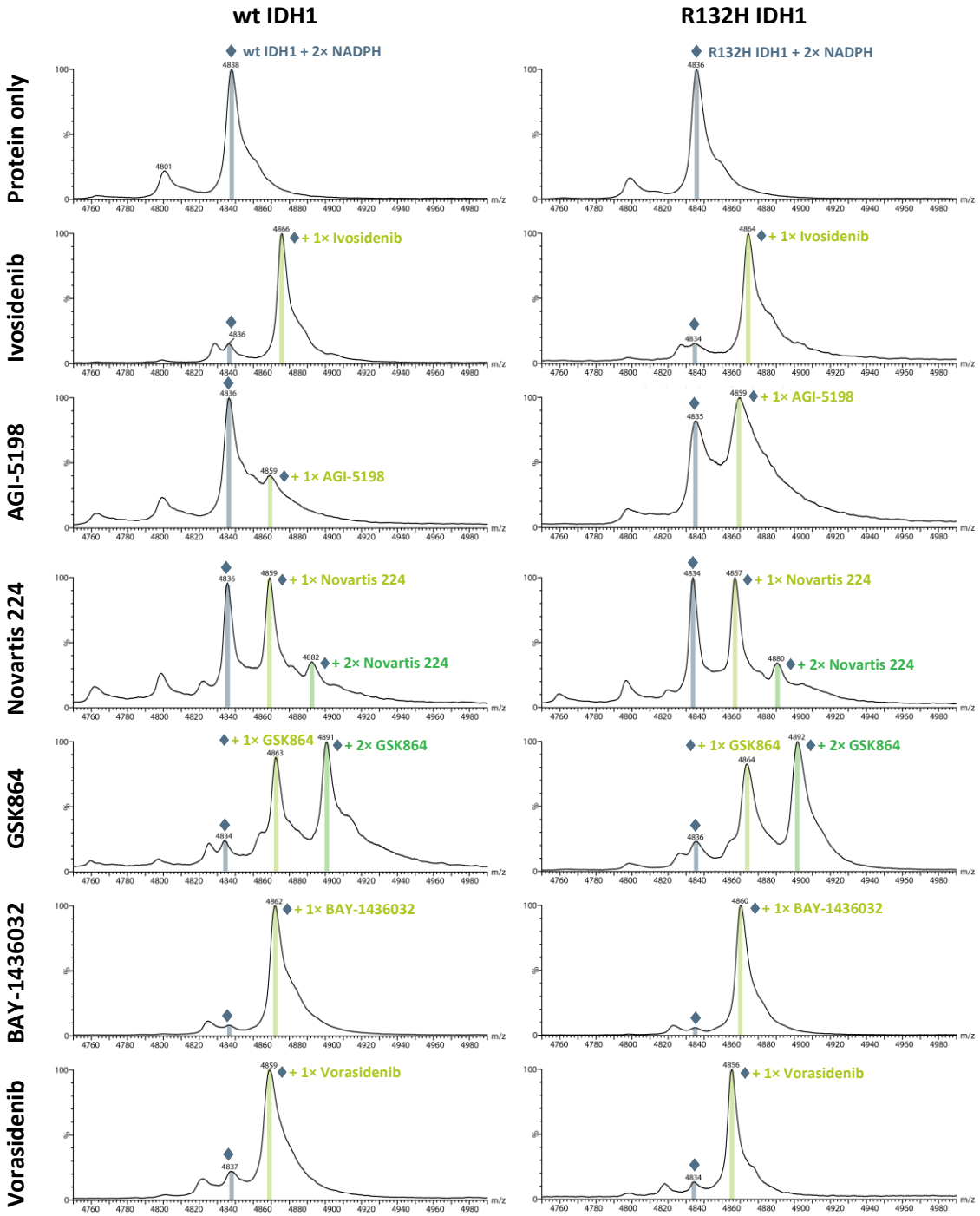



**Figure 5.6**. R132H IDH1 inhibitors binding to wt IDH1 and R132H IDH1. Mass spectrometric analysis (non-denaturing) of wt IDH1 and R132H IDH1 with or without inhibitors. Data for the m/z= $20^{+}$ charge state are shown. Cone voltage= 100 V. Buffer: 200 mM ammonium acetate, pH 7.5. R132H IDH1: inhibitor= 50 µM: 200 µM for all cases. See Experimental Methods: Protein non-denaturing MS for method details. For clarity, only 2× NADPH bound protein peaks are annotated. Ivosidenib, AGI-5198, BAY-1436032 and Vorasidenib bind to wt IDH1 and R132H IDH1 with a stoichiometry of 1 inhibitor per IDH1 dimer. Novartis 224 and GSK864 bind to wt IDH1 and R132H IDH1 with a stoichiometry of 2 inhibitors per IDH1 dimer.

The results of the non-denaturing MS analyses revealed that Ivosidenib, AGI-5198, BAY-1436032 and Vorasidenib bind to wt IDH1 and R132H IDH1 with a stoichiometry of 1 inhibitor per IDH1 dimer, whereas Novartis 224 and GSK864 bind to wt IDH1 and R132H IDH1 with the stoichiometry of 2 inhibitors per IDH1 dimer (**Figure 5.6**). The stoichiometry determined by non-denaturing MS is consistent with the observations in reported X-ray[118,169,177,178] and cryo-EM[172] structures of these inhibitors or their analogues with R132H IDH1.

**Figure 5.7** shows a set of representative non-denaturing MS spectra used to determine $K_D$ of Ivosidenib for R132H IDH1. The IDH1 concentration was fixed at 50 µM that gave a good signal:noise ratio. Depending on the binding affinity and solubility of the inhibitors, the inhibitor concentrations were varied from a low concentration, *e.g.* IDH1:inhibitor= 8:1, to a high concentration, *e.g.* IDH1:inhibitor= 1:2, where no further binding was observed, or where the solubility limit of the inhibitor has been reached.

**Table 5.2** shows the $K_D$ of Ivosidenib, AGI-5198, Novartis 224 and GSK864, to wt IDH1 and R132H IDH1, as calculated by co-worker, Victor Mikhailov, using the method described by Kitova *et al*.[241] Note that due to 50 µM protein being used in non-denaturing MS experiments, the $K_D$ of the inhibitors to IDH1 has a theoretical lower limit of 12.5 µM or 25 µM, for 1 or 2 inhibitor(s) binding to an IDH1 dimer respectively, and cannot be accurately determined to nanomolar values, which are achievable by ITC (**Figure 5.5**).

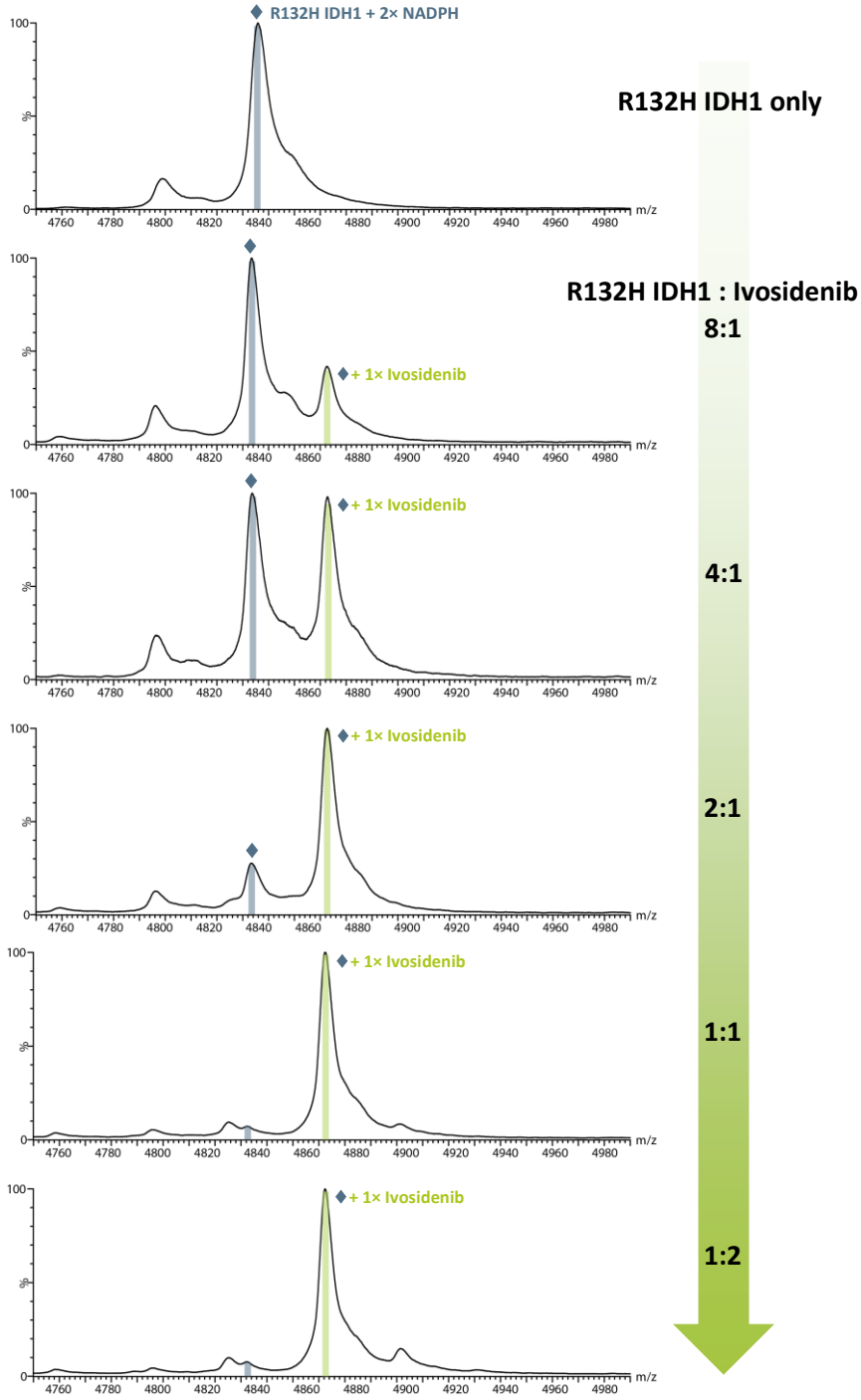



**Figure 5.7**. A series of non-denaturing MS spectra used to determine $K_D$ of Ivosidenib for R132H IDH1. Data for the m/z= $20^+$ charge state are shown. Cone voltage= 100 V. Buffer: 200 mM ammonium acetate, pH 7.5. See Experimental Methods: Protein non-denaturing MS for method details. For clarity, only 2× NADPH bound protein peaks are annotated. The R132H IDH1 concentration is fixed at 50 µM whilst the Ivosidenib concentrations are increased from 6.25 µM to 100 µM (full saturation) in two-fold step changes. The Ivosidenib-bound protein peak (green) increases in intensity relative to the protein-only peak (blue) as the Ivosidenib concentration increases. For inhibitors with a binding stoichiometry of two inhibitors per IDH1 dimer, the inhibitor-bound protein peak intensity is a sum of first and second inhibitor-bound protein peak intensities. $K_D$ at each mixture ratio was calculated using a method described by Kitova *et al*[241]. The calculated $K_D$ values were averaged to give the final $K_D$ values in **Table 5.2**.

| $K_D$/ µM | Ivosidenib | AGI-5198 | Novartis 224 | GSK864 |
|---|---|---|---|---|
| wt IDH1 | 9.7 ± 2.7 | 608 ± 68 | 140 ± 6 | 24 ± 6.0 |
| R132H IDH1 | 11 ± 5.5 | 98 ± 9 | 142 ± 18 | 23 ± 6.8 |

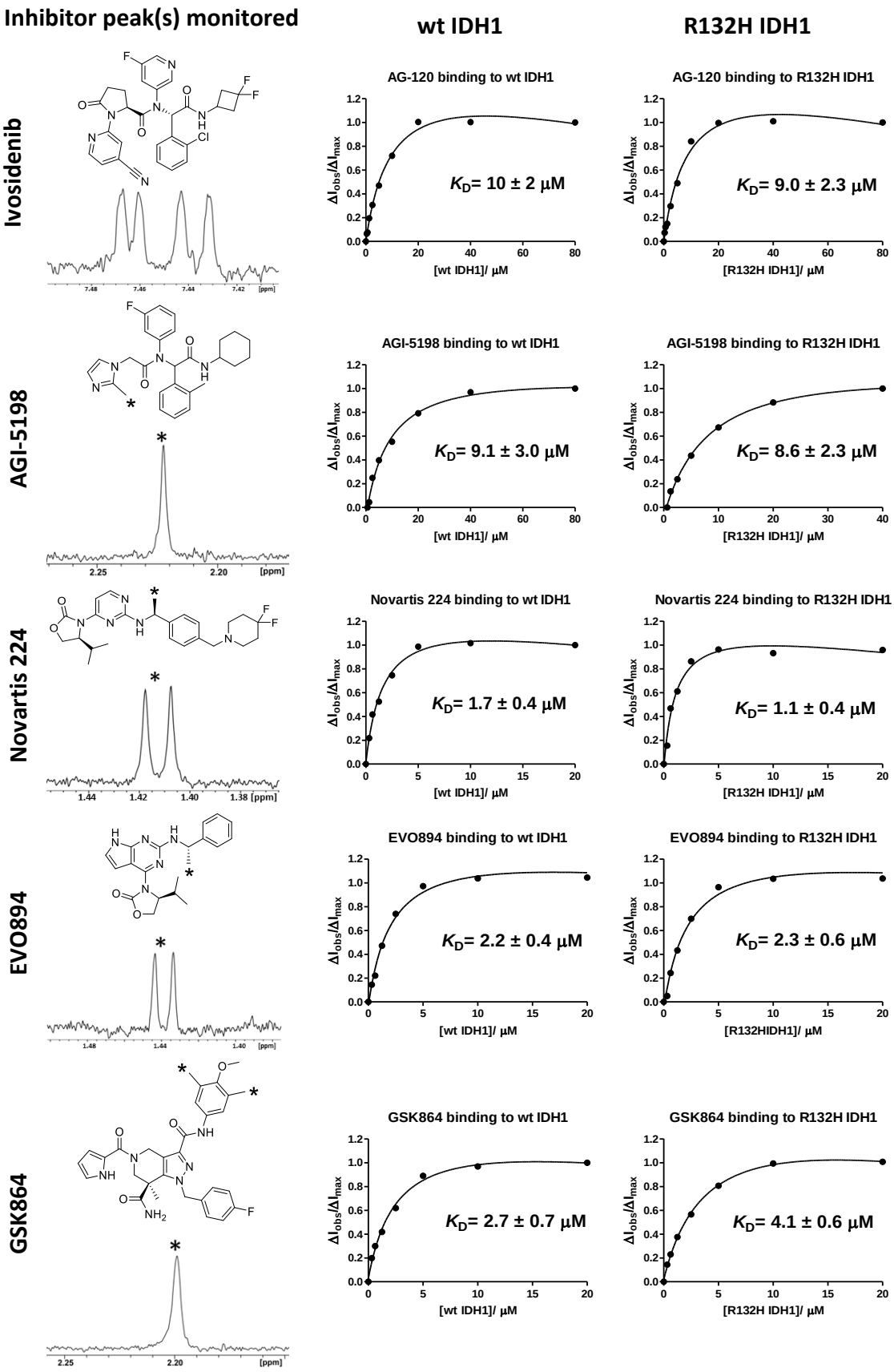
**Table 5.2**. $K_D$ of mIDH1 inhibitors determined by non-denaturing MS.

Consistent with the observations by DSF (**Section 5.2.1**) and ITC (**Section 5.2.2**), the tested mIDH1 inhibitors have similar binding affinities for wt IDH1 and R132H IDH1, except for AGI-5189 whose $K_D$ for wt IDH1 is approximately 6 times higher than that for R132H IDH1. Among those tested, Ivosidenib, the most potent inhibitor of R132H IDH1 as measured by turnover assays (**Table 5.1**), shows the lowest $K_D$ for wt IDH1 and R132H IDH1. The order of $K_D$ of Ivosidenib, AGI-5198 and GSK864, as measured by non-denaturing MS, follows that of their biochemical potencies (**Table 5.1**). It has also been shown that the addition of $MgCl_2$ does not affect the binding affinity of Ivosidenib and GSK864 to wt IDH1 and R132H IDH1 (**Figure S3.4B**). Unexpectedly, Novartis 224, which has a low $IC_{50}$ of 8.2 nM against R132H IDH1, shows a relatively high $K_D$ of 142 µM for R132H IDH1 by non-denaturing MS. Further experiments with variable cone voltages showed that binding of the second molecule of Novartis 224 to wt IDH1 or R132H IDH1, by lowering cone voltage from 100 V to 80 V, can be significantly enhanced, compared to GSK864 (data not shown). The greater sensitivity of Novartis 224 binding to IDH1 to changes in cone voltage suggests that Novartis 224 may bind less specifically or near the surface of IDH1, a phenomenon that is not reflected by X-ray crystallography to date (**Figure 3.18**)[177].

### 5.2.4 NMR Spectroscopy analyses on IDH inhibition

Each of the abovementioned biophysical techniques employed for binding affinity determination has its limitations: DSF is generally not quantitative, ITC has a high demand for protein quantity, and non-denaturing MS is inherently a non-solution technique. To address these limitations, complementary biophysical techniques are often employed. NMR spectroscopy is a solution-based technique that can be used to measure binding affinity of mIDH inhibitors to wt IDH1 and R132H IDH1. In this case, $^{1}$H NMR (700 MHz) spectroscopy was employed to observe the changes in inhibitor signal intensities, as wt IDH1 or R132H IDH1 (from 312.5 nM to ≥20 μM in two-fold step changes) was titrated into 10 μM inhibitor. Inhibitor binding to IDH1 leads to slow tumbling rate of the inhibitor and line broadening of its signals. The changes in the signal intensities of the inhibitor with protein concentrations allow the determination of $K_D$. As 10 μM inhibitor was used, $K_D$ of the inhibitors to IDH1 determined by NMR spectroscopy has a theoretical lower limit of 10 μM or 5 μM, for 1 or 2 inhibitor(s) binding to an IDH1 dimer respectively.

Consistent with the observations by DSF, ITC and non-denaturing MS, similar $K_D$ values were observed for the eight inhibitors binding to wt IDH1 and R132H IDH1 based on NMR spectroscopy (**Figure 5.8**). It was also found that the addition of $MgCl_2$ (10 mM) does not affect the binding affinity of AGI-5198 and GSK864 to wt IDH1 and R132H IDH1 (**Figure S3.4C**). The rank order of the binding affinity of mIDH inhibitors to R132H IDH1 (from the smallest to the largest $K_D$) is Novartis 224 < BAY-1436032 < EVO894 < GSK864 < Vorasidenib < AGI-5198 < Ivosidenib < Enasidenib. Novartis 224 has the highest binding affinity to wt IDH1 and R132H IDH1 as measured by NMR spectroscopy, despite a relatively high $K_D$ as determined by non-denaturing MS. This observation reveals discrepancies between gas- and solution- phase techniques, and/or protein-based versus ligand-based techniques particularly when the inhibitor:protein binding stoichiometry is not 1:1. Enasidenib has the lowest binding affinity to wt IDH1 and R132H IDH1 as it is a mIDH2 inhibitor. Ivosidenib, a strong inhibitor and binder as measured by absorbance-based assays, DSF, ITC and non-denaturing MS, unexpectedly shows relatively high $K_D$ values of 10 μM and 9 μM for wt IDH1 and R132H IDH1 respectively.


Inhibitor peak(s) monitored
wt IDH1
R132H IDH1
Ivosidenib
AG-120 binding to wt IDH1
AG-120 binding to R132H IDH1
$K_D$= 10 ± 2 μM
$K_D$= 9.0 ± 2.3 μM
AGI-5198
AGI-5198 binding to wt IDH1
AGI-5198 binding to R132H IDH1
$K_D$= 9.1 ± 3.0 μM
$K_D$= 8.6 ± 2.3 μM
Novartis 224
Novartis 224 binding to wt IDH1
Novartis 224 binding to R132H IDH1
$K_D$= 1.7 ± 0.4 μM
$K_D$= 1.1 ± 0.4 μM
EVO894
EVO894 binding to wt IDH1
EVO894 binding to R132H IDH1
$K_D$= 2.2 ± 0.4 μM
$K_D$= 2.3 ± 0.6 μM
GSK864
GSK864 binding to wt IDH1
GSK864 binding to R132H IDH1
$K_D$= 2.7 ± 0.7 μM
$K_D$= 4.1 ± 0.6 μM
$\Delta I_{obs}/\Delta I_{max}$
[wt IDH1]/ μM
[R132H IDH1]/ μM
[R132HIDH1]/ μM
[ppm]

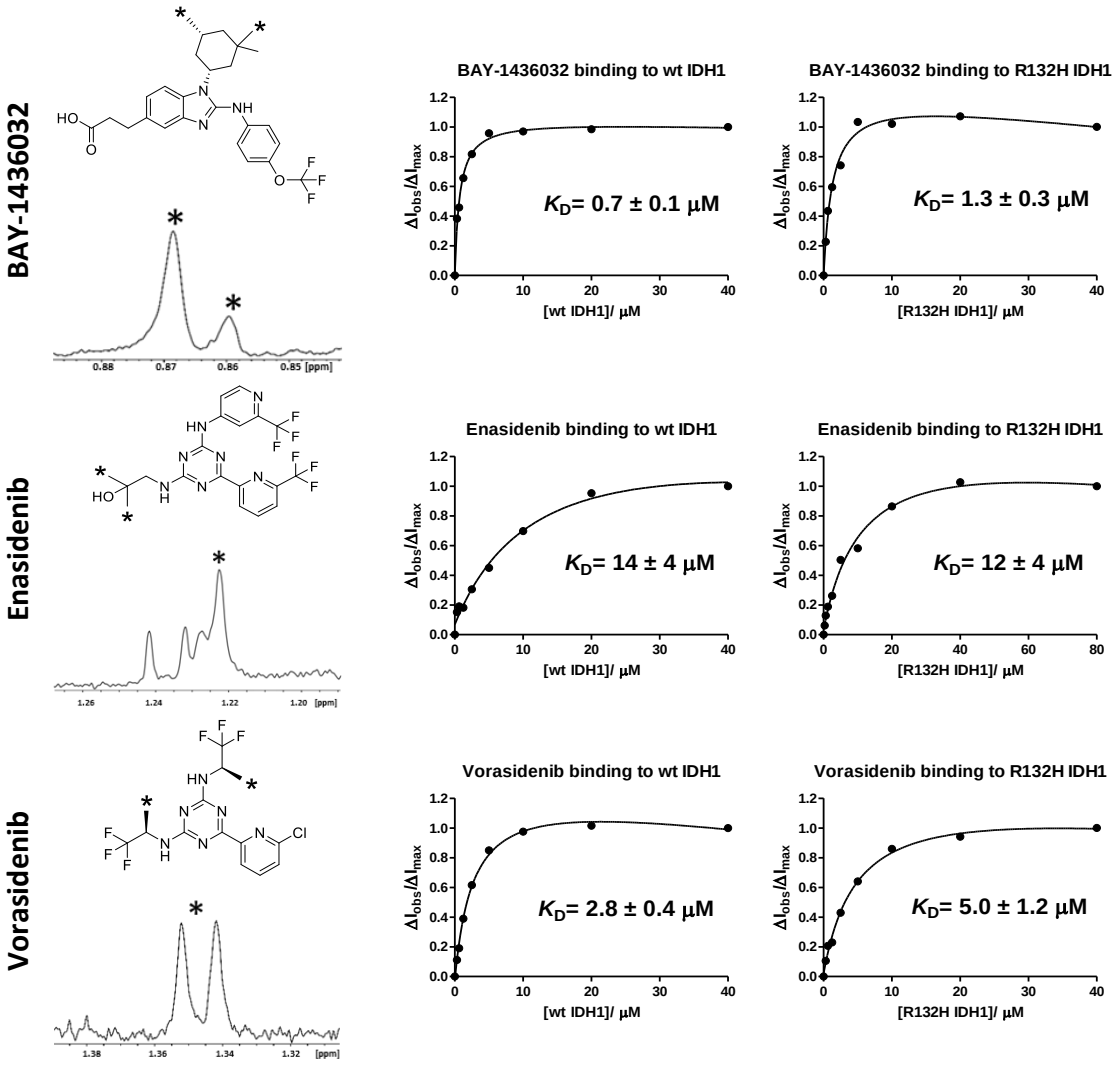



**Figure 5.8**. $K_D$ of mIDH1 inhibitors determined by $^1$H NMR (CPMG-edited, 700 MHz) spectroscopy. See Experimental Methods: Nuclear Magnetic Resonance for method details. The intensity of the inhibitor peak(s) shown was monitored. Note that for Enasidenib, the inhibitor signals partially overlap with the protein signals. Graphs of $\Delta I_{obs}/\Delta I_{max}$ against [protein]/μM are fitted using GraphPad Prism to obtain $K_D$. $\Delta I_{obs}/\Delta I_{max}=(I_{max}-I_{obs})/(I_{max}-I_{min})$ where $I_{max}$ is the maximum inhibitor peak intensity observed when no protein is added, $I_{obs}$ is the observed inhibitor peak intensity at a particular protein concentration, and $I_{min}$ is the minimum inhibitor peak intensity (typically ~0) when the binding is fully saturated.

### 5.2.5 CD analyses on IDH inhibition

CD spectroscopy was then employed to study how the binding of mIDH1 inhibitors to wt IDH1 and R132H IDH1 affects their secondary structures. Two inhibitors were chosen for this study: AGI-5198 which is relatively selective for R132H IDH1 over wt IDH1 in turnover assays (**Section 5.1.1**) and binds to IDH1 with a stoichiometry of one inhibitor per protein dimer (**Section 5.2.3**), and GSK864 which is relatively non-selective

for R132H IDH1 in turnover assays and binds to IDH1 with a stoichiometry of two inhibitors per protein dimer. Inhibitors were dissolved in MeOH instead of DMSO as DMSO absorbs strongly below ~220 nm. **Figure 5.9** shows that the CD spectra of IDH1 with and without inhibitors overlap very well, suggesting no significant changes in the secondary structures of wt IDH1 and R132H IDH1 upon the binding of AGI-5198 and GSK864. Co-worker, Raphel Reinbold, has further shown that other mIDH inhibitors also display no significant changes to the CD spectra of wt IDH1 and R132H IDH1.

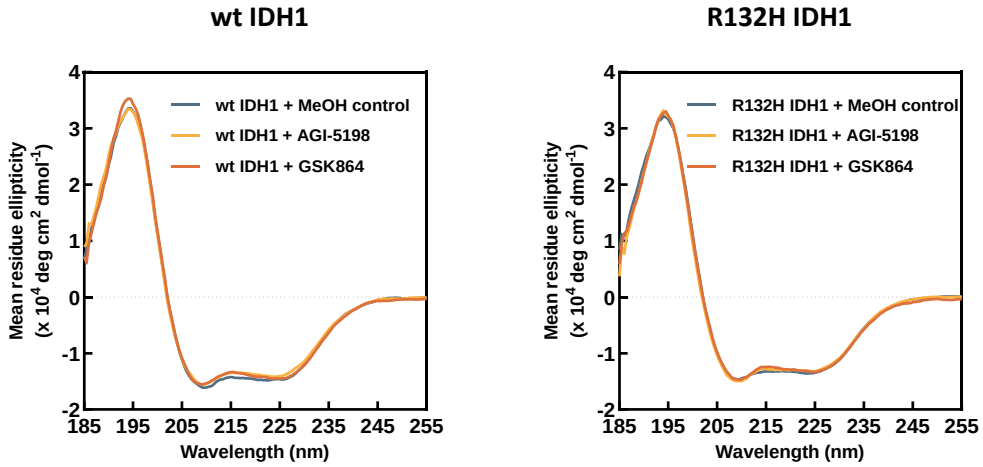
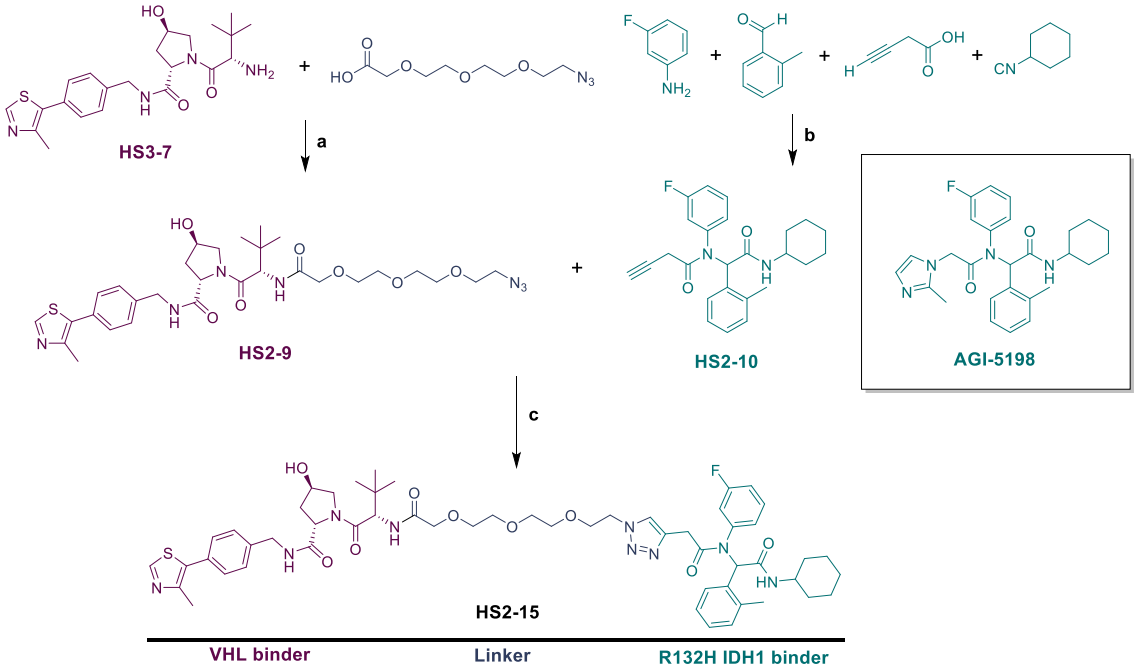



**Figure 5.9**. CD spectra of wt IDH1 and R132H IDH1 with or without inhibitors, AGI-5198 and GSK864. The spectra were recorded from 185 nm to 260 nm. Buffer: 10 mM sodium phosphate, pH 7.5. wt IDH1 or R132H IDH1 concentration: 0.2 mg/mL (4.2 µM), inhibitor concentration: 10× molar excess of [IDH1], 42 µM in 0.42% (v/v) MeOH final concentration.

## 5.3 PROTAC

Protein degradation is considered to be a more powerful therapeutic strategy than protein inhibition due to its irreversibility. Such a strategy is exemplified by PROTAC based inhibitors, which are bifunctional molecules that recruit an E3 ubiquitin ligase to a target protein leading to its degradation[242]. No known PROTAC compound for mutant IDH has been reported. Thus, a PROTAC compound (HS2-15, **Scheme 5.1**) was designed by Martine Abboud and synthesised by Hidenori Someya, linking a R132H IDH1 inhibitor (AGI-5198)[174] with a VHL inhibitor[243] via a polyethylene glycol (PEG) linker. Bringing R132H IDH1 and VHL in proximity potentially allows for ubiquitination and subsequent proteasomal degradation of R132H IDH1. In **Scheme 5.1**, HS3-7 is an analogue of the VHL inhibitor[243]. HS2-10 is an analogue of AGI-5198, functionalised with an alkyne handle for a subsequent 'click' reaction. As there is no X-ray crystal structure for AGI-

5198 or its analogues in complex with R132H IDH1, the position of the alkyne handle was chosen at a site where substitution was tolerated based on the published structure-activity relationship (SAR) studies[174]. A PEG linker of three ethylene glycol units was preliminarily chosen with the aim of bringing R132H IDH1 and VHL in close proximity without steric clash.




**Scheme 5.1**. Synthetic route of the PROTAC compound, HS2-15, based on the R132H IDH1 inhibitor, AGI-5198, by co-worker, Hidenori Someya. (**a**) HATU, DIPEA, DMF, r.t., 4hr. (**b**) The Ugi reaction. MeOH, r.t., 5 hr. (**c**) The 'click' reaction. $CuSO_4$, TBTA, sodium ascorbate, $^tBuOH/H_2O$ (1:1), r.t., 27 hr.

The relative inhibition of wt IDH1 and R132H IDH1 by HS3-7, AGI-5198, HS2-10 and HS2-15 was measured by absorbance-based assays (**Figure 5.10**). In general, all the tested compounds (at 25× and 250× molar excess of IDH1 concentrations) do not inhibit wt IDH1 significantly, suggesting that these compounds have good selectivity for mutant IDH1. Minimising off-target effects is important as PROTAC is essentially catalytic and trace amount can cause undesired and irreversible protein degradation. HS3-7 does not inhibit R132H IDH1 significantly, as it is a VHL inhibitor. Replacing the methyl imidazole with an alkyne in AGI-5198 results in ~10% less potency against R132H IDH1. However, further functionalisation of HS2-10 with the PEG linker and VHL inhibitor results in loss of approximately half of its potency against R132H IDH1. To validate these inhibition

results, the reductive conversion of 2OG to 2HG catalysed by R132H IDH1 was also monitored by $^{1}$H NMR spectroscopy. When used at a 20× molar excess of R132H IDH1 concentration, a gradual decrease in the inhibitory potency of HS2-10 and HS2-15 was observed compared to AGI-5198 (**Figure 5.11**). $IC_{50}$ measurements by absorbance-based assays (**Figure 5.12**) reveal that compared to AGI-5198 ($IC_{50}$= 0.16 µM), HS2-10 ($IC_{50}$= 0.33 µM) experiences a slight ~2-fold decrease in its inhibitory potency against R132H IDH1, whereas HS2-15 ($IC_{50}$= 6.5 µM) is ~40-fold less potent against R132H IDH1.

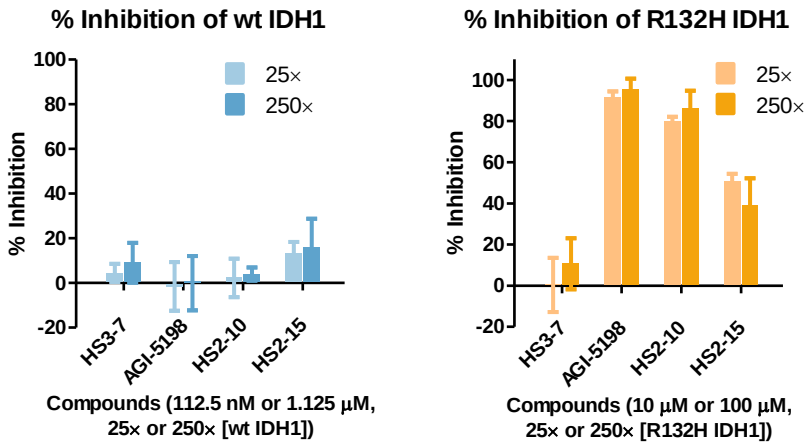



**Figure 5.10**. Inhibition of wt IDH1 and R132H IDH1 by PROTAC related compounds, as measured by absorbance-based assays. Data are mean ± SD, n= 3 technical replicates. See Experimental Methods: Biochemical assays for general assay conditions. wt activity is measured by oxidative conversion of isocitrate to 2OG whilst R132H IDH1 activity is measured by reductive conversion of 2OG to 2HG. All compounds were tested at 25× and 250× the enzyme concentration.

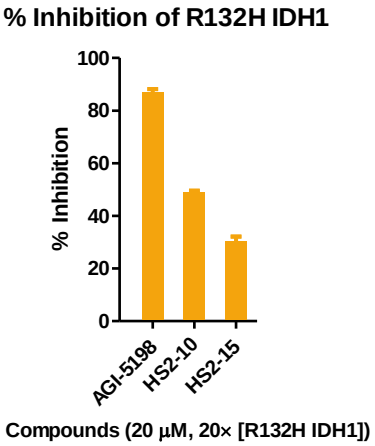



**Figure 5.11**. Inhibition of R132H IDH1 by PROTAC related compounds, AGI-5198, HS2-10 and HS2-15, as measured by $^{1}$H NMR (excitation sculpting suppression with perfect-echo, 700 MHz). Buffer: 50 mM Tris-$D_{11}$-HCl, pH 7.5 in 90% $H_2O$/ 10% $D_2O$ (v/v). R132H IDH1 activity is measured by 2OG conversion to 2HG, using 1 µM R132H IDH1, 1.5 mM 2OG, 1.5 mM NADPH and 10 mM $MgCl_2$. Data are mean NMR signals of 2OG, 2HG, $NADP^+$ and NADPH, ± SEM. The % inhibition is calculated by (1 – activity of (treated/DMSO control)) × 100%.

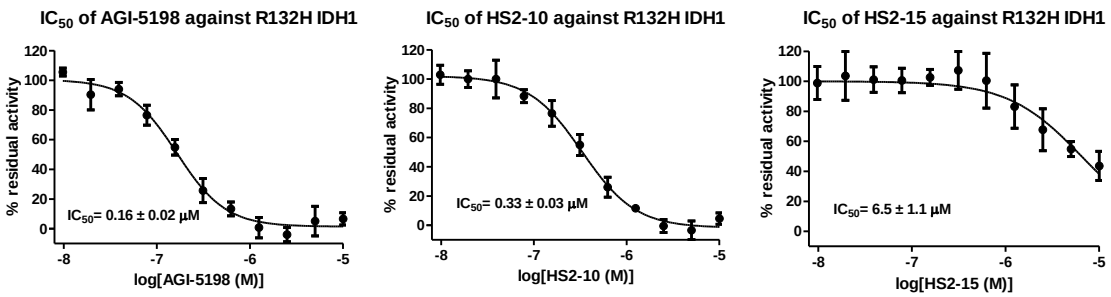



**Figure 5.12**. $IC_{50}$ graphs of PROTAC related compounds, AGI-5198, HS2-10 and HS2-15, against R132H IDH1 (400 nM) in the conversion of 2OG to 2HG, as measured by absorbance-based assays. The error bars represent mean ± SD, n= 3 technical replicates. The $IC_{50}$ values are reported as mean ± SD from the data fit. See Experimental Methods: Biochemical assays for general assay conditions. Note that $IC_{50}$ of AGI-5198 is different from its value reported in **Table 5.1** because 400 nM instead of 30 nM R132H IDH1 was used in the assessment of these R132H IDH1 inhibitors with micromolar potencies.

Although HS2-15 has a relatively high $IC_{50}$ of 6.5 μM in biochemical studies, due to its catalytic nature there is a reasonable chance that it is able to degrade R132H IDH1 in a cellular context. The degradation of R132H IDH1 by HS2-15 was assessed by western blot, following incubation of HS2-15 in LN18 cells overexpressing the gene encoding for R132H IDH1. Cell pellets were provided by co-workers, John Walsby-Tickle and Joan Gannon. Unfortunately, at different concentrations (1/10/100 μM) and incubation time (2/4/6/48 hr) of HS2-15 in LN18 cells overexpressed with R132H IDH1, no evidence for PROTAC degradation of R132H IDH1 was observed (**Figure 5.13**).

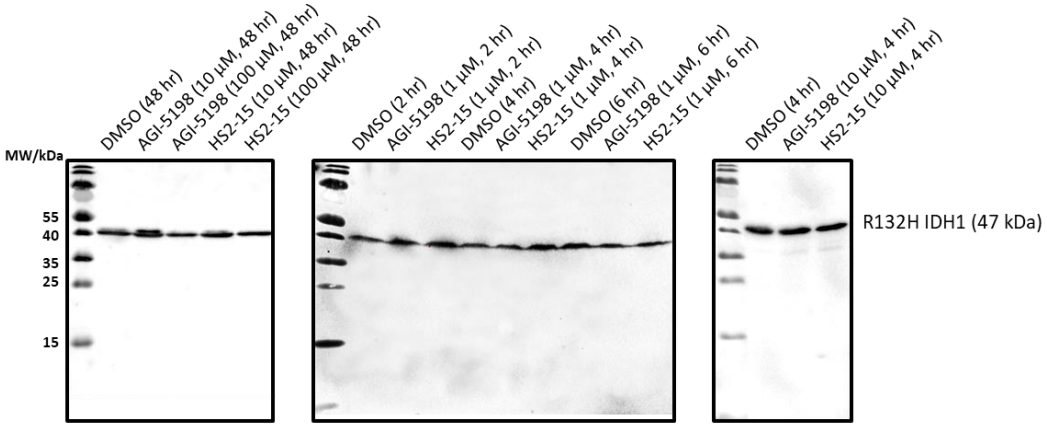
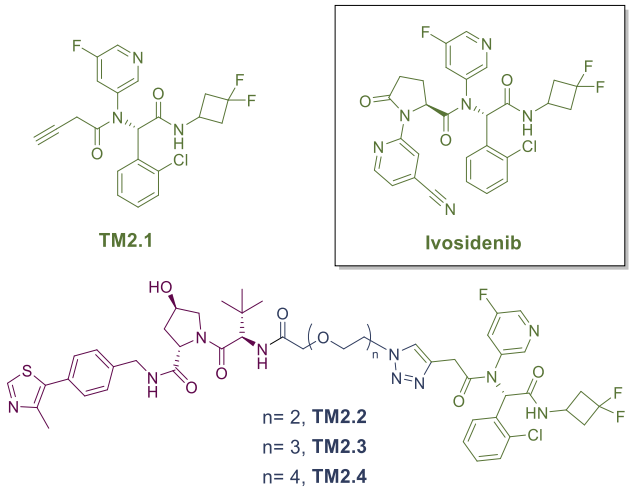



**Figure 5.13**. Western blot results showing no degradation of R132H IDH1 following incubation of DMSO (negative control), AGI-5198 (negative control) and HS2-15 in LN18 cells overexpressed with R132H IDH1. R132H IDH1 antibody (Merck, MABC171) was used at 1:100 dilution after optimisation.

One reason for the failed degradation of R132H IDH1 by HS2-15 might be due to its high $IC_{50}$. Subsequent PROTAC compounds were designed based on Ivosidenib, as

Ivosidenib has ~12× lower $IC_{50}$ than AGI-5198 (**Table 5.1**). Variable PEG linker lengths of 2, 3 or 4 ethylene glycol units were also introduced to give TM2.2, TM2.3 and TM2.4 respectively (**Figure 5.14**). TM2.1–2.4 are generous gifts from co-worker, Jia Chen. However, the high $IC_{50}$ value of TM2.1 suggests that the alkyne substitution is not well tolerated. This is further confirmed by published SAR studies which suggest that the pyridine substituted with the electron-withdrawing nitrile group is important for potency[113]. Consequently, the $IC_{50}$ values of the PROTAC compounds, TM2.2–2.4, are high at >5 µM. The $IC_{50}$ trend also implies that longer PEG linker lengths may decrease the PROTAC potency for R132H IDH1, although potential steric clash between R132H IDH1 and VHL must also be considered with shorter linker length in future work.




| Compound | $IC_{50}$/ µM |
|---|---|
| TM2.1 | 6.5 |
| TM2.2 | 4.8 |
| TM2.3 | ~15 |
| TM2.4 | ~30 |

**Figure 5.14**. PROTAC compounds designed based on Ivosidenib and their $IC_{50}$ values against R132H IDH1 in the conversion of 2OG to 2HG, as measured by absorbance-based assays. See Experimental Methods: Biochemical assays for general assay conditions.

Another possible reason for the failed degradation of R132H IDH1 by HS2-15 might be the poor cell permeability of HS2-15. To validate this, a fluorescence probe was designed for R132H IDH1 by coupling a suitable fluorophore, azide-fluor 545 (tetramethylrhodamine-PEG3-azide (TAMRA), absorbance/emission= 545/565 nm), to HS2-10. This particular fluorophore was chosen as it has an azide for the 'click' reaction, has good cellular permeability[244] and does not interfere with the fluorescence emitted by NADPH (tight binding cofactor of R132H IDH1, **Figures 2.4** and **2.5**) at 460 ± 50 nm. The fluorescence probe can also be useful in elucidating the subcellular localisation of R132H IDH1, which has been previously detected using western blot/immunohistochemistry[245], immunofluorescence microscopy[246] and green

fluorescent protein[247]. Due to time and resource constraints, the proposed fluorescence probe has not yet been synthesised.

## 5.4 Summary

This chapter first describes the biochemical potencies of reported mIDH1 and mIDH2 inhibitors on wt IDH1 and R132H IDH1, by both absorbance-based assays and NMR spectroscopy. Overall, Ivosidenib is the most potent among the tested inhibitors, consistent with results from the reported comparative biochemical studies of mIDH1 inhibitors[173]. mIDH1 inhibitors generally show good selectivity for R132H IDH1 over wt IDH1. Such biochemical selectivity is, however, not manifested in multiple biophysical assays. Binding studies of mIDH inhibitors to wt IDH1 and R132H IDH1, by employing DSF, ITC, non-denaturing MS and NMR spectroscopy (**Figure 5.15**), reveal that mIDH1 inhibitors bind with similar binding affinities to both wt IDH1 and R132H IDH1, demonstrating that binding of mIDH1 inhibitors to IDH1 does not necessarily correlate with inhibition of IDH1. Lastly, modifications of the mIDH1 inhibitors to PROTAC compounds for targeted R132H IDH1 degradation, or to fluorescence probes for cell permeability and subcellular localisation studies, have been discussed. Overall, the results on the potency, selectivity, binding affinity and binding stoichiometry of mIDH inhibitors should be useful in selecting and designing better mIDH inhibitors.

| | **$IC_{50}$/ nM (absorbance-based assays)** | **$\Delta T_m$/ °C (highest observed, DSF)** | | **$K_D$/ µM (ITC)** | | **$K_D$/ µM (non-denaturing MS)** | | **$K_D$/ µM (NMR spectroscopy)** | |
|---|---|---|---|---|---|---|---|---|---|
| | R132H | wt | R132H | wt | R132H | wt | R132H | wt | R132H |
| **Ivosidenib** | 4.9 | 9.4 | 8.5 | 0.42 | 0.49 | 9.7 | 11 | 10 | 9.0 |
| **AGI-5198** | 61 | 6.9 | 6.0 | >400 | | 608 | 98 | 9.1 | 8.6 |
| **Agios135** | 18 | 7.5 | 6.2 | ND | | ND | | ND | |
| **ML309 HCl** | 73 | 8.1 | 6.6 | | | | | | |
| **Novartis 224** | 8.2 | 12.1 | 11.7 | >400 | | 140 | 142 | 1.7 | 1.1 |
| **Novartis 556** | 25 | ND | ND | ND | | ND | | ND | |
| **EVO894** | 29 | 12.5 | 11.5 | | | | | 2.2 | 2.3 |
| **GSK864** | 20 | 9.1 | 7.9 | >400 | | 24 | 23 | 2.7 | 4.1 |
| **BAY-1436032** | 18 | 11.6 | 9.9 | | | ND | | 0.7 | 1.3 |
| **Sanofi 1** | $4.5 \times 10^3$ | 1.1 | 2.0 | | | | | ND | |
| **SYC-435** | $> 10 \times 10^3$ | 0.7 | 0.5 | ND | | | | | |
| **AGI-6780** | $> 10 \times 10^3$ | 3.3 | 1.3 | | | | | | |
| **Enasidenib** | $> 10 \times 10^3$ | 4.4 | 1.5 | >400 | | | | 14 | 12 |
| **Vorasidenib** | 21 | 8.5 | 6.2 | | | | | 2.8 | 5.0 |

**Figure 5.15**. Summary of biochemical and biophysical profile of mIDH inhibitors against wt IDH1 and R132H IDH1. ND: not determined. Refer to **Sections 5.1** and **5.2** for details.

## 5.5 Supplementary Figures

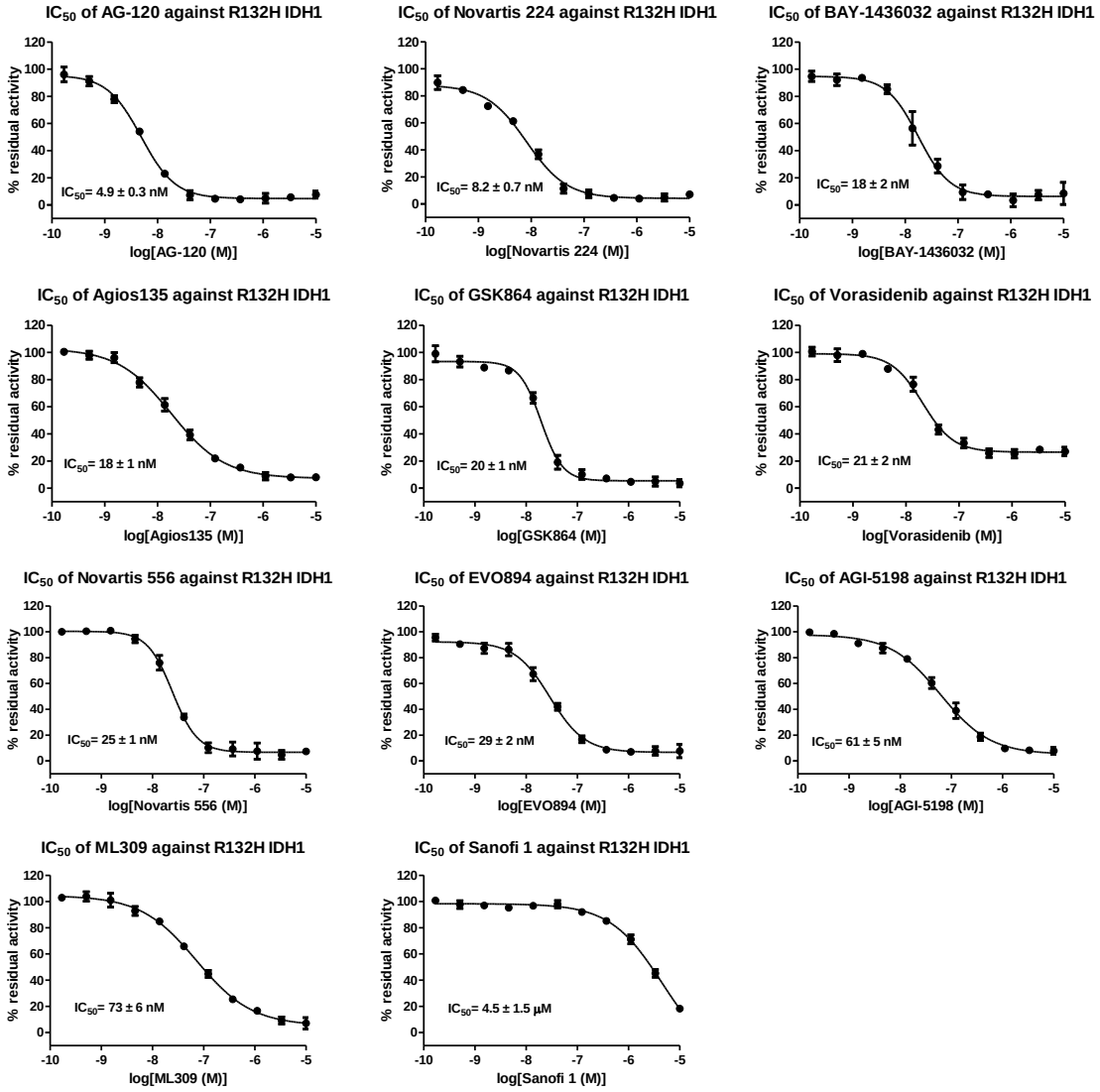



**Figure S5.1**. $IC_{50}$ graphs of mIDH inhibitors against R132H IDH1 (30 nM) in the conversion of 2OG to 2HG, as measured by absorbance-based assays. The error bars represent mean ± SD, n= 3 technical replicates. The $IC_{50}$ values are reported as mean ± SD from the data fit.

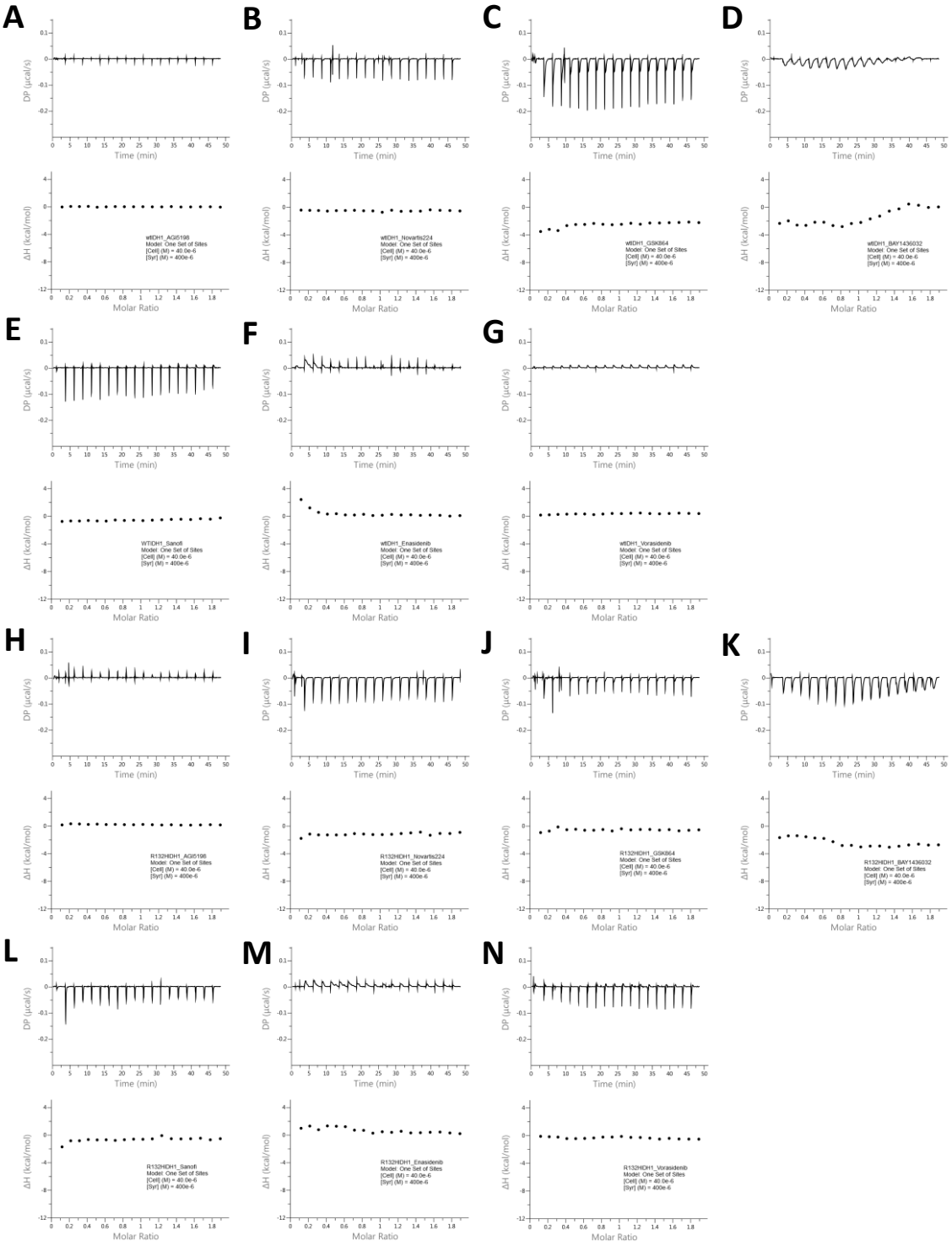



**Figure S5.2**. ITC analyses of mIDH inhibitors (400 µM) titrated against wt IDH1 or R132H IDH1 (40 µM), in 50 mM Tris-HCl, pH 7.5. Inhibitors shown are AGI-5198, Novartis 224, GSK864, BAY-1436032, Sanofi 1, Enasidenib, Vorasidenib, from (**A**) to (**G**) for wt IDH1, and from (**H**) to (**N**) for R132H IDH1, in the respective order. No significant binding is observed for all the inhibitors shown. See Experimental Methods: Isothermal Titration Calorimetry for method details.

# CHAPTER 6. COVALENT INHIBITORS OF R132H IDH1

Although covalent inhibitors of enzymes can react both reversibly and irreversibly, they are sometimes considered as conceptually distinct from non-covalent inhibitors. Some covalent inhibitors react in a manner that is independent of protein conformation, as they can form non-specific covalent bonds with their protein targets. Covalent inhibitors have sometimes been disfavoured in drug development due to concerns in their potential off-target reactivity, especially those with highly reactive functional groups. However, covalent inhibitors can provide massive therapeutic benefits, as exemplified by the widespread use of aspirin[248] and the penicillin type antibiotics[249]. Three of the ten top-selling drugs (clopidogrel, lansoprazole and esomeprazole) in the US in 2009 are covalent inhibitors of their targets[250]. The exceptionally high potency and long residence time of covalent inhibitors can be advantageous in drug design, particularly for target proteins with slow biogenesis.

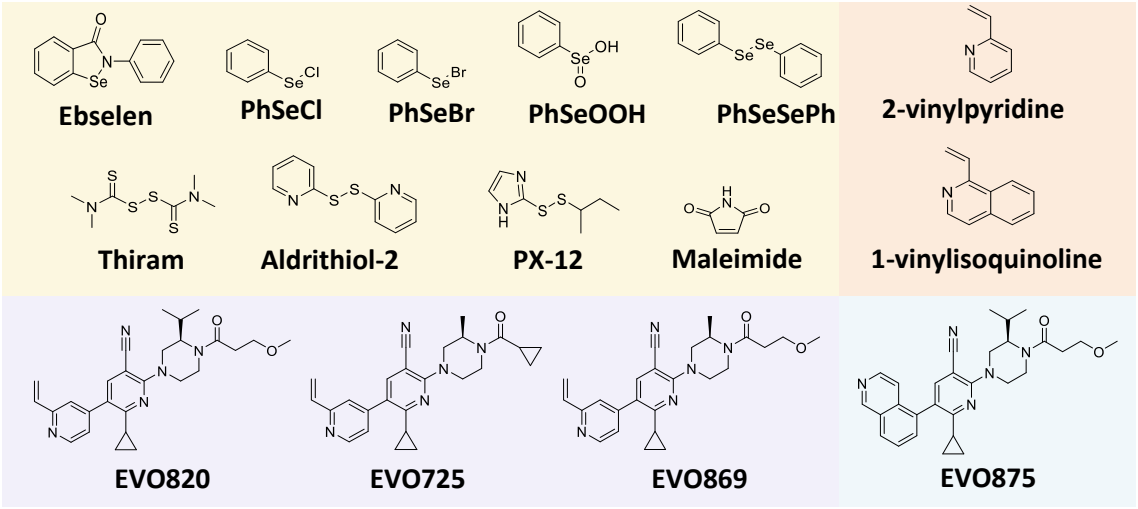



**Figure 6.1**. Cysteine-targeting covalent modifiers[195,196] (shaded in yellow), covalent inhibitors of R132H IDH1 from Evotec (shaded in violet) as well as their vinyl warhead analogues (shaded in orange) and non-covalent control (shaded in blue). 1-Vinylisoquinoline was a generous gift from co-worker, Alistair Farley.

The interest in covalent inhibitors of mIDH stems from the reported clinical resistance to Enasidenib and Ivosidenib owing to the second mutations in the inhibitor binding site in mIDH1 and mIDH2[140]. Covalent inhibitors could be more effective in targeting drug resistant mutations compared to non-covalent inhibitors. Prior examples of covalent inhibitors overcoming drug resistance that was acquired after treatment with non-

covalent inhibitors are seen in cancer and infectious diseases, including the inhibitors of epidermal growth factor receptor (EGFR)[251] and hepatitis C virus (HCV) protease[252].

This chapter describes the characterisation of cysteine-targeting covalent inhibitors of R132H IDH1 (**Figure 6.1**). Compounds investigated include selenium- and sulfur-based compounds, such as ebselen and thiram[195,196], as well as the Michael acceptor, maleimide[253], all of which are known to react with cysteine residues, but which are likely non-selective for R132H IDH1. In addition, potentially selective covalent inhibitors of IDH1 were investigated, *i.e.* EVO820, EVO725 and EVO869, which were obtained from collaborators at Evotec (Abingdon, UK). These inhibitor scaffolds are related to compounds described in a patent application from Agios[254]. EVO725 is identical to compound 443 in the patent, although its covalent modification feature has not been described in literature. EVO820 and EVO869 are structural analogues of EVO725. EVO875 is a non-covalent counterpart of EVO820, and serves as the negative control for the activity of the analogous covalently reacting Evotec inhibitors. Researchers at Evotec have obtained an X-ray crystal structure of EVO869 in complex with R132H IDH1 (unpublished data), which reveals that the vinyl group of EVO869 undergoes Michael addition with the thiol group of C269 on both R132H IDH1 monomers present in the crystallographically observed dimer (**Figure 6.2**).

The abovementioned Evotec inhibitors were expected to be, at least partially, selective for IDH1, in part because they react with a less exposed cysteine (C269) at the dimer interface, instead of the more exposed cysteine residues (C297 and C379) on the R132H IDH1 surface (**Figure 6.2**). Covalent modification by these Evotec inhibitors likely occurs after binding to the dimer interface that enables close proximity and subsequent reaction between the electrophilic vinyl warhead and the nucleophilic thiol group of C269.

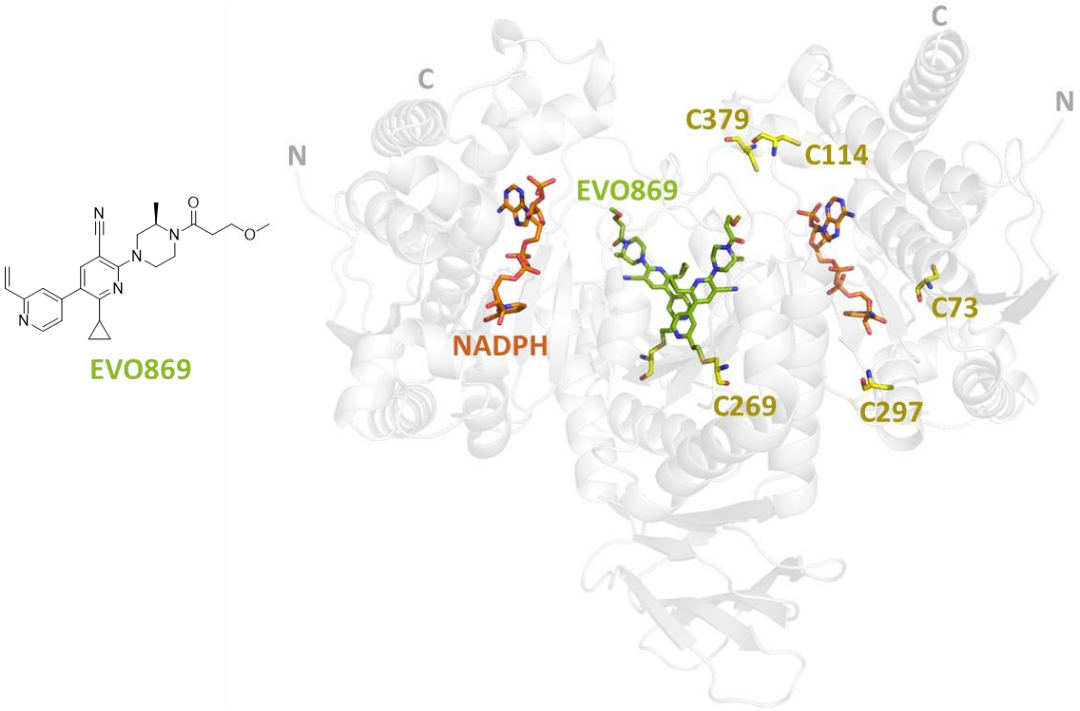



**Figure 6.2**. Overall view of an X-ray crystal structure of EVO869 (green) which has covalently modified C269 of R132H IDH1 (translucent grey), unpublished results by Evotec (Abingdon, UK). The cofactor, NADPH (orange), binds at the active site and EVO869 (green) binds at the dimer interface of R132H IDH1 with a stoichiometry of 2 inhibitors per R132H IDH1 dimer. Each R132H IDH1 monomer has five cysteine residues (yellow), of which C297 and C379 are solvent exposed (from a surface view analysis of the crystal structure).

## 6.1 Time-dependent inhibition studies

Inhibition activity of the compounds investigated were first assessed by absorbance-based assays using standard conditions as defined in **Table 2.2**. Following a fixed 12-min preincubation of Evotec covalent inhibitors (EVO820, EVO725 and EVO869) with wt IDH1 or R132H IDH1, these covalent inhibitors show no significant differences in their inhibitory activities compared to their non-covalent counterpart, EVO875 (**Figure 6.3A**). All the Evotec inhibitors tested generally have good wt/mutant IDH1 selectivity as they inhibit the neomorphic (reductive) reaction of R132H IDH1 fully but have minimal effect on the normal (oxidative) reaction of wt IDH1 (**Figure 6.3A**). Interestingly, the Evotec inhibitors, particularly EVO820, also inhibit the reverse (reductive) reaction of wt IDH1 (**Figure 6.3A**). The inhibition of R132H IDH1 by EVO820 was validated by reaction monitoring using $^{1}$H NMR (700 MHz) spectroscopy. The results showed that EVO820 fully inhibits R132H IDH1 at the tested conditions, as the initial levels of reactants did not change with time (**Figure 6.3B**).

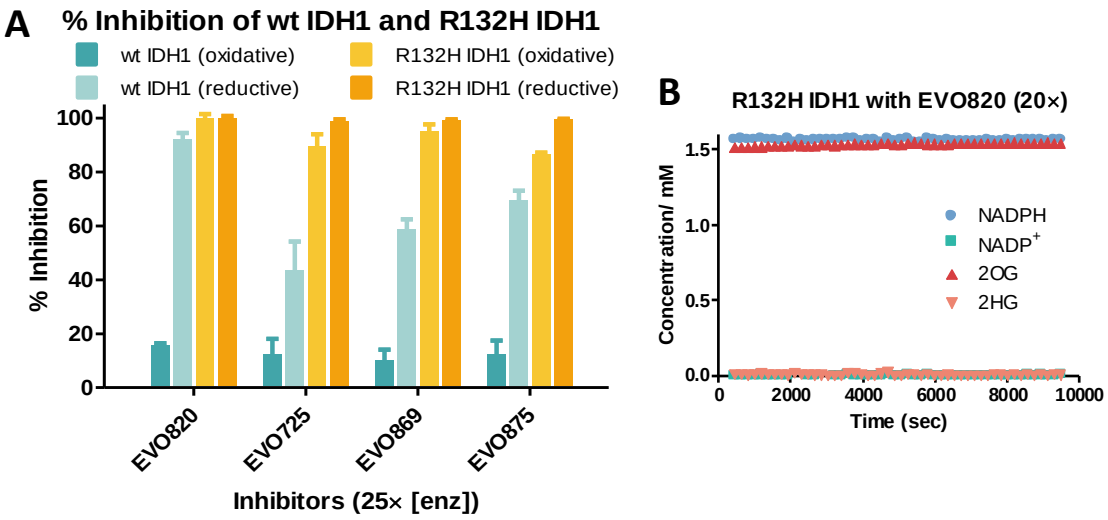



**Figure 6.3.** (**A**) Inhibition of wt IDH1 and R132H IDH1 catalysed reactions by the Evotec covalent inhibitors of R132H IDH1 (EVO820, EVO725, EVO869) and the non-covalent counterpart (EVO875), as measured by absorbance-based assays. Data are mean ± SD, n= 3 technical replicates. The % inhibition is calculated by (1 – activity of (treated/DMSO control)) × 100%. See Experimental Methods: Biochemical assays for general assay conditions. The compounds were tested at 25× the enzyme concentrations used in the respective reactions. Preincubation time: 12 min. Cyan: % inhibition of wt IDH1 catalysed conversion of isocitrate to 2OG. [Inhibitor]= 112.5 nM. Light blue: % inhibition of wt IDH1 catalysed conversion of 2OG to isocitrate. [Inhibitor]= 2.5 µM. Yellow: % inhibition of R132H IDH1 catalysed conversion of isocitrate to 2OG. [Inhibitor]= 10 µM. Orange: % inhibition of R132H IDH1 catalysed conversion of 2OG to 2HG. [Inhibitor]= 10 µM.
(**B**) Inhibition of R132H IDH1 by EVO820 (20× molar excess of R132H IDH1 concentration), as measured by $^{1}$H NMR (excitation sculpting suppression with perfect-echo, 700 MHz) spectroscopy. Buffer: 50 mM Tris-$D_{11}$-HCl, pH 7.5 in 90% $H_2O$/ 10% $D_2O$ (v/v). Conditions: 1 µM R132H IDH1, 20 µM EVO820, 1.5 mM 2OG, 1.5 mM NADPH and 10 mM $MgCl_2$.

Irreversibly binding inhibitors are often identified by their time-dependent inhibitory activity. Time-dependent $IC_{50}$ values with different preincubation times, *i.e.* 1, 5, 15 and 30 min, were measured by absorbance-based assays for all the compounds listed in **Table 6.1**. All the reported covalent modifiers[195,196] (shaded in yellow in **Table 6.1**) and Evotec covalent inhibitors (shaded in violet in **Table 6.1**) showed a decrease in their $IC_{50}$ values with increasing preincubation time. The $IC_{50}$ values of EVO875 did not change with time, as expected for non-covalent compounds. Overall, EVO820 is the most potent covalent inhibitor amongst those tested. These Evotec inhibitors show good selectivity for R132H IDH1, as their $IC_{50}$ values against wt IDH1 are in the micromolar range (**Figure S6.2**), several orders of magnitude higher than those for R132H IDH1.

2-Vinylpyridine, the 'warhead' of the Evotec covalent inhibitors, shows $IC_{50}$ values of >100 μM at all preincubation times. This suggests that the 2-vinylpyridine itself is not sufficiently potent to inhibit R132H IDH1. Thus, the entirety or most of the scaffold in the Evotec inhibitors is likely required for the inhibitor binding to the dimer interface of R132H IDH1; this likely brings the vinyl motif of Evotec inhibitors in close proximity to C269 of R132H IDH1 to enable the covalent modification in a stereoelectronically favoured manner. 1-Vinylisoquinoline is reasoned to be more reactive than 2-vinylpyridine in nucleophilic substitution with thiol group as the negative charge in the intermediate is more delocalised, and indeed it shows low micromolar $IC_{50}$ values for R132H IDH1 (**Table 6.1**). However, without the entire inhibitor scaffold for binding specificity, 1-vinylisoquinoline is likely non-selective for C269. Denaturing LC-MS (**Section 6.2**) can elucidate the number of cysteine residues of R132H IDH1 that a compound modifies, hence providing further evidence on the selectivity and mode of action of the tested compounds.

The relatively low reactivity of the vinyl warhead was also inferred from compound stability studies. It was observed that Evotec inhibitors can tolerate repeated freeze-thaw cycles without affecting their inhibitory activities. The selenium- and sulfur-based compounds (**Table 6.1**), however, were found to quickly lose their inhibitory activities if left in DMSO at r.t. for hours or after repeated freeze-thaw cycles. These compounds were thus prepared freshly or as fresh aliquots before any experiments. The reactivity trend of the selenium-based compounds can generally be rationalised by the stability of their leaving groups following nucleophilic substitution with the thiol groups of the cysteine residues. Note that some common covalent modifiers of thiols such as iodoacetamide (IAA)[255] and 3-bromo-1,1,1- trifluoroacetone (BTFA)[256] showed no covalent modification of R132H IDH1 as measured by denaturing LC-MS at the tested concentrations (10 μM) in **Section 6.2** and are thus excluded from the list of compounds shown in **Table 6.1**.

| | Compound | $IC_{50}$/ nM (mean ± SD) against R132H IDH1 | | | |
|---|---|---|---|---|---|
| | | 1 min | 5 min | 15 min | 30 min |
| 1 | **Ebselen** | 105 ± 4 | 75 ± 4 | 59 ± 3 | 41 ± 3 |
| 2 | **PhSeCl** | 135 ± 12 | 60 ± 7 | 27 ± 4 | 16 ± 2 |
| 3 | **PhSeBr** | 170 ± 16 | 73 ± 5 | 33 ± 4 | 21 ± 2 |
| 4 | **PhSeOOH** | $(1.2 \pm 0.1) \times 10^3$ | 639 ± 55 | 289 ± 34 | 129 ± 16 |
| 5 | **PhSeSePh** | 52 ± 5 | 28 ± 3 | 6.7 ± 1.0 | 2.5 ± 0.5 |
| 6 | **Thiram** | 95 ± 8 | 61 ± 4 | 42 ± 3 | 38 ± 2 |
| 7 | **Aldrithiol-2** | 95 ± 7 | 76 ± 4 | 46 ± 4 | 30 ± 3 |
| 8 | **PX-12** | 179 ± 13 | 139 ± 11 | 83 ± 7 | 50 ± 5 |
| 9 | **Maleimide** | 657 ± 91 | 356 ± 36 | 225 ± 26 | 128 ± 15 |
| 10 | **2-vinylpyiridine** | $> 100 \times 10^3$ | $> 100 \times 10^3$ | $> 100 \times 10^3$ | $> 100 \times 10^3$ |
| 11 | **1-vinylisoquinoline** | $(2.8 \pm 0.3) \times 10^3$ | $(1.4 \pm 0.1) \times 10^3$ | 977 ± 144 | 651 ± 78 |
| 12 | **EVO820** | 11 ± 1 | 7.7 ± 0.3 | 6.8 ± 0.4 | 6.0 ± 0.4 |
| 13 | **EVO725** | 28 ± 3 | 20 ± 2 | 13 ± 2 | 5.8 ± 0.8 |
| 14 | **EVO869** | 71 ± 5 | 60 ± 4 | 48 ± 3 | 39 ± 3 |
| 15 | **EVO875 (non-covalent)** | 16 ± 2 | 13 ± 2 | 13 ± 1 | 16 ± 2 |

**Table 6.1**. Time-dependency of $IC_{50}$ determination for cysteine-targeting covalent modifiers (shaded in yellow), covalent inhibitors of R132H IDH1 from Evotec (shaded in violet) as well as their vinyl warhead analogues (shaded in orange) and non-covalent control (shaded in blue) against R132H IDH1. R132H IDH1 catalysed reductive conversion of 2OG to 2HG were initiated by the addition of 2OG and NADPH after the specified preincubation time with compounds and R132H IDH1. The reactions were measured by absorbance-based assays using standard conditions (except 30 nM R132H IDH1 being used to lower the measurement limit for $IC_{50}$) as defined in **Table 2.2**. $IC_{50}$ values are reported as mean ± SD from three technical replicates. Time-dependent $IC_{50}$ graphs are presented in **Figure S6.1**.

## 6.2 Covalent modifications as measured by denaturing LC-MS

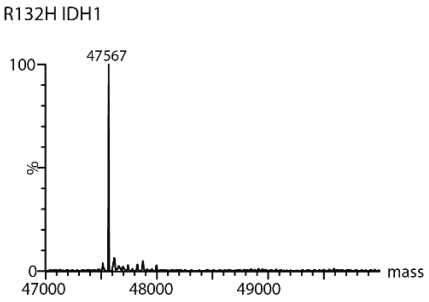
Each R132H IDH1 monomer has five cysteine residues (**Figure 6.2**). Denaturing LC-MS studies were conducted with R132H IDH1 to provide information on the number of cysteine residues being modified and the rate of covalent modifications, which would facilitate understanding on the selectivity and the mode of action of the tested covalent compounds. It was assumed that the Evotec covalent compounds modify only C269 of R132H IDH1, as evidenced by the X-ray crystal structure (**Figure 6.2**). The other covalent modifiers in **Table 6.1** also likely target cysteine residues; this proposal is presently being validated by trypsin digest and LC-MS/MS studies.

Denaturing LC-MS analyses were conducted at two time points *i.e.* 15 min and 1.5 hr preincubation of R132H IDH1 (1 μM) and all the covalent compounds in **Table 6.1** (10 μM) (**Figure 6.4**). The extent of covalent modification of R132H IDH1 by the tested covalent compounds generally increases with time. For selenium- and sulfur-based covalent modifiers (shaded in yellow in **Figure 6.4**), up to five molecules were observed to covalently attach to each R132H IDH1 monomer, likely via reaction with the five cysteine residues in each monomer. The multiple sites of covalent modifications on R132H IDH1 suggest that these compounds are not selective for C269 but react with all available cysteine residues. The extent of covalent modification largely matches the inhibitory activities of these covalent modifiers in **Table 6.1**.

For the Evotec inhibitors (shaded in violet in **Figure 6.4**), only one molecule of each inhibitor was observed to covalently attach to each monomer of R132H IDH1, likely via reaction with C269. The covalent modification was relatively slow as no modification was observed after 15 min preincubation of R132H IDH1 with each of the Evotec compounds. After 1.5 hr preincubation, the peak intensity of the covalently modified R132H IDH1 correlates well with the inhibitory activities of the Evotec inhibitors in **Table 6.1**, with the ranking order of EVO820 (strongest)> EVO725> EVO869. The non-covalent counterpart, EVO875 (shaded in blue in **Figure 6.4**), showed no covalent modification of R132H IDH1 at all time points as expected.

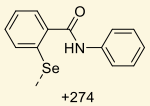
The vinyl warhead motif, 2-vinylpyridine (shaded in orange in **Figure 6.4**), showed no covalent modification of R132H IDH1, consistent with the observation in **Section 6.1** that the warhead motif, in isolation, is not a sufficiently potent covalent modifier. The more reactive analogue, 1-vinylisoquinoline, covalently modified R132H IDH1 with more than one molecules of the compound attached to R132H IDH1, confirming that the warhead itself is not selective for C269 and the selectivity is brought by the entire scaffold of the inhibitor to the binding site at the dimer interface of R132H IDH1.

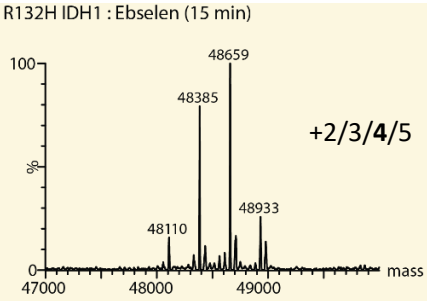
R132H IDH1 only

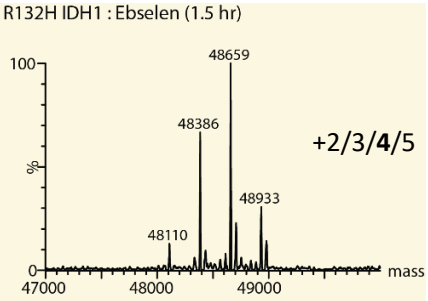



**15 min** **1.5 hr**

Ebselen

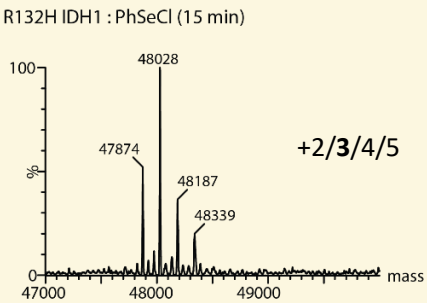


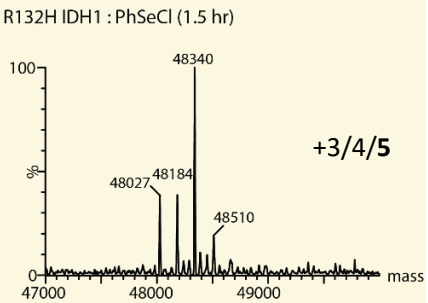




PhSeCl

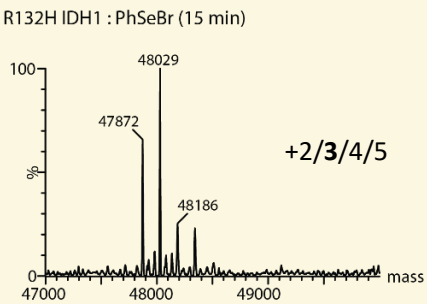


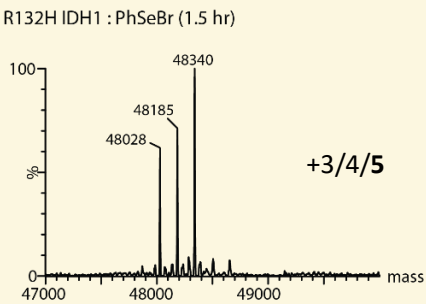




PhSeBr

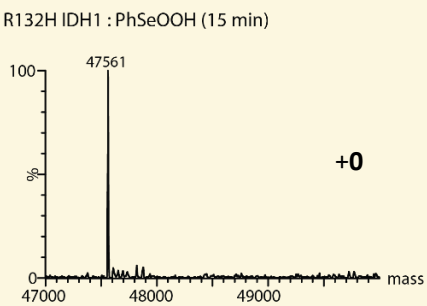


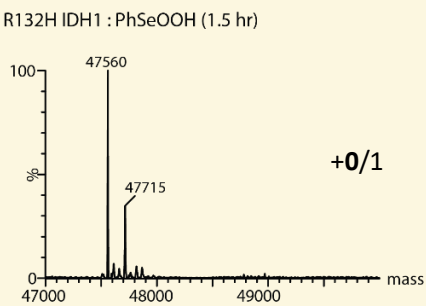




PhSeOOH



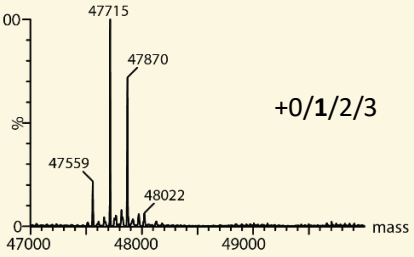



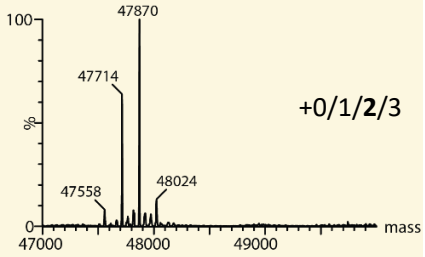



PhSeSePh




+155

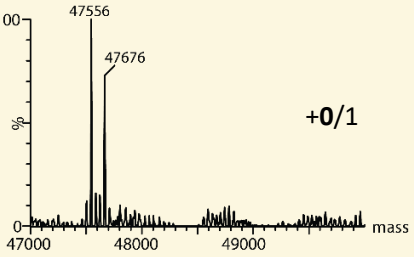


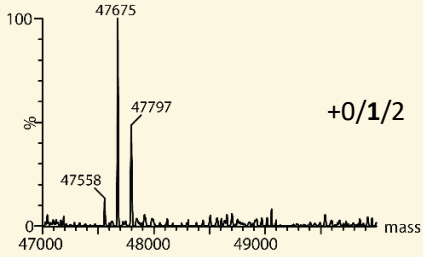




Thiram




+119

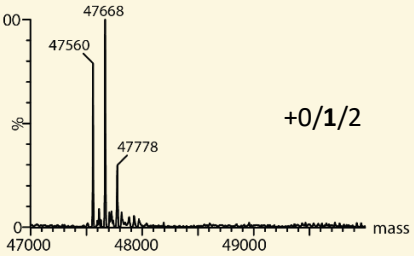


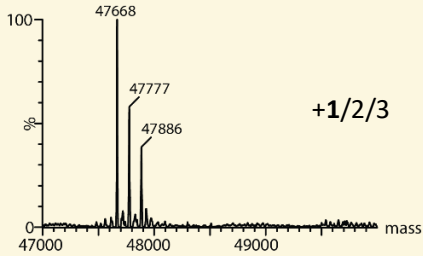




Aldrithiol-2




+109

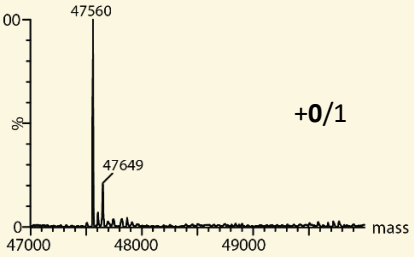


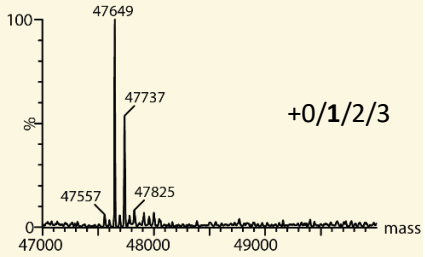




PX-12

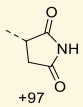



+88

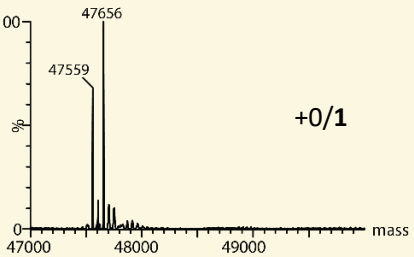


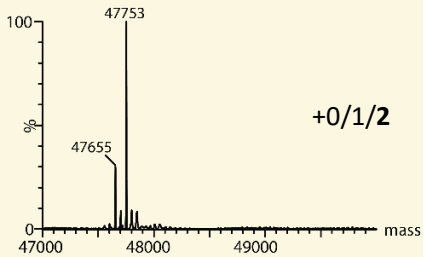




Maleimide

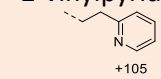



+97

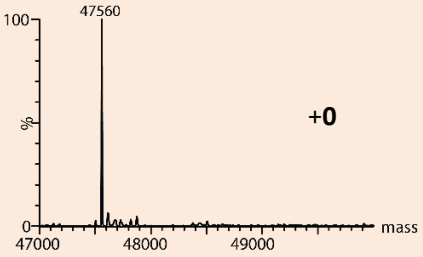


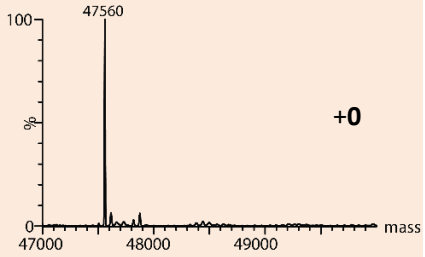
2-vinylpyridine



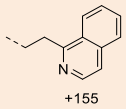

R132H IDH1 : 2-vinylpyridine (15 min)



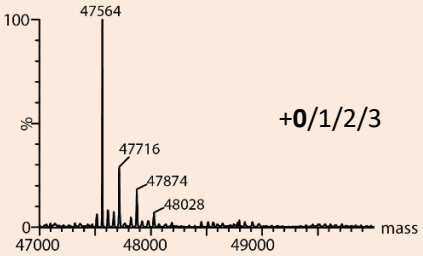

R132H IDH1 : 2-vinylpyridine (1.5 hr)



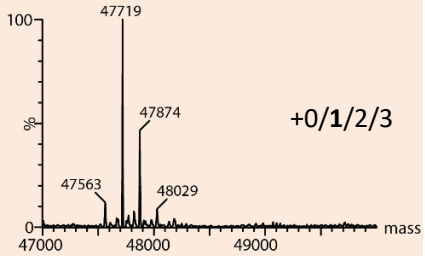

1-vinyl-isoquinoline



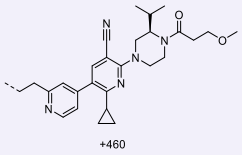

R132H IDH1 : 1-vinylisoquinoline (15 min)



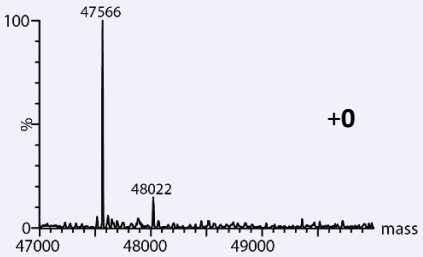

R132H IDH1 : 1-vinylisoquinoline (1.5 hr)



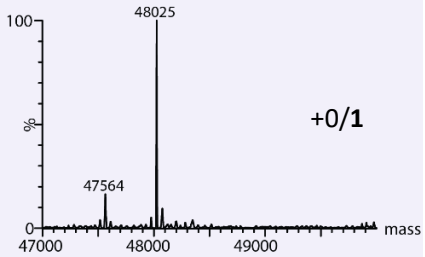

EVO820



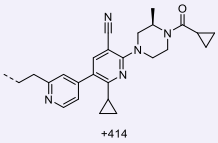

R132H IDH1 : EVO820 (15 min)



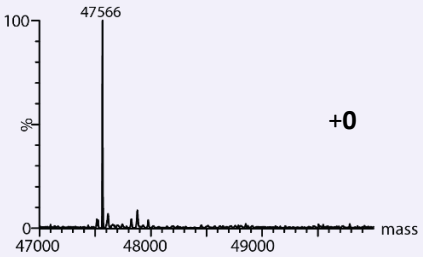

R132H IDH1 : EVO820 (1.5 hr)



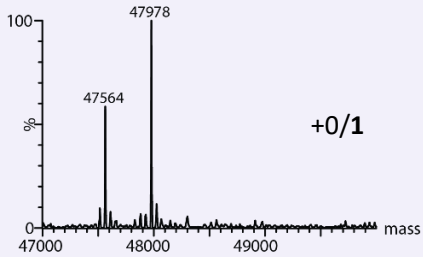

EVO725



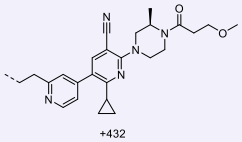

R132H IDH1 : EVO725 (15 min)



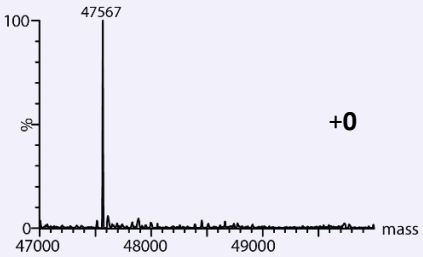

R132H IDH1 : EVO725 (1.5 hr)



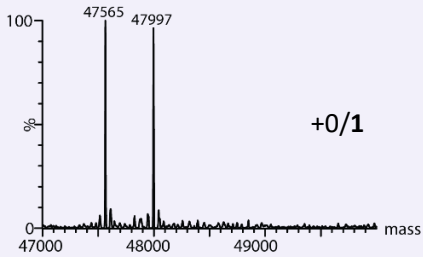

EVO869




R132H IDH1 : EVO869 (15 min)




R132H IDH1 : EVO869 (1.5 hr)



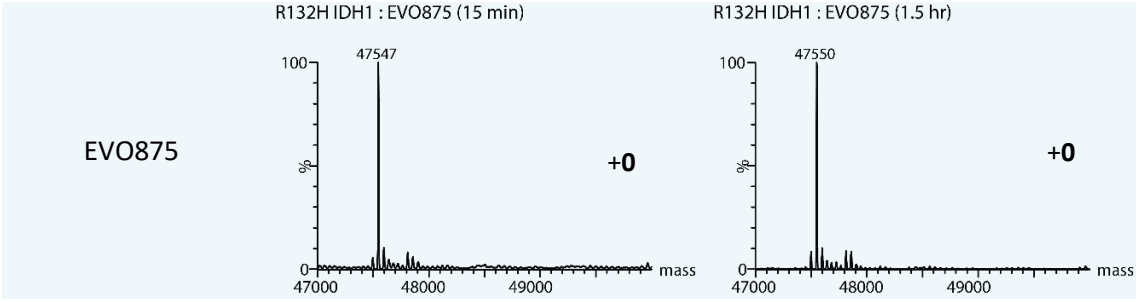



**Figure 6.4**. Denaturing protein LC-MS spectra of R132H IDH1 with cysteine-targeting covalent modifiers (shaded in yellow), covalent inhibitors of R132H IDH1 from Evotec (shaded in violet) as well as their vinyl warhead analogues (shaded in orange) and non-covalent control (shaded in blue). R132H IDH1: 1 µM, compounds: 10 µM, buffer: 50 mM Tris-HCl, pH 7.5. R132H IDH1 and compounds were preincubated for 15 min or 1.5 hr before running the sample. The numbers shown on the spectra refer to the number of molecules that are covalently attached to R132H IDH1, with the predominant number in bold.

Interestingly, the same LC-MS experiments with wt IDH1 showed that the Evotec covalent inhibitors also react with wt IDH1 (**Figure 6.5A**), despite the inhibition studies showing that these inhibitors are selective for R132H IDH1 (**Table 6.1** and **Figure S6.2**). The covalent reaction with wt IDH1 is faster than that with R132H IDH1, as completely modified wt IDH1 (**Figure 6.5A**) but not R132H IDH1 (**Figure 6.4**) was observed at 1.5 hr.

This observation is reminiscent of the binding studies in **Chapter 5**, where non-covalent mIDH1 inhibitors have similar binding affinities to wt IDH1 and R132H IDH1. Covalent modification by the Evotec covalent inhibitors can be viewed as a two-step process of an initial non-covalent binding of the inhibitor to the protein, followed by a relatively slow reaction at the warhead. If non-covalent binding occurs for both wt and R132H IDH1, it is not surprising that the subsequent covalent modifications are also on both proteins. The covalent modification remains selective for C269 presumably, as only one molecule of the Evotec compounds is attached to wt IDH1 even after prolonged incubation of 6 hr (data similar to that of 1.5 hr in **Figure 6.5A**).

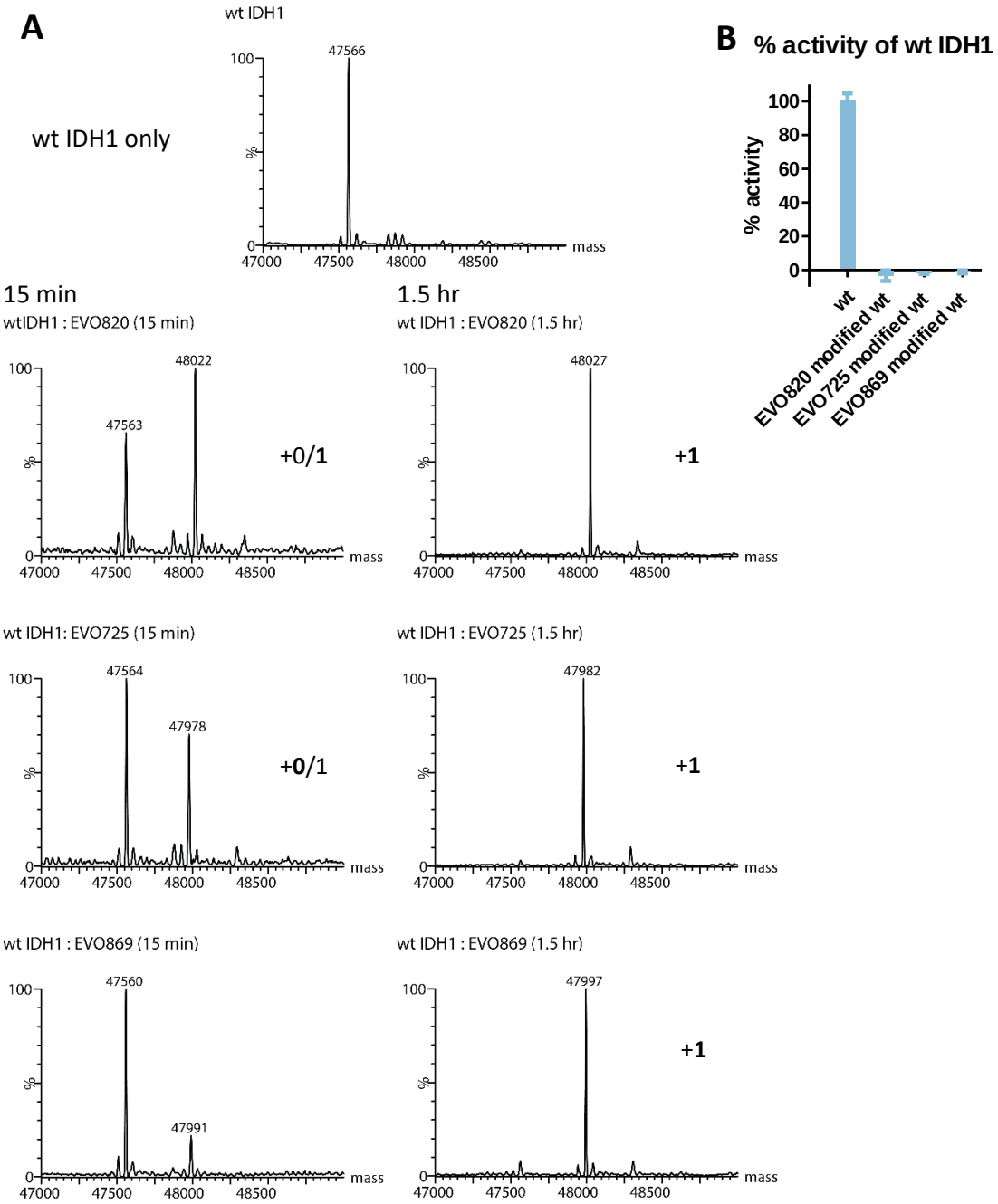



**Figure 6.5**. (**A**) Denaturing protein LC-MS spectra of wt IDH1 with covalent inhibitors of R132H IDH1 from Evotec. wt IDH1: 1 µM, compounds: 10 µM, buffer: 50 mM Tris-HCl, pH 7.5. wt IDH1 and compounds were preincubated for 15 min or 1.5 hr before running the sample. The numbers shown on the spectra refer to the number of molecules that are covalently attached to R132H IDH1, with the predominant number in bold. (**B**) Activity of covalently modified wt IDH1 after 3.5 hr preincubation of wt IDH1 and the Evotec covalent inhibitors, as measured by absorbance-based assays. Data are mean ± SD, n= 3 technical replicates, using the activity of non-modified wt IDH1 (0.10 µM $s^{-1}$) as the 100% reference. See Experimental Methods: Biochemical assays for general assay conditions.

Activity assessment by absorbance-based assays of the LC-MS samples after 3.5 hr (the time lag is due to LC-MS confirmation on complete modification of R132H IDH1 with one

molecule of the compound and buffer exchange to remove the excess compounds) showed that the covalently modified wt IDH1 proteins derived from the LC-MS mixtures were all inactive (**Figure 6.5B**). However, this incubation duration of 3.5 hr is longer than what was used in the inhibition studies *i.e.* 12 min. A more suitable reference is the LC-MS results after 15 min incubation (**Figure 6.5A**). Approximately half of the wt IDH1 is covalently modified at 15 min by EVO820 and EVO725, but their $IC_{50}$ (12 min preincubation) against wt IDH1 is high at 2.6 µM and 3.5 µM respectively. Such discrepancies between covalent modification and inhibition could be due to samples for LC-MS being apo-protein deprived of (co)substrates, which may not reflect the dynamic reaction in the inhibition studies. In particular, the substrate-$Mg^{2+}$ complex may be important in stabilising the regulatory segment of wt IDH1[213] (as discussed in **Chapters 3** and **5**) to restrict binding of the Evotec inhibitors at the dimer interface of R132H IDH1.

## 6.3 Binding studies

### 6.3.1 Non-denaturing MS

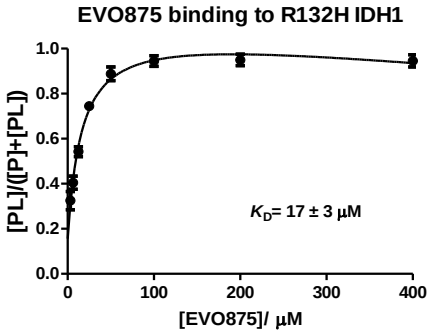



**Figure 6.6**. $K_D$ of EVO875 for R132H IDH1, as measured by non-denaturing MS. Cone voltage= 100 V. Buffer: 200 mM ammonium acetate, pH 7.5. See Experimental Methods: Protein non-denaturing MS for method details. The error bars represent the mean of three charge states (m/z= $18^+$, $19^+$ and $20^+$) ± SEM. The $K_D$ value is reported as mean ± SEM from the data fit by GraphPad Prism, from a plot of [PL]/([P]+[PL]) against the inhibitor concentration (3.125–400 µM), where [PL] is the peak intensity of the inhibitor-bound R132H IDH1 (a sum of both $PL_1$ and $PL_2$ as two molecules of EVO875 can bind to a R132H IDH1 dimer) and [P] is the peak intensity of R132H IDH1 only. Note that this method of $K_D$ calculation is different from what was used for **Table 5.2**, as binding saturation was achieved at high inhibitor:protein ratios in this case. Original non-denaturing spectra are presented in **Figure S6.3**.

Besides the denaturing LC-MS work described in **Section 6.2**, non-denaturing LC-MS was also conducted with the Evotec inhibitors to detect any non-covalent

interactions besides the observed covalent modifications. EVO875 (the non-covalent counterpart) and EVO725 were used as the model compounds, with EVO725 being chosen because its MW is most different from EVO875 to help distinguish between the two inhibitors in the subsequent competition studies. The $K_D$ of EVO875 for R132H IDH1 is 17 µM, as measured by non-denaturing MS using a titration curve (**Figure 6.6**). It is not meaningful to measure $K_D$ of the covalent inhibitors to R132H IDH1 as the observed binding is time dependent.

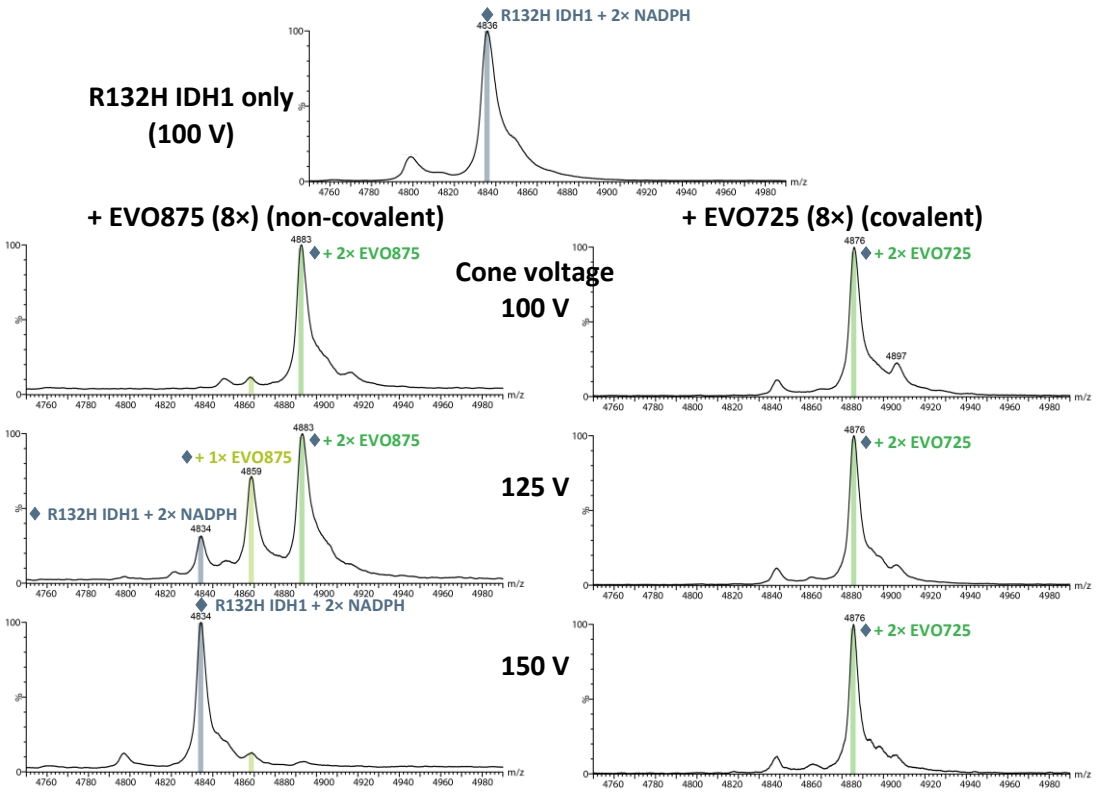



**Figure 6.7**. Mass spectrometric analysis (non-denaturing) of EVO875 and EVO725 binding to R132H IDH1 under different cone voltages. Data for the m/z= $20^+$ charge state are shown. Cone voltage= 100/ 125/ 150 V. Buffer: 200 mM ammonium acetate, pH 7.5. R132H IDH1: inhibitor= 50 µM: 400 µM for all. EVO725 was preincubated with R132H IDH1 for at least 5 min before running the sample. See Experimental Methods: Protein non-denaturing MS for method details. For clarity, only 2× NADPH bound protein peaks are annotated.

When the cone voltage was increased from 100 V to 150 V, distinct differences in the mass spectra were observed for R132H IDH1 preincubated with EVO875 and that with EVO725 (**Figure 6.7**). At 100 V, R132H IDH1 is saturated with binding of two molecules of EVO875 or EVO725 (after at least 5 min of preincubation to ensure complete modification). At 125 V, the increased energy applied to the sample weakens the binding of EVO875 such that protein bound with zero, one and two molecules of

EVO875 was observed. At 150 V, almost all binding of EVO875 to R132H IDH1 was lost as only the protein-only peak was observed. By contrast, EVO725 remains bound to R132H IDH1 at all tested cone voltages, likely due to the formation of a covalent bond.

Competition studies of EVO875 and EVO725 binding to R132H IDH1 were also conducted to investigate how the presence of a non-covalent inhibitor affects the covalent reactivity of EVO725, and similarly, how EVO725 affects the binding of the non-covalent inhibitor. In **Figure 6.8**, at 100 V, with increasing preincubation time of R132H IDH1, EVO875 and EVO725, the m/z peak (20+ charge state) corresponding to two molecules of inhibitors bound R132H IDH1 decreases from 4885 to 4880. As EVO725 (MW 414) has a lower molecular weight than EVO875 (MW 484), the decreasing m/z suggests a slow dominance of EVO725 binding to R132H IDH1. At 150 V, EVO875 binding to R132H IDH1 should be lost but EVO725 should remain bound, as shown in **Figure 6.7**. No inhibitor-bound protein peak was observed at 10 min of preincubation of R132H IDH1 with both EVO875 and EVO725, suggesting that EVO875 is the predominant binder to R132H IDH1. As the preincubation time increases, the peak intensity corresponding to the protein bound with one molecule of inhibitor, identified as EVO725 based on the mass difference, increases, suggesting that EVO725 is slowly covalently modifying R132H IDH1. Notably, the rate of covalent modification of R132H IDH1 by EVO725 is significantly diminished by the presence of EVO875. EVO725 can modify R132H IDH1 completely within 5 min in the absence of EVO875 (**Figure 6.7**). By contrast, in the presence of EVO875, full covalent modification of R132H IDH1 by EVO725 was not observed after 2 hr (**Figure 6.8**).

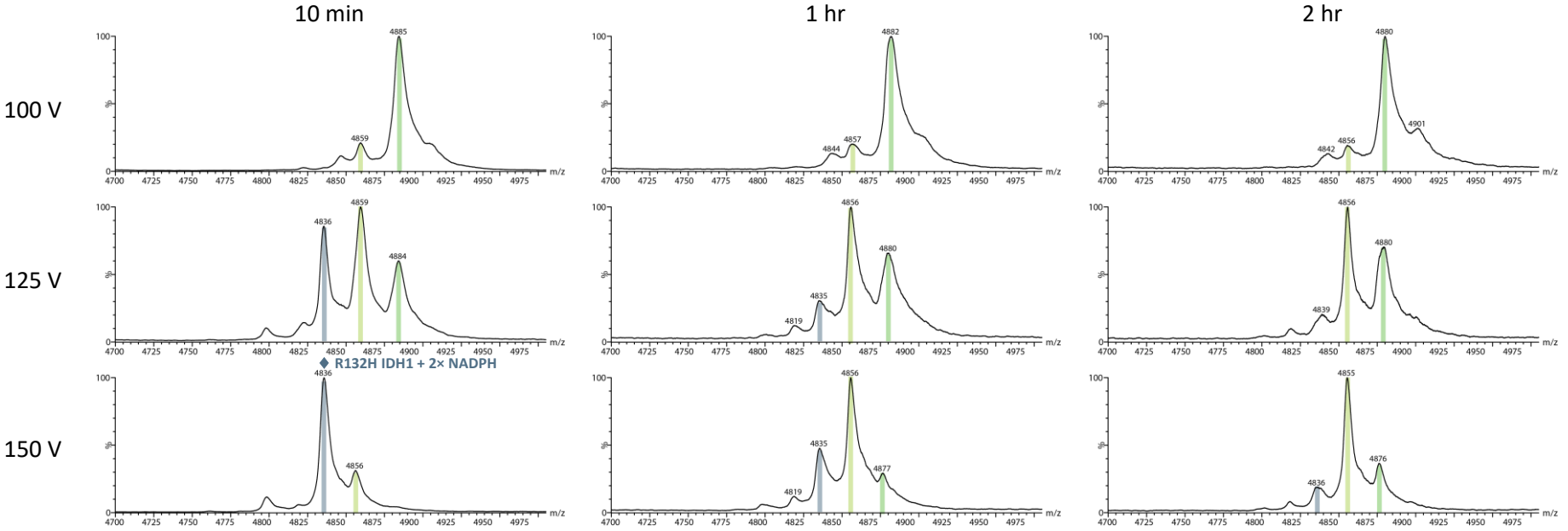



**Figure 6.8**. Mass spectrometric analysis (non-denaturing) of a mixture of EVO875 (400 µM) and EVO725 (400 µM) binding to R132H IDH1 (50 µM) under different cone voltages with different preincubation times (10 min/ 1 hr/ 2 hr) of the mixture. Data for the m/z= $20^{+}$ charge state are shown. Cone voltage= 100/ 125/ 150 V. Buffer: 200 mM ammonium acetate, pH 7.5. See Experimental Methods: Protein non-denaturing MS for method details. For clarity, only 2× NADPH bound protein peaks are annotated.

### 6.3.2 DSF

DSF studies were conducted to investigate the thermal stabilisation of wt IDH1 and R132H IDH1 by the Evotec inhibitors. As shown in **Figure 6.9A**, the DSF results imply that the Evotec inhibitors thermally stabilise wt IDH1 and R132H IDH1 to similar extents, consistent with the trend observed for other reported mIDH1 inhibitors (**Figure 5.4**). All the Evotec covalent inhibitors, EVO820, EVO725 and EVO869, achieved a significant thermal stabilisation of wt IDH1 and R132H IDH1 (8–10 °C) even at the lowest inhibitor concentration tested (3.125 µM). By contrast, the non-covalent counterpart, EVO875, showed a dose-dependent thermal stabilisation of R132H IDH1 by up to 6 °C.

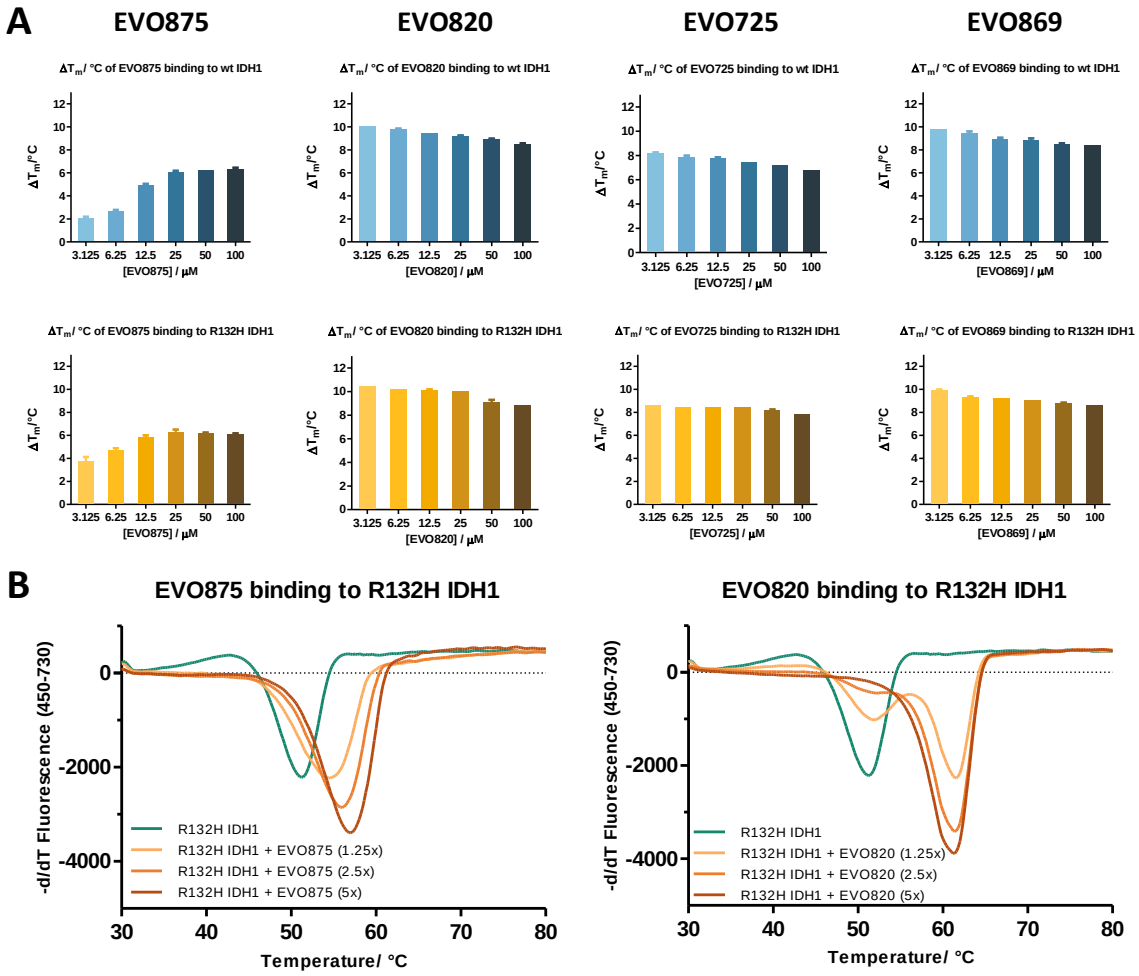



**Figure 6.9**. (**A**) Dose-dependent thermal stabilisation of wt IDH1 (blue gradient, 2.5 µM) and R132H IDH1 (orange gradient, 2.5 µM) by Evotec inhibitors (3.125 to 100 µM), in 50 mM Tris-HCl, pH 7.5, as measured by DSF. Data are mean ± SD, n= 3 technical replicates. (**B**) Negative derivatives of the raw melting curves (DSF) of R132H IDH1 (2.5 µM) with EVO875 or EVO820 (0, 3.125, 6.25 and 12.5 µM).

Interestingly, the melting curves revealed distinct features for non-covalent and covalent inhibitors (**Figure 6.9B**). The non-covalent R132H IDH1 inhibitor, EVO875, showed a dose-dependent rightward shift in the melting temperature with increasing inhibitor concentrations, whereas the covalent R132H IDH1 inhibitor, such as EVO820, have two distinct states corresponding to the non-modified and covalently modified R132H IDH1.

## 6.3 Summary

A set of non-selective (mainly selenium- and sulfur-based) and selective (from Evotec) covalent modifiers of R132H IDH1 were characterised for their interactions with R132H IDH1 and wt IDH1 in this chapter. All the covalent inhibitors have a time-dependent inhibitory activity on R132H IDH1, with EVO820 being the most potent and selective covalent inhibitor. Denaturing LC-MS studies suggest that the Evotec inhibitors are slow-reacting and modify only one cysteine residue of R132H IDH1 at the dimer interface, whereas the non-selective covalent modifiers can potentially modify all available cysteine residues of R132H IDH1. Non-denaturing MS showed that R132H IDH1 covalently modified with EVO725 can withstand increasing cone voltage applied to the protein. However, the covalent activity of EVO725 decreases drastically in the presence of the non-covalent competitor, EVO875, suggesting that they are competing for the same binding site. DSF studies demonstrated that once covalently modified by the Evotec covalent inhibitors, R132H IDH1 is significantly thermally stabilised. Overall, the formation of a stable inhibitor-protein complex implicates a sustained period of target inhibition, potentially preventing the development of drug resistance that may be a consequence of repeated periods of incomplete target inhibition[250]. Therefore, covalent inhibition of R132H IDH1 is an interesting strategy to pursue to combat the emerging drug resistance to current mIDH therapies.

## 6.4 Supplementary Figures

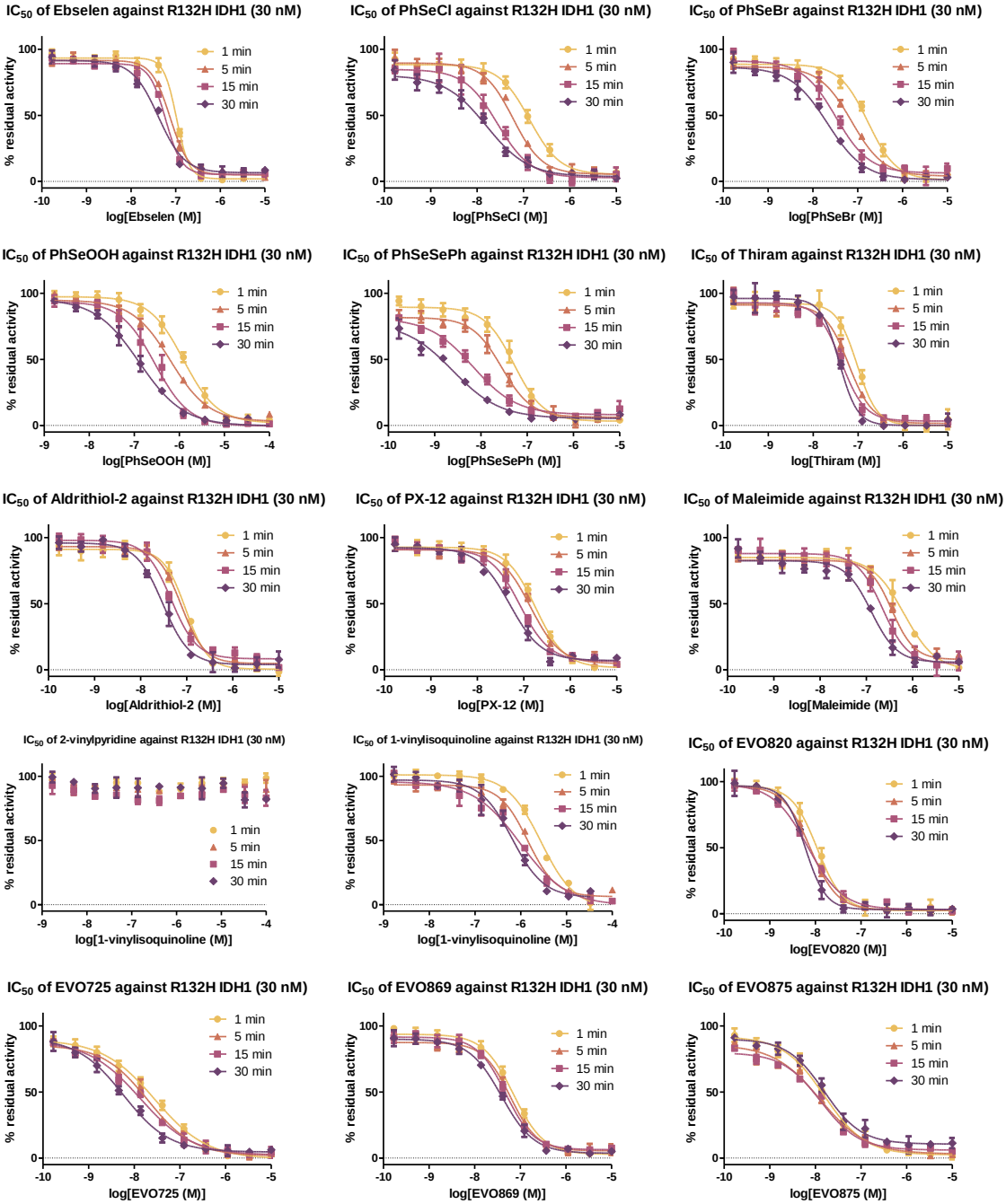



**Figure S6.1**. Time-dependent $IC_{50}$ graphs of cysteine-targeting covalent modifiers, covalent inhibitors of R132H IDH1 from Evotec, their vinyl warhead analogues and the non-covalent counterpart (EVO875) against R132H IDH1 (30 nM) in the conversion of 2OG to 2HG, as measured by absorbance-based assays. The error bars represent mean ± SD, n= 3 technical replicates. The $IC_{50}$ values are reported as mean ± SD from the data fit. Compounds and R132H IDH1 were preincubated for 1, 5, 15 and 30 min before initiating the reaction with 2OG and NADPH.

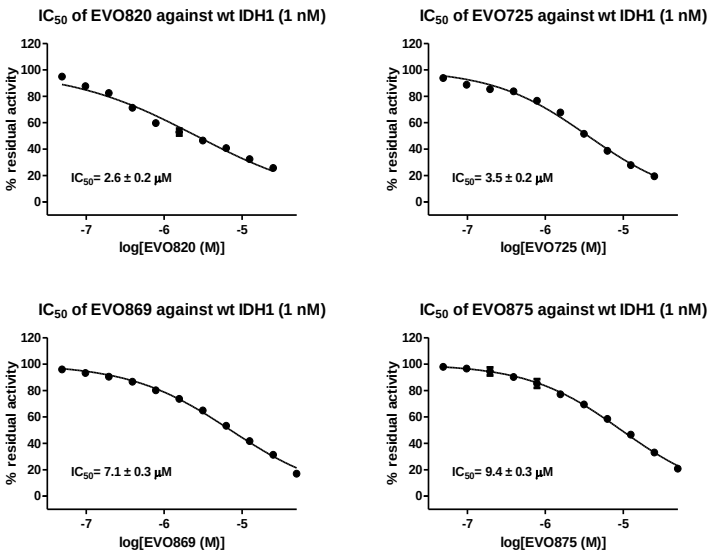



**Figure S6.2**. $IC_{50}$ graphs of covalent inhibitors of R132H IDH1 from Evotec and their non-covalent counterpart (EVO875) against wt IDH1 (1 nM) in the conversion of isocitrate to 2OG, as measured by absorbance-based assays. The error bars, some of which are too small to be visible, represent mean ± SD, n= 3 technical replicates. The $IC_{50}$ values are reported as mean ± SD from the data fit. See Experimental Methods: Biochemical assays for general assay conditions. Compounds and wt IDH1 were preincubated for 12 min before initiating the reaction with isocitrate and $NADP^+$.

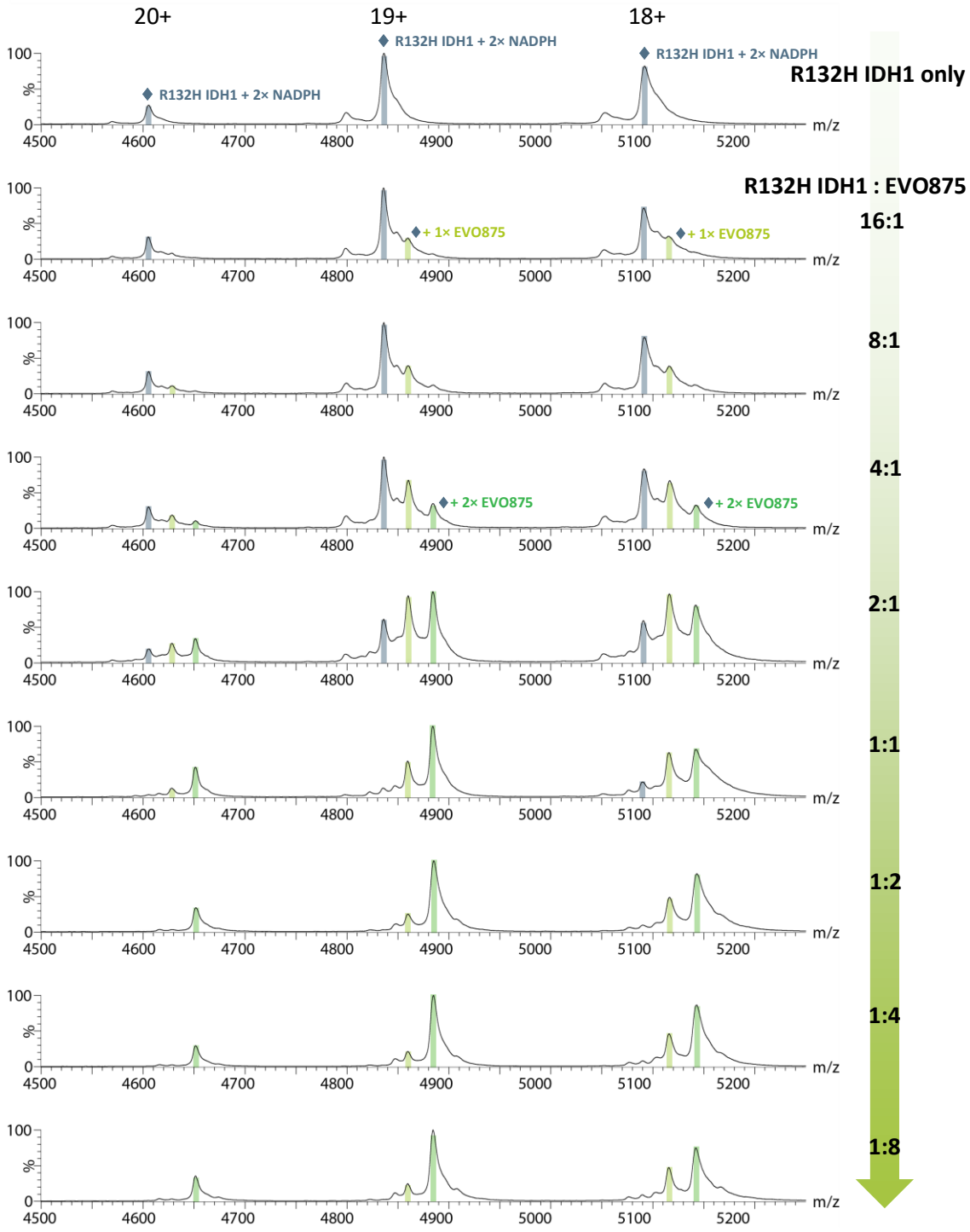



**Figure S6.3**. A series of non-denaturing MS spectra used to determine $K_D$ of EVO875 for R132H IDH1. Data for the m/z= $18^+$, $19^+$ and $20^+$ charge states are shown. Cone voltage= 100 V. Buffer: 200 mM ammonium acetate, pH 7.5. See Experimental Methods: Protein non-denaturing MS for method details. For clarity, only 2× NADPH bound protein peaks are annotated. The R132H IDH1 concentration is fixed at 50 µM whilst the EVO875 concentrations are increased from 3.125 µM to 400 µM with two-fold step changes.

# CHAPTER 7. TWO-WAY FUNCTIONAL 2OG ANALOGUES

It was highlighted in **Chapters 1**, **3** and **5** that all the potent ($IC_{50}$< 100 nM) mutant IDH inhibitors developed to date are allosteric[118,169,172,176,213]. The inherent inhibition mechanisms of mutant IDH seem to impose a 'natural selection' on the type of hit compounds generated from the various high-throughput screens. Future screenings using similar conditions will, quite possibly, continue to yield allosteric inhibitors for mutant IDH. However, the effectiveness of these allosteric inhibitors may be compromised by the emerged drug resistance, which involves a second-site mutation of the enzyme at the dimer interface in an attempt to eject the inhibitors[140].

Thus, alternative classes of mutant IDH inhibitors are desirable in the long term. A PROTAC approach for targeted R132H IDH1 degradation was described in **Chapter 5**, and covalent inhibitors of R132H IDH1 were described in **Chapter 6**. In this chapter, substrate (2OG) analogues of R132H IDH1 were investigated as potential active site inhibitors of mutant IDH, which can be achieved through rational drug design. Interestingly, during the course of this work, some 2OG analogues were observed to be alternative substrates for R132H IDH1.

## 7.1 TCA cycle intermediates and their analogues

Apart from the use of NOG as an inhibitor in the kinetic studies of IDH1[181], the activities of 2OG analogues on IDH1 have not been reported. Therefore, a set of TCA cycle intermediates and their analogues (**Figure 7.1**) was assessed for their activities against wt IDH1 and R132H IDH1 by absorbance-based assays. Most of the tested compounds are natural metabolites; it was envisaged that examining their activities may shed light on the metabolic changes associated with mutant IDH. All the compounds tested (**Figure 7.1**) were obtained from commercial sources.

The inhibitory effect of the compounds in **Figure 7.1** on wt IDH1 was first investigated. All the compounds were used at 1 mM, assaying for competition with DL-isocitrate (150 μM); note that only D-isocitrate is the active substrate as described in **Section 2.4.1**. As shown in **Figure 7.2A**, most of the compounds did not elicit any significant inhibitory effects towards wt IDH1.

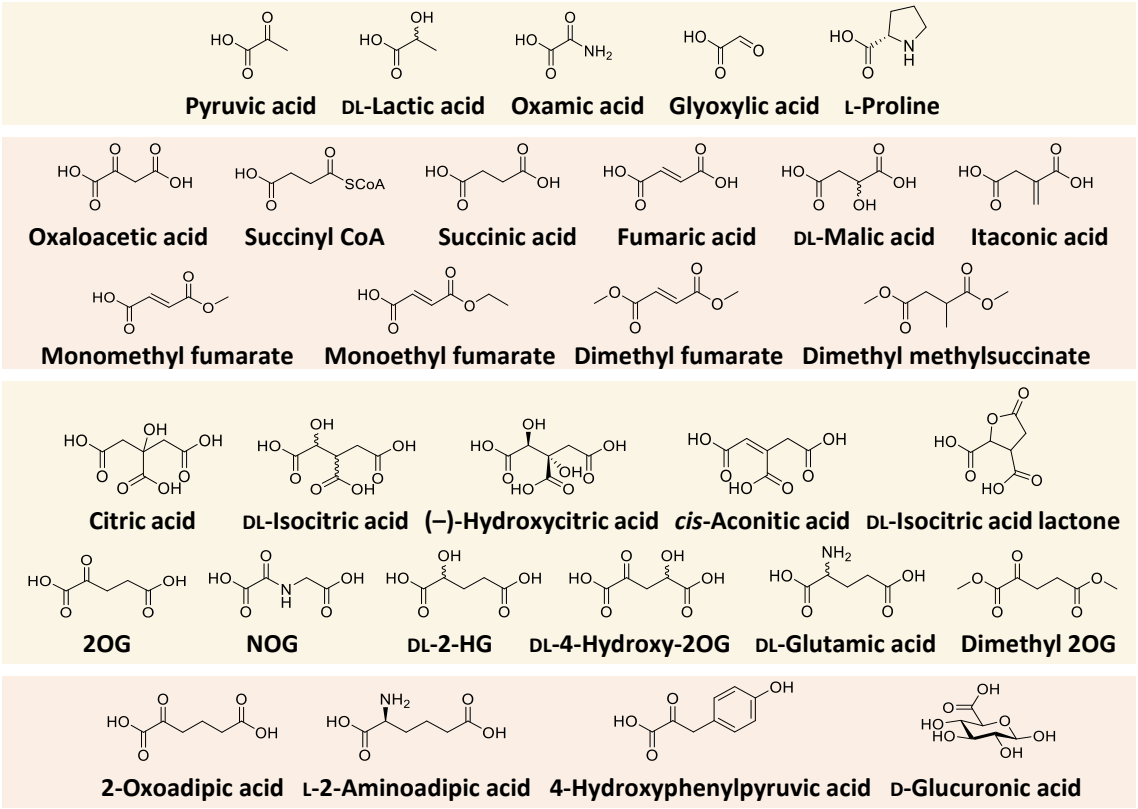



**Figure 7.1**. TCA cycle intermediates and their analogues investigated by absorbance-based assays, arranged generally in increasing backbone lengths. Note that the stereochemistry of hydroxycitrate was determined by Mukram Mackeen (Universiti Kebangsaan Malaysia), as the commercial vendor (Sigma-Aldrich) did not label this information clearly. All the compounds are shown in their acid form but in the assays some of them were used in their salt form.

The three compounds which exhibited (weak) inhibitory activities against wt IDH1 (**Figure 7.2A**) are 2OG (38% inhibition), NOG (29% inhibition) and 4-hydroxyphenylpyruvic acid (20% inhibition). 2OG is the product of wt IDH catalysed conversion of isocitrate. The 'inhibition' of wt IDH1 by 2OG is likely due to the presence of excess product that shifts the position of equilibrium for the reaction of wt IDH1 towards isocitrate. NOG is a 2OG analogue that has been reported to be an inhibitor of wt IDH1[181], so its inhibition on wt IDH1 was expected. 4-Hydroxyphenylpyruvic acid is the only compound amongst the tested that bears an aromatic group. The hydrophobicity of the phenyl group likely enhances its binding to the binding pocket of the protein that is often also hydrophobic. This may lead to the observed weak inhibition (20%) of wt IDH1 by 4-hydroxyphenylpyruvic acid.

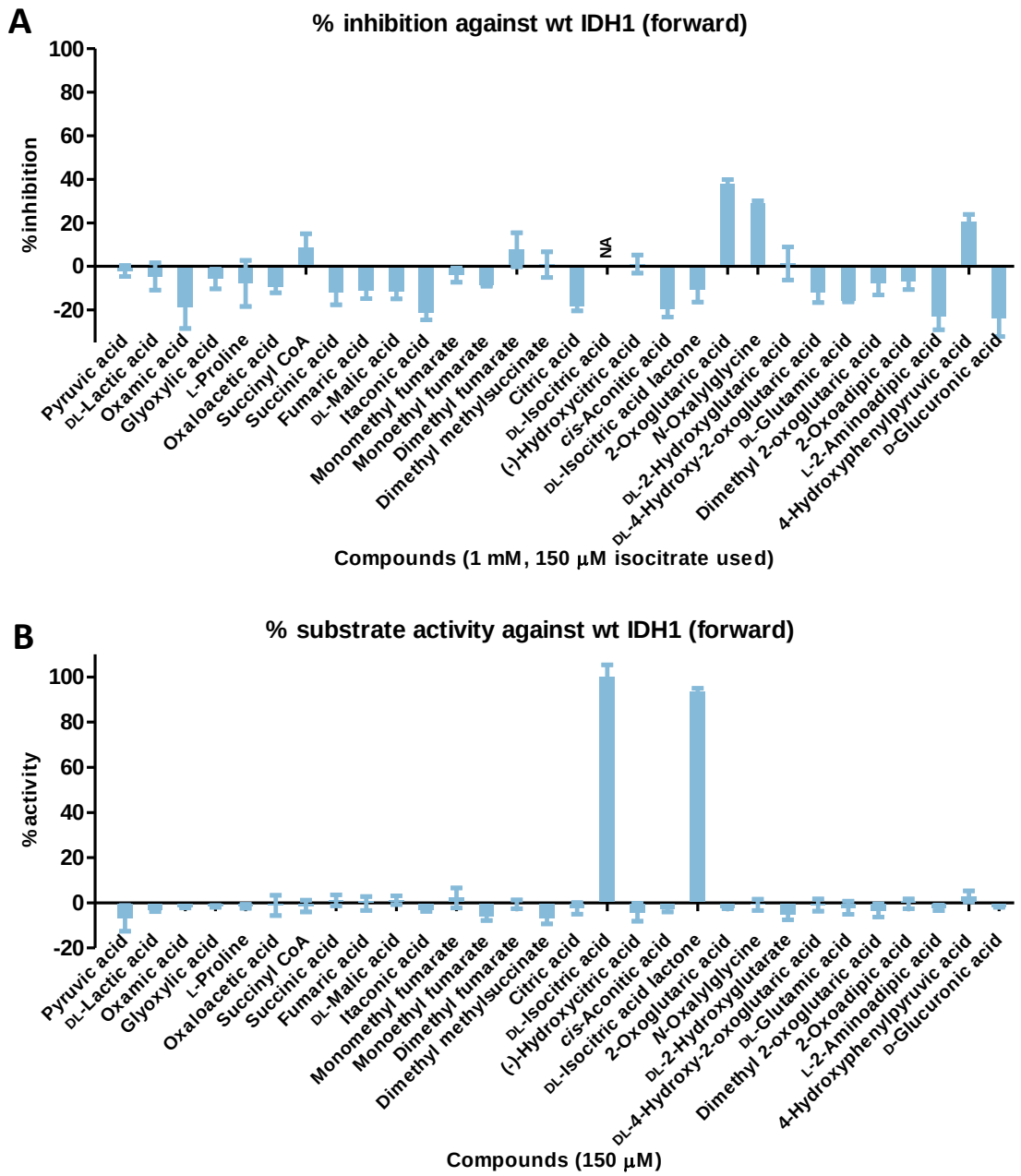



**Figure 7.2**. Activity of TCA cycle intermediates and their analogues (**Figure 7.1**) in wt IDH1 catalysed reactions, as measured by absorbance-based assays. Data are mean ± SD, n= 3 technical replicates. See Experimental Methods: Biochemical assays for general assay conditions. (**A**) The % inhibition of wt IDH1 catalysed conversion of isocitrate to 2OG. The compounds were tested at 1 mM, ~7× higher than DL-isocitrate (150 µM, but only D-isocitrate is the active substrate). The % inhibition is calculated by (1 – activity of (treated/buffer control)) × 100%. (**B**) The % substrate activity of wt IDH1 catalysed conversion of isocitrate to 2OG based on initial velocities of the reaction profile. The compounds were tested at the same concentration as DL-isocitrate (150 µM, but only D-isocitrate is the active substrate). The % activity is calculated by (activity of (treated/DL-isocitrate)) × 100%, using the activity of wt IDH1 with DL-isocitrate (0.24 µM $s^{-1}$) as the 100% reference.

Besides inhibiting wt IDH1, TCA cycle intermediates and their analogues may also be alternative substrates for wt IDH1. Therefore, their substrate activity in replacement of isocitrate was subsequently assessed by absorbance-based assays (**Figure 7.2B**). Apart from the natural IDH substrate isocitrate, isocitrate lactone was the only compound which showed significant substrate activity (93%) for wt IDH1. Isocitrate lactone may be first converted to isocitrate, enzymatically or non-enzymatically by hydrolysis[257]. This hypothesis has yet to be validated by MS and NMR spectroscopy.

Similarly, the inhibitory and substrate activities of the TCA cycle intermediates and their analogues were assessed by absorbance-based assays for R132H IDH1. All the compounds were tested at 10 mM to compete with the native substrate of R132H IDH1, 2OG (1.5 mM). In general, a higher % inhibition was observed for R132H IDH1 than for wt IDH1, likely because the absolute concentration (10 mM) of the compounds tested is 10× higher than that (1 mM) used for wt IDH1, so non-specific binding and/or pH deviations may be more apparent.

Compounds which showed >70% inhibitory activity on R132H IDH1 (**Figure 7.3A**) are succinyl CoA (80%), dimethyl fumarate (78% inhibition), (–)-hydroxycitric acid (89% inhibition) and NOG (95% inhibition). The adenosine, ribose and phosphate backbone in succinyl CoA is also found in the structure of NADPH, potentially making it a NADPH competitive inhibitor. Dimethyl fumarate is a prodrug of monomethyl fumarate and is used to treat psoriasis and multiple sclerosis[258]. (–)-Hydroxycitrate, an analogue of citrate and isocitrate, has been reported to be a potent inhibitor of ATP citrate lyase, and inhibits IDH, malate dehydrogenase and aconitate hydratase at millimolar concentrations[259]. Its reported inhibition of IDH is consistent with the findings in **Figure 7.3A**. Lastly, NOG, a 2OG analogue, has been reported to inhibit R132H IDH1[181]. The $IC_{50}$ of NOG was determined to be 227 ± 22 μM (**Figure S7.1**), and NOG is expected to be a 2OG competitor due to their structural similarity.

The substrate activity of the compounds of the TCA cycle intermediates and their analogues on R132H IDH1 was shown in **Figure 7.3B**. None of the tested compounds showed any significant substrate activity except for the native substrate of R132H IDH1, 2OG.

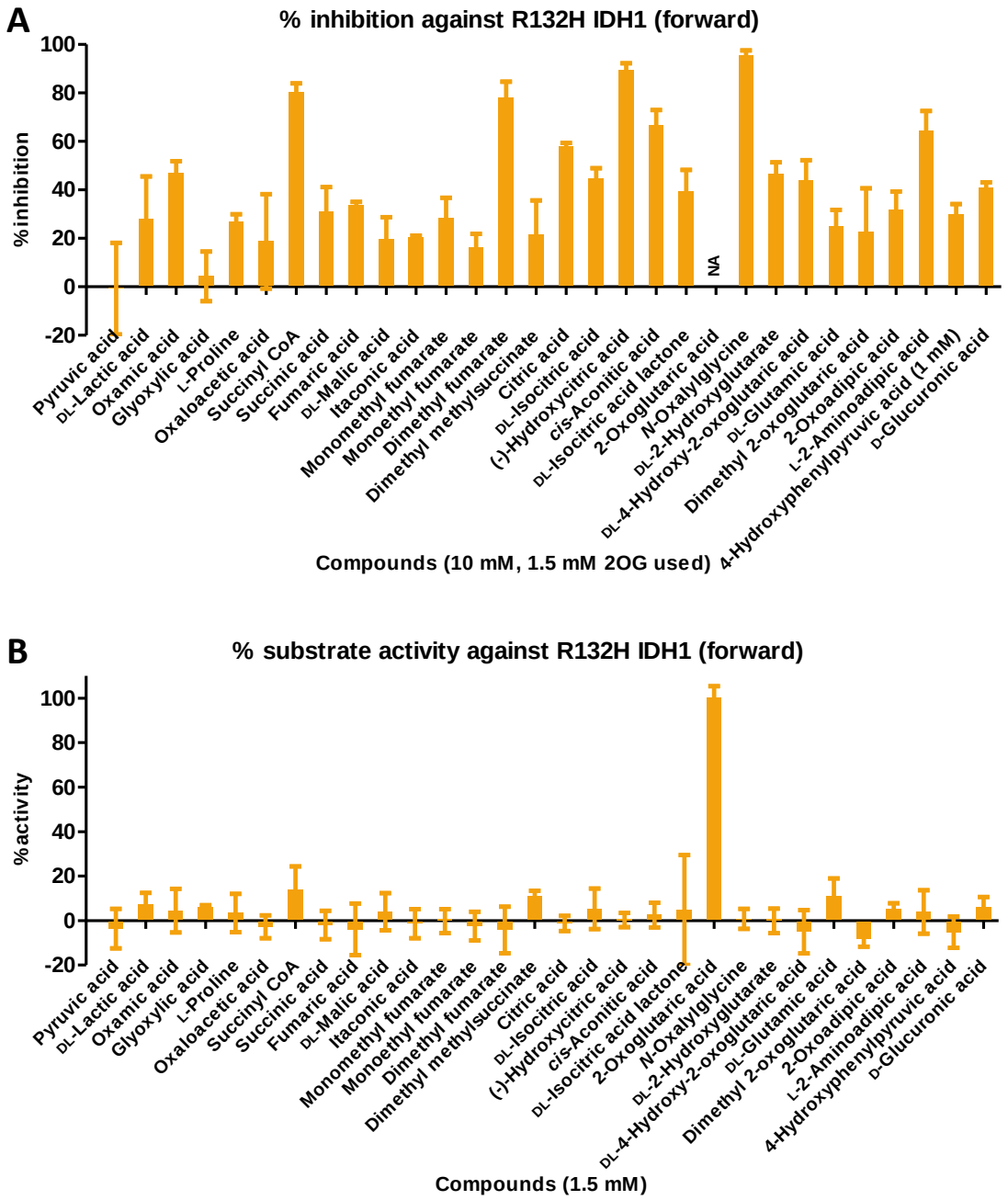



**Figure 7.3**. Activity of TCA cycle intermediates and their analogues (**Figure 7.1**) in R132H IDH1 catalysed reactions, as measured by absorbance-based assays. Data are mean ± SD, n= 3 technical replicates. See Experimental Methods: Biochemical assays for general assay conditions. (**A**) The % inhibition of R132H IDH1 catalysed conversion of 2OG to 2HG. The compounds were tested at 10 mM, ~7× higher than 2OG (1.5 mM). 4-Hydroxyphenylpyruvic acid was tested at 1 mM as its high absorbance interfered with the results at 10 mM. The % inhibition is calculated by (1 – activity of (treated/buffer control)) × 100%. (**B**) The % substrate activity of R132H IDH1 catalysed conversion of 2OG to 2HG based on initial velocities of the reaction profile. The compounds were tested at the same concentration as 2OG (1.5 mM). The % activity is calculated by (activity of (treated/2OG)) × 100%, using the activity of R132H IDH1 with 2OG (0.22 μM $s^{-1}$) as the 100% reference.

## 7.2 Synthetic 2OG analogues

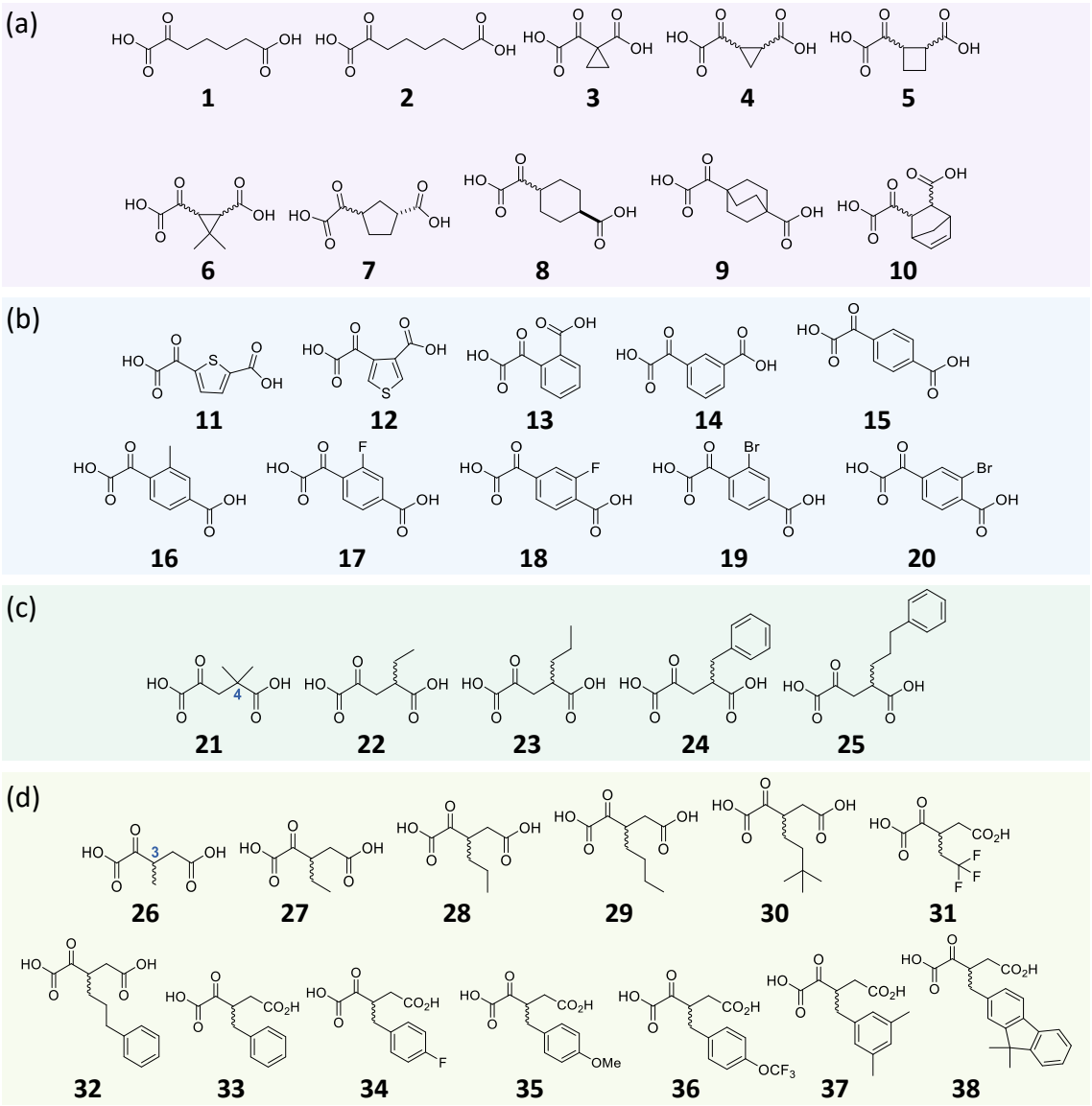



**Figure 7.4**. Synthetic 2OG analogues synthesised by co-worker, Lennart Brewitz and investigated by absorbance-based assays as substrates or inhibitors for IDH1. The compounds can be categorised into four subgroups based on their structural scaffolds: (a) varying lengths of carbon backbone joined by aliphatic chains or cyclic rings, (b) aromatic rings substituted with the ketoacid group, the carboxyl group and any additional functional groups, (c) 2OG substituted at the C-4 position, and (d) 2OG substituted at the C-3 position. The relevant carbon positions for categories (c) and (d) are labelled in blue (for compounds **21** and **26**). All the compounds are shown in their acid form but their dilithium salts were used in the assays.

The data on the inhibitory and substrate activities of TCA cycle intermediates and their analogues for R132H IDH1 suggested that 2OG analogues may be a good starting point to design 2OG competitive inhibitors and/or to discover alternative substrates for R132H IDH1. A set of non-naturally occurring 2OG analogues (**Figure 7.4**) was

synthesised by co-worker, Lennart Brewitz. All these analogues bear an α-ketoacid group on one terminal and a carboxyl group on the other terminal. They can also be categorised into four structural types: (a) varying lengths of carbon backbone joined by aliphatic chains or cyclic rings, (b) aromatic rings substituted with the ketoacid group, the carboxyl group and any additional functional groups, (c) 2OG substituted at the C-4 position, and (d) 2OG substituted at the C-3 position.

### 7.2.1 Biochemical studies on synthetic 2OG analogues

The inhibitory effect of the synthetic 2OG analogues on R132H IDH1 were first investigated. Surprisingly, a vast majority of 2OG analogues substituted at the C-3 position showed significant negative inhibition *i.e.* enhancement of R132H IDH1 activity, by as much as ~750% for the case of 3-butyl-2OG (compound **29**) (**Figure 7.5A**). It was hypothesised that the enhanced activity observed may be a result of these compounds being alternative substrates for R132H IDH1.

Subsequent assessment of the substrate activity of the synthetic 2OG analogues on R132H IDH1 (**Figure 7.5B**) revealed that, as expected, most of the compounds that show 'negative inhibition' of R132H IDH1 in **Figure 7.5A** are also substrates being converted by R132H IDH1. 3-Butyl-2OG has a substrate activity of ~450% with respect to 2OG (the reference for 100% activity) for R132H IDH1. Amongst the tested compounds, the 3-butyl substituent on 2OG appears to manifest the greatest enhancement in substrate activity for R132H IDH1, with the enhancement in substrate activity diminishing to ~270% for the 3-methyl- (compound **26**), 3-ethyl- (compound **27**) and 3-propyl- (compound **28**) substituents, and to <200% with other aromatic or branched substituents (compounds **31**–**38**). Besides the C-3 substituted 2OG analogues, the cyclopropyl- (compound **4**) and cyclobutyl- (compound **5**) analogues of 2OG also showed 64% and 49% substrate activity on R132H IDH1, respectively. These alternative substrates for R132H IDH1 suggest a possible use of R132H IDH1 in biocatalysis in the (potentially chiral) reduction of ketoacids.

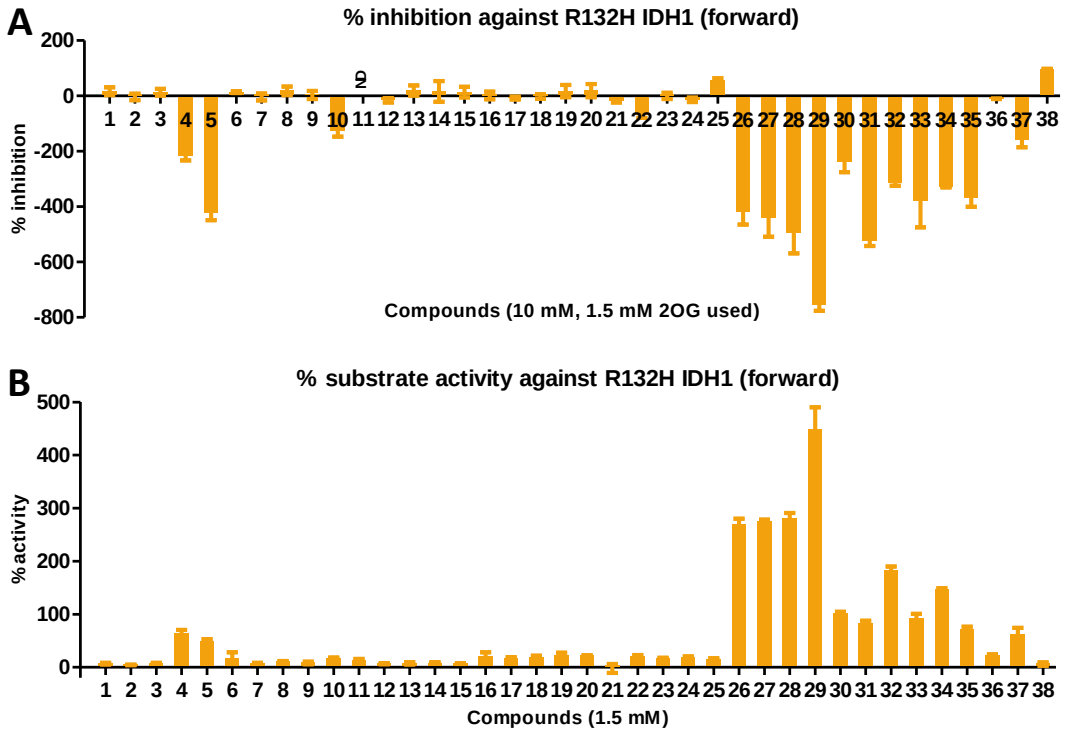



**Figure 7.5**. Activity of synthetic 2OG analogues (**Figure 7.4**) in R132H IDH1 catalysed reactions, as measured by absorbance-based assays using standard conditions as defined in **Table 2.2** (30 nM R132H IDH1 used instead). Data are mean ± SD, n= 3 technical replicates. (**A**) The % inhibition of R132H IDH1 catalysed conversion of 2OG to 2HG. The compounds were tested at 10 mM, ~7× higher than 2OG (1.5 mM). The % inhibition is calculated by (1 – activity of (treated/buffer control)) × 100%. (**B**) The % substrate activity of R132H IDH1 catalysed conversion of 2OG to 2HG based on initial velocities of the reaction profile. The compounds were tested at the same concentration as 2OG (1.5 mM). The % activity is calculated by (activity of (treated/2OG)) × 100%, using the activity of R132H IDH1 (30 nM) with 2OG (17 nM $s^{-1}$) as the 100% reference. ND: not determined due to strong absorbance of the compound at the tested conditions.

Notably, compound **38** demonstrated 96% inhibition and no substrate activity on R132H IDH1 (**Figure 7.5**), suggesting that it can be potentially developed into a substrate competitive inhibitor of R132H IDH1. Current drug resistance to IDH therapies involves a second point mutation at the dimer interface of mutant IDH1 to disrupt the binding of the allosteric inhibitors[140]. Arguably, substrate competitive inhibitors may also induce drug resistance in the form of a second mutation around the active site to displace the inhibitor. However, such a mutation at the active site would also likely result in a weaker binding of the native substrate, 2OG, to R132H IDH1, hence abolishing the neomorphic activity. The $IC_{50}$ of compound **38** against R132H IDH1 is 634 ± 11 µM (**Figure S7.1**) as measured by the absorbance-based assays. Structural analysis based on the published X-ray crystal structure of R132H IDH1[11] with 2OG and NADPH bound (**Figure S7.2**) shows

that compound **38** potentially exerts its inhibitory effect as a 2OG-NADPH transition state mimic, as its gem-dimethylfluorene side chain may extend into the NADPH binding pocket.

The inhibitory and substrate activities of the synthetic 2OG analogues (**Figure 7.6**) were also assessed for wt IDH1 using absorbance-based assays. Most of the compounds do not inhibit wt IDH1 (**Figure 7.6A**), except for compounds **36** (23% inhibition) and **38** (37% inhibition) which bear bulky (and relatively polar for compound **36**) substituents at C-3 of 2OG. The inhibition of wt IDH1 observed for compound **38** suggests that it is not very selective for R132H IDH1. Similar to the case for R132H IDH1, compounds **36** and **38** may be inhibiting wt IDH1 by occupying the $NADP^+$ binding pocket (the same pocket as NADPH for R132H IDH1).

Assessment of the substrate activity of the synthetic 2OG analogues (**Figure 7.6B**) revealed that none of the synthetic 2OG analogues are substrates for wt IDH1. This in turn reflects that the 2OG analogues which showed substrate activity for R132H IDH1 (**Figure 7.5B**) have good wt/mutant selectivity. Compared to isocitrate, the missing carboxyl group at the C-3 position in the 2OG analogues is probably crucial in conferring substrate activity for wt IDH1.

2OG is also a substrate for the wt IDH1 catalysed conversion of 2OG to isocitrate *i.e.* the reverse reaction. It was thus of interest to assess the substrate activity of the synthetic 2OG analogues in the reverse reaction catalysed by wt IDH1 (**Figure 7.6C**). By contrast with the case for R132H IDH1 (**Figure 7.5B**), 3-butyl-2OG is no longer an effective substrate for wt IDH1 in the reverse reaction. Smaller 2OG analogues, such as compounds **4**, **5**, **26** and **27**, are better substrates for wt IDH1. Notably, the reaction with the native substrate 2OG reached an equilibrium after ~15 min as the forward reaction of wt IDH1 comes into play, whereas these 2OG analogues showed a slow but continuous conversion without reaching an equilibrium, as measured by both their initial velocities and their conversions 2.5 hr after initiating the reaction. This implies that the products to which the synthetic 2OG analogues have formed cannot convert back to the original 2OG analogues.

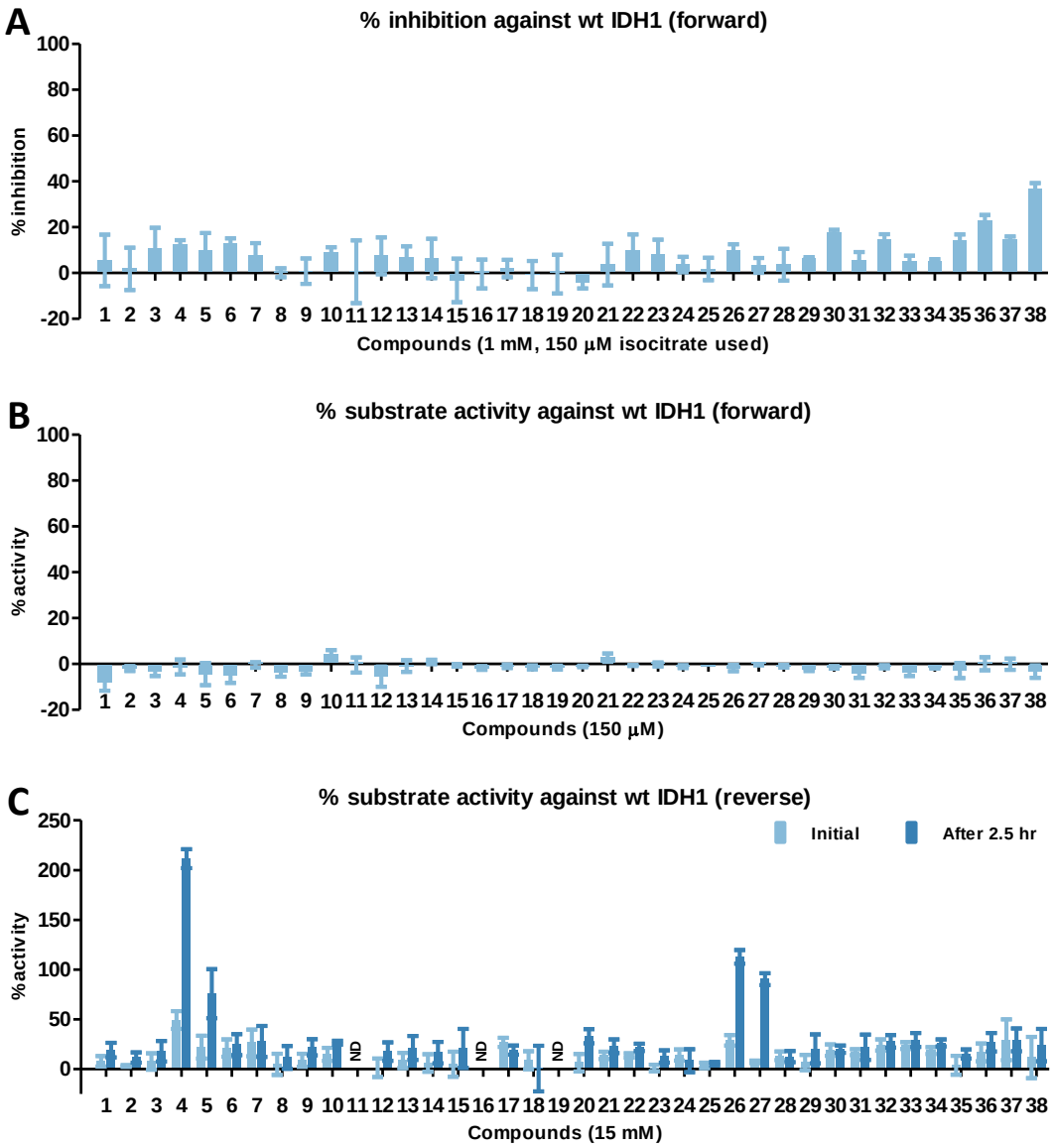



**Figure 7.6**. Activity of synthetic 2OG analogues (**Figure 7.4**) in wt IDH1 catalysed reactions, as measured by absorbance-based assays. Data are mean ± SD, n= 3 technical replicates. See Experimental Methods: Biochemical assays for general assay conditions. (**A**) The % inhibition of wt IDH1 catalysed conversion of isocitrate to 2OG. The compounds were tested at 1 mM, ~7× higher than DL-isocitrate (150 µM, but only D-isocitrate is the active substrate). The % inhibition is calculated by (1 – activity of (treated/buffer control)) × 100%. (**B**) The % substrate activity of wt IDH1 catalysed conversion of isocitrate to 2OG based on initial velocities of the reaction profile. The compounds were tested at the same concentration as DL-isocitrate (150 µM, but only D-isocitrate is the active substrate). The % activity is calculated by (activity of (treated/DL-isocitrate)) × 100%, using the activity of wt IDH1 with DL-isocitrate (0.15 µM $s^{-1}$) as the 100% reference. (**C**) The % substrate activity of wt IDH1 catalysed conversion of 2OG to isocitrate, measured with initial velocities (blue) or conversions 2.5 hr after initiating the reaction (dark blue). The compounds were tested at the same concentration as 2OG (15 mM). The % activity is calculated by (activity of (treated/2OG)) × 100%, using the activity of wt IDH1 with 2OG (0.38 µM $s^{-1}$ for initial rate; 0.15 µM $s^{-1}$ for 2.5 hr time point) as the 100% reference. ND: not determined due to strong absorbance and interference of the compounds at the tested conditions.

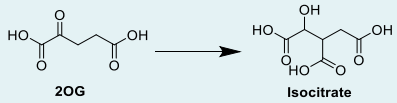
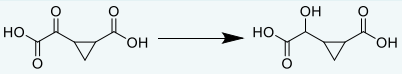
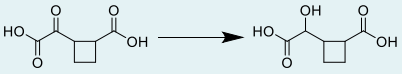
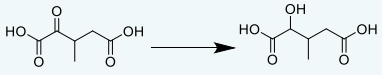
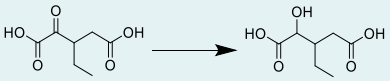
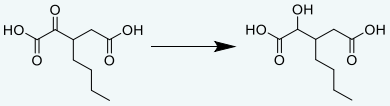
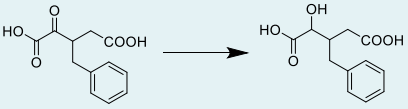
### 7.2.2 Product identification by Anion Exchange Chromatography-MS

The absorbance-based assays employed in **Section 7.2.1** only measure changes in the levels of NADPH, but cannot inform on the identity of the products of the wt IDH1 (**Figure 7.6C**) and R132H IDH1 (**Figure 7.5B**) catalysed reactions with the 2OG analogues. MS is a useful technique to identify products of such reactions, but the standard LCMS setup is not suitable to analyse these small and highly polar compounds. Hence, the products were analysed using anion exchange chromatography-MS (AEC-MS) by co-worker, John Walsby-Tickle.

Besides the positive control, 2OG, six 2OG analogues (compounds **4, 5**, **26**, **27**, **29** and **33**) were analysed for their products following wt IDH1 catalysed reverse reaction and R132H IDH1 catalysed forward reaction. Both reactions were quenched with 80% (v/v) MeOH after 2.5 hr. For the wt IDH1 catalysed reverse reaction, 2OG and its analogues are in a 10× molar excess relative to the cofactor, NADPH, based on the difference in the $K_M$ of 2OG and NADPH in **Table 2.1**. Hence, a theoretical maximum of 10% conversion of 2OG and its analogues should be observed. The actual conversion (**Table 7.1**) may be lower than 10% as it is an equilibrium reaction for 2OG, and the other 2OG analogues are chiral compounds for which only one isomer may be active.

2OG is converted mainly to isocitrate (a normalised conversion of 6.9%) by wt IDH1 in the presence of $NaHCO_3$, with a trace of 2HG (a normalised conversion of 0.34%) also being observed (**Table 7.1A**). For the 2OG analogues tested, the 'reverse' reaction with wt IDH1 is only a partial reaction, one in which the 2OG analogue is reduced but not carboxylated, thereby forming the 2HG analogues rather than the anticipated isocitrate analogues. This implies that even a small substituent, such as the methyl group of compound **26** at the C-3 position of 2OG, hinders the carboxylation reaction by wt IDH1. Interestingly, this essentially means that in the case of these compounds, wt IDH1 is catalysing the 'mutant reaction'. In fact, the neomorphic reaction of mutant IDH can be viewed as a wt IDH catalysing its reverse reaction without CO2, for which the absence may be a result of weakened binding caused by the R132H substitution. The relative substrate activity among the 2OG analogues, as measured by the % conversion by AEC-MS (**Table 7.1A**), is similar to that measured in absorbance-based assays (**Figure 7.6C**).

**A**

| Reactants for wt IDH1 | % 2HG analogues | % isocitrate analogues | Proposed reactions based on the AEC-MS results m/z $[M-H]^-$: theoretical/observed |
|---|---|---|---|
| 2OG | 0.0337 | 0.691 |  2OG → Isocitrate; 145.0/145.0 → 191.0/191.0 |
| **4** | 1.81 | 0 |  157.0/157.0 → 159.0/159.0 |
| **5** | 0.224 | 0 |  171.0/171.0 → 173.1/173.0 |
| **26** (3-methyl-2OG) | 0.517 | 0 |  159.0/159.0 → 161.0/161.0 |
| **27** (3-ethyl-2OG) | 0.433 | 0 |  173.1/173.0 → 175.1/175.1 |
| **29** (3-butyl-2OG) | 0.0158 | 0 |  201.1/201.1 → 203.1/203.1 |
| **33** | 0.00772 | 0 |  235.1/235.1 → 237.1/237.1 |

**B**

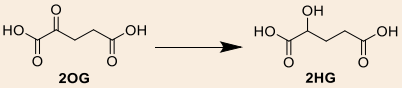
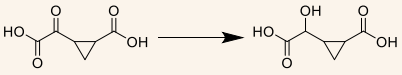
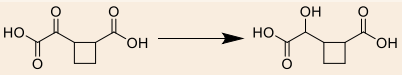
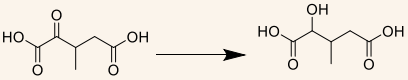
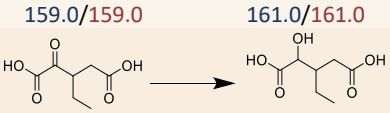
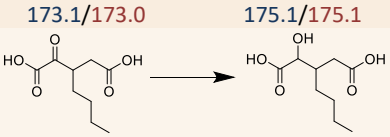
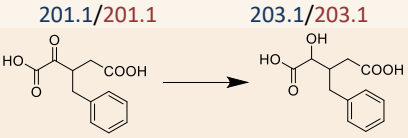
| Reactants for R132H IDH1 | % 2HG analogues | % isocitrate analogues | Proposed reactions based on the AEC-MS results m/z $[M-H]^-$: theoretical/observed |
|---|---|---|---|
| 2OG | 65.4 | 0 |  2OG → 2HG; 145.0/145.0 → 147.0/147.0 |
| **4** | 12.2 | 0 |  157.0/157.0 → 159.0/159.0 |
| **5** | 9.33 | 0 |  171.0/171.0 → 173.1/173.0 |
| **26** (3-methyl-2OG) | 51.4 | 0 |  159.0/159.0 → 161.0/161.0 |
| **27** (3-ethyl-2OG) | 47.0 | 0 |  173.1/173.0 → 175.1/175.1 |
| **29** (3-butyl-2OG) | 47.5 | 0 |  201.1/201.1 → 203.1/203.1 |
| **33** | 12.7 | 0 |  235.1/235.1 → 237.1/237.1 |

**Table 7.1**. Conversion of 2OG and its synthetic analogues by wt IDH1 and R132H IDH1, as measured by AEC-MS. (**A**) The % conversion of 2OG and its synthetic analogues by wt IDH1. Each sample submitted for AEC-MS includes 3 µL of reaction mixture containing 100 nM wt IDH1, 1 mM NADPH, 10 mM 2OG or its analogue, 100 mM $NAHCO_3$ and 10 mM $MgCl_2$ in 100 mM Tris-HCl, pH 8.0, diluted to 20 µL with water and then to 200 µL with 80% (v/v) MeOH 2.5 hr after initiating the reaction at r.t.. (**B**) The % conversion of 2OG and its synthetic analogues by R132H IDH1. The sample submitted for AEC-MS includes 20 µL of 400 nM R132H IDH1, 0.75 mM NADPH, 1.5 mM 2OG or its analogue, and 10 mM $MgCl_2$ in 100 mM Tris-HCl, pH 8.0, diluted to 200 µL with 80% (v/v) MeOH 2.5 hr after initiating the reaction at r.t.. The % conversion to 2HG or isocitrate analogues is calculated using peak areas of the corresponding compounds at different retention times, (product/(reactant + product)) × 100%, and is presented without normalising concentrations of the limiting reagent nor the effective concentrations of the active isomer of the 2OG analogues. See Experimental Methods: AEC-MS for method details.

The 2OG analogues were reduced to their corresponding 2HG analogues by R132H IDH1 (**Table 7.1B**). 2OG and its analogues are in a 2× molar excess relative to the cofactor, NADPH. A theoretical maximum conversion of 50% should be observed for all the tested compounds due to NADPH being the limiting reagent. A conversion of 65.4% (>50%) was observed for 2OG, possibly due to differences in the extent of MS ionisation of 2OG and 2HG. Compounds **26**, **27** and **29** reached the theoretical maximum conversion (~50%), which is expected from results of the absorbance-based assays (**Figure 7.5B**) as these 2OG analogues have higher substrate activities compared to 2OG.

### 7.2.3 Mechanistic studies by NMR spectroscopy

2OG analogues, such as 3-methyl- (compound **26**), 3-ethyl- (compound **27**) and 3-propyl- (compound **28**) 2OG, are reduced by R132H IDH1 to their corresponding 2HG analogues, with a significantly enhanced activity compared to 2OG, as measured by absorbance-based assays (**Figure 7.5B**) and AEC-MS (**Table 7.1B**). It was of interest to understand the mechanism of action behind the enhanced rate in the conversion of these 2OG analogues catalysed by R132H IDH1.

X-ray crystallography was conducted by co-crystallising 3-methyl- or 3-butyl-2OG with R132H IDH1. Multiple protein crystals (**Figure S7.3A**) with a lowest resolution of 1.8 Å were obtained, but the subsequent molecular replacement modelling by co-worker, Yu Nakashima, revealed that the electron density is missing for both the 2OG analogues and the nearby dimer interface of R132H IDH1. Nonetheless, the electron density for 3-

methyl-2OG in complex with R132H IDH1 was observed for one protein crystal with a relatively low resolution of 3.5 Å (**Figure S7.3B**). Although the absolute orientation of 3-methyl-2OG cannot be accurately determined at this resolution, the electron density of $Ca^{2+}$ was apparently shifted by ~6 Å further from the active site, coupled with the movement of 3-methyl-2OG from the original 2OG binding pocket. Overall, the flexibility at the dimer interface of R132H IDH1 with either the protein itself or the protein in complex with the 2OG analogues limited further insights into the mechanisms of action of the 2OG analogues using X-ray crystallography.

The reductive conversion of 2OG and 3-butyl-2OG catalysed by R132H IDH1 were subsequently monitored by $^{1}$H NMR (700 MHz) spectroscopy. Equimolar (1.5 mM) NADPH and 2OG/3-butyl-2OG were added to ensure the complete conversion of 2OG/3-butyl-2OG (**Figure 7.7A**). However, ~50% conversion was observed for 3-butyl-2OG at these conditions, implying that only one isomer of the enantiomeric 3-butyl-2OG is active substrate for R132H IDH1.

The reaction profile (**Figure 7.7A)** also revealed that the rate of conversion of 3-butyl-2OG catalysed by R132H IDH1 was fast initially but slowed down significantly with time. This seems to contrast with results using the absorbance-based assays (**Figure 7.5B**), which suggests that the conversion of 3-butyl-2OG is 4.5× faster than 2OG by R132H IDH1. However, 2OG and its analogues (1.5 mM) were used at a 30× molar excess of NADPH (50 μM) in the absorbance-based assays, which is essentially equivalent to the first ~200 s of the reaction profile shown in **Figure 7.7A** that could not be captured using the current setup for NMR reaction monitoring. The slowing down of the conversion of 3-butyl-2OG with time may be due to the reduced product of 3-butyl-2OG (**Table 7.1B**) exerting a negative effect on R132H IDH1 catalysis, *i.e.* there is a product inhibition effect. By contrast, 2HG possibly exerts no or a positive cooperativity on the R132H IDH1 catalysis.

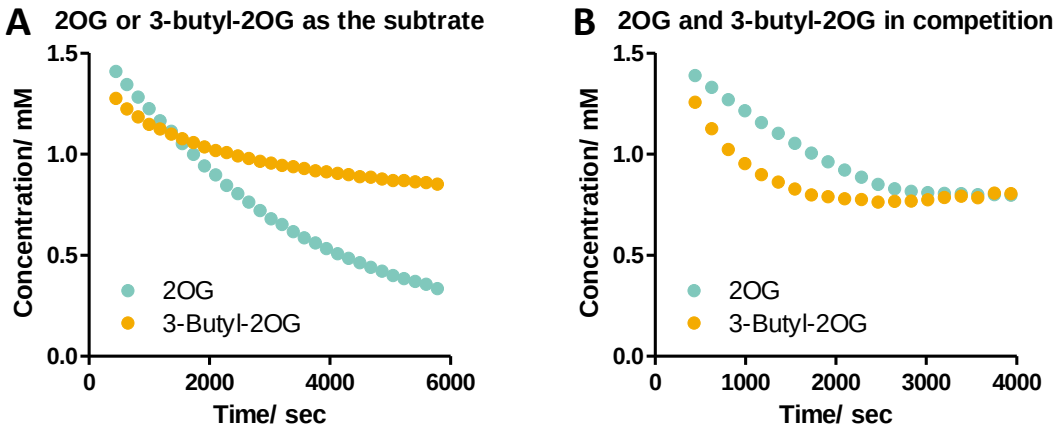



**Figure 7.7**. (**A**) Conversion of 2OG (green) or 3-butyl-2OG (compound **29**, orange) catalysed by R132H IDH1, as monitored by $^{1}$H NMR (excitation sculpting suppression with perfect-echo, 700 MHz). The conditions are 1 µM R132H IDH1, 1.5 mM 2OG or 3-butyl-2OG, 1.5 mM NADPH and 10 mM $MgCl_2$. (**B**) Competitive conversion of 2OG (green) and 3-butyl-2OG (orange) catalysed by R132H IDH1 in the same NMR tube, as monitored by $^{1}$H NMR (excitation sculpting suppression with perfect-echo, 700 MHz). The conditions are 1 µM R132H IDH1, 1.5 mM 2OG, 1.5 mM 3-butyl-2OG, 1.5 mM NADPH and 10 mM $MgCl_2$. Buffer: 50 mM Tris-$D_{11}$-HCl, pH 7.5 in 90% $H_2O$/ 10% $D_2O$ (v/v).

Competition studies of 2OG and 3-butyl-2OG were also conducted using $^{1}$H NMR (700 MHz) spectroscopy by having equimolar 2OG, 3-butyl-2OG and NADPH (1.5 mM each) in the same NMR tube. Half conversion of both 2OG and 3-butyl-2OG was observed (**Figure 7.7B**), as only one enantiomer of 3-butyl-2OG is active and the conversion of 2OG is limited by the remaining NADPH. The initial velocity of 2OG in the presence of 3-butyl-2OG (**Figure 7.7B**) is almost identical to (94% of) that in the absence of 3-butyl-2OG (**Figure 7.7A**). Unexpectedly, the initial velocity of 3-butyl-2OG in the presence of 2OG (**Figure 7.7B**) is 235% of that in the absence of 2OG (**Figure 7.7A**). In the case where 3-butyl-2OG and 2OG coexist in the same NMR tube (**Figure 7.7B**), the activity of 3-butyl-2OG is consistently higher compared to 2OG. This change in the activity of 3-butyl-2OG upon the addition of 2OG suggests a possibility that the conformation of R132H IDH1 bound with 2OG in one monomer of the dimer facilitates the reaction of 3-butyl-2OG in another monomer of the dimer *i.e.* positive cooperativity from the binding of 2OG. On the other hand, the binding of 3-butyl-2OG to R132H IDH1 is probably weaker compared to 2OG, or exerts no cooperativity effect on the reaction of 2OG.

## 7.3 Summary

The activities of TCA cycle intermediates and their analogues as well as synthetic 2OG analogues in wt IDH1 and R132H IDH1 catalysed reactions were investigated in this chapter. NOG and compound **38** were found to have micromolar inhibitory activities against R132H IDH1, suggesting the possibility of developing substrate competitive inhibitors of R132H IDH1, a promising approach to overcome the current drug resistance to allosteric inhibitors. Interestingly, several synthetic 2OG analogues such as 3-methyl-2OG (compound **26**) and 3-butyl-2OG (compound **29**) showed higher substrate activities for R132H IDH1 compared to 2OG, suggesting a potential use of R132H IDH1 in biocatalysis. The capability of 2OG analogues to act as either inhibitors or substrates of IDH1 depending on their structural designs highlights the utility of this class of compounds; their two-way functions could also be examined for other 2OG-dependent enzymes. Mechanistic studies of R132H IDH1 catalysed reactions using 2OG and 3-butyl-2OG as the substrates provided further evidence of crosstalk and cooperativity between the monomeric units of the R132H IDH1 dimer.

## 7.4 Supplementary Figures

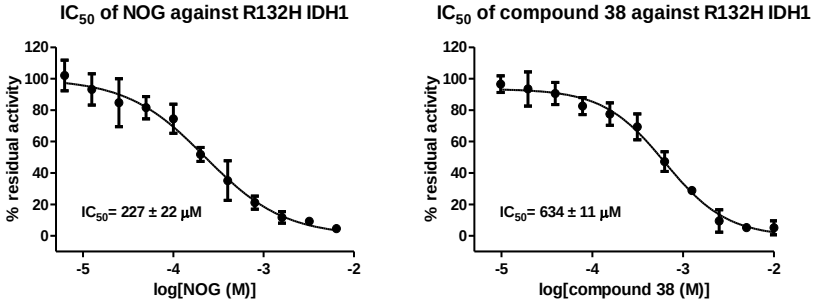



**Figure S7.1**. $IC_{50}$ graphs of NOG and compound **38** against R132H IDH1 (400 nM) in the conversion of 2OG to 2HG, as measured by absorbance-based assays. The error bars represent mean ± SD, n= 3 technical replicates. The $IC_{50}$ values are reported as mean ± SD from the data fit.

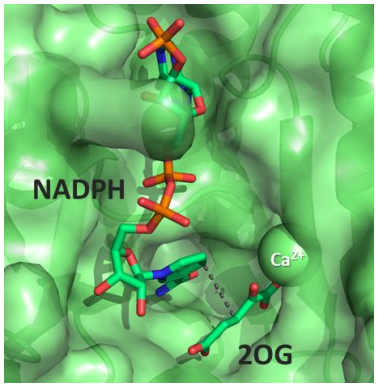



**Figure S7.2**. Active site view from an X-ray crystal structure of R132H IDH1 (PDB 3INM)[11] showing that the nicotinamide of NADPH is ~3.8 Å away from 2OG.

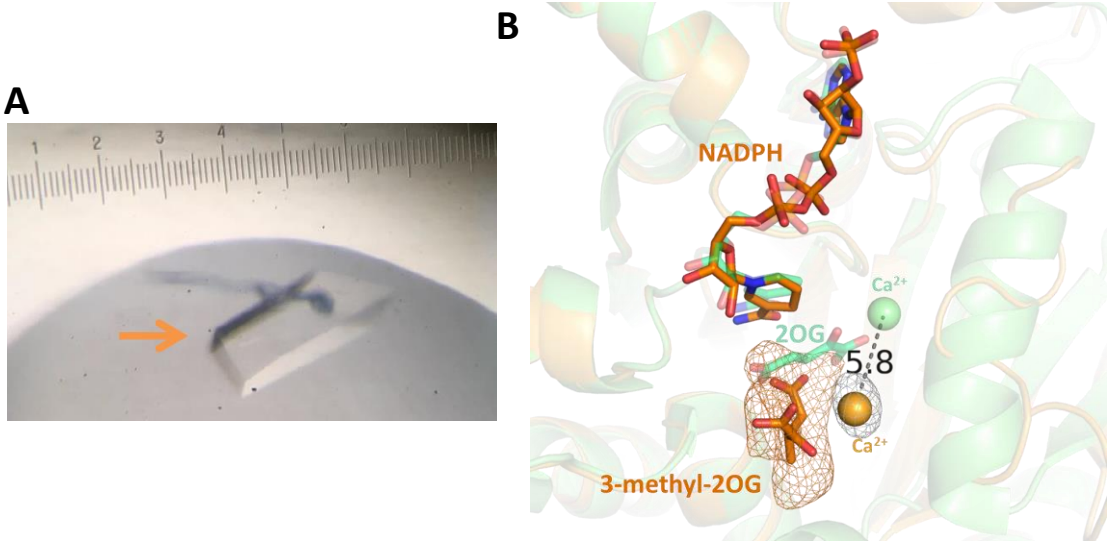



**Figure S7.3**. (**A**) An example of a protein crystal obtained from co-crystallisation of R132H IDH1 and 3-butyl-2OG. The conditions are 10.5 mg/mL R132H IDH1, 75 mM 3-butyl-2OG, 10 mM $CaCl_2$, 10 mM NADPH in 50 mM Tris-HCl, 200 mM NaCl, 5 mM DTT and 5% (v/v) glycerol, pH 7.5, mixed in 1:1 ratio with the reservoir solution containing 0.2 M ammonium sulfate, pH 5.0, 0.1 M Bis-Tris and 25% (v/v) PEG 3,350. (**B**) A view of the X-ray crystal structures of 2OG in complex with R132H IDH1 (green, PDB 3INM)[11] superimposed with 3-methyl-2OG in complex with R132H IDH1 (orange, in-house, 3.5 Å). The diffraction data were collected by Serena Rocchio and Stephanie Duclos from Evotec (Abingdon, UK) and the refinement was done by co-worker, Yu Nakashima.

# CHAPTER 8. CONCLUSIONS

The work described in this thesis uses chemical, biochemical and biophysical approaches to propel a deeper understanding of human IDH1 and its oncogenic variants. Due to the strong correlation between *IDH1* mutations and human cancers, the ultimate aim was to help the identification of clinically relevant therapeutic strategies to treat IDH bearing malignancies. Given the pivotal role of IDH in metabolism, it was also considered that improving our understanding of the mechanisms of IDH was of interest from a basic biological science perspective.

Cancer linked aspects of the biology of IDH were introduced in **Chapter 1**. The cellular impacts of *IDH* mutations in malignancies are multifaceted as demonstrated by the elevated levels of 2HG, the depletion of NADPH, the change in the levels of 2OG, and other downstream effects. Controversies on the clinical outcomes of current IDH therapies were evident from the paradoxically better prognosis associated with *IDH1* mutations in glioma patients[24,25,78,133–135]. Therefore, alternative inhibition strategies such as the inhibition of wt IDH might be beneficial under certain circumstances. A list of potent mIDH1 and mIDH2 inhibitors developed to date highlights the unusual phenomenon that they are all allosteric (**Table 1.2** and **Figure 3.18**), binding at the dimer interface of mIDH[118,169,172,176,213].

Studies on IDH1 began with the basic characterisation of wt IDH1 and R132H IDH1 using biochemical assays and various biophysical techniques, as described in **Chapter 2**. Despite similarity in their overall structures, differences in the kinetic parameters, the binding of (co)substrates (notably isocitrate), and pH dependences were observed between wt IDH1 and R132H IDH1. Importantly, profound differences in metal ion dependencies between wt IDH1 and R132H IDH1 were observed.

Investigations on the roles of metal ions in substrate binding and inhibition of IDH1 are described in more detail in **Chapter 3**. The application of complementary biophysical techniques, such as non-denaturing MS and $^{1}$H NMR spectroscopy, showed that divalent metal ions enable or enhance substrate binding with both wt IDH1 and R132H IDH1. The differential preference for metal ions by wt IDH1 and R132H IDH1

might be the biological reason behind the selectivity of mIDH1 inhibitors for mutant IDH1 over its wt counterpart. A key finding is that allosteric mIDH inhibitors likely work by displacing the catalytic $Mg^{2+}$, through an interaction cascade involving inhibitor-α helix-$Mg^{2+}$-substrate. Further efforts towards understanding the effects of $Mg^{2+}$ on IDH inhibition in cells is ongoing. The findings have informed the mechanistic basis for IDH1 inhibition and may reveal new opportunities for improved therapies through metal ion interference.

Inspired by the studies on the roles of metal ions that the actual substrate for wt IDH1 is the isocitrate-$Mg^{2+}$ complex rather than isocitrate, the interactions of metabolites and metal ions as well as the structures of their complexes in aqueous environment were investigated by various types of NMR spectroscopy, particularly DOSY, as described in **Chapter 4**. The findings provided new structural information on small molecule-metal complexes in solution, which is distinct from the published X-ray crystal structures. The results suggested that at equimolar isocitrate and $MgCl_2$, one $Mg^{2+}$ ion coordinates to one molecule of isocitrate to give a more symmetrical conformation of the isocitrate-$Mg^{2+}$ complex (**Figure 4.5**). Such a metal coordination effect was diminished for other TCA cycle intermediates including 2OG, fumarate and succinate, possibly shedding light on the role of divalent metal ions in regulating biological processes through complexation with substrates.

Even though many mIDH inhibitors are in clinical trials or on the market, there is still a lack of comprehensive and comparative studies on mIDH inhibitors. Moving towards the application side of the project, commercial mIDH inhibitors were assessed for their potency, selectivity, binding affinity and binding stoichiometry, as described in **Chapter 5**, which may be useful in selecting and designing better inhibitors. Complementary biophysical techniques such as DSF and $^1H$ NMR spectroscopy showed that mIDH inhibitors have similar binding affinities to wt IDH1 and R132H IDH1, despite their inhibitory selectivity for mutant IDH. Targeted degradation of mutant IDH was investigated by designing PROTAC compounds based on the mIDH inhibitors. Further optimisations are likely required for the PROTAC compounds, and such a therapeutic strategy remains promising due to its irreversibility.

Another irreversible therapeutic approach to altering mutant IDH activity is via the covalent inhibition, as described in **Chapter 6**. Covalent inhibitors can have improved potency and pharmacodynamics compared to their non-covalent counterparts. A number of selenium- and sulfur-based covalent modifiers were selected and their interactions with R132H IDH1 were characterised. In addition, covalent inhibitors from Evotec were found to be potent, selective and slow-reacting through one of the cysteine residues of R132H IDH1. Development of selective covalent inhibitors may help overcome the reported drug resistance to IDH therapies.

Lastly, potential new broad spectrum active site binding inhibitors based on 2OG analogues were investigated in **Chapter 7**. Current results suggest that a 2OG competitive inhibitor for R132H IDH1 could be designed as a transition state mimic of NADPH-2OG. Further optimisations are needed to improve the potency of the inhibitors. Interestingly, some 2OG analogues were found to have higher substrate activity for R132H IDH1 than the native substrate, 2OG, suggesting a potential use of R132H IDH1 in biocatalytic reduction of ketoacids. Further research could also transform these 2OG analogues into useful chemical probes to study the mechanism of action of mutant IDH, both *in vitro* and *in vivo*.

# APPENDIX

## Novel approaches for antibody-based targeted drug delivery

### A.1 Introduction

The clinical use of most potent drugs in cancer chemotherapy is limited by their non-specific action against all rapidly dividing cells, resulting in toxicity to both cancerous and healthy cells. Strategies to reduce such side effects by targeting the drugs to tumours are thus crucial. Antibody-drug conjugates (ADCs) have shown promise in this regard[260]. In this approach, a monoclonal antibody (mAb) which binds to a specific antigen on the surface of tumour cells is covalently linked to a highly cytotoxic agent to display target-specific cytotoxicity. Upon antigen binding, the ADC is internalised by endocytosis and degraded inside the cell to release the cytotoxic agent, thereby killing the tumour cells[261].

The key characteristics for an optimal ADC are shown in **Figure A1**. Ideally, the antibody should have high affinity and specificity to the antigen that is highly expressed and exclusive to the surface of tumour cells but not normal cells. The cytotoxic agent should be highly potent to effectively kill the tumour cells. The linker which covalently joins the cytotoxic agent and the antibody should be stable in the blood circulation, such that the cytotoxic agent is only released after the antibody-carrying drug reaches the tumour site.

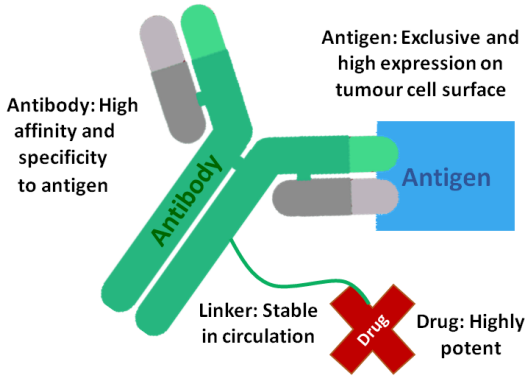



**Figure A1**. Desired key characteristics for an ADC.

Only four ADCs have achieved clinical applications[262], whilst the others have been unsuccessful as they showed no therapeutic benefit of targeted delivery[263]. This can be attributed to low potency of the drug, expression of the antigen on normal tissues, non-specific cleavage of the linker or ineffective internalisation (a process which is still poorly

understood)[260]. This led to my interest in exploring approaches based on extracellular drug production, which would hopefully circumvent problems associated with internalisation and intracellular enzymatic degradation of ADCs.

With the aim to develop novel approaches for antibody-based targeted drug delivery, this work began with a literature research to select potential strategies and model systems. It was anticipated that a proof-of-principle for the chosen approaches could be achieved eventually, to produce a new generation of targeted therapeutics for treating cancer and even other diseases in the long term.

## A.2 The model system and the strategies employed

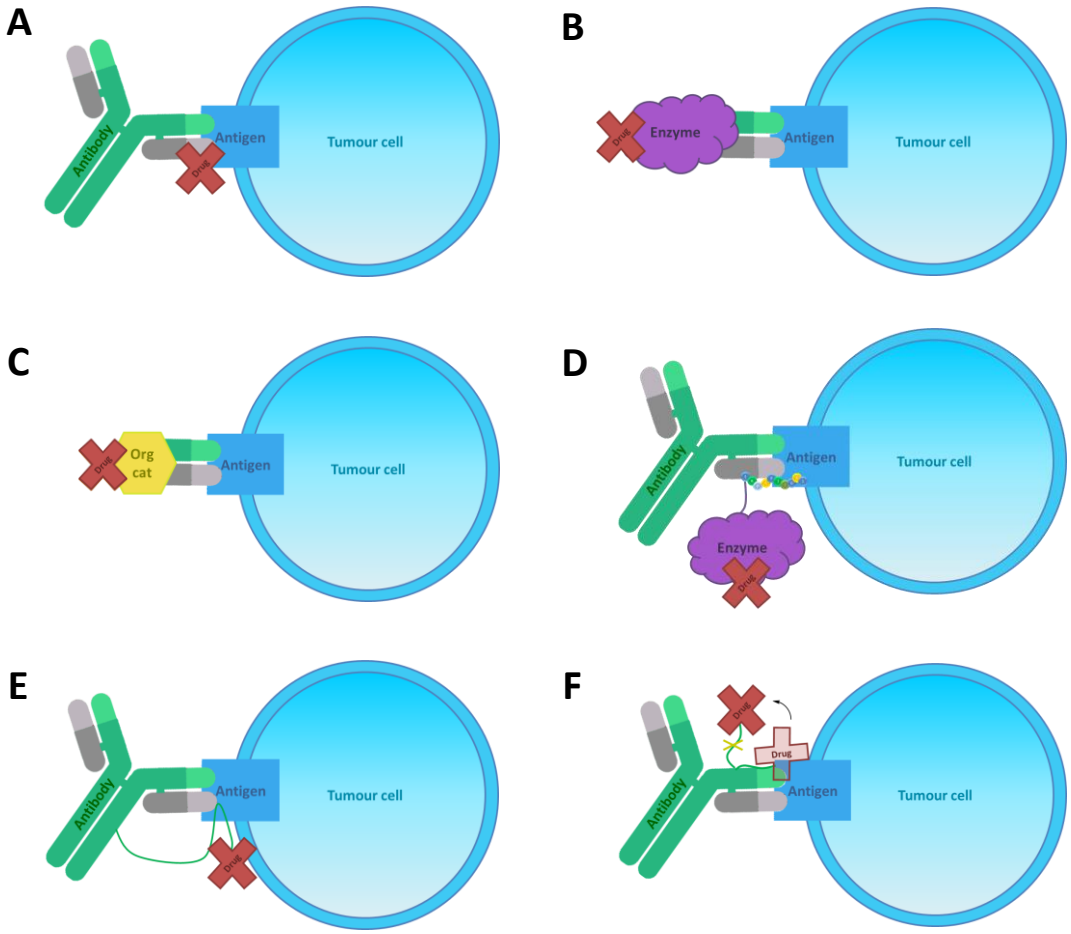



**Figure A2**. Illustrations of various approaches for antibody-based targeted drug delivery.

Multiple approaches were proposed initially for antibody-based targeted drug delivery. One of these approaches (**Figure A2.A**) envisioned the synthesis of the toxic antitumour drug at the site of the tumour using the antibody-antigen complex as a catalyst. However, a survey of the literature showed that there are very few catalytic

antibodies in nature, and designing an antibody, let alone an antibody-antigen complex, with biocatalytic functions *de novo* would be challenging.

Another approach (**Figure A2.B**) would be having an inactive enzyme grafted to the antibody paratope (part of the antibody which recognises and binds to an antigen). The enzyme can then be activated upon paratope binding to the antigen and catalyse the conversion of a pro-drug to an active drug, which is then released into the tumour cells by diffusion. However, there is limited known one-step reaction for the enzymatic conversion of pro-drugs to active drugs.

Alternatively, an organocatalyst can be conjugated to the antibody paratope and catalyse the conversion of a pro-drug to an active drug (**Figure A2.C**). Unfortunately, the reactions types that can be achieved by known water-compatible organocatalysts are limited to Michael or Aldol reactions[264–270], which are not relevant for the conversion of pro-drug to drug in most cases.

A fourth approach (**Figure A2.D**) would be to find a peptide that binds specifically to the interface of the antibody-antigen complex. The peptide can then be covalently linked to an enzyme that catalyses the conversion of a pro-drug to an active drug, which is then released into the tumour cells by diffusion. This approach greatly relies on the specificity of the peptide to the antibody-antigen complex, which can be difficult to design.

The fifth approach (**Figure A2.E**) is to have the active drug covalently linked to an antibody, as of ADC. The linker should be designed to be cleaved by a nucleophile *e.g.* cysteine or lysine on the antigen epitope upon antibody binding to antigen. This approach still faces the risk of non-specific nucleophilic cleavage of the linker in blood circulation and requires specific positioning of the cysteine or lysine on the antigen.

The sixth approach (**Figure A2.F**) also has the active drug covalently linked to an antibody, as of ADC. In this case, the linker itself is designed to bind to the antibody with high affinity such that it is not exposed in blood circulation. Binding of the antibody to the antigen leads to a conformational change of the antibody, causing displacement of the linker which is then exposed to cleavage by extracellular proteases to release the drug.

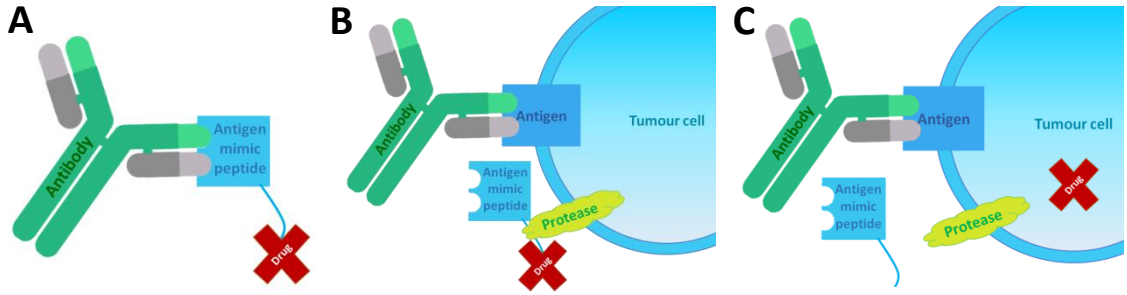



**Figure A3**. Schematic representations of the chosen initial approach. (**A**) Noncovalent binding between the mAb and the AMP-drug conjugate. (**B**) Displacement of the AMP-drug conjugate by the antigen upon binding, followed by cleavage of the linker by extracellular protease overexpressed on the tumour cell. (**C**) Active drug released into the tumour cell by diffusion.

In the final chosen approach (**Figure A3**), the covalent linkage which joins the cytotoxic agent to the mAb in conventional ADCs is replaced with a noncovalent interaction between the mAb and an antigen mimicking peptide (AMP) that is covalently linked to a cytotoxic drug. The affinity of this interaction should be high enough for the AMP-drug conjugate to remain bound to the mAb in circulation, but weaker than the binding affinity between the mAb and its natural antigen, allowing the AMP to be displaced by the antigen at the tumour site. The displaced AMP-drug conjugate is likely too large to be cell permeable and has less chance to be cleaved around normal cells where the specific proteases are not overexpressed, thereby reducing the toxic effects of the drug should it dissociate from the mAb prior to reaching the tumour site. The linker could be cleaved by extracellular proteases *e.g.* cathepsin B[271] overexpressed on tumour cells, releasing the active drug into the tumour cell by diffusion.

Examples of both mAb-binding AMP[272,273] and protease-cleavable peptide-drug conjugates[274] have been reported. However, the former was mainly applied as vaccines and the latter faced specificity problems. This approach combined both concepts by targeting delivery of the mAb-AMP-drug conjugates to the tumour cells. The chosen model system was Herceptin (trastuzumab) as the mAb, and human epidermal growth factor receptor 2 (HER2) as the antigen, due to their clinical relevance, availability of crystal structures[275–277], high binding affinity ($K_D$= 0.1 nM)[278] and tumour-specific overexpression of HER2[279].

## A.3 Results

### A.3.1 Preparation of Fab

The antigen-binding fragment (Fab) instead of full-length Herceptin was produced since the Fab retains the binding specificity of full-length Herceptin while reducing the complexity of the whole antibody. The smaller size of Fab will facilitate future biophysical studies such as NMR spectroscopy, which would elucidate the binding interactions between Herceptin and the AMP-drug conjugate. The Herceptin Fab could not be overexpressed in *E. coli* expression systems, such as using BL21(DE3) or Rosetta™ 2(DE3) cells. However, it was prepared by papain digestion[280,281] of the clinical grade Herceptin (**Figure A4**).

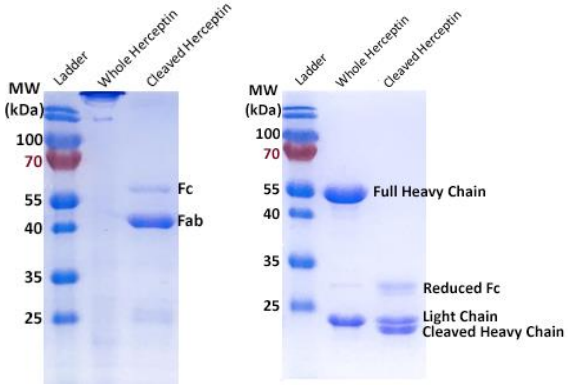



**Figure A4**. SDS-PAGE gels of Herceptin Fab obtained by proteolytic digestion of Herceptin with papain, under non-reducing (left) and reducing (right, added 10% (v/v) β-mercaptoethanol) conditions.

### A.3.2 Binding studies between Herceptin and HER2

BLI[282] (**Figure A5.A**) and AlphaScreen™ [283] (**Figure A6.A**) assays were developed to study the binding between Herceptin and HER2; these studies would serve as an initial line of investigation, allowing for subsequent binding studies of AMP to Herceptin. Note that the full-length Herceptin was used in both BLI and AlphaScreen™ assays, as the Fc region was required to immobilise Herceptin to the protein A/G-coated biosensor tips or donor beads. BLI showed that HER2 binds to Herceptin with a $K_D$ of 0.20 ± 0.13 nM (**Figure A5.B**). The conditions for AlphaScreen™ were optimised (**Figure A6.B**) and a competition experiment was conducted using the untagged HER2 and the His-tagged HER2. The untagged HER2 inhibited the binding of His-tagged HER2 (immobilised to the nickel chelate acceptor beads) to Herceptin (immobilised to the protein A donor beads) with an $EC_{50}$ of 13.0 ± 1.3 nM (**Figure A6.C**). The untagged HER2, which was used as a control for this competition study, could be replaced with any AMPs to validate their binding to Herceptin.

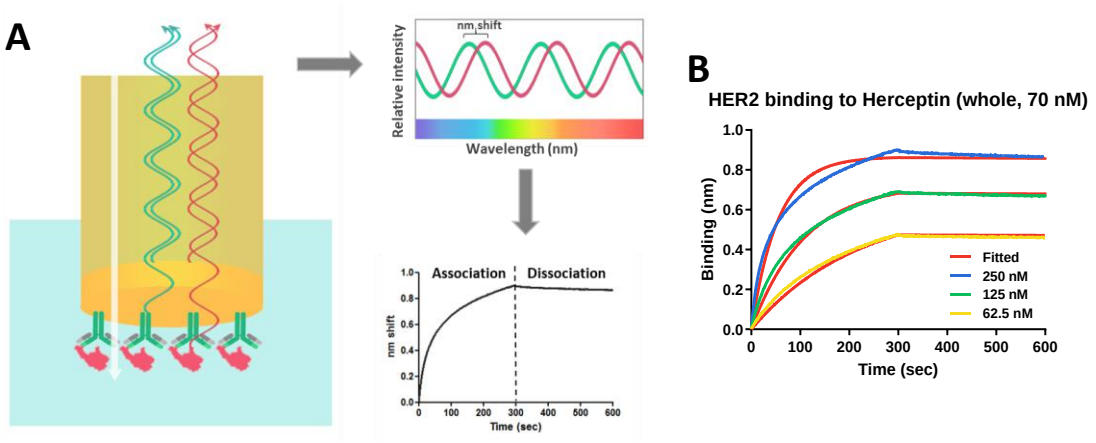



**Figure A5**. (**A**) The working principle of BLI. In this case, Herceptin is immobilised on the protein G-coated biosensor tip. Binding of HER2 to Herceptin increases the optical thickness at the biosensor tip, resulting in a shift in the interference pattern of the beam and generating a response profile. HER2 can be replaced by a peptide to measure the binding affinity of the peptide to Herceptin. (**B**) Binding of HER2 (62.5, 125 and 250 nM) to immobilised full-length Herceptin (70 nM), in PBS, pH 7.4, as measured by BLI.

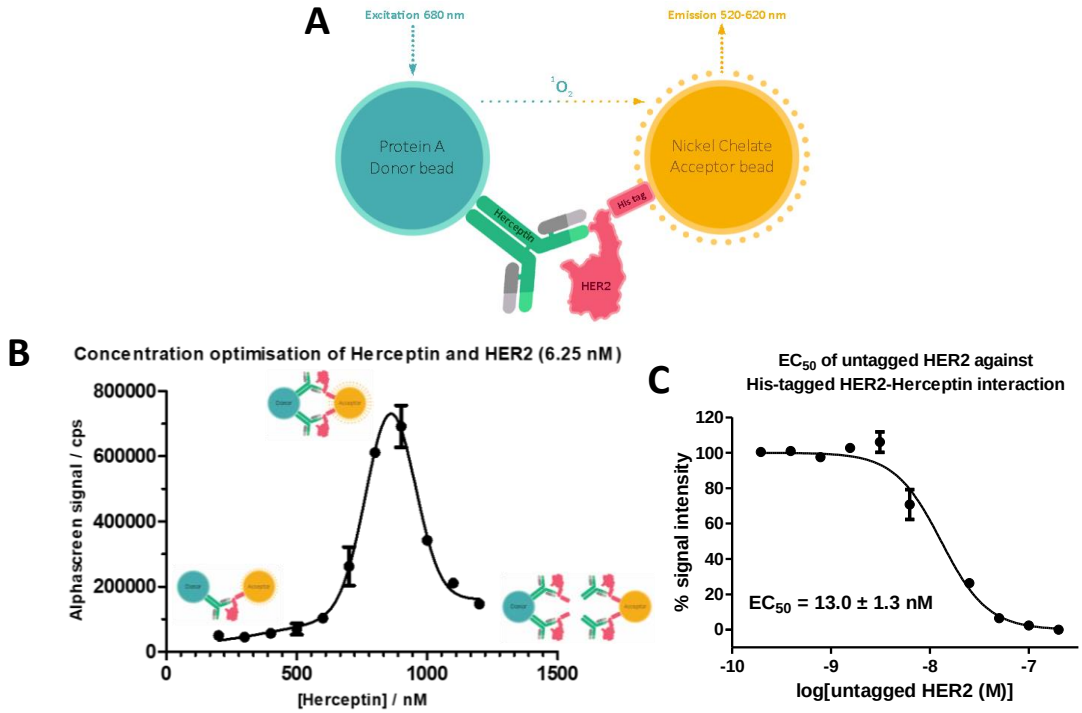



**Figure A6**. **(A)** Set up of the AlphaScreen™ assay. Upon excitation of the donor bead at 680 nm, ambient oxygen is converted to the more excited singlet oxygen, which diffuses across to react with the nearby (in the case of a binding event) acceptor bead, generating fluorescence at 520–620 nm. **(B)** Concentration optimisation of Herceptin and HER2 for the AlphaScreen™ assay where a 'hook' effect was observed. The error bars represent mean ± SD, n= 2 technical replicates. The optimised concentrations were 6.25 nM for both Herceptin and HER2. (**C**) $EC_{50}$ of untagged HER2 to disrupt His-tagged HER2-Herceptin interaction, in PBS, pH 7.0, as measured by competition studies using AlphaScreen™ assays. The error bars represent mean ± SD, n= 2 technical replicates. The $EC_{50}$ value is reported as mean ± SD from the data fit.

### A.3.3 Evaluation of HER2 mimicking peptides

A linear peptide, LLGPYELWELSH, and a cyclic peptide, CQMWAPQWGPDC (intramolecular C–C linkage), each generated from a phage display library, have been reported to mimic HER2 in binding to Herceptin in cells[272,273]. However, direct biophysical evidence showing their binding affinity to Herceptin has not been reported. Two additional cyclic peptides, $^{D}$YGPWRSGTAC and $^{D}$YGVWSSGTAC (intramolecular linkage between the amide backbone of $^{D}$Y and the thiol group of C) were identified as binders of Herceptin from an mRNA display[284] by co-worker, Tom McAllister. All the four peptides were synthesised and evaluated for their binding affinity to Herceptin. Unfortunately, they displayed very weak or no binding (when used at ≥100 μM) to Herceptin using multiple biophysical techniques including DSF, ITC, BLI and AlphaScreen™. The results indicated that identifying potent binders to an antibody may not be straightforward, perhaps due to the complexity of the paratope conformation of the antibody. Alternative assays such as fluorescence polarisation may also be considered to validate binding of the AMP candidates to the mAb in the future. These results raised questions on the effectiveness of the selected biophysical assays to measure weak binders and/or on the validity of the reported cellular results, likely reflecting that more complicated binding interactions could take place in cells.

## A.4 Conclusion

Although the AMP candidates have not shown positive binding data with Herceptin in this work, various forms of ADC remain promising to solve the specificity issue in drug development. It is anticipated that such a strategy which combines the high potency of cytotoxic agents with the target specificity conferred by the mAb would represent a potentially new paradigm in cancer treatment.

# EXPERIMENTAL METHODS

## E.1 General Methods

All reagents and solvents were purchased from Sigma-Aldrich unless otherwise stated. Water was purified using a Millipore Milli-Q system.

Specifications of commonly used materials: DL-isocitrate: trisodium salt, hydrate (MP Biomedicals or Insight Biotechnology); D-isocitrate: monopotassium salt; 2OG: disodium salt; $NADP^+$: disodium salt, ~98%; NADPH: tetrasodium salt, ~98%; $MgCl_2$: hexahydrate; Tris-HCl: Tris base solution adjusted with HCl solution.

Sources of mIDH inhibitors: Ivosidenib (AG-120), AGI-5198, Agios 135 (HY-12475), Novartis 224 (HY-18717), Novartis 556 (HY-13972), Vorasidenib (AG-881), BAY-1436032, AGI-6780 and Enasidenib (AG-221) were purchased from MedChem Express. ML309 hydrochloride, GSK864 and Sanofi 1 (SML1430) were purchased from Sigma-Aldrich. SYC-435 (TC-E 5008) was purchased from Bio-Techne. EVO894, EVO820, EVO725, EVO869, EVO875 were gifts from Evotec, Abingdon, UK.

The pH of buffer was measured at 25 °C using a Hanna Instruments HI 9321 pH meter and a 5 mm diameter electrode. Prior to measurements, the pH meter was calibrated for pH 4–7 or pH 7–10 with buffer solutions of phthalate (pH 4), phosphate (pH 7) and borate (pH 10) (Thermo Fisher Scientific). The pH was adjusted with HCl or NaOH solutions. The probe was stored in 4M KCl solution between uses. All buffers were filtered with 0.2 µm cellulose membrane.

## E.2 IDH1 protein expression and purification

Sequences of wt and R132H IDH1 (Theoretical MW= 47.7 kDa)

```
wt      1    MSKKISGGSVVEMQGDEMTRIIWELIKEKLIFPYVELDLHSYDLGIENRDATNDQVTKDA  60
R132H   1    MSKKISGGSVVEMQGDEMTRIIWELIKEKLIFPYVELDLHSYDLGIENRDATNDQVTKDA  60

wt      61   AEAIKKHNVGVKCATITPDEKRVEEFKLKQMWKSPNGTIRNILGGTVFREAIICKNIPRL  120
R132H   61   AEAIKKHNVGVKCATITPDEKRVEEFKLKQMWKSPNGTIRNILGGTVFREAIICKNIPRL  120

wt      121  VSGWVKPIIIGRHAYGDQYRATDFVVPGPGKVEITYTPSDGTQKVTYLVHNFEEGGGVAM  180
R132H   121  VSGWVKPIIIGHHAYGDQYRATDFVVPGPGKVEITYTPSDGTQKVTYLVHNFEEGGGVAM  180

wt      181  GMYNQDKSIEDFAHSSFQMALSKGWPLYLSTKNTILKKYDGRFKDIFQEIYDKQYKSQFE  240
R132H   181  GMYNQDKSIEDFAHSSFQMALSKGWPLYLSTKNTILKKYDGRFKDIFQEIYDKQYKSQFE  240
```

```
wt      241  AQKIWYEHRLIDDMVAQAMKSEGGFIWACKNYDGDVQSDSVAQGYGSLGMMTSVLVCPDG  300
R132H   241  AQKIWYEHRLIDDMVAQAMKSEGGFIWACKNYDGDVQSDSVAQGYGSLGMMTSVLVCPDG  300

wt      301  KTVEAEAAHGTVTRHYRMYQKGQETSTNPIASIFAWTRGLAHRAKLDNNKELAFFANALE  360
R132H   301  KTVEAEAAHGTVTRHYRMYQKGQETSTNPIASIFAWTRGLAHRAKLDNNKELAFFANALE  360

wt      361  EVSIETIEAGFMTKDLAACIKGLPNVQRSDYLNTFEFMDKLGENLKIKLAQAKLLEHHHH  420
R132H   361  EVSIETIEAGFMTKDLAACIKGLPNVQRSDYLNTFEFMDKLGENLKIKLAQAKLLEHHHH  420

wt      421  HH  422
R132H   421  HH  422
```

Wildtype and R132H IDH1 were produced and purified by Martine Abboud according to the reported procedures[12]. In brief, *Hs IDH1* gene (wt or the R132H variant), fused with a $His_6$ tag at the C-terminus, was contained in a pET-22b(+) plasmid. Expression trials in *E. coli* BL21(DE3) pLyS cells were performed at different temperatures (18, 30 and 37 °C) using various isopropyl-β-D-1-thiogalactopyranoside (IPTG) concentrations (0, 0.1, 0.2, 0.5, 0.7 and 1 mM) and different induction times (6, 12 and 20 hr). Cells from small-scale production were lysed using the BugBuster kit; the preferred conditions for expression were assessed by SDS-PAGE analyses and followed thereafter for large-scale expression. All recombinant IDH1 proteins were produced in *E. coli* BL21(DE3) pLysS cells using 2× tryptone yeast extract (2TY) growth medium (16 g bacto-tryptone, 10 g yeast extract and 5 g NaCl per 1 L of Milli-Q water, prepared and autoclaved by Herminio Manso Jubier) supplemented with 50 µg/mL ampicillin and 34 µg/mL chloramphenicol. Cells were grown at 37 °C until they reached $OD_{600}$= 0.6–0.8. Expression was induced with 1 mM IPTG at 18 °C for 12 hr. After centrifugation, cells were resuspended in 50 mL of lysis buffer (20 mM Tris-HCl, 500 mM NaCl, pH 7.4) supplemented with DNase I, TCEP, lysozyme and a tablet of ethylenediaminetetraacetic acid (EDTA)-free protease inhibitors. The cells were then lysed by sonication on ice. After centrifugation, cell lysates were loaded onto a 5 mL HisTrap HP column (GE Healthcare Life Sciences, Little Chalfont, UK), with 50 mM Tris-HCl, 500 mM NaCl, 20 mM imidazole-HCl, pH 7.4, then eluted with an imidazole gradient (up to 500 mM imidazole-HCl). Fractions containing recombinant IDH1 were further purified using a Superdex S200 column (300 mL) equilibrated with 20 mM Tris-HCl, 100 mM NaCl, pH 7.4. Fractions containing the purified protein were concentrated by centrifugal ultra-filtration. The apo-proteins were generated by overnight treatment at 4 °C with EDTA (2000× molar excess; EDTA:protein), followed by purification by PD-10 desalting column. The purity of the resulting proteins

was assessed as >95% (by SDS-PAGE) and their concentrations were determined using a ND-1000 NanoDrop spectrophotometer.

## E.3 Biochemical assays for IDH1

In general, IDH activity was measured spectrophotometrically by monitoring the formation of NADPH as observed by the increase in absorbance at 340 nm for wt IDH1, or the depletion of NADPH as observed by the decrease in absorbance at 340 nm for R132H IDH1. Reactions were monitored at 25 °C in 96-well half area clear microtiter plates (Greiner Bio-One 675001) in a final volume of 100 µL continuously over 15–60 min (1-min interval) using a PHERAstar FS Microplate Reader. The standard assay buffer consists of 100 mM Tris-HCl, 10 mM $MgCl_2$ (hexahydrate), 0.005% (v/v) Tween 20, 0.1 mg/mL BSA and 0.2 mM DTT, pH 8.0. The standard assay conditions are defined as 4.5 nM wt IDH1, 150 µM isocitrate (DL- mixture unless otherwise stated) and 75 µM $NADP^+$ for the oxidative reaction catalysed by wt IDH1; 400 nM R132H IDH1, 1.5 mM isocitrate and 75 µM $NADP^+$ for the oxidative reaction catalysed by R132H IDH1; 100 nM wt IDH1, 15 mM 2OG (disodium salt), 500 µM NADPH and 100 mM $NaHCO_3$ for the reductive reaction catalysed by wt IDH1; 400 nM R132H IDH1, 1.5 mM 2OG and 50 µM NADPH for the reductive reaction catalysed by R132H IDH1, unless otherwise stated. All experiments were performed in technical triplicates (dependent repeats).

### Kinetic parameters determination

The conditions used for kinetic parameters determination followed the standard assay conditions. The $K_M$ values were determined by varying the concentrations of the substrate or cofactor (range as shown in **Figures S2.1**, **S2.2**, **S3.1** and **S3.2**) under investigation while maintaining the concentrations of the other components at the standard conditions. The reaction rate (µM $s^{-1}$) was calculated from the linear range of the reaction profile as $\Delta A_{340}$/ 6.22 $mM^{-1}$ $cm^{-1}$ (extinction coefficient of NADPH)/ 0.509 cm (path length)*1000/ time in sec. $K_M$ and $V_{max}$ with SEM were obtained using nonlinear regression curve fits in the enzyme kinetics model of GraphPad Prism 5.04.

### $IC_{50}$ determination

Inhibitors were prepared as 10 mM stock in DMSO and diluted to 4× final concentration (typically 10 µM as the final concentration, 0.1% DMSO) in the standard assay buffer. $IC_{50}$ of inhibitors against R132H IDH1 was typically determined with 30 nM R132H IDH1 and monitored over 60 min continuously (1-min interval). Time-dependent $IC_{50}$s of covalent inhibitors were determined using 384-well microtiter plates (Greiner Bio-One 781906) in a final volume of 80 µL instead. Varying concentrations of inhibitors from 0 to 10 µM were incubated with R132H IDH1 (or wt IDH1) for 12 min at 25 °C, followed by the addition of 2OG (or isocitrate) and NADPH (or $NADP^+$) to initiate the reaction. The difference in absorbance, $\Delta A_{340}$, in the linear range of the reaction profile was converted to % residual activity with the DMSO control being the 100% residual activity reference. $IC_{50}$ values were obtained using nonlinear regression curve fits in the dose-dependent inhibition model of GraphPad Prism 5.04. Errors were reported as ± SD, assuming 95% confidence intervals (in GraphPad Prism)= 1.96 SD.

## E.4 Biophysical assays for IDH1

### Differential Scanning Fluorimetry

Thermal shift experiments were carried out using sypro orange dye on a CFX96 Touch™ Real-Time PCR Detection System (Bio-Rad). A 96-well white PCR plate was used in the assay, in which each well contained 20 µL of 2.5 µM wt or R132H IDH1 with 5× sypro orange. The standard assay buffer contained 50 mM Tris-HCl, pH 7.5. Various concentrations of compounds were mixed with IDH1 for thermal stabilisation studies. The samples in triplicates were subjected to temperature increases from 20 °C to 95 °C at 0.2 °C $min^{-1}$. Bio-Rad CFX Manager 3.1 was used to determine the melting temperature, $T_m$, corresponding to the minimum point of the negative first derivatives of the melting curves.

### Isothermal Titration Calorimetry

Thermodynamic studies of both wt and R132H IDH1 were carried out by ITC experiments using Malvern MicroCal PEAQ-ITC Automated. In general, the protein was prepared in an assay buffer containing 50 mM Tris-HCl, pH 7.5 and the compounds were dissolved

in the same buffer. 400 µL of cell and 200 µL of titrant were transferred to an ITC plate. Titrations were conducted at 25 °C with an initial delay of 60 seconds and a stir speed of 750 rpm. The injection setup consisted of 19 injections which have one initial injection of 0.4 µL and 18 injections of 2.0 µL each with 150 seconds between the injections. The thermodynamic parameters were obtained using the MicroCal PEAQ-ITC analysis software.

## Circular Dichroism

Circular dichroism spectra were acquired using Chirascan CD spectrometer (Applied Photophysics) with a Peltier temperature-control cell holder. IDH1 was buffer exchanged using a Micro Bio-Spin™ 6 column (Bio-Rad 732-6221) in 10 mM sodium phosphate, pH 7.5 to a final concentration of 0.2 mg/mL. Experiments were carried out in a 0.1 cm path length quartz cuvette at 25 °C. Data were collected in triplicates continuously over wavelengths between 185 and 260 nm with a bandwidth of 1.0 nm in 0.5 nm steps. Traces were averaged (n=3) and smoothed (window size=7) to give the final spectra.

## Nuclear Magnetic Resonance

NMR binding studies were done at 298 K using a Bruker AVIII 700 MHz NMR spectrometer equipped with a 5-mm inverse triple resonance inverse (TCI) cryoprobe. $^{1}$H Carr-Purcell-Meiboom-Gill (CPMG) NMR experiments were conducted using the PROJECT pulse sequence[285] with a total filter time of 40 ms. Water suppression was achieved by presaturation for 2 s. Samples contained 160 µL of 10–50 µM compound of interest in 50 mM Tris-$D_{11}$-HCl, pH 7.5 in 90% $H_2O$/ 10% $D_2O$ (v/v) in 3 mm MATCH NMR tubes (Cortectnet). Additional protein or inhibitor was added to the mixture with negligible increase (<1.5%) in the total volume. Data were processed with TopSpin 3.6.1 software.

NMR reaction monitoring was done at 298 K using a Bruker AVIII 700 MHz NMR spectrometer equipped with a 5-mm inverse TCI cryoprobe. Data were recorded with a relaxation delay of 2 s and 32 scans, employing a pulse sequence with water suppression ($^{1}$H excitation sculpting suppression with perfect-echo using a 2 ms Sinc selective inversion pulse). There is a time delay of 184 s between acquired spectra over the time-

course experiment. Unless otherwise stated, conversion of isocitrate to 2OG by wt IDH1 was monitored using 500 µL of 6 nM wt IDH1, 550 µM (effectively ~400 µM) DL-isocitrate or 200 µM D-isocitrate, 400 µM $NADP^+$, 10 mM $MgCl_2$, in 50 mM Tris-$D_{11}$-HCl, pH 7.5 in 90% $H_2O$/ 10% $D_2O$ (v/v). Conversion of 2OG to 2HG by R132H IDH1 was monitored using 500 µL of 1 µM R132H IDH1, 1.5 mM 2OG, 1.5 mM NADPH, 10 mM $MgCl_2$, in 50 mM Tris-$D_{11}$-HCl, pH 7.5 in 90% $H_2O$/ 10% $D_2O$ (v/v). All samples were prepared in 5-mm NMR tubes (Norell). Data were processed with TopSpin 3.6.1 software.

All DOSY spectra were recorded at 298 K (unless otherwise stated) on a Bruker AVIII 600 MHz NMR spectrometer with a 5-mm broad band (BB)-$^{19}F/^{1}H$ Prodigy $N_2$ cryoprobe, equipped with a z-gradient coil with a maximum nominal gradient strength of 67.5 G $cm^{-1}$. The pulse sequence used was stimulated echo with bipolar pulsed field gradients ("stebpgp1s" on Bruker instrument). The number of data points for the acquired FID was set to 32k and zero-filled to 64k before Fourier transformation. To acquire the diffusion dimension 16 gradient levels were used and number of scans was set to 32. Samples contained 500 µL of 1 mM compound of interest with various concentrations of metal chloride salts in $D_2O$ in 5-mm Norell NMR tubes. Data were processed with TopSpin 3.6.1 and Dynamic Centre 2.5.6 softwares.

## Protein non-denaturing MS

Non-denaturing mass spectra were obtained by the method of non-denaturing ('native') MS on a quadrupole time-of-flight (qTOF) mass spectrometer (Synapt HD MS, Waters, Wilmslow, Manchester, UK), conducted jointly with Victor Mikhailov. IDH1 was buffer exchanged using a Micro Bio-Spin™ 6 column (Bio-Rad 732-6221) into water. Protein concentrations were measured using a Nanodrop spectrometer (Thermo Scientific™ NanoDrop™ One). 20 µL of 50 µM wt or R132H IDH1 with compounds of interest in 200 mM ammonium acetate at pH 7.5 were pipetted in the wells on a sample plate of an automated chip-based nano-electrospray ion source (TriVersa Nanomate, Advion, Ithaka, NY, USA). The solution was then sprayed through a nozzle in a Nanomate chip at a spray voltage of 1.8-2.0 kV (spray backing gas pressure 0.8-1.0 psi, inlet pressure 3.8 mbar). Sample and extractor cone voltages were kept at 100 V and 5.2 V respectively. The rest of voltages and pressures in the mass spectrometer were adjusted for the best resolution and minimum fragmentation. Data collection and analysis were carried out

using Waters MassLynx 4.1 software. Mass spectra were calibrated externally using CsI solution to produce CsI cluster ions.

## Protein denaturing LCMS

Studies on IDH1 with covalent compounds under denaturing conditions were conducted on an open access liquid chromatography mass spectrometry (LC-MS) system with a Waters Acquity quaternary solvent manager and acquity FTN sample manager as the LC, and Waters LCT Premier XE equipped with electrospray interface as the MS. Samples contained wt IDH1 or R132H IDH1 (1 µM) and the compound (10 µM) incubated in 50 mM Tris-HCl, pH 7.5 for either 15 min or 1.5 hr before injection. 5 µL of each sample was injected onto a 1 × 5 Proswift RP 4H column (Thermo Fisher Scientific). A mixed eluent gradient with acetonitrile (solvent A) and 0.1% (v/v) formic acid in water (solvent B) was employed. The gradient used was as follows: 0-1 min 3% A, 1–7 min 3–99% A, 7–8 min 99% A, 8–8.1 min 99–3% A, 8.1–10 min 3% A. Flow rate: 0.2 mL/min. Data were processed using MassLynx 4.1.

## Anion exchange chromatography-MS

Each sample of 2OG analogues following reaction with R132H IDH1 was analysed by John Walsby-Tickle using a Thermo Scientific ICS-5000+ ion chromatography system coupled directly to a Q-Exactive HF Hybrid Quadrupole-Orbitrap mass spectrometer with a HESI II electrospray ionisation source (Thermo Scientific, San Jose, CA). An electrolytic anion generator (KOH) which was programmed to produce a $OH^-$ gradient over 37 min and an inline electrolytic suppressor removed $OH^-$ ions and cations from the post-column eluent stream prior to MS analysis (Thermo Scientific Dionex AERS 500). A 5 µL partial loop injection was used for all analyses and the chromatographic separation was performed using a Thermo Scientific Dionex IonPac AS11-HC 2 × 250 mm, 4 µm particle size column. The IC flow rate was 0.250 mL/min and the column temperature was kept at 30 °C throughout the experiment. The total run time was 37 min and the hydroxide ion gradient comprised as follows: 0 min, 0 mM; 1 min, 0 mM; 15 min, 60 mM; 25 min, 100 mM; 30 min, 100 mM; 30.1 min, 0 mM; 37 min, 0 mM. MS analysis was performed in negative ion mode using a scan-range from m/z 60-900 and resolution set to 70,000. The tune file source parameters were set as follows: Sheath

gas flow 60 mL/min; Aux gas flow 20 mL/min; Spray voltage 3.6 V; Capillary temperature 320 °C; S-lens RF value 70; Heater temperature 350 °C. AGC target was set to 1e6v ions and the Max IT value was 250 ms. Full scan data were acquired in continuum mode and peak areas were extracted from the raw data using Xcalibur (Thermo Scientific, San Jose, CA).

### X-ray crystallography

For co-crystallisation of R132H IDH1 and 2OG analogues, a mixture of R132H IDH1 (10.5 mg/mL), $CaCl_2$ (10 mM), NADPH (10 mM) and 2OG analogues (75 mM) in 70 µL of 50 mM Tris-HCl, 200 mM NaCl, 5 mM DTT and 5% (v/v) glycerol at pH 7.5 was incubated for 3 hr at 4 °C. The samples were centrifuged (14,000 rpm, 4 °C) for 5 min to remove any precipitate. Crystallisation conditions were screened using JCSG-plus™ (Molecular Dimensions Limited, Suffolk, UK), Crystal Screen (Hampton Research, CA, USA) and PACT premier™ HT-96 (Molecular Dimensions Limited, Suffolk, UK) by the sitting drop vapour diffusion method at 20 °C. The protein solution and the reservoir solutions were dispersed onto 96-well Intelliplates in the ratios of 1:2, 1:1 and 2:1 using the Phoenix RE Liquid Handling System (Art Robbins Instruments) at 25 °C. X-ray diffraction data was collected using a synchrotron beam line (Diamond Light Source I24 with a 5 µm focused beam, Oxford, UK) by Yu Nakashima, Mike McDonough, Serena Rocchio (Evotec, UK) or Stephanie Duclos (Evotec, UK), and the structures were solved by Yu Nakashima.

## E.5 Western blot for validating PROTAC

LN18 cell pellets were obtained from John Walsby-Tickle. Cells were lysed by adding 20 µL of lysis buffer containing 50 mM Tris-HCl, 150 mM NaCl, 0.1% (v/v) Triton X-100, pH 8.0 and 1× protease inhibitor cocktail (Sigma-Aldrich P8340), to the cell pellets. The mixture was sonicated at r.t. for 5 min, incubated at 4 °C for 30 min, and centrifuged at 12,000 rpm, 4 °C for 20 min. 4 µL of the supernatant (diluted with equal volume of 2× loading buffer) from the lysed cells were loaded into a SDS-PAGE gel (90 V for 12 min followed by 160 V for 65 min). Proteins were transferred from the gel to a nitrocellulose blotting membrane (pore size 0.2 µm, GE Life Sciences 10600001) using a wet transfer set-up (200 mA for 80 min at 4 °C, in transfer buffer made of 3g Tris and 14.4 g glycine in 800 mL Milli-Q water and 200 mL methanol). The membrane was stained with

Ponceau S solution (0.1% (w/v) PonceauS in 5% (v/v) acetic acid, Sigma-Aldrich P7170) to check that all proteins were transferred to the membrane. The stain was removed by incubating the membrane in tris-buffered saline with Tween 20 (TBST) (20 mM Tris-HCl, 150 mM NaCl, 0.1% (v/v) Tween 20, pH 7.6) for 2 × 5 min. The membrane was incubated in 5% (w/v) blocking buffer (0.5 g milk powder in 10 mL TBST) for 1 hr at r.t. to prevent subsequent non-specific binding of the antibodies to the membrane and was then washed with 10 mL TBST. The membrane was then incubated in the primary antibody (R132H IDH1, Merck MABC171, 1:100 in 5% blocking buffer) overnight at 4 °C, washed with TBST (5 × 15 min), incubated with the secondary antibody (anti-mouse HRP-conjugated, Promega W4021, 1:2800 in 5% blocking buffer) for 1 hr at r.t. and washed with TBST (3 × 5 min). The membrane was developed with Amersham ECL Prime Western Blotting Detection Reagent (GE healthcare RPN2232) in the dark for 5 min before detection for chemiluminescence.

## E.6 Preparation of Herceptin Fab

### Preparation of glycerol stock and purification of plasmid DNA

The pMKRQ-Herceptin Fab plasmid was received as a soft agar stab culture in *E. coli* K-12 TOP10 strain from Mark Shepherd (University of Kent, UK). The plasmid carries kanamycin resistance and allows secretion of the recombinant Fab fragment of Herceptin into the periplasm in which the oxidative environment allows the formation of disulfide bridges between the light chain and the heavy chain.

Sequence of Herceptin Fab (Theoretical MW= 47.1 kDa)

```
Light Chain
      1    DIQMTQSPSSLSASVGDRVTITCRASQDVNTAVAWYQQKPGKAPKLLIYSASFLYSGVPS  60
      61   RFSGSRSGTDFTLTISSLQPEDFATYYCQQHYTTPPTFGQGTKVEIKRTVAAPSVFIFPP  120
      121  SDEQLKSGTASVVCLLNNFYPREAKVQWKVDNALQSGNSQESVTEQDSKDSTYSLSSTLT  180
      181  LSKADYEKHKVYACEVTHQGLSSPVTKSFNRGEC  214

Heavy Chain
      1    EVQLVESGGGLVQPGGSLRLSCAASGFNIKDTYIHWVRQAPGKGLEWVARIYPTNGYTRY  60
      61   ADSVKGRFTISADTSKNTAYLQMNSLRAEDTAVYYCSRWGGDGFYAMDYWGQGTLVTVSS  120
      121  ASTKGPSVFPLAPSSKSTSGGTAALGCLVKDYFPEPVTVSWNSGALTSGVHTFPAVLQSS  180
      181  GLYSLSSVVTVPSSSLGTQTYICNVNHKPSNTKVDKKVEPKSC  223
```

The stab culture was touched with a pipette tip which was incubated in 5 mL of 2TY medium with 50 µg/mL kanamycin at 37 °C overnight in a G25 environmental incubator shaker (New Brunswick Scientific) at 220 rpm. Glycerol stocks were prepared by adding

800 µL of the overnight culture to 200 µL of 100% sterile glycerol in a cryotube, prior to storage at -80 °C.

The remaining overnight culture was centrifuged at 3,750 rpm for 10 min at 4 °C in an Allegra™ X-30R Centrifuge. The supernatant was discarded and the cell pellets were subjected to lysis and plasmid purification using the GeneJET Plasmid Miniprep Kit (Thermo Scientific) according to the manufacturer's instructions. 457 ng/µL of plasmid DNA was obtained and stored at -20 °C.

The plasmid generated was sequenced to ensure there were no errors in the cloned genes. 10 µL of 100 ng/µL purified plasmid DNA was sent for sequencing by the SourceBioscience sequencing facility (Oxford, UK). The entire sequence of Herceptin Fab was confirmed using a forward primer, a reverse primer and an internal forward primer for which the sequences and positions are shown as follows.

Forward primer: `gttgtaaaacgacggccagt`
Reverse primer: `catggtcatagctgtt`
Internal forward primer: `ccgccatctgatgagcagttgaaatctg`

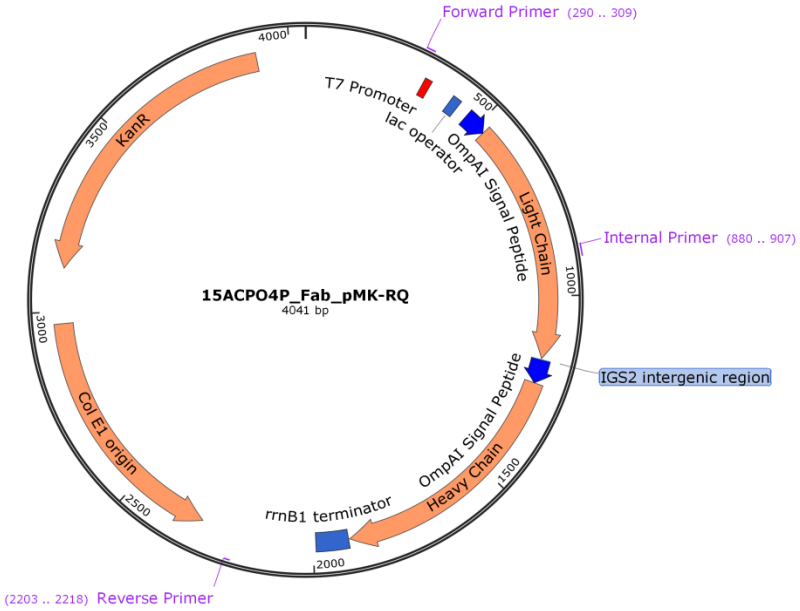



**Figure E1**. Map of the pMKRQ-Herceptin Fab plasmid

## Transformation of Herceptin Fab plasmid into BL21(DE3) and Rosetta™ 2(DE3) cells

Purified Herceptin Fab plasmid (1 µL of 50 ng/µL) was transformed into thawed BL21-Gold(DE3) *E. coli* competent cells (20 µL) in a pre-chilled 1.5 mL Eppendorf, allowing

plasmid amplification. The eppendorf was left on ice for 20 min before being heat shocked for 30 seconds at 42 °C. This was followed by a 5 min recovery step on ice. 2TY medium (300 µL) was then added and the mixture was incubated at 37 °C for 1 hr, allowing the bacteria to generate the antibiotic resistance proteins encoded on its plasmid backbone. The mixture (40 µL) was spread onto a LB-agar plate (containing ~20 mL of LB-agar that was prepared as follows: 15 g agar, 10 g bacto-tryptone, 5 g yeast extract and 10 g NaCl per 1 L of Milli-Q water, autoclaved at 121 °C for 20 min) containing kanamycin (30 µg/mL) and was allowed to grow at 37 °C overnight. Transformation of Herceptin Fab plasmid into Rosetta™ 2(DE3) *E. coli* competent cells was conducted similarly to the procedures described above.

## Expression Trials of Herceptin Fab

The starter culture was prepared by incubating a single bacterial colony from the freshly transformed BL21-Gold(DE3) *E. coli* plate in 100 mL of 2TY medium containing kanamycin (30 µg/mL) at 37 °C overnight in a G25 environmental incubator shaker (New Brunswick Scientific) at 220 rpm. Fifteen conditions (**Table E1**) were tested for small scale expression of Herceptin Fab. 150 µL of the starter culture was added to 15 mL of 2TY medium containing kanamycin (30 µg/mL) in a 50 mL Falcon™ tube and the cells were grown at 37 °C until an optical density at 600 nm ($OD_{600}$) of 1.0 was reached. 3 mL of the cells were centrifuged (12,000 rpm, 1 min) to serve as the 'control'.

| Temperature/ °C | Incubation time | IPTG concentration (mM) |
|---|---|---|
| **37** | 4 hr, overnight | 0.1, 0.2, 0.5 |
| **28** | 4 hr, overnight | 0.1, 0.2, 0.5 |
| **18** | overnight | 0.1, 0.2, 0.5 |

**Table E1**. Expression trials conditions for Herceptin Fab

Protein production was induced by the addition of various concentrations of isopropyl β-D-1-thiogalactopyranoside (IPTG) (0.1, 0.2 and 0.5 mM). The culture was then incubated at different temperatures (18, 28 and 37 °C) for various time periods (4 hr or overnight). 3 mL of the cells grown from each condition were used as 'whole cell' samples. Another 3 mL of the cells were centrifuged (12,000 rpm, 1 min) and used as 'cell lysate' samples. The cell pellets from the 'control' and 'cell lysate' samples were resuspended in 300 µL lysis buffer (100 mM HEPES and 100 mM NaCl at pH 7.6) and

lysed on ice by sonication (3 × 10 seconds sonication with 20 seconds rest in between) using a Sonics Vibracell VCX750 Ultrasonic Cell Disruptor at 40% amplitude. 15 µL of the 'whole cell' samples or supernatant from the lysed cells in the 'control' and 'cell lysate' samples was loaded into SDS-PAGE gel and no overexpression of Herceptin Fab was observed.

## Papain digestion of Herceptin

Herceptin Fab fragment was produced by digestion of Herceptin using immobilised papain similarly to the reported procedures[286,287]. 1 mL (250 µg/mL) of immobilised papain gel (Thermo Fisher Scientific 20341) was equilibrated by addition of 4 mL of digestion buffer containing 80 mM cysteine HCl (Thermo Fisher Scientific 44889), 20 mM sodium phosphate monobasic and 10 mM disodium EDTA at pH 7.0 degassed with nitrogen. The buffer was separated from the gel by centrifugation (4,000 rpm, 2 min). The wash procedure was repeated for four times with a final volume of gel of 1 mL. 2.5 mg of lyophilised Herceptin (Roche, clinical grade containing 3.36 mg L-histidine HCl, 2.16 mg L-histidine, 136.2 mg α,α-trehalose dihydrate and 0.6 mg polysorbate 20 for every 150 mg of Herceptin) was gently dissolved in 1 mL of digestion buffer and added to the gel. The mixture was purged with nitrogen for 5 min before incubating for 20 hr at 37 °C in a sealed 15 mL Falcon™ tube in a G25 environmental incubator shaker (New Brunswick Scientific) at 220 rpm to achieve maximum Fab yield without undigested Herceptin.

After digestion, the immobilised papain was separated from the digest by adding 1 mL of PBS (8 g NaCl, 0.2 g KCl, 1.44 g $Na_2HPO_4$ and 0.24 g $KH_2PO_4$ per 1 L of Milli-Q water) at pH 7.0 to the mixture and centrifuging (200 × *g*, 5 min) to collect the supernatant. Another 3 mL of PBS (pH 7.0) was added and centrifuged (200 × *g*, 5 min). The supernatant containing Fab was combined and concentrated to a volume of 200 µL using Amicon®Ultra-15 centrifugal filter with a molecular weight cut-off of 30 kDa (Merck UFC903024) to remove low molecular weight proteolytic contaminants including fragmented Fc[281] and cysteine. The Fab was buffer exchanged into PBS (pH 7.0) using the same Amicon®Ultra-15 centrifugal filter (4 × 12 mL PBS). The purified Fab (200 µL) concentration was measured at 280 nm to give 1.85 mg/mL Herceptin Fab (molar extinction coefficient for Herceptin Fab[286], ε= 68,590 $M^{-1}$ $cm^{-1}$, 47.5 kDa). The sample

was analysed by LC-MS and revealed a mixture of Fab products at 47,270 Da and 47,637 Da, due to different (aspartate or histidine) but close (separated by three amino acids *i.e.* KTH) cleavage sites of papain[288].

## E.7 Peptide synthesis

### Solid Phase Peptide Synthesis

Peptides were synthesised using a Liberty Blue™ automated microwave peptide synthesiser (CEM Corporation). Synthesis proceeded from *C* to *N* terminus. Amino acids were $N^{\alpha}$-Fmoc-protected and, where appropriate, side chain was protected by an acid-labile protecting group *e.g.* tert-butyloxycarbonyl (Boc), tert-butyl (tBu) and trityl (Trt). 0.10 mmol of rink amide-4-methylbenzhydrylamine (MBHA) resin (AGTC Bioproducts) was used per peptide. 5 mL of 0.2 M amino acids in dimethylformamide (DMF) were prepared per residue in the peptide sequence. The amino acids were activated by 0.5 M diisopropylcarbodiimide (DIC) and 1 M ethyl (hydroxyimino)cyanoacetate (Oxyma) in DMF to facilitate coupling and their $N^{\alpha}$-Fmoc-protected amino groups were deprotected by 20% (v/v) piperidine in DMF.

Peptides $^{D}$YGPWRSGTAC and $^{D}$YGVWSSGTAC were cyclised by mixing 4 mL of 180 mM *N*-(chloroacetoxy)succinimide with the reaction mixture for 2.5 hr at r.t..

The product was collected using a phase separator, washed with DMF followed by dichloromethane (DCM) and dried in a dessicator for 1 hr. Cleavage of the peptides from the resin and removal of the side chain protecting groups were achieved by mixing the peptide-resin mixture with a solution of water (125 µL), triisopropylsilane (TIPS, 125 µL), 1,3-dimethoxybenzene (125 µL) and trifluoroacetic acid (TFA, 4.625 mL) for 3 hr at r.t. in a glass vial. The mixture was filtered using a phase separator and cold diethyl ether (45 mL) was added to precipitate the peptide from the filtrate. The mixture was centrifuged (2000 rpm, 10 min, 5 °C) using an Allegra™ X-30R Centrifuge and supernatant was discarded. The peptide was air dried for 1 hr, dissolved in 2 mL of water and 1 mL of acetonitrile and lyophilised to give the crude product.

Peptide CQMWAPQWGPDC was cyclised by adding the crude linear peptide (30 mg) in 30 mL of 15 mM ammonium acetate at pH 7.5 and 10 mL of acetonitrile. The peptide

was sufficiently diluted to prevent intermolecular cyclisation. The reaction was tracked by LC-MS and the mixture was stirred at r.t. for 22 hr to allow the formation of intramolecular disulfide bonds by air oxidation. The resulting mixture was lyophilised to give the crude cyclic peptide.

### Peptide purification

The crude product was purified using reverse-phase high-performance liquid chromatography (HPLC) with a Vydac 218TP 250 mm x 22 mm C18 column (Grace Division Discovery Sciences™) fitted to a Jasco HPLC system (PU-2086 Plus Pumps, MX-2080-32 Dynamic Mixer and DG-2080-54 Degasser). The system was controlled with Jasco ChromNAV Control Center software. Injection and fraction collection were conducted by Jasco AS-2055 Plus autosampler and CHF1225C fraction collector. Peptides (10-30 mg) were dissolved in 1.2 mL Milli-Q water and 0.8 mL acetonitrile before injecting into the system. A mixed eluent gradient with 0.1% (v/v) trifluoroacetic acid (TFA) in acetonitrile (solvent A) and 0.1% (v/v) TFA in water (solvent B) was employed. The gradients used were as follows: peptide LLGPYELWELSH: 0–3 min 25% A, 3–37 min 25–50% A, 37–40 min 50–98% A, 40–45 min 98–2% A. Cyclic CQMWAPQWGPDC: 0–3 min 20% A, 3–50 min 20–40% A, 50–55 min 40–98% A, 55–60 min 98–2% A. Cyclic $^{D}$YGPWRSGTAC and $^{D}$YGVWSSGTAC: 0–3 min 20% A, 3–37 min 20–40% A, 37–39 min 40–98% A, 39–41 min 98–2% A. Flow rate: 20 mL min$^{-1}$. The fractions containing the product were pooled and lyophilised to give the final purified product.

## E.8 Biophysical assays for Herceptin

### Differential Scanning Fluorimetry

Thermal shift experiments were carried out using sypro orange dye on a CFX96 Touch™ Real-Time PCR Detection System (Bio-Rad). A 96-well white PCR plate was used in the assay, in which each well contained 20 µL of 5 µM Herceptin (whole) with 10× sypro orange. The assay buffer contained PBS at pH 7.0. Various concentrations of peptides from 0 to 250 µM were mixed with Herceptin for thermal stabilisation studies. The samples in triplicates were subjected to temperature increases from 20 °C to 95 °C at 0.2 °C min$^{-1}$. Bio-Rad CFX Manager 3.1 was used to determine the melting temperature, $T_m$.

## Isothermal Titration Calorimetry

Herceptin (whole) was buffer exchanged to PBS at pH 7.0 to remove all the additives in the clinical grade product and the peptides were diluted in the same buffer. 400 µL of 5 µM Herceptin (whole) and 200 µL of 100 µM peptides were transferred to an ITC plate. Standard protocols were described in **E.4 Biophysical assays for IDH1**.

## Biolayer Interferometry

The binding affinity between Herceptin and HER2 was quantified using an OctetRed 384 machine (ForteBio) in BLI buffer (PBS at pH 7.4). Herceptin (whole, 70 nM) was immobilised onto Protein G biosensors (Fortebio 18-5082) for 5 min and subjected to a cycle of association/dissociation with different HER2 concentrations (250, 125, 62.5 and 0 nM) in BLI buffer. The binding affinity between Herceptin and peptides was determined by replacing HER2 with 50/100 µM peptides. For experiments with the peptides, a background binding control was performed without Herceptin and was subtracted from the other sensors to account for non-specific binding. $K_D$ value for the Herceptin-HER2 interaction was fitted using the ForteBio Data Analysis 6.4 software.

## AlphaScreen binding assays

AlphaScreen assays were carried out in ProxiPlate$^{TM}$-384 Plus plates (PerkinElmer) with a total volume of 20 µL assay mixture in PBS at pH 7.0 in each well. All experiments were conducted in duplicates. The reagent concentration optimisation was conducted by mixing 5 µL of Herceptin (whole, a series of 2-fold dilution from 200 nM final) and 5 µL of HER2 (a series of 2-fold dilution from 200 nM final), followed by the addition of 5 µL of Protein A Alpha donor beads (PerkinElmer AS102D, 0.02 mg/mL final). The mixture was incubated for 1 hr at r.t. in the dark. 5 µL of nickel chelate (Ni-NTA) AlphaScreen acceptor beads (PerkinElmer 6760619C, 0.02 mg/mL final) was then added and the mixture was incubated for 1 hr at r.t. in the dark. Fluorescence readings at 520-620 nm after excitation at 680 nm were obtained on an EnVision 2104 Multilabel Reader (PerkinElmer).

The competition experiment was conducted by incubating 4 µL of untagged HER2 (a series of 2-fold dilution from 200 nM final) with 4 µL of Herceptin (whole, 6.25 nM final) for 15 min at r.t., followed by the addition of 4 µL of His-tagged HER2 (6.25 nM final) and

incubation of the mixture for 30 min at r.t.. Protein A donor beads (4 µL, 0.02 mg/mL final) and nickel chelate acceptor beads (4 µL, 0.02 mg/mL final) were added as described above with 1 hr incubation at r.t. in the dark after each addition. Data were normalised to a no untagged-HER2 control (100% residual activity). $EC_{50}$ values were obtained using nonlinear regression curve fits in the dose-dependent inhibition model of GraphPad Prism 5.04.

# REFERENCES


1. Hanahan, D. & Weinberg, R. A. Review Hallmarks of Cancer : The Next Generation. *Cell* **144**, 646–674 (2011).

2. Pasini, B. & Stratakis, C. A. SDH mutations in tumorigenesis and inherited endocrine tumours: lesson from the phaeochromocytoma-paraganglioma syndromes. *J. Intern. Med.* **266**, 19–42 (2009).

3. Cardaci, S. & Ciriolo, M. R. TCA Cycle Defects and Cancer: When Metabolism Tunes Redox State. *Int. J. Cell Biol.* **2012**, 1–9 (2012).

4. Cascón, A. *et al.* Whole-Exome Sequencing Identifies MDH2 as a New Familial Paraganglioma Gene. *J. Natl. Cancer Inst.* **107**, djv53 (2015).

5. Ohgaki, H. & Kleihues, P. The Definition of Primary and Secondary Glioblastoma. *Clin. Cancer Res.* **19**, 764–772 (2013).

6. Golub, D. *et al.* Mutant Isocitrate Dehydrogenase Inhibitors as Targeted Cancer Therapeutics. *Front. Oncol.* **9**, (2019).

7. Cazzola, M. IDH1 and IDH2 mutations in myeloid neoplasms - Novel paradigms and clinical implications. *Haematologica* **95**, 1623–1627 (2010).

8. Medeiros, B. C. *et al.* Isocitrate dehydrogenase mutations in myeloid malignancies. *Leukemia* **31**, 272–281 (2017).

9. Losman, J. A. & Kaelin, W. G. What a difference a hydroxyl makes: mutant IDH, (*R*)-2-hydroxyglutarate, and cancer. *Genes Dev.* **27**, 836–852 (2013).

10. Oermann, E. K., Wu, J., Guan, K. L. & Xiong, Y. Alterations of metabolic genes and metabolites in cancer. *Semin. Cell Dev. Biol.* **23**, 370–380 (2012).

11. Dang, L. *et al.* Cancer-associated IDH1 mutations produce 2-hydroxyglutarate. *Nature* **462**, 739–744 (2009).

12. Xu, X. *et al.* Structures of Human Cytosolic NADP-dependent Isocitrate Dehydrogenase Reveal a Novel Self-regulatory Mechanism of Activity. *J. Biol. Chem.* **279**, 33946–33957 (2004).

13. Yang, H., Ye, D., Guan, K. L. & Xiong, Y. IDH1 and IDH2 Mutations in Tumorigenesis: Mechanistic Insights and Clinical Perspectives. *Clin. Cancer Res.* **18**, 5562–5571 (2012).

14. Gabriel, J. L., Zervos, P. R. & Plaut, G. W. E. Activity of purified NAD-specific isocitrate dehydrogenase at modulator and substrate concentrations approximating conditions in mitochondria. *Metabolism* **35**, 661–667 (1986).

15. Reitman, Z. J. & Yan, H. Isocitrate Dehydrogenase 1 and 2 Mutations in Cancer: Alterations at a Crossroads of Cellular Metabolism. *J. Natl. Cancer Inst.* **102**, 932–941 (2010).

16. Lemons, J. M. S. *et al.* Quiescent Fibroblasts Exhibit High Metabolic Activity. *PLoS Biol.* **8**, e1000514 (2010).

17. Comte, B., Vincent, G., Bouchard, B., Benderdour, M. & Des Rosiers, C. Reverse flux through cardiac $NADP^+$-isocitrate dehydrogenase under normoxia and ischemia. *Am. J. Physiol. Circ. Physiol.* **283**, H1505–H1514 (2002).

18. Mondesir, J., Willekens, C., Touat, M. & de Botton, S. IDH1 and IDH2 mutations as novel therapeutic targets: current perspectives. *J. Blood Med.* **7**, 171–80 (2016).

19. Neves, R. P. P., Fernandes, P. A. & Ramos, M. J. Unveiling the Catalytic Mechanism of $NADP^+$-Dependent Isocitrate Dehydrogenase with QM/MM Calculations. *ACS Catal.* **6**, 357–368 (2016).

20. Ochoa, S. Biosynthesis of tricarboxylic acids by carbon dioxide fixation; the preparation and properties of oxalosuccinic acid. *J. Biol. Chem.* **174**, 115–22 (1948).

21. Louis, D. N. *et al.* The 2016 World Health Organization Classification of Tumors of the Central Nervous System: a summary. *Acta Neuropathol.* **131**, 803–820 (2016).

22. Johnson, B. E. *et al.* Mutational Analysis Reveals the Origin and Therapy-Driven Evolution of Recurrent Glioma. *Science (80-. ).* **343**, 189–193 (2014).

23. Tamimi, A. F. & Juweid, M. Epidemiology and Outcome of Glioblastoma. in *Glioblastoma* 143–153 (Codon Publications, 2017). doi:10.15586/codon.glioblastoma.2017.ch8.

24. Parsons, D. W. *et al.* An Integrated Genomic Analysis of Human Glioblastoma Multiforme. *Science (80-. ).* **321**, 1807–1812 (2008).

25. Yan, H. *et al.* IDH1 and IDH2 Mutations in Gliomas. *N. Engl. J. Med.* **360**, 765–773 (2009).

26. Brennan, C. W. *et al.* The Somatic Genomic Landscape of Glioblastoma. *Cell* **155**, 462–477 (2013).

27. Balss, J. *et al.* Analysis of the IDH1 codon 132 mutation in brain tumors. *Acta Neuropathol.* **116**, 597–602 (2008).

28. Bleeker, F. E. *et al.* IDH1 mutations at residue p.R132 (IDH1 R132 ) occur frequently in high-grade gliomas but not in other solid tumors. *Hum. Mutat.* **30**, 7–11 (2009).

29. Hartmann, C. *et al.* Type and frequency of IDH1 and IDH2 mutations are related to astrocytic and oligodendroglial differentiation and age: a study of 1,010 diffuse gliomas. *Acta Neuropathol.* **118**, 469–474 (2009).

30. Mardis, E. R. *et al.* Recurring Mutations Found by Sequencing an Acute Myeloid Leukemia Genome. *N. Engl. J. Med.* **361**, 1058–1066 (2009).

31. Green, A. & Beer, P. Somatic Mutations of IDH1 and IDH2 in the Leukemic

Transformation of Myeloproliferative Neoplasms. *N. Engl. J. Med.* **362**, 369–370 (2010).

32. Pusch, S. *et al.* Scientific correspondence. *Neuropathol. Appl. Neurobiol.* **37**, 428–430 (2011).

33. Gupta, R. *et al.* Expanding the spectrum of IDH1 mutations in gliomas. *Mod. Pathol.* **26**, 619–625 (2013).

34. Chotirat, S., Thongnoppakhun, W., Promsuwicha, O., Boonthimat, C. & Auewarakul, C. U. Molecular alterations of isocitrate dehydrogenase 1 and 2 (IDH1 and IDH2) metabolic genes and additional genetic mutations in newly diagnosed acute myeloid leukemia patients. *J. Hematol. Oncol.* **5**, 5 (2012).

35. Rose, N. R., McDonough, M. A., King, O. N. F., Kawamura, A. & Schofield, C. J. Inhibition of 2-oxoglutarate dependent oxygenases. *Chem. Soc. Rev.* **40**, 4364 (2011).

36. Joharapurkar, A. A., Pandya, V. B., Patel, V. J., Desai, R. C. & Jain, M. R. Prolyl Hydroxylase Inhibitors: A Breakthrough in the Therapy of Anemia Associated with Chronic Diseases. *J. Med. Chem.* **61**, 6964–6982 (2018).

37. Ward, P. S. *et al.* The Common Feature of Leukemia-Associated IDH1 and IDH2 Mutations Is a Neomorphic Enzyme Activity Converting α-Ketoglutarate to 2-Hydroxyglutarate. *Cancer Cell* **17**, 225–234 (2010).

38. Gross, S. *et al.* Cancer-associated metabolite 2-hydroxyglutarate accumulates in acute myelogenous leukemia with isocitrate dehydrogenase 1 and 2 mutations. *J. Exp. Med.* **207**, 339–344 (2010).

39. Kalinina, J. *et al.* Detection of “oncometabolite” 2-hydroxyglutarate by magnetic resonance analysis as a biomarker of IDH1/2 mutations in glioma. *J. Mol. Med.* **90**, 1161–1171 (2012).

40. Borger, D. R. *et al.* Circulating Oncometabolite 2-Hydroxyglutarate Is a Potential Surrogate Biomarker in Patients with Isocitrate Dehydrogenase-Mutant Intrahepatic Cholangiocarcinoma. *Clin. Cancer Res.* **20**, 1884–1890 (2014).

41. Engqvist, M., Drincovich, M. F., Flügge, U. I. & Maurino, V. G. Two D-2-Hydroxy-acid Dehydrogenases in Arabidopsis thaliana with Catalytic Capacities to Participate in the Last Reactions of the Methylglyoxal and β-Oxidation Pathways. *J. Biol. Chem.* **284**, 25026–25037 (2009).

42. Lin, A. P. *et al.* D2HGDH regulates alpha-ketoglutarate levels and dioxygenase function by modulating IDH2. *Nat. Commun.* **6**, 7768 (2015).

43. Struys, E. A. *et al.* Mutations in the D-2-Hydroxyglutarate Dehydrogenase Gene Cause D-2-Hydroxyglutaric Aciduria. *Am. J. Hum. Genet.* **76**, 358–360 (2005).

44. Steenweg, M. E. *et al.* An overview of L-2-hydroxyglutarate dehydrogenase gene (L2HGDH) variants: a genotype-phenotype study. *Hum. Mutat.* **31**, 380–390

(2010).

45. Chowdhury, R. *et al.* The oncometabolite 2-hydroxyglutarate inhibits histone lysine demethylases. *EMBO Rep.* **12**, 463–469 (2011).

46. Xu, W. *et al.* Oncometabolite 2-Hydroxyglutarate Is a Competitive Inhibitor of α-Ketoglutarate-Dependent Dioxygenases. *Cancer Cell* **19**, 17–30 (2011).

47. Lu, C. *et al.* IDH mutation impairs histone demethylation and results in a block to cell differentiation. *Nature* **483**, 474–478 (2012).

48. Schvartzman, J. M., Reuter, V. P., Koche, R. P. & Thompson, C. B. 2-hydroxyglutarate inhibits MyoD-mediated differentiation by preventing H3K9 demethylation. *Proc. Natl. Acad. Sci.* **116**, 12851–12856 (2019).

49. Carbonneau, M. *et al.* The oncometabolite 2-hydroxyglutarate activates the mTOR signalling pathway. *Nat. Commun.* **7**, 12700 (2016).

50. Figueroa, M. E. *et al.* Leukemic IDH1 and IDH2 Mutations Result in a Hypermethylation Phenotype, Disrupt TET2 Function, and Impair Hematopoietic Differentiation. *Cancer Cell* **18**, 553–567 (2010).

51. Walport, L. J. *et al.* Arginine demethylation is catalysed by a subset of JmjC histone lysine demethylases. *Nat. Commun.* **7**, 11974 (2016).

52. Varier, R. A. & Timmers, H. T. M. Histone lysine methylation and demethylation pathways in cancer. *Biochim. Biophys. Acta - Rev. Cancer* **1815**, 75–89 (2011).

53. Ito, S. *et al.* Role of Tet proteins in 5mC to 5hmC conversion, ES-cell self-renewal and inner cell mass specification. *Nature* **466**, 1129–1133 (2010).

54. Wu, H. & Zhang, Y. Mechanisms and functions of Tet protein-mediated 5-methylcytosine oxidation. *Genes Dev.* **25**, 2436–2452 (2011).

55. Moore, L. D., Le, T. & Fan, G. DNA Methylation and Its Basic Function. *Neuropsychopharmacology* **38**, 23–38 (2013).

56. Turcan, S. *et al.* IDH1 mutation is sufficient to establish the glioma hypermethylator phenotype. *Nature* **483**, 479–483 (2012).

57. Oberley, L. W., Oberley, T. D. & Buettner, G. R. Cell differentiation, aging and cancer: the possible roles of superoxide and superoxide dismutases. *Med. Hypotheses* **6**, 249–68 (1980).

58. Yang, M. & Pollard, P. J. Succinate: A New Epigenetic Hacker. *Cancer Cell* **23**, 709–711 (2013).

59. Yang, M., Soga, T., Pollard, P. J. & Adam, J. The emerging role of fumarate as an oncometabolite. *Front. Oncol.* **2**, (2012).

60. Sasaki, M. *et al.* D-2-hydroxyglutarate produced by mutant IDH1 perturbs collagen maturation and basement membrane function. *Genes Dev.* **26**, 2038–2049 (2012).

61. Koivunen, P. *et al.* Transformation by the (*R*)-enantiomer of 2-hydroxyglutarate linked to EGLN activation. *Nature* **483**, 484–488 (2012).

62. Wang, P. *et al.* Oncometabolite D-2-Hydroxyglutarate Inhibits ALKBH DNA Repair Enzymes and Sensitizes IDH Mutant Cells to Alkylating Agents. *Cell Rep.* **13**, 2353–2361 (2015).

63. Chen, F. *et al.* Oncometabolites D- and L-2-Hydroxyglutarate Inhibit the AlkB Family DNA Repair Enzymes under Physiological Conditions. *Chem. Res. Toxicol.* **30**, 1102–1110 (2017).

64. Elkashef, S. M. *et al.* IDH Mutation, Competitive Inhibition of FTO, and RNA Methylation. *Cancer Cell* **31**, 619–620 (2017).

65. Su, R. *et al. R*-2HG Exhibits Anti-tumor Activity by Targeting FTO/m6A/MYC/CEBPA Signaling. *Cell* **172**, 90-105.e23 (2018).

66. Fu, X. *et al.* 2-Hydroxyglutarate Inhibits ATP Synthase and mTOR Signaling. *Cell Metab.* **22**, 508–515 (2015).

67. Yang, Z. *et al.* 2-HG Inhibits Necroptosis by Stimulating DNMT1-Dependent Hypermethylation of the RIP3 Promoter. *Cell Rep.* **19**, 1846–1857 (2017).

68. McBrayer, S. K. *et al.* Transaminase Inhibition by 2-Hydroxyglutarate Impairs Glutamate Biosynthesis and Redox Homeostasis in Glioma. *Cell* **175**, 101-116.e25 (2018).

69. Smith, E. H., Janknecht, R. & Maher, L. J. Succinate inhibition of α-ketoglutarate-dependent enzymes in a yeast model of paraganglioma. *Hum. Mol. Genet.* **16**, 3136–3148 (2007).

70. Xiao, M. *et al.* Inhibition of α-KG-dependent histone and DNA demethylases by fumarate and succinate that are accumulated in mutations of FH and SDH tumor suppressors. *Genes Dev.* **26**, 1326–1338 (2012).

71. Tarhonskaya, H. *et al.* Studies on the Interaction of the Histone Demethylase KDM5B with Tricarboxylic Acid Cycle Intermediates. *J. Mol. Biol.* **429**, 2895–2906 (2017).

72. Selak, M. A. *et al.* Succinate links TCA cycle dysfunction to oncogenesis by inhibiting HIF-α prolyl hydroxylase. *Cancer Cell* **7**, 77–85 (2005).

73. Pollard, P. J. *et al.* Accumulation of Krebs cycle intermediates and over-expression of HIF1α in tumours which result from germline FH and SDH mutations. *Hum. Mol. Genet.* **14**, 2231–2239 (2005).

74. Hewitson, K. S. *et al.* Structural and Mechanistic Studies on the Inhibition of the Hypoxia-inducible Transcription Factor Hydroxylases by Tricarboxylic Acid Cycle Intermediates. *J. Biol. Chem.* **282**, 3293–3301 (2007).

75. Rose, N. R. *et al.* Inhibitor Scaffolds for 2-Oxoglutarate-Dependent Histone Lysine Demethylases. *J. Med. Chem.* **51**, 7053–7056 (2008).

76. Isaacs, J. S. *et al.* HIF overexpression correlates with biallelic loss of fumarate hydratase in renal cancer: Novel role of fumarate in regulation of HIF stability. *Cancer Cell* **8**, 143–153 (2005).

77. Jo, S. H. *et al.* Control of Mitochondrial Redox Balance and Cellular Defense against Oxidative Damage by Mitochondrial $NADP^+$-dependent Isocitrate Dehydrogenase. *J. Biol. Chem.* **276**, 16168–16176 (2001).

78. Bleeker, F. E. *et al.* The prognostic IDH1 R132 mutation is associated with reduced $NADP^+$-dependent IDH activity in glioblastoma. *Acta Neuropathol.* **119**, 487–494 (2010).

79. Lee, S. M. *et al.* Cytosolic $NADP^+$-dependent isocitrate dehydrogenase status modulates oxidative damage to cells. *Free Radic. Biol. Med.* **32**, 1185–1196 (2002).

80. Shi, J. *et al.* Decreasing GSH and increasing ROS in chemosensitivity gliomas with IDH1 mutation. *Tumor Biol.* **36**, 655–62 (2015).

81. Gelman, S. J. *et al.* Consumption of NADPH for 2-HG Synthesis Increases Pentose Phosphate Pathway Flux and Sensitizes Cells to Oxidative Stress. *Cell Rep.* **22**, 512–522 (2018).

82. Hollinshead, K. E. R. *et al.* Oncogenic IDH1 Mutations Promote Enhanced Proline Synthesis through PYCR1 to Support the Maintenance of Mitochondrial Redox Homeostasis. *Cell Rep.* **22**, 3107–3114 (2018).

83. Ohka, F. *et al.* Quantitative metabolome analysis profiles activation of glutaminolysis in glioma with IDH1 mutation. *Tumor Biol.* **35**, 5911–5920 (2014).

84. Warburg, O. The Metabolism of Carcinoma Cells. *J. Cancer Res.* **9**, 148–163 (1925).

85. RuizRodado, V. *et al.* Metabolic reprogramming associated with aggressiveness occurs in the G-CIMP-high molecular subtypes of $IDH1^{mut}$ lower grade gliomas. *Neuro. Oncol.* **22**, 480–492 (2020).

86. Chen, J. Q. & Russo, J. Dysregulation of glucose transport, glycolysis, TCA cycle and glutaminolysis by oncogenes and tumor suppressors in cancer cells. *Biochim. Biophys. Acta, Rev. Cancer* **1826**, 370–384 (2012).

87. Pavlova, N. N. & Thompson, C. B. The Emerging Hallmarks of Cancer Metabolism. *Cell Metab.* **23**, 27–47 (2016).

88. Eagle, H. Nutrition Needs of Mammalian Cells in Tissue Culture. *Science (80-. ).* **122**, 501–504 (1955).

89. Jiang, J., Srivastava, S. & Zhang, J. Starve Cancer Cells of Glutamine: Break the Spell or Make a Hungry Monster? *Cancers (Basel).* **11**, 804 (2019).

90. Kaelin, W. G. & Ratcliffe, P. J. Oxygen Sensing by Metazoans: The Central Role of the HIF Hydroxylase Pathway. *Mol. Cell* **30**, 393–402 (2008).

91. Metellus, P. *et al.* IDH mutation status impact on *in vivo* hypoxia biomarkers

expression: new insights from a clinical, nuclear imaging and immunohistochemical study in 33 glioma patients. *J. Neurooncol.* **105**, 591–600 (2011).

92. Williams, S. C. *et al.* R132H-mutation of isocitrate dehydrogenase-1 is not sufficient for HIF-1α upregulation in adult glioma. *Acta Neuropathol.* **121**, 279–281 (2011).

93. Zhao, S. *et al.* Glioma-Derived Mutations in IDH1 Dominantly Inhibit IDH1 Catalytic Activity and Induce HIF-1α. *Science (80-. ).* **324**, 261–265 (2009).

94. Das, S. & Marsden, P. A. Angiogenesis in Glioblastoma. *N. Engl. J. Med.* **369**, 1561–1563 (2013).

95. Losman, J. A. *et al.* (*R*)-2-Hydroxyglutarate is sufficient to promote leukemogenesis and its effects are reversible. *Science (80-. ).* **339**, 1621–1625 (2013).

96. Tarhonskaya, H. *et al.* Non-enzymatic chemistry enables 2-hydroxyglutarate-mediated activation of 2-oxoglutarate oxygenases. *Nat. Commun.* **5**, 3423 (2014).

97. Kaelin, W. G. Cancer and Altered Metabolism: Potential Importance of Hypoxia-Inducible Factor and 2-Oxoglutarate-Dependent Dioxygenases. *Cold Spring Harb. Symp. Quant. Biol.* **76**, 335–345 (2011).

98. Acker, T. *et al.* Genetic evidence for a tumor suppressor role of HIF-2α. *Cancer Cell* **8**, 131–141 (2005).

99. Blouw, B. *et al.* The hypoxic response of tumors is dependent on their microenvironment. *Cancer Cell* **4**, 133–46 (2003).

100. Song, L. P. *et al.* Hypoxia-inducible factor-1α-induced differentiation of myeloid leukemic cells is its transcriptional activity independent. *Oncogene* **27**, 519–527 (2008).

101. Chesnelong, C. *et al.* Lactate dehydrogenase A silencing in IDH mutant gliomas. *Neuro. Oncol.* **16**, 686–695 (2014).

102. Kickingereder, P. *et al.* IDH mutation status is associated with a distinct hypoxia/angiogenesis transcriptome signature which is non-invasively predictable with rCBV imaging in human glioma. *Sci. Rep.* **5**, 16238 (2015).

103. Wakimoto, H. *et al.* Targetable signaling pathway mutations are associated with malignant phenotype in IDH-mutant gliomas. *Clin. Cancer Res.* **20**, 2898–909 (2014).

104. Amatangelo, M. D. *et al.* Enasidenib induces acute myeloid leukemia cell differentiation to promote clinical response. *Blood* **130**, 732–741 (2017).

105. Chen, C. *et al.* Cancer-associated IDH2 mutants drive an acute myeloid leukemia that is susceptible to Brd4 inhibition. *Genes Dev.* **27**, 1974–1985 (2013).

106. Bunse, L. *et al.* Suppression of antitumor T cell immunity by the oncometabolite (*R*)-2-hydroxyglutarate. *Nat. Med.* **24**, 1192–1203 (2018).

107. Dang, L., Yen, K. & Attar, E. C. IDH mutations in cancer and progress toward development of targeted therapeutics. *Ann. Oncol.* **27**, 599–608 (2016).

108. Waitkus, M. S., Diplas, B. H. & Yan, H. Biological Role and Therapeutic Potential of IDH Mutations in Cancer. *Cancer Cell* **34**, 186–195 (2018).

109. FDA. FDA approves ivosidenib as first-line treatment for AML with IDH1 mutation. https://www.fda.gov/drugs/resources-information-approved-drugs/fda-approves-ivosidenib-first-line-treatment-aml-idh1-mutation (2019).

110. FDA. FDA granted regular approval to enasidenib for the treatment of relapsed or refractory AML. https://www.fda.gov/drugs/resources-information-approved-drugs/fda-granted-regular-approval-enasidenib-treatment-relapsed-or-refractory-aml (2017).

111. Sulkowski, P. L. *et al.* 2-Hydroxyglutarate produced by neomorphic IDH mutations suppresses homologous recombination and induces PARP inhibitor sensitivity. *Sci. Transl. Med.* **9**, eaal2463 (2017).

112. Pardridge, W. M. The blood-brain barrier: bottleneck in brain drug development. *NeuroRx* **2**, 3–14 (2005).

113. Popovici-Muller, J. *et al.* Discovery of AG-120 (Ivosidenib): A First-in-Class Mutant IDH1 Inhibitor for the Treatment of IDH1 Mutant Cancers. *ACS Med. Chem. Lett.* **9**, 300–305 (2018).

114. Konteatis, Z. *et al.* Vorasidenib (AG-881): A First-in-Class, Brain-Penetrant Dual Inhibitor of Mutant IDH1 and 2 for Treatment of Glioma. *ACS Med. Chem. Lett.* **11**, 101–107 (2020).

115. FDA Centre for drug evaluation and research. 209606Orig1s000 Multi-discipline review. 24, 27, 28 https://www.accessdata.fda.gov/drugsatfda_docs/nda/2017/209606Orig1s000MultidisciplineR.pdf (2017).

116. Johannessen, T. C. A. *et al.* Rapid Conversion of Mutant IDH1 from Driver to Passenger in a Model of Human Gliomagenesis. *Mol. Cancer Res.* **14**, 976–983 (2016).

117. Tateishi, K. *et al.* Extreme Vulnerability of IDH1 Mutant Cancers to NAD+ Depletion. *Cancer Cell* **28**, 773–784 (2015).

118. Pusch, S. *et al.* Pan-mutant IDH1 inhibitor BAY 1436032 for effective treatment of IDH1 mutant astrocytoma *in vivo*. *Acta Neuropathol.* **133**, 629–644 (2017).

119. Kopinja, J. *et al.* A Brain Penetrant Mutant IDH1 Inhibitor Provides *in vivo* Survival Benefit. *Sci. Rep.* **7**, 13853 (2017).

120. Turcan, S. *et al.* Efficient induction of differentiation and growth inhibition in IDH1

mutant glioma cells by the DNMT Inhibitor Decitabine. *Oncotarget* **4**, (2013).

121. Borodovsky, A. *et al.* 5-azacytidine reduces methylation, promotes differentiation and induces tumor regression in a patient-derived IDH1 mutant glioma xenograft. *Oncotarget* **4**, (2013).

122. Cruz, F. D. & Matushansky, I. Solid Tumor Differentiation Therapy – Is It Possible? *Oncotarget* **3**, (2012).

123. Xu, W. P., Zhang, X. & Xie, W. F. Differentiation therapy for solid tumors. *J. Dig. Dis.* **15**, 159–165 (2014).

124. Iqbal, S. *et al.* Insights into protein structural, physicochemical, and functional consequences of missense variants in 1,330 disease-associated human genes. *bioRxiv* 693259 (2019) doi:10.1101/693259.

125. Dietlein, F. *et al.* Identification of cancer driver genes based on nucleotide context. *Nat. Genet.* **52**, 208–218 (2020).

126. Bardella, C. *et al.* Expression of $Idh1^{R132H}$ in the Murine Subventricular Zone Stem Cell Niche Recapitulates Features of Early Gliomagenesis. *Cancer Cell* **30**, 578–594 (2016).

127. Amankulor, N. M. *et al.* Mutant IDH1 regulates the tumor-associated immune system in gliomas. *Genes Dev.* **31**, 774–786 (2017).

128. Philip, B. *et al.* Mutant IDH1 Promotes Glioma Formation *in vivo*. *Cell Rep.* **23**, 1553–1564 (2018).

129. Modrek, A. S. *et al.* Low-Grade Astrocytoma Mutations in IDH1, P53, and ATRX Cooperate to Block Differentiation of Human Neural Stem Cells via Repression of SOX2. *Cell Rep.* **21**, 1267–1280 (2017).

130. Seah, C. *et al.* Neuronal Death Resulting from Targeted Disruption of the Snf2 Protein ATRX Is Mediated by p53. *J. Neurosci.* **28**, 12570–12580 (2008).

131. Liu, C. *et al.* Mosaic Analysis with Double Markers Reveals Tumor Cell of Origin in Glioma. *Cell* **146**, 209–221 (2011).

132. Zheng, H. *et al.* p53 and Pten control neural and glioma stem/progenitor cell renewal and differentiation. *Nature* **455**, 1129–1133 (2008).

133. Sanson, M. *et al.* Isocitrate Dehydrogenase 1 Codon 132 Mutation Is an Important Prognostic Biomarker in Gliomas. *J. Clin. Oncol.* **27**, 4150–4154 (2009).

134. Wang, P. *et al.* Mutations in isocitrate dehydrogenase 1 and 2 occur frequently in intrahepatic cholangiocarcinomas and share hypermethylation targets with glioblastomas. *Oncogene* **32**, 3091–3100 (2013).

135. Molenaar, R. J. *et al.* The combination of IDH1 mutations and MGMT methylation status predicts survival in glioblastoma better than either IDH1 or MGMT alone. *Neuro. Oncol.* **16**, 1263–1273 (2014).

136. Ceccarelli, M. *et al.* Molecular Profiling Reveals Biologically Discrete Subsets and Pathways of Progression in Diffuse Glioma. *Cell* **164**, 550–563 (2016).

137. Tran, A. N. *et al.* Increased sensitivity to radiochemotherapy in IDH1 mutant glioblastoma as demonstrated by serial quantitative MR volumetry. *Neuro. Oncol.* **16**, 414–420 (2014).

138. Rohle, D. *et al.* An Inhibitor of Mutant IDH1 Delays Growth and Promotes Differentiation of Glioma Cells. *Science (80-. ).* **340**, 626–630 (2013).

139. Wang, F. *et al.* Targeted inhibition of mutant IDH2 in leukemia cells induces cellular differentiation. *Science* **340**, 622–6 (2013).

140. Intlekofer, A. M. *et al.* Acquired resistance to IDH inhibition through *trans* or *cis* dimer-interface mutations. *Nature* **559**, 125–129 (2018).

141. FDA. FDA warns that symptoms of a serious condition affecting the blood cells are not being recognized with the leukemia medicine Idhifa (enasidenib). https://www.fda.gov/drugs/drug-safety-and-availability/fda-warns-symptoms-serious-condition-affecting-blood-cells-are-not-being-recognized-leukemia (2018).

142. Ramsey, M. R. & Sharpless, N. E. ROS as a tumour suppressor? *Nat. Cell Biol.* **8**, 1213–1215 (2006).

143. Juan, M. E., Wenzel, U., Daniel, H. & Planas, J. M. Resveratrol Induces Apoptosis through ROS-Dependent Mitochondria Pathway in HT-29 Human Colorectal Carcinoma Cells. *J. Agric. Food Chem.* **56**, 4813–4818 (2008).

144. Toler, S. M., Noe, D. & Sharma, A. Selective enhancement of cellular oxidative stress by chloroquine: implications for the treatment of glioblastoma multiforme. *Neurosurg. Focus* **21**, 1–4 (2006).

145. Renschler, M. F. The emerging role of reactive oxygen species in cancer therapy. *Eur. J. Cancer* **40**, 1934–1940 (2004).

146. Oliva, C. R., Moellering, D. R., Gillespie, G. Y. & Griguer, C. E. Acquisition of Chemoresistance in Gliomas Is Associated with Increased Mitochondrial Coupling and Decreased ROS Production. *PLoS One* **6**, e24665 (2011).

147. Liu, Y. *et al.* Targeting IDH1-Mutated Malignancies with NRF2 Blockade. *J. Natl. Cancer Inst.* **111**, 1033–1041 (2019).

148. Wang, J. & Yi, J. Cancer cell killing via ROS: To increase or decrease, that is the question. *Cancer Biol. Ther.* **7**, 1875–1884 (2008).

149. Molenaar, R. J. *et al.* Radioprotection of IDH1-Mutated Cancer Cells by the IDH1-Mutant Inhibitor AGI-5198. *Cancer Res.* **75**, 4790–4802 (2015).

150. Shi, J. *et al.* An IDH1 mutation inhibits growth of glioma cells via GSH depletion and ROS generation. *Neurol. Sci.* **35**, 839–845 (2014).

151. Zhu, H. *et al.* IDH1 R132H Mutation Enhances Cell Migration by Activating AKT-mTOR Signaling Pathway, but Sensitizes Cells to 5-FU Treatment as NADPH and GSH Are Reduced. *PLoS One* **12**, e0169038 (2017).

152. Sasaki, M. *et al.* IDH1(R132H) mutation increases murine haematopoietic progenitors and alters epigenetics. *Nature* **488**, 656–659 (2012).

153. Chaturvedi, A. *et al.* Mutant IDH1 promotes leukemogenesis *in vivo* and can be specifically targeted in human AML. *Blood* **122**, 2877–2887 (2013).

154. Molenaar, R. J., Maciejewski, J. P., Wilmink, J. W. & van Noorden, C. J. F. Wild-type and mutated IDH1/2 enzymes and therapy responses. *Oncogene* **37**, 1949–1960 (2018).

155. Jin, G. *et al.* Disruption of Wild-Type IDH1 Suppresses D-2-Hydroxyglutarate Production in IDH1-Mutated Gliomas. *Cancer Res.* **73**, 496–501 (2013).

156. Robinson, G. *et al. In vitro* visualization and characterization of wild type and mutant IDH homo- and heterodimers using Bimolecular Fluorescence Complementation. *Cancer Res. Front.* **2**, 311–329 (2016).

157. Brooks, E. *et al.* Identification and Characterization of Small-Molecule Inhibitors of the R132H/R132H Mutant Isocitrate Dehydrogenase 1 Homodimer and R132H/Wild-Type Heterodimer. *J. Biomol. Screen.* **19**, 1193–1200 (2014).

158. Yang, B., Zhong, C., Peng, Y., Lai, Z. & Ding, J. Molecular mechanisms of “off-on switch” of activities of human IDH1 by tumor-associated mutation R132H. *Cell Res.* **20**, 1188–1200 (2010).

159. Ward, P. S. *et al.* The Potential for Isocitrate Dehydrogenase Mutations to Produce 2-Hydroxyglutarate Depends on Allele Specificity and Subcellular Compartmentalization. *J. Biol. Chem.* **288**, 3804–3815 (2013).

160. Ye, J. *et al.* IDH1 deficiency attenuates gluconeogenesis in mouse liver by impairing amino acid utilization. *Proc. Natl. Acad. Sci.* **114**, 292–297 (2017).

161. Itsumi, M. *et al.* Idh1 protects murine hepatocytes from endotoxin-induced oxidative stress by regulating the intracellular $NADP^+$/NADPH ratio. *Cell Death Differ.* **22**, 1837–1845 (2015).

162. Anderson, N. M. *et al.* The TCA cycle transferase DLST is important for MYC-mediated leukemogenesis. *Leukemia* **30**, 1365–1374 (2016).

163. Hardacre, J. CPI-613 in Combination With Modified FOLFIRINOX in Locally Advanced Pancreatic Cancer. *ClinicalTrials.gov Identifier: NCT03699319* https://clinicaltrials.gov/ct2/show/NCT03699319 (2018).

164. Xu, C. *et al.* HNF4α pathway mapping identifies wild-type IDH1 as a targetable metabolic node in gastric cancer. *Gut* **69**, 231–242 (2020).

165. Sun, N. *et al.* Isocitrate Dehydrogenase 1 Is a Novel Plasma Biomarker for the Diagnosis of Non-Small Cell Lung Cancer. *Clin. Cancer Res.* **19**, 5136–5145 (2013).

166. Calvert, A. E. *et al.* Cancer-Associated IDH1 Promotes Growth and Resistance to Targeted Therapies in the Absence of Mutation. *Cell Rep.* **19**, 1858–1873 (2017).

167. Tommasini-Ghelfi, S. *et al.* Cancer-associated mutation and beyond: The emerging biology of isocitrate dehydrogenases in human disease. *Sci. Adv.* **5**, eaaw4543 (2019).

168. Cairns, R. A. & Mak, T. W. Oncogenic isocitrate dehydrogenase mutations: Mechanisms, models, and clinical opportunities. *Cancer Discov.* **3**, 730–741 (2013).

169. Okoye-Okafor, U. C. *et al.* New IDH1 mutant inhibitors for treatment of acute myeloid leukemia. *Nat. Chem. Biol.* **11**, 878–886 (2015).

170. Li, Z. *et al.* FTO Plays an Oncogenic Role in Acute Myeloid Leukemia as a $N^6$-Methyladenosine RNA Demethylase. *Cancer Cell* **31**, 127–141 (2017).

171. Molenaar, R. J. *et al.* IDH1/2 Mutations Sensitize Acute Myeloid Leukemia to PARP Inhibition and This Is Reversed by IDH1/2-Mutant Inhibitors. *Clin. Cancer Res.* **24**, 1705–1715 (2018).

172. Merk, A. *et al.* Breaking Cryo-EM Resolution Barriers to Facilitate Drug Discovery. *Cell* **165**, 1698–1707 (2016).

173. Urban, D. J. *et al.* Assessing inhibitors of mutant isocitrate dehydrogenase using a suite of pre-clinical discovery assays. *Sci. Rep.* **7**, 12758 (2017).

174. Popovici-Muller, J. *et al.* Discovery of the First Potent Inhibitors of Mutant IDH1 That Lower Tumor 2-HG *in vivo*. *ACS Med. Chem. Lett.* **3**, 850–855 (2012).

175. Chaturvedi, A. *et al.* Pan-mutant-IDH1 inhibitor BAY1436032 is highly effective against human IDH1 mutant acute myeloid leukemia *in vivo*. *Leukemia* **31**, 2020–2028 (2017).

176. Cho, Y. S. *et al.* Discovery and Evaluation of Clinical Candidate IDH305, a Brain Penetrant Mutant IDH1 Inhibitor. *ACS Med. Chem. Lett.* **8**, 1116–1121 (2017).

177. Levell, J. R. *et al.* Optimization of 3-Pyrimidin-4-yl-oxazolidin-2-ones as Allosteric and Mutant Specific Inhibitors of IDH1. *ACS Med. Chem. Lett.* **8**, 151–156 (2017).

178. Ma, R. & Yun, C. H. H. Crystal structures of pan-IDH inhibitor AG-881 in complex with mutant human IDH1 and IDH2. *Biochem. Biophys. Res. Commun.* **503**, 2912–2917 (2018).

179. Yen, K. *et al.* AG-221, a First-in-Class Therapy Targeting Acute Myeloid Leukemia Harboring Oncogenic IDH2 Mutations. *Cancer Discov.* **7**, 478–493 (2017).

180. Matzapetakis, M. *et al.* Manganese Citrate Chemistry: Syntheses, Spectroscopic Studies, and Structural Characterizations of Novel Mononuclear, Water-Soluble Manganese Citrate Complexes. *Inorg. Chem.* **39**, 4044–4051 (2000).

181. Rendina, A. R. *et al.* Mutant IDH1 enhances the production of 2-hydroxyglutarate due to its kinetic mechanism. *Biochemistry* **52**, 4563–4577 (2013).

182. Hirata, M. *et al.* Mutant IDH is sufficient to initiate enchondromatosis in mice. *Proc. Natl. Acad. Sci.* **112**, 2829–2834 (2015).

183. Deng, G. *et al.* Selective inhibition of mutant isocitrate dehydrogenase 1 (IDH1) via disruption of a metal binding network by an allosteric small molecule. *J. Biol. Chem.* **290**, 762–774 (2015).

184. Berg, J. M., Tymoczko, J. L. & Stryer, L. The Michaelis-Menten Model Accounts for the Kinetic Properties of Many Enzymes. in *Biochemistry* Section 8.4 (New York: W H Freeman, 2002).

185. Pietrak, B. *et al.* A Tale of Two Subunits: How the Neomorphic R132H IDH1 Mutation Enhances Production of αHG. *Biochemistry* **50**, 4804–4812 (2011).

186. Avellaneda Matteo, D. *et al.* Molecular mechanisms of isocitrate dehydrogenase 1 (IDH1) mutations identified in tumors: The role of size and hydrophobicity at residue 132 on catalytic efficiency. *J. Biol. Chem.* **292**, 7971–7983 (2017).

187. Fielding, L. NMR Methods for the Determination of Protein- Ligand Dissociation Constants. *Curr. Top. Med. Chem.* **3**, 39–53 (2003).

188. Roman, J. V, Melkonian, T. R., Silvaggi, N. R. & Moran, G. R. Transient-State Analysis of Human Isocitrate Dehydrogenase I: Accounting for the Interconversion of Active and Non-Active Conformational States. *Biochemistry* **58**, 5366–5380 (2019).

189. Stoddard, B. L., Dean, A. & Koshland, D. E. Structure of isocitrate dehydrogenase with isocitrate, nicotinamide adenine dinucleotide phosphate, and calcium at 2.5-Å resolution: A pseudo-Michaelis ternary complex. *Biochemistry* **32**, 9310–9316 (1993).

190. Webb, B. A., Chimenti, M., Jacobson, M. P. & Barber, D. L. Dysregulated pH: a perfect storm for cancer progression. *Nat. Rev. Cancer* **11**, 671–677 (2011).

191. White, K. A. *et al.* Cancer-associated arginine-to-histidine mutations confer a gain in pH sensing to mutant proteins. *Sci. Signal.* **10**, eaam9931 (2017).

192. Szpiech, Z. A. *et al.* Prominent features of the amino acid mutation landscape in cancer. *PLoS One* **12**, e0183273 (2017).

193. Anoosha, P., Sakthivel, R. & Michael Gromiha, M. Exploring preferred amino acid mutations in cancer genes: Applications to identify potential drug targets. *Biochim. Biophys. Acta - Mol. Basis Dis.* **1862**, 155–165 (2016).

194. Intlekofer, A. M. *et al.* L-2-Hydroxyglutarate production arises from noncanonical enzyme function at acidic pH. *Nat. Chem. Biol.* **13**, 494–500 (2017).

195. Rydzik, A. M. *et al.* Ejection of structural zinc leads to inhibition of γ-butyrobetaine hydroxylase. *Bioorg. Med. Chem. Lett.* **24**, 4954–4957 (2014).

196. de Munnik, M. *et al.* Targeting the Mycobacterium tuberculosis transpeptidase $Ldt_{Mt2}$ with cysteine-reactive inhibitors including ebselen. *Chem. Commun.* **55**,

10214–10217 (2019).

197. Capper, M. J. *et al.* The cysteine-reactive small molecule ebselen facilitates effective SOD1 maturation. *Nat. Commun.* **9**, 1693 (2018).

198. Bavetsias, V. *et al.* 8-Substituted Pyrido[3,4-*d*]pyrimidin-4(3*H*)-one Derivatives As Potent, Cell Permeable, KDM4 (JMJD2) and KDM5 (JARID1) Histone Lysine Demethylase Inhibitors. *J. Med. Chem.* **59**, 1388–1409 (2016).

199. Saito, K., Adachi, N., Koyama, H. & Matsushita, M. OGFOD1, a member of the 2-oxoglutarate and iron dependent dioxygenase family, functions in ischemic signaling. *FEBS Lett.* **584**, 3340–7 (2010).

200. Hewitson, K. S. *et al.* Hypoxia-inducible Factor (HIF) Asparagine Hydroxylase Is Identical to Factor Inhibiting HIF (FIH) and Is Related to the Cupin Structural Family. *J. Biol. Chem.* **277**, 26351–26355 (2002).

201. Siehl, D. L. *et al.* Broad 4-Hydroxyphenylpyruvate Dioxygenase Inhibitor Herbicide Tolerance in Soybean with an Optimized Enzyme and Expression Cassette. *Plant Physiol.* **166**, 1162–1176 (2014).

202. Damm, F. *et al.* Prevalence and prognostic value of IDH1 and IDH2 mutations in childhood AML: a study of the AML–BFM and DCOG study groups. *Leukemia* **25**, 1704–1710 (2011).

203. Mayers, J. R. & Vander Heiden, M. G. BCAT1 defines gliomas by IDH status. *Nat. Med.* **19**, 816–817 (2013).

204. Plaut, G. W. E., Schramm, V. L. & Aogaichi, T. Action of magnesium ion on diphosphopyridine nucleotide linked isocitrate dehydrogenase from bovine heart. Characterization of the forms of the substrate and the modifier of the reaction. *J. Biol. Chem.* **249**, 1848–1856 (1974).

205. Villafranca, J. J. & Colman, R. F. Role of Metal Ions in Reactions Catalyzed by Pig Heart Triphosphopyridine Nucleotide-dependent Isocitrate Dehydrogenase. *J. Biol. Chem.* **247**, 215–223 (1972).

206. Villafranca, J. J. & Colman, R. F. Role of Metal Ions in Reactions Catalyzed by Pig Heart Triphosphopyridine Nucleotide-dependent Isocitrate Dehydrogenase. *J. Biol. Chem.* **247**, 209–214 (1972).

207. Christianson, D. W. Structural biology of zinc. *Adv. Protein Chem.* **42**, 281–355 (1991).

208. Bhattacharya, P. K. *Metal Ions in Biochemistry*. (Alpha Science International Limited, 2005).

209. Maguire, M. E. & Cowan, J. A. Magnesium chemistry and biochemistry. *Biometals* **15**, 203–10 (2002).

210. Wolf, F. I. & Cittadini, A. Chemistry and biochemistry of magnesium. *Mol. Aspects Med.* **24**, 3–9.

211. de Valk, H. W. Magnesium in diabetes mellitus. *Neth. J. Med.* **54**, 139–46 (1999).

212. Berridge, M. J. Elementary and global aspects of calcium signalling. *J. Exp. Biol.* **200**, 315–9 (1997).

213. Xie, X. *et al.* Allosteric Mutant IDH1 Inhibitors Reveal Mechanisms for IDH1 Mutant and Isoform Selectivity. *Structure* **25**, 506–513 (2017).

214. Shannon, R. D. Revised effective ionic radii and systematic studies of interatomic distances in halides and chalcogenides. *Acta Crystallogr. Sect. A* **32**, 751–767 (1976).

215. Persson, I. Hydrated metal ions in aqueous solution: How regular are their structures? *Pure Appl. Chem.* **82**, 1901–1917 (2010).

216. Pellecchia, M., Sem, D. S. & Wüthrich, K. NMR in drug discovery. *Nat. Rev. Drug Discov.* **1**, 211–219 (2002).

217. Grubbs, R. D. Intracellular magnesium and magnesium buffering. *Biometals* **15**, 251–259 (2002).

218. Altura, B. T. & Altura, B. M. Measurement of ionized magnesium in whole blood, plasma and serum with a new ion-selective electrode in healthy and diseased human subjects. *Magnes. Trace Elem.* **10**, 90–8.

219. Taylor, J. S. *et al.* Free magnesium levels in normal human brain and brain tumors : $^{31}$P chemical-shift imaging measurements at 1.5 T. *Proc. Natl. Acad. Sci.* **88**, 6810–6814 (1991).

220. Chandra, S., Parker, D. J., Barth, R. F. & Pannullo, S. C. Quantitative imaging of magnesium distribution at single-cell resolution in brain tumors and infiltrating tumor cells with secondary ion mass spectrometry (SIMS). *J. Neurooncol.* **127**, 33–41 (2016).

221. Rydzewski, R. M. *Real World Drug Discovery: A Chemist's Guide to Biotech and Pharmaceutical Research*. (Elsevier Science, 2008).

222. Bock, J. L. The binding of metal ions to ATP: A proton and phosphorus NMR investigation of diamagnetic metal-ATP complexes. *J. Inorg. Biochem.* **12**, 119–130 (1980).

223. Phillips, R. Adenosine and the Adenine Nucleotides. Ionization, Metal Complex Formation, and Conformation in Solution. *Chem. Rev.* **66**, 501–527 (1966).

224. Izatt, R. M., Christensen, J. J. & Rytting, J. H. Sites and thermodynamic quantities associated with proton and metal ion interaction with ribonucleic acid, deoxyribonucleic acid, and their constituent bases, nucleosides, and and nucleotides. *Chem. Rev.* **71**, 439–481 (1971).

225. Dudev, T., Grauffel, C. & Lim, C. How Native and Alien Metal Cations Bind ATP: Implications for Lithium as a Therapeutic Agent. *Sci. Rep.* **7**, 42377 (2017).

226. Evans, R., Dal Poggetto, G., Nilsson, M. & Morris, G. A. Improving the Interpretation of Small Molecule Diffusion Coefficients. *Anal. Chem.* **90**, 3987–3994 (2018).

227. Gawronska, K. & Niewiadomska, E. Participation of citric acid and isocitric acid in the diurnal cycle of carboxylation and decarboxylation in the common ice plant. *Acta Physiol. Plant.* **37**, 61 (2015).

228. Costello, L. C. & Franklin, R. B. Aconitase Activity, Citrate Oxidation, and Zinc Inhibition in Rat Ventral Prostate. *Enzyme* **26**, 281–287 (1981).

229. Zabiszak, M. *et al.* Carboxyl groups of citric acid in the process of complex formation with bivalent and trivalent metal ions in biological systems. *J. Inorg. Biochem.* **182**, 37–47 (2018).

230. Johnson, C. S. Diffusion ordered nuclear magnetic resonance spectroscopy: principles and applications. *Prog. Nucl. Magn. Reson. Spectrosc.* **34**, 203–256 (1999).

231. Helm, L. & Merbach, A. E. Inorganic and Bioinorganic Solvent Exchange Mechanisms. *Chem. Rev.* **105**, 1923–1960 (2005).

232. Dudev, T. & Lim, C. Tetrahedral vs Octahedral Zinc Complexes with Ligands of Biological Interest: A DFT/CDM Study. *J. Am. Chem. Soc.* **122**, 11146–11153 (2000).

233. Westergaard, N., Waagepetersen, H. S., Belhage, B. & Schousboe, A. Citrate, a Ubiquitous Key Metabolite with Regulatory Function in the CNS. *Neurochem. Res.* **42**, 1583–1588 (2017).

234. Lindberg, J. S., Zobitz, M. M., Poindexter, J. R. & Pak, C. Y. Magnesium bioavailability from magnesium citrate and magnesium oxide. *J. Am. Coll. Nutr.* **9**, 48–55 (1990).

235. Silva, A. M. N., Kong, X. & Hider, R. C. Determination of the pKa value of the hydroxyl group in the α-hydroxycarboxylates citrate, malate and lactate by $^{13}C$ NMR: implications for metal coordination in biological systems. *BioMetals* **22**, 771–778 (2009).

236. Davis, M. I. *et al.* Biochemical, Cellular, and Biophysical Characterization of a Potent Inhibitor of Mutant Isocitrate Dehydrogenase IDH1. *J. Biol. Chem.* **289**, 13717–13725 (2014).

237. Zheng, B. *et al.* Crystallographic investigation and selective inhibition of mutant isocitrate dehydrogenase. *ACS Med. Chem. Lett.* **4**, 542–546 (2013).

238. Watts, J. M. *et al.* A phase 1 dose escalation study of the IDH1 m inhibitor, FT-2102, in patients with acute myeloid leukemia (AML) or myelodysplastic syndrome (MDS). *J. Clin. Oncol.* **36**, 7009–7009 (2018).

239. Cho, Y. S. *et al.* 3-pyrimidin-4-yl-oxazolidin-2-ones as inhibitors of mutant IDH. WO 2013/046136 Al. 283–300 (2013).

240. Konermann, L. Addressing a Common Misconception: Ammonium Acetate as Neutral pH “Buffer” for Native Electrospray Mass Spectrometry. *J. Am. Soc. Mass Spectrom.* **28**, 1827–1835 (2017).

241. Kitova, E. N., El-Hawiet, A., Schnier, P. D. & Klassen, J. S. Reliable Determinations of Protein–Ligand Interactions by Direct ESI-MS Measurements. Are We There Yet? *J. Am. Soc. Mass Spectrom.* **23**, 431–441 (2012).

242. Ottis, P. & Crews, C. M. Proteolysis-Targeting Chimeras: Induced Protein Degradation as a Therapeutic Strategy. *ACS Chem. Biol.* **12**, 892–898 (2017).

243. Galdeano, C. *et al.* Structure-Guided Design and Optimization of Small Molecules Targeting the Protein–Protein Interaction between the von Hippel–Lindau (VHL) E3 Ubiquitin Ligase and the Hypoxia Inducible Factor (HIF) Alpha Subunit with in Vitro Nanomolar Affinities. *J. Med. Chem.* **57**, 8657–8663 (2014).

244. Yang, N. J. & Hinner, M. J. Getting Across the Cell Membrane: An Overview for Small Molecules, Peptides, and Proteins. in *Site-Specific Protein Labeling* 29–53 (2015). doi:10.1007/978-1-4939-2272-7_3.

245. Capper, D. *et al.* Characterization of R132H Mutation-specific IDH1 Antibody Binding in Brain Tumors. *Brain Pathol.* **20**, 245–254 (2010).

246. Haraguchi, C. M., Mabuchi, T. & Yokota, S. Localization of a Mitochondrial Type of NADP-dependent Isocitrate Dehydrogenase in Kidney and Heart of Rat: An Immunocytochemical and Biochemical Study. *J. Histochem. Cytochem.* **51**, 215–226 (2003).

247. Galvez, S. *et al.* Mitochondrial localization of a NADR-dependent isocitrate dehydrogenase isoenzyme by using the green fluorescent protein as a marker. *Proc. Natl. Acad. Sci.* **95**, 7813–7818 (1998).

248. Tóth, L., Muszbek, L. & Komáromi, I. Mechanism of the irreversible inhibition of human cyclooxygenase-1 by aspirin as predicted by QM/MM calculations. *J. Mol. Graph. Model.* **40**, 99–109 (2013).

249. Waxman, D. J. & Strominger, J. L. Penicillin-Binding Proteins and the Mechanism of Action of Beta-Lactam Antibiotics1. *Annu. Rev. Biochem.* **52**, 825–869 (1983).

250. Singh, J., Petter, R. C., Baillie, T. A. & Whitty, A. The resurgence of covalent drugs. *Nat. Rev. Drug Discov.* **10**, 307–317 (2011).

251. Kwak, E. L. *et al.* Irreversible inhibitors of the EGF receptor may circumvent acquired resistance to gefitinib. *Proc. Natl. Acad. Sci.* **102**, 7665–7670 (2005).

252. Hagel, M. *et al.* Selective irreversible inhibition of a protease by targeting a noncatalytic cysteine. *Nat. Chem. Biol.* **7**, 22–24 (2011).

253. Kim, Y. *et al.* Efficient Site-Specific Labeling of Proteins via Cysteines. *Bioconjug. Chem.* **19**, 786–791 (2008).

254. Cao, S. *et al.* WO 2012171337 A1. 1–431 (2012).

255. Mendoza, V. L. & Vachet, R. W. Probing protein structure by amino acid-specific covalent labeling and mass spectrometry. *Mass Spectrom. Rev.* **28**, 785–815 (2009).

256. Chrisman, I. M. *et al.* Defining a conformational ensemble that directs activation of PPARγ. *Nat. Commun.* **9**, 1794 (2018).

257. Pucher, G. W., Abrahams, M. D. & Vickery, H. B. The preparation of optically active isocitric acid from Bryophyllum leaf tissue. *J. Biol. Chem.* **172**, 579–88 (1948).

258. Mrowietz, U., Morrison, P. J., Suhrkamp, I., Kumanova, M. & Clement, B. The Pharmacokinetics of Fumaric Acid Esters Reveal Their *in vivo* Effects. *Trends Pharmacol. Sci.* **39**, 1–12 (2018).

259. Szutowicz, A., Stepień, M., Lysiak, W. & Angielski, S. Effect of (-)hydroxycitrate on the activities of ATP citrate lyase and the enzymes of acetyl-CoA metabolism in rat brain. *Acta Biochim. Pol.* **23**, 227–34 (1976).

260. Perez, H. L. *et al.* Antibody–drug conjugates: current status and future directions. *Drug Discov. Today* **19**, 869–881 (2014).

261. Chari, R. V *et al.* Immunoconjugates containing novel maytansinoids: promising anticancer drugs. *Cancer Res.* **52**, 127–31 (1992).

262. Hoffmann, R. M. *et al.* Antibody structure and engineering considerations for the design and function of Antibody Drug Conjugates (ADCs). *Oncoimmunology* **7**, e1395127 (2018).

263. Chari, R. V. J. Targeted cancer therapy: Conferring specificity to cytotoxic drugs. *Acc. Chem. Res.* **41**, 98–107 (2008).

264. Vishnumaya & Singh, V. K. Highly Enantioselective Water-Compatible Organocatalyst for Michael Reaction of Ketones to Nitroolefins. *Org. Lett.* **9**, 1117–1119 (2007).

265. Rogozińska-Szymczak, M. & Mlynarski, J. Unmodified Primary Amine Organocatalysts for Asymmetric Michael Reactions in Aqueous Media. *Eur. J. Org. Chem.* **2015**, 6047–6051 (2015).

266. Hayashi, Y. *et al.* Combined Proline–Surfactant Organocatalyst for the Highly Diastereo- and Enantioselective Aqueous Direct Cross-Aldol Reaction of Aldehydes. *Angew. Chemie Int. Ed.* **45**, 5527–5529 (2006).

267. Panowski, S., Bhakta, S., Raab, H., Polakis, P. & Junutula, J. R. Site-specific antibody drug conjugates for cancer therapy. *MAbs* **6**, 34–45 (2014).

268. Mondal, M. A. & Mandal, D. Carbohydrate-based organocatalysts in direct asymmetric aqueous aldol reaction. *J. Carbohydr. Chem.* **35**, 181–200 (2016).

269. Bayat, S. *et al.* Various Polar Tripeptides as Asymmetric Organocatalyst in Direct Aldol Reactions in Aqueous Media. *Chirality* **25**, 726–734 (2013).

270. Nugent, T. C., Umar, M. N. & Bibi, A. Picolylamine as an organocatalyst template for highly diastereo- and enantioselective aqueous aldol reactions. *Org. Biomol. Chem.* **8**, 4085 (2010).

271. Choi, K. Y., Swierczewska, M., Lee, S. & Chen, X. Protease-Activated Drug Development. *Theranostics* **2**, 156–179 (2012).

272. Jiang, B. *et al.* A Novel Peptide Isolated from a Phage Display Peptide Library with Trastuzumab Can Mimic Antigen Epitope of HER-2. *J. Biol. Chem.* **280**, 4656–4662 (2005).

273. Riemer, A. B. *et al.* Generation of Peptide mimics of the epitope recognized by trastuzumab on the oncogenic protein Her-2/neu. *J. Immunol.* **173**, 394–401 (2004).

274. Weidle, U. H., Tiefenthaler, G. & Georges, G. Proteases as activators for cytotoxic prodrugs in antitumor therapy. *Cancer Genomics Proteomics* **11**, 67–79.

275. Cho, H. S. *et al.* Structure of the extracellular region of HER2 alone and in complex with the Herceptin Fab. *Nature* **421**, 756–760 (2003).

276. Bostrom, J. *et al.* Variants of the Antibody Herceptin That Interact with HER2 and VEGF at the Antigen Binding Site. *Science (80-. ).* **323**, 1610–1614 (2009).

277. Franklin, M. C. *et al.* Insights into ErbB signaling from the structure of the ErbB2-pertuzumab complex. *Cancer Cell* **5**, 317–28 (2004).

278. Baselga, J. Clinical trials of Herceptin (trastuzumab). *Eur. J. Cancer* **37 Suppl 1**, S18-24 (2001).

279. Iqbal, N. N. & Iqbal, N. N. Human Epidermal Growth Factor Receptor 2 (HER2) in Cancers: Overexpression and Therapeutic Implications. *Mol. Biol. Int.* **2014**, 1–9 (2014).

280. Seldon, T. A., Hughes, K. E., Munster, D. J., Chin, D. Y. & Jones, M. L. Improved protein-A separation of V H3 fab from FC after papain digestion of antibodies. *J. Biomol. Tech.* **22**, 50–52 (2012).

281. Raju, T. S. & Scallon, B. J. Glycosylation in the Fc domain of IgG increases resistance to proteolytic cleavage by papain. *Biochem. Biophys. Res. Commun.* **341**, 797–803 (2006).

282. Fang, Y. Label-Free Cell-Based Assays with Optical Biosensors in Drug Discovery. *Assay Drug Dev. Technol.* **4**, 583–595 (2006).

283. Eglen, R. M. *et al.* The Use of AlphaScreen Technology in HTS: Current Status. *Curr. Chem. Genomics* **1**, 2–10 (2008).

284. McAllister, T. E. *et al.* Non-competitive cyclic peptides for targeting enzyme–substrate complexes. *Chem. Sci.* **9**, 4569–4578 (2018).

285. Aguilar, J. A., Nilsson, M., Bodenhausen, G. & Morris, G. A. Spin echo NMR spectra

without J modulation. *Chem. Commun.* **48**, 811–813 (2012).

286. Tang, Y. *et al.* Imaging of HER2/neu-positive BT-474 human breast cancer xenografts in athymic mice using 111In-trastuzumab (Herceptin) Fab fragments. *Nucl. Med. Biol.* **32**, 51–58 (2005).

287. Castañeda, L. *et al.* Acid-cleavable thiomaleamic acid linker for homogeneous antibody-drug conjugation. *Chem. Commun. (Camb).* **49**, 8187–9 (2013).

288. Lasorsa, A. *et al.* Probing the interaction between cisplatin and the therapeutic monoclonal antibody trastuzumab. *RSC Adv.* **6**, 29229–29236 (2016).